Department of biotechnology and bioscience

PhD program in life science

Cycle XXIX

Curriculum in industrial biotechnology

Dissecting the critical role of cancer/endothelial interactions in metastatic cascade through engineered 3D vascularized microfluidic and mesoscale models

Surname Gilardi

Name Mara

Registration number

Tutor: Prof. Marco Vanoni

Co-tutor: Dr. Matteo Moretti

Coordinator: Prof. Marco Vanoni

ACADEMIC YEAR 2017

...To everyone who

believed in me....

…Impossible is nothing…

Index

Chapter3

Chapter5

A 3D vascularized bone remodeling model combining osteoblasts and osteoclasts in a CaP nanoparticle-enriched matrix

Chapter 7

Chapter 8

Chapter 9

Chapter10

Introduction

Cancer Metastases

From: M. Gilardi, M. Vanoni, M. Moretti

Review in preparation

Metastasis is responsible of more than 90% of cancer related death. In fact, as reported in a recent analysis of the American Cancer Society, there were 14.1 million new cancer cases, 8.2 million cancer deaths and 32.6 million people living with cancer (within 5 years of diagnosis) in 2012 worldwide. Furthermore, 57% (8 million) of new cancer cases, 65% (5.3 million) of the cancer deaths and 48% (15.6 million) of the 5-year prevalent cancer cases occurred in the less developed regions (1).

During the colonization of distant organs, circulating tumor cells must face many challenges through mechanisms that science is only now starting to elucidate. The metastatic process consists of a series of steps (FIG. 1), all of which must be successfully completed to give rise to a metastatic tumor. As a primary tumor grows, it needs to develop a blood supply that can support its metabolic needs. These new blood vessels also provide an escape route through which cells enter into the body's circulatory blood system (intravasation). To an effective metastatization, cells must survive to the circulation shear stress and to the interaction with immune system until they extravasate towards the secondary organ site (2). Once in the new organ, cancer cells start the growth, first as micro and then as macro-metastasis, sustained by the so called "early-metastatic niche" in order for a macroscopic tumor to form (3).

Escape from primary tumor

During metastatic dissemination, (Fig1) cancer cells from a primary tumor can invade the surrounding tissues either as single cells or collectively as groups (4-9). In this context, cancer cells which invade as single cells may dig a path through the extracellular matrix fibers (5), in particular they can move following collagen fibers (10) or migrate collectively in groups establishing the tumor invasion front (9). In this field it has been showed that distinct cancer-cell clones show cooperative behavior promoting their mutual survival and metastatic capacity (11, 12). Thus, patients with prostate cancer evidenced polyclonal metastatic seeding and in experimental models polyclonal clusters of CTCs gave rise to more metastases than single cells (13, 14). Invasive cancer cells subsequently enter into the circulation by breaching directly through blood vessel wall in a process called intravasation. During metastatic progression, tumor cells can undergo the epithelial-to-mesenchymal transition (EMT), which is defined as a reversible phenotypic modification in which cancer cells lose intercellular adhesion and epithelial polarization to acquire motility and invasiveness (15). In addition, EMT can promote intravasation while a reversal of EMT phenotype after extravasation (in which cancer cells exit the circulation to enter in secondary organs) can facilitate metastatic colonization (16). Furthermore, recent studies has evidenced a critical role of EMT in chemoresistence (17).
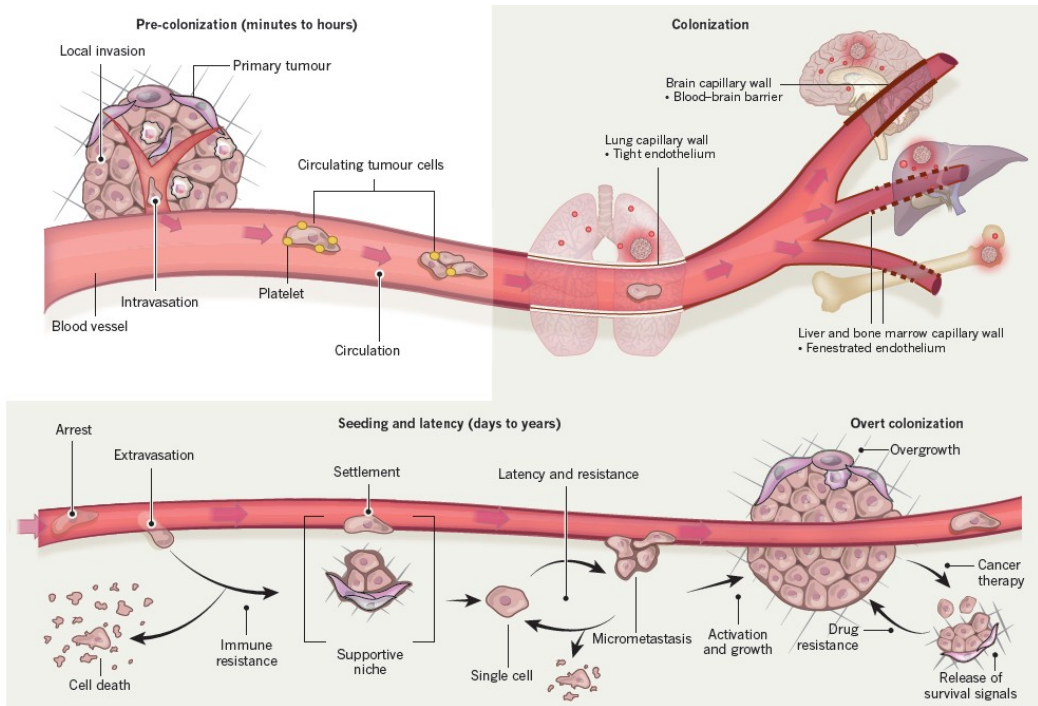
(From: Massagué et al. Metastatic colonization by circulating tumour cells)

Fig1: Metastatic dissemination. Metastasis proceeds through multiple steps and restrictive bottlenecks. The pre-colonization phase of metastasis comprises a series of events that occur on a timescale of minutes to hours. Local invasion of the primary tumour by cancer cells is followed by their intravasation into the tumour vasculature. The cancer cells then enter the circulatory system as single cells or clusters that are coated with platelets. Circulatory patterns, which move blood through the lungs and then on to other organs, and the differing structure of the capillary walls in each organ influence the dissemination of CTCs. On their arrest in capillaries at distant sites, the cancer cells extravasate into the parenchyma of target organs to commence colonization. Colonization can be parsed into many steps that occur on a timescale of years. After extravasation, colonizing cancer cells must develop resistance to immunity and other host-tissue defences to survive. Settlement in supportive niches enables them to survive and retain their stem-like tumour-initiating capacity. The cancer cells then enter a latent state as single cells or micrometastases. During latency, which can last from months to decades in a process called dormancy, disseminated cells must achieve long-term survival. They might also acquire traits that are required to overtake host tissue. When the cancer cells break out of latency, they reinitiate overt outgrowth and overtake the local tissue

microenvironment. Therapeutic treatment can partially eliminate clinically manifest metastases. However, under therapy-induced stress, cancer cells and non-neoplastic stromal cells mobilize survival signals that nurture the residual disease until minority drug-resistant clones emerge to lead the outgrowth of a drug-resistant tumor. Different host-tissue microenvironments select for cancer cells with distinct metastatic traits, which gives rise to organ-specific populations of metastatic cells.

Intravasation

Intravasation and extravasation of cancer cells both require the disruption of endothelial junctions for the cancer cells to cross the endothelium in a process that is known as transendothelial migration (TEM). However, intravasation and extravasation are fundamentally different processes because cancer cells approach the endothelium from opposite sides (18). To intravasate, tumor cells need to invade the tissues through the matrix and towards blood vessels. Tumors induce new blood vessels formation in a process called local angiogenesis, and these new vessels generally have weak cell–cell junctions through which cancer cells can easier enter the circulation (19). Cancer cells transmigration can occur either paracellularly through the endothelial cell (EC) junctions or transcellularly through the EC body (18).

Matrix metalloproteinase 1 (MMP1) seems to be required for paracellular intravasation in regions where protease-activated receptor 1 (PAR1) on ECs mediates the remodelling of endothelial junctions. Alternatively, a disintegrin and metalloproteinase 12 (ADAM12) on ECs can induce cleavage of vascular endothelial cadherin (VE‑cadherin) and angiopoietin 1 receptor (TIE2), which leads to disruption of endothelial junctions leading to extravasation.

Into the circulation

Circulating cancer cells (CTCs) are present in the circulation of patients with primary solid tumors, and it is generally assumed that some of these cells will eventually give rise to overt metastases (20). Into the circulatory system tumor cells encounter different environmental challenges and stimuli that profoundly regulate their metastatic potential (Fig2). These actors assist tumor cell in extravasation to secondary sites and hence in the establishment of tumor cells in the early metastatic niche (21). If cancer cells survive to the shear stress and to the immune surveillance attack, during their stay in the bloodflow helped by circulating elements they may eventually interact with endothelial cells (ECs) that line the blood vessels in the "rolling" process leading to more stable vascular adhesion. During vascular adhesion, cancer cells are attached to endothelial cells and interact with many other circulating cells in the bloodstream, including platelets, and neutrophils which modulate the efficiency of extravasation (3, 22). Furthermore, cytokines and chemokines that modulate endothelial barrier permeability are often secreted by cancer cells or by associated circulating cells and these stimuli can impact extravasation.
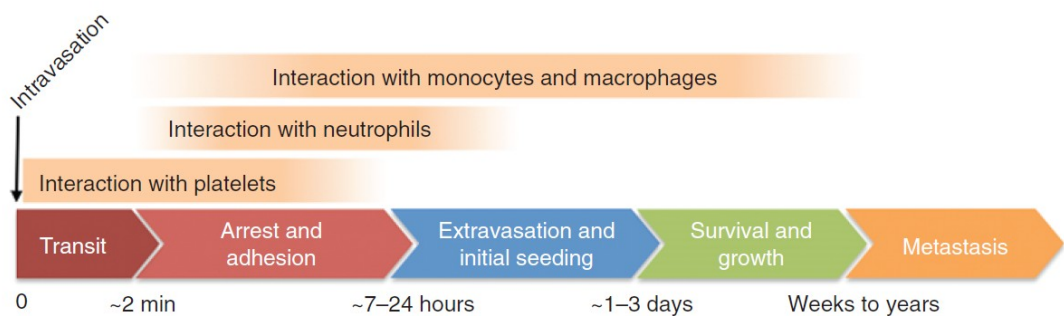
(From Labelle et al. The Initial Hours of Metastasis:The Importance of Cooperative Host–Tumor Cell Interactions during Hematogenous Dissemination)

Fig2: Temporal dynamics of host–tumor cell interactions during the early steps of the metastatic cascade. Tumor cells intravasate, rapidly transit through the circulation and arrest in the vasculature of a secondary organ, generally within a few minutes. During this period, platelets form aggregates around CTCs or arrested tumor cells. Neutrophils also interact with tumor cells within the first day. Seven to 48 hours after tail-vein injection of tumor cells, monocytes/macrophages are also recruited to their vicinity. Extravasation typically takes place within the first 1 to 3 days after initial arrest. By that time, most tumor cells have exited the bloodstream and seeded into the stroma of the secondary site and additional myeloid cells are recruited to this initial metastatic niche. The tumor cells may reinitiate growth to form metastases within a few weeks. Alternatively, tumor cells can survive and stay dormant for a long period before reinitiating growth and thus form clinically relevant metastases only months or years later. Overall, only a few cells successfully complete the metastatic cascade and give rise to overt metastases.

In fact, during the limited period into the bloodflow tumor cells take advantage of circulating elements modulating their features with the aim to escape to immune surveillance. In this context, platelets that are associated with CTCs can stimulate extravasation by releasing TGF-β and triggering EMT in the cancer cells or by secreting adenine nucleotides, which relax endothelial cell junctions (23). As reported by Labelle et al. platelet-derived TGFb and direct platelet-tumor cell contacts synergistically activate the TGFb/Smad and NF-kB signaling pathways in cancer cells, leading to their transition to an invasive mesenchymal-like phenotype (EMT) and enhanced metastasis in vivo (Fig3) (22).

The activation of the coagulation and the formation of platelet shields wrapping tumor cells has been proposed to be responsible of CTC survival to blood shear stress and from lysis performed by natural killer cells (24). Sustained contacts between platelet receptors and their ligands, which are presented upon exposure of the endothelial extracellular matrix or lie on the surface of tumor cells lead to platelet activation. This activation causes a rapid remodeling of the cytoskeleton and a morphological change of the cells from discoidal to spherical shape followed by spreading on the reactive surface. Platelet activation also triggers the secretion

of α- and dense granules, small intracellular vesicles that are only found in platelets and their progenitors megakaryocytes. All major platelet signaling events converge in the "final common pathway" of platelet activation, the functional upregulation of integrin adhesion receptors, leading to stable adhesion and platelet aggregation crucial to limit blood loss after tissue trauma but are also major determinants of hematogenous tumor metastases (25).
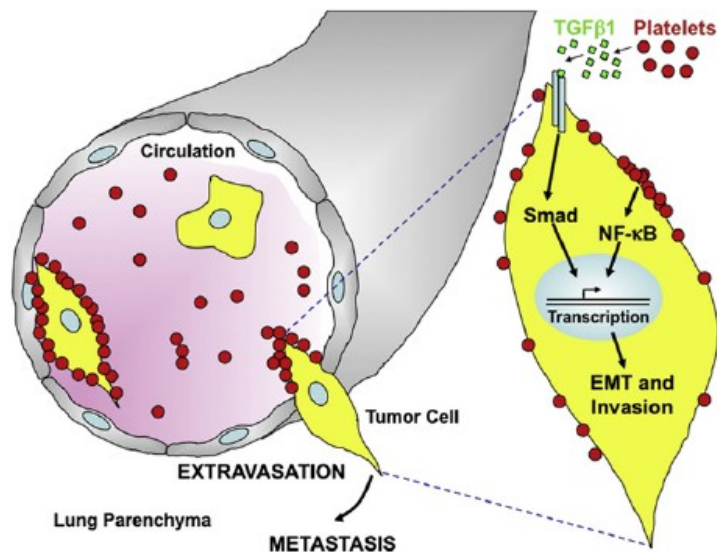
(From: Labelle at al. Direct Signaling between Platelets and Cancer Cells Induces an Epithelial-Mesenchymal-Like Transition and Promotes Metastasis)

Fig3: Platelet-Tumor Cell Contact and Platelet-Derived TGFb1 Synergize to Promote an EMT and Metastasis. Platelets secrete TGFb1, which activates the TGFb/Smad pathway in tumor cells. Upon direct platelet-tumor cell contact, the NF-kB pathway is also activated in tumor cells and synergizes with TGFb/Smad signaling to induce a rapid EMT, enhance invasiveness and promote metastasis.

On the other side, thrombocytopenia caused by platelet depletion dramatically decreased the metastatic foci (26). Beyond 'hijacking' platelets to escape immune cell attack, cancer cells express adhesion molecules and receptors performing the said 'platelet-mimicry' (27). Probably, the anti-metastatic effects of some of the

anti-platelet drugs could be based on insufficient shielding of tumor cells. However, the metastatic mechanism seems to be more complex involving the interaction of all members of the early metastatic niche such as endothelial cells, platelets and immune cells. For this reason, underlying the anti-metastatic effects of anti-platelets agents need to be analyzed in complex models including all the actors present in the early metastatic niche (3). All these observations support the hypothesis that signaling pathways involved in platelet-tumor cell interactions are crucial determinants of cancer metastasis and potential targets for anti-metastatic drugs.

Besides platelets, once in the circulatory system cancer cells encounter leucocytes (Fig4). Indeed, emerging findings also implicate that beyond macrophages, neutrophils as active participants in cancer progression starting from their recruitment by platelets in the circulation (3).
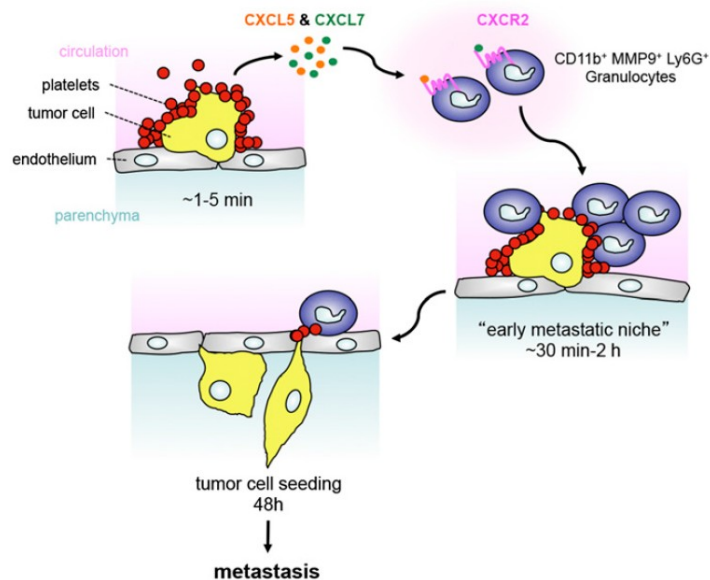
(From: Labelle et al. Platelets guide the formation of early metastatic niches)

Fig4: Platelet-derived CXCL5 and CXCL7 chemokines guide the formation of the early metastatic niche. Platelet–tumor cell aggregates form very rapidly and localize to the site of initial arrest within 1 min of tumor cell entry into the circulation. Upon contact with tumor cells, platelets are activated and release CXCL5 and CXCL7 chemokines, which both signal via the CXCR2 receptor to recruit granulocytes to platelet–tumor cell aggregates, forming an early metastatic niche within the next hours.

The tumor microenvironment, characterized by a chronic inflammation and consisting of various host cellular players among which stromal cells, blood vessels and inflammatory infiltrate (including macrophages and neutrophils), is known to perform critical roles in cancer progression. A wide spectrum of leukocytes takes part in inflammation events exerting a dual role on the tumor development. Indeed, immune system should directly eliminate the tumor cells but can also be appropriately trained by tumor stimuli facilitating tumor growth (28).

Neutrophils have long been viewed as terminally differentiated effector cells, playing a major role in resistance against microbes and during the acute phase of inflammation. However, recent evidence indicated that neutrophils can interact within the tumor microenvironment with many cell populations and produce a wide number of stimuli including cytokines and enzymes. Therefore, neutrophils as well as macrophages are key players in the regulation of the innate and adaptive immune responses in different inflammatory contexts, including cancer (29, 30).

Although neutrophils are generally present in tumors, and often tumor progression is associated with neutrophilia, the increase of neutrophilic leukocytes in blood or tissues (31), the role of neutrophils in tumor growth and metastasis is still controversial. Recent research demonstrated neutrophil cytotoxicity toward tumor cells in vitro and in vivo (32, 33) while other works suggest a pro-tumoral role in metastatic progression (34). Similarly to macrophages, neutrophils can be phenotypically plastic (35) in response to microenvironment stimuli, thus explaining their dual roles in cancer growth. Regardless of the neutrophil polarization, increasing evidence indicates that the metastatic niche is actively

modifying the phenotype of TANs. In fact, TANs from early stage tumors were more cytotoxic towards tumor cells and overexpressed TNFα, nitric oxide (NO) and H_2O_2. By contrast, in TANs from later stage tumors these genes were downregulated switching to expression of different chemokines (such as CCL17, CCL2, CCL5) and VEGF indicating a pro-tumor phenotype. In this context, tumor progression was only impaired when neutrophils were depleted at later stages of tumor development (36). These evidences suggest that the neutrophils were educated toward a pro-tumor phenotype during tumor progression. In support of this, it is well known that cancer cells induce an immunosuppressive microenvironment by affecting antigen presentation, secretion of immunosuppressive factors, induction of immunologic tolerance and recruitment of immune cells equipped with tumor-supporting machineries (37).

Although the therapeutic potential of targeting neutrophils in cancer has yet to be fully elucidated, recent studies reported encouraging data. In fact it has been demonstrated that TAN number decreased in murine models of tumor angiogenesis (38). Also, in preclinical studies IL-8 antagonists targeting the recruitment of TAN resulted in reduced metastasis and angiogenesis (39). Other example of events involving multiple types of host cells promoting metastases was provided by Laubli et al., who showed that colon carcinoma derived cells together with platelets and neutrophils, activate the endothelium. In turn, the activated endothelium secrete CCL5 leading to increased recruitment of monocytes to the tumor cells. (40). These results support the hypothesis that anti-neutrophils strategy could be effective in human cancer treatments. Nevertheless, in the application of this approach potential side effects affecting vital functions of neutrophils, such as the immune response, will need to be carefully evaluated.

Extravasation: vascular adhesion, trans-endothelial migration and early invasion

Extravasation efficiency and kinetics is depend from both tumor cells characteristics and host tissue behaviors including vessel adhesive molecule expression and effect on cancer cell phenotype consequent to the interactions with circulatory elements.

The Vascular adhesion of cancer cells to ECs is the first step of the extravasation process followed by TEM (18). Vascular adhesion requires the expression of ligands and receptors respectively on both cancer cells and ECs. Many couple of ligand–receptor complex contribute to extravasation event, such as integrins and cadherins. Cancer cells can roll on the endothelium under flow conditions *in vitro*, in a similar way to leukocytes (41) and then initiate more stable attachment (42) leading to firm vascular adhesion. Once attached, cancer cells are able to crawl on the endothelium searching the optimal place through which overcome the vascular wall (43).

Cancer cell extravasation usually occurs in tiny capillaries, where the cancer cells can be trapped by size restriction and can then form stable adhesive interaction with endothelial cells (18, 44, 45). Once firm adhered to the vessels cancer cells to complete the vascular breaching need to pass through endothelial junction undermining vascular integrity. Endothelial cell-to-cell junctions have crucial roles in endothelial integrity since they maintain intercellular adhesion and in addition they transfer intracellular signals modulating cell polarity, lumen formation, and interactions with pericytes and smooth muscle cells.

VE-cadherin is a component of intercellular endothelial adherens junctions, which play a regulatory role in the maintenance of vascular integrity. The mechanisms of action of VE-cadherin are complex and include conformational changes in endothelial cell cytoskeleton and modulation of gene transcription. At endothelial adherens junctions, adhesion is mediated by the cadherins, which are calcium-

11

dependent adhesion molecules. The organization of adherens junctions is due to vascular endothelial cadherin (VE-cadherin) linked to p120-catenin and b-catenin or plakoglobin (46). Moreover, VE-cadherin and adherens junctions transfer intracellular signals. This evidences the hypothesis that adhesion is related to intracellular signaling and that endothelial cells communicate each other to build and maintain the vascular organization (47).

In signaling context, VEGF stimulation of endothelial cells activates Src, which stimulates Vav2, Rac1, and its downstream effector PAK1. As a result, PAK1 phosphorylates VE-cadherin promoting its endocytosis increasing vascular permeability (Fig5) (48). VEGF promotes displacement of the RhoA-specific GEF Syx from cell junctions, thus promoting junction disassembly (49) on the contrary angiopoietin-1 treatment maintains Syx localized at the adherens junctions resulting in adherens junction stabilization leading to the prevention of VEGF-induced permeability (50).

All these data suggest the importance of Rho family GTPases and related proteins for the maintenance of endothelium integrity.

Also, cancer cells induce the retraction of endothelial junctions by Notch receptor which binds to Notch ligands on ECs or by transforming growth factor β1 (TGFβ1), helping cancer transmigration through the vessel junctions. Noteworthy is that different inflammatory and angiogenic molecules released by the tumour microenvironment modulate VE-cadherin behavior (51). In fact, since it is generally accepted that tumor related vessels display aberrant characteristic, restoring VE-cadherin function could be a promising target to normalize the vascular beds in cancer therapies.

In addition cancer-endothelial cell interactions should be consider also to cancer cell side. In fact, the metastatic spreading is also defined by the expression of specific proteins involved pseudopodia formation and in migration efficiency.

Focal adhesion complex proteins and integrins are well known to have a central role in cytoskeletal remodeling required for effective ability to generate metastasis (52). Integrins are a family of receptors consists of heterodimers of α-subunits and β-subunits, which interact with extracellular matrix ligands and cell surface receptors (53). In extravasation process, several integrins have been implicated in cancer cell vascular adhesion, transmigration, and subsequent attachment to the stromal matrix that surrounds the blood vessels (54). In fact it has been demonstrate that β1 integrin depletion in prostate cancer reduced cancer cell interaction with ECs *in vitro(55)*and to reduce extravasation of breast cancer cells *in vivo* in a zebrafish model (43). Thus, the αVβ3 integrin on melanoma cells was shown to be required for their adhesion to platelets (56), while β1 integrin and β4 and αVβ3 integrin contributed to the strong adhesion between prostate cancer cells and ECs *in vitro (57)*; Even though these promising results provide support to potential therapies based on integrin inhibition, it should be considered that dramatic side effects could occur since their involvement in vital signaling pathways. Despite the challenges implicated in this approach, it is important to dissect the integrin downstream signaling pathways focusing on cancer cell specific protein activation avoiding therapy side effects on healthy tissues.

Circulating cancer cells once extravasated start to proliferate in the stroma of the secondary organ however, sometimes they start to proliferate inside the blood vessels. Once reached cluster size called micro-metastases (58) they cross the endothelium and invade the underlying tissues as groups (59). These new tumor micro-metastases need to survive and proliferate in the new environment to form clinically detectable macro-metastases.
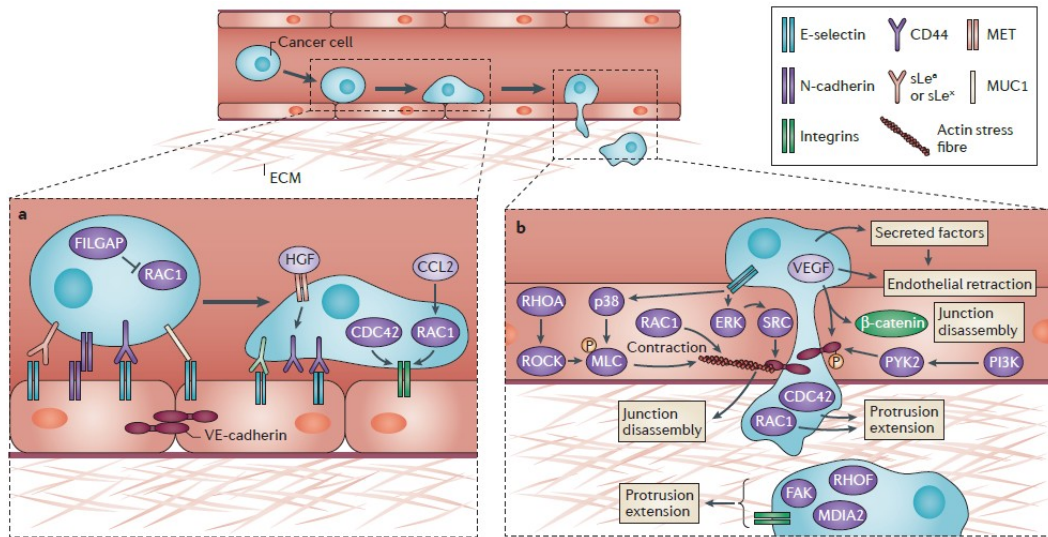
(From: Reymondet al. Crossing the endothelial barrierduring metastasis)

Fig5: Adhesion and signaling molecules that contribute to cancer cell extravasation.

(a) Vascular adhesion can be mediated by the interaction of endothelial selectin (E‑selectin) with its ligands sialyl Lewis a (sLea) or sLex and CD44, expressed by cancer cells. Theneuronal cadherin (N‑cadherin) could also mediate the interactions. At this stage, cells maintain a rounded shape, partly because RHO GTPase-activating protein 24 (FILGAP) induced RAC1 inhibition. Subsequent stable adhesion of cancer cells to ECs depends on integrins, (CD44 and MUC1). Hepatocyte growth factor (HGF) increases CD44 expression, whereas cell division control protein 42 (CDC42) controls β1 integrin expression and in turn RAC1 stimulates β1 integrin activity.

(b) CDC42 and RAC1 in cancer cells drive pseudopodia generation during TEM. EC junction opening can be induced by various factors that are secreted by cancer cells and/or by adhesion molecules. Cancer cells promote activation of RAC1, RHOA–RHO-associated protein kinase (ROCK) and p38 MAPK in ECs which lead to myosin light chain (MLC) phosphorylation increasing stress fiber mediated tension on EC junctions. Cancer cells increase ERK-induced activation of SRC and they can activate PI3K that functions upstream of the proline-rich tyrosine kinase 2 (PYK2) leading to phosphorylation (P) and disassembly of the vascular endothelial cadherin (VE‑cadherin)–β‑catenin complex inducing EC junction opening. β1 integrin, focal adhesion kinase (FAK), RHOF and MDIA2 drive the formation of filopodium-like protrusions that are important for the invasion of the basement membrane that surrounds blood vessels and for the subsequent proliferation in the surrounding tissues.

14

The inefficiency of metastatic colonization and therapeutic implication

The treatment of cancer has advanced significantly over the past 15 years, driven by many scientific insights through the discovery of oncogenes and cancer-related molecular pathways (60), much remains to be learned about the metastatic process, including the mechanisms driving extravasation or cancer cell dormancy and colonization. The metastatic cascade encloses the acquisition of a set of functional behaviors including the ability to evade apoptosis, a limitless cellular replicative potential, the capability to promote angiogenesis and the potential to invade and colonize distant organs (28). Moreover, not to be overlooked is the ability to escape immune detection and destruction on which is based the forefront immunotherapy.

Recent discoveries disclosed novel mechanisms of metastasis lying in the crosstalk between disseminated cancer cells and the host microenvironment. Indeed, the identification of organ-specific signals involved in metastatic development will open the way to new therapeutic strategies.

Noteworthy, intricate interactions within the tumor microenvironment comprising vasculature, stroma and immune system play a significant role in in the regulation of both metastatic dissemination and host tissue survival (61). For all these reasons it is clear that will be fundamental to focus new therapies on more than one step. This will improve the possibilities to find the perfect combination of treatments challenging the strength points of the entire metastatic cascade.

Although, it has been recognized for many years that metastasis is inherently an inefficient process (62-64), however, malignant tumors begin early on the way which lead to metastatic progression. Long before the tumor diagnosis invasive and motile cancer cells can already have been entered into the circulation. Many circulating cells will die, but a small portion will infiltrate secondary organ site to give rise to an eventual relapse. These metastatic cancer cells will overcome many obstacles before they can reach their host organ and generate clinically relevant

lesions. Indeed, secondary organ colonization is the most complex and rate-limiting phase of metastasis (65).

Which particular steps are the most inefficient?

Using high-resolution in vivo video microscopy and quantitative cell-fate analyses that monitor the loss of cells over time during metastasis, many studies demonstrated that millions of cancer cells could be injected into mouse circulation however these give rise to only a few metastases (63, 66). Similarly, patients with large numbers of cancer cells in the blood vessels resulted in very few development of overt metastases (67). These studies highlight that the early steps in the haematogenous metastatic process including cancer cells entering the bloodstream until they extravasate into secondary organs are extraordinarily efficient. Conversely, subsequent steps in the metastatic process are classified as inefficient, with only a small portion of cancer cells in a secondary organ site starting cell division becoming micro-metastases. Furthermore, only a small proportion of these micro-metastases persisting to generate vascularized and progressively growing macroscopic and clinically detectable lesions.

Which steps in the metastatic process are the most suitable targets for new therapies?

Clinically, at diagnosis time the primary tumor might have already seeded the circulation with thousands of cells. Theoretically, inhibition of any of the steps in the metastatic process from the initial release of cells into the circulation at the site of the primary tumor, to the final stages of growth in the new organ could offer therapeutic targets. So, targeting efficient steps in metastasis is more likely to be effective, as they might impact the entire metastatic burden. Moreover, targeting a very efficient biological process might be easier than targeting an inefficient one, because many cells would have to be inhibited lead to a reduction also in the inefficient steps of the cascade. However, cancer cells in different stages of

metastatic cascade might be present in the same organ at the same time. For this reason, any therapy targeting each specific different step that prevents the progression of metastases has the potential to benefit patients survival.

Nowadays, although some potential anti-metastatic molecules have been included in clinical trials, no anti-metastatic therapies based on their prevention are available for patients (68). Given that tumor cells can spread early during tumor progression, and it is likely that a subset of escaped cancer cells have already accomplished the early steps of the metastatic process by the time of tumor diagnosis (69) the early steps of the metastatic cascade are not usually treated as attractive clinical targets.

Hence, the later steps including awakening from dormancy, proliferation, growth and survival colonization of the metastatic niche are considered better targets for therapeutic attack. In fact, the colonization and dormancy escape can be significantly delayed and metastatic growth occurs over an extended period of time while CTCs can complete the metastatic process leading to extravasation within a few days (21).

Late steps in metastatic dissemination could be affected by cytotoxic or anti-proliferative effect of many traditional anticancer therapies. For these reasons, the early steps of metastatic dissemination may offer new opportunities for therapy development targeting molecular mechanisms belonging to the early metastatic niche such as epithelial–mesenchymal transition, vascular adhesion, trans endothelial migration and early invasion.

It has been demonstrated that tumor cells from metastases are able to re-enter the blood flow and seed back the primary tumor site or seed other organs with new metastatic foci (70). Further, cells transiting in the blood flow are particularly vulnerable to drug intervention thus targeting the circulation may be an effective approach.

Recently, it has been evidenced the efficacy of therapies combinations affecting not only the colonization ability of cancer cells but also their interactions with host cells in the early metastatic niche. In fact, recent studies highlight the importance of

the interaction with the metastatic microenvironment (71-75), beyond therapies targeting cancer cells, new strategy that targets the 'soil' in addition than the 'seed' composing the metastatic niche will be of primary importance (76).

In this context, it has been demonstrated the efficacy of targeted therapies on tumor interacting cell in the metastatic microenvironment. In particular, it is possible to enhance aspects of cancer immunity, such as tumor antigenicity, T cell trafficking and infiltration into tumor mass, which provides a rationale for combining them with checkpoint inhibitors that will lead to synergistic efficacy (77). Persisting along this way could result in enhanced life span in patients in which primary tumor ablation is not recommended, or after surgery which may promote CTCs infiltration into the circulation (78). Furthermore, patients which do not have the detectable tumor yet but are at high risk to develop metastasis or who have been diagnosed at early stages of cancer progression may take advantage of this approach. For all these patients it will be important to persist forward the study of the early metastatic niche formation to develop new molecules interfering with the ability of tumor cells to recruit or interact with supportive host cells during metastatic progression.

Paget or Ewing theory? Origin of organ-specific metastases

Stephen Paget (1855–1926) was an English surgeon in 1908 he founded the Royal Defense Society to provide scientific input into the animal-welfare debate and to support the need for animal research for the benefit of cancer patients. In 1889, he published in The Lancet, a theory describing the propensity of some types of cancer to give rise to secondary growth ('metastasis') in specific secondary organ site (79). This study led to the generation of the 'seed and soil' theory of cancer spreading. The following are some key observation from Paget's article:

"An attempt is made in this paper to consider 'metastasis' in malignant disease, and to show that the distribution of the secondary growths is not a matter of chance."

"What is it that decides which organs shall suffer in a case of disseminated cancer?"

"When a plant goes to seed, its seeds are carried in all directions; but they can only live and grow if they fall on congenial soil"

The ''seed and soil'' theory suggests the colonization of distant secondary sites was driven by the interplay between specific cancer cell types, the seed, and properly receptive microenvironments, the soil.

James Ewing (1866–1943) was an American cancer pathologist and he co-founded the American Association for Cancer Research and the current American Cancer Society. He wrote the successful textbook Neoplastic Diseases. In the text, he says relatively little about the role of 'seed' and 'soil' in metastasis (80). The following is a quote from the metastasis chapter of his book:

" 'Genius loci,' or the particular susceptibility of a tissue to develop secondary tumors, is an interesting phase of study of metastases...The mechanisms of the circulation will doubtless explain most of these peculiarities, there is as yet no evidence that any one parenchymatous organ is more adapted than others to the growth of embolic tumor cells. The spleen seems to escape with peculiar frequency".

The James Ewing hypothesis suggests that the metastatic dissemination was purely guided by mechanical factors and circulatory patterns

Starting from the two hypothesis of Paget and Ewing, over the years several theories have been proposed. Recently the most accepted is a combination of both. The majority of cancer cells that escape from the primary tumor after extravasation are driven based on circulatory patterns to the first capillary bed and then CTCs are arrested by size retention. In fact, the initial delivery and arrest of cancer cells to specific vascular districts it is probably primarily 'mechanical' according with Ewing theory. After that, once seeded in the secondary site cancer cells subsequent growth is dependent on the affinity of the 'seed' with the 'soil' according with Paget theory.

Metastatic establishment is regulated by the biological interactions throughout the entire metastatic niche. Even though cancer cells are usually said to 'home' to specific secondary organs site, this specific colonization is likely due to efficient organ-specific survival rather than preferential 'homing' of cancer cells in a specific secondary tissue.

Many observations indicate that specific stimuli present in specific organs influence the efficiency of metastatization. These evidenced the concept that in the first part of metastatic cascade mechanical interactions but mostly in the end seed–soil factors contribute to the ability of specific types of cancer to spread to various target organs (80-83).

All together these studies suggest that treatments targeting the specific 'seed–soil' affinity will give a boost to anti-metastatic treatment. In the circulation cancer cells are flowed inside vessels and usually extravasation occurs in capillaries. Indeed, capillaries are small and are typically characterized by 3–8 μm in diameter and allow the passage of highly deformable red blood cells (average 7 μm in diameter) whereas most of cancer cells are characterized by a large diameter around 20 μm influencing physical trapping. The percentage of circulating cancer cells arrested by size restriction in a defined organ is likely dependent by physical factors, such as the relative sizes of the cells, the deformability of cell itself, the capillaries diameters, the local blood pressure (Fig6).

However, a subset of cancer cells can undergo adhesive arrest in the liver in portal venules that are larger than the cell diameter, when the endothelium has been activated by the cytokine interleukin IL-1α (84). So, given the very high initial arrest of cancer cells in the first capillary bed they encounter, it is reasonable to propose that organ-specific adhesive interactions are indicative of organ-specific signaling, rather than factors that enhance the physical arrest of cancer cells in specific sites. Many evidences indicate that molecular factors present in specific organs can drive whether or not various types of cancer cell will grow generating overt metastases.
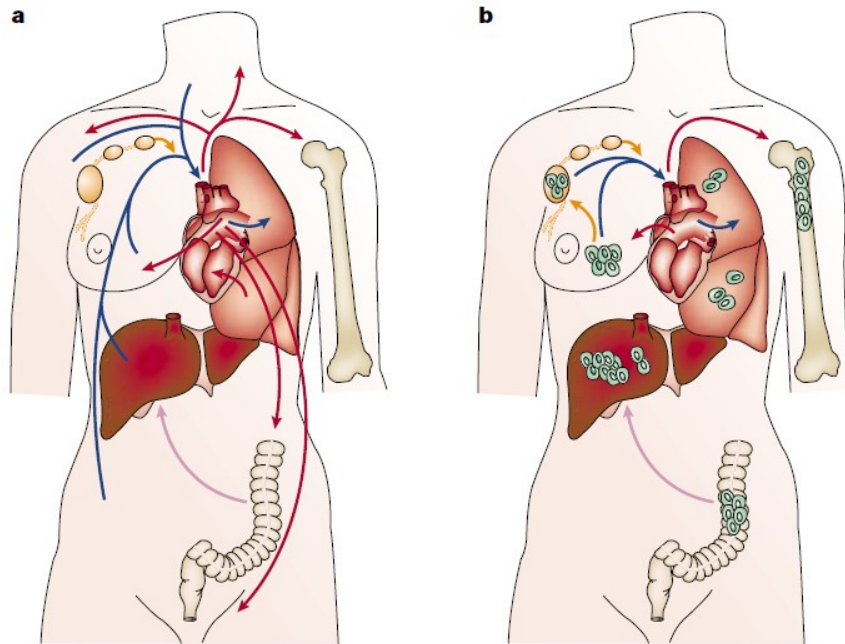
(From: Chambers et al. Dissemination and growth of cancer cells in metastatic site)

Fig6: Vascular flow patterns and corresponding movement of cancer cells arising in different organs. (a) Blood from most organs of the body is carried directly to the heart by the venous system and passes to the lungs (blue). It then returns to the heart and is circulated to all organs of the body by the systemic arterial system (red). Blood from splanchnic organs, such as the intestines, passes first to the liver (pink) before entering the venous system. Throughout the body, excess extravascular fluid enters lymphatic vessels (yellow), passes through lymph nodes and is returned to the venous system. (b) Breast cancer cells that leave the primary tumour by blood vessels will be carried by the blood flow first through the heart and then to the capillary beds of the lungs. Some cancer cells might pass through the lung to enter the systemic arterial system, where they are transported to remote organs, such as bone. Others might form metastases in the lung, which might then shed cells to the arterial flow. By contrast, colon cancer cells will be taken by the hepatic-portal circulatory system first to the liver. There is no direct flow from the lymphatic system to other organs, so cancer cells within it — for example, breast cancer cells — must enter the venous system to be transported to remote organs.

21

ECs belonging to different organs are characterized by distinct structural, phenotypic and functional attributes. Indeed, different works highlighted unique and peculiar properties of ECs within diverse vascular beds. In fact, the endothelium of lung capillaries has tight junctions and a basement membrane, while the capillary walls of the brain are reinforced by pericytes and astrocytes, composing the blood–brain barrier (85). It is well known for example that while molecular transport process is passive in many vascular beds, in the blood brain barrier this is endowed by a specific and restrictive molecular trafficking process (86). Conversely, with respect to the restrictive brain barrier vessels characterized by strong tight junctions, the capillary EC of the bone marrow, kidney glomeruli and liver are fenestrated (41, 87). These endothelial gaps might be responsible of the augmented extravasation of CTCs and contributing to the high incidence of liver and bone metastasis (4, 88). In terms of microvasculature endothelium is composed by arterial, venous, and lymphatic systems (85, 89). For these reasons, the behavior of microvascular capillary beds of different organs cannot be neglected in the study of metastatic cascade since they are the major site of extravasation of cancer cells.

It is generally accepted that the endothelium is more than an inert pipe for blood and lymph flows. In fact, the vasculature is composed by an heterogeneous endothelial cell population, depending of the organ of isolation. Even though the diverse architecture belonging to different endothelia are representative of each organ, the human tissue-specific properties of different endothelia due to unique molecular signatures of the microvascular endothelial cells are far to be defined. In this context, Nolan et al. demonstrated the presence of effective differences in vascular gene expression profiling isolating ECs from many organs such as heart, bone marrow, spleen, liver and testis. They also evidenced the existence of clusters of transcription factors, angiocrine growth factors, adhesion molecules, and

chemokines which are expressed in unique combinations by ECs of each organ in mice (Fig**7**). However if the same difference regulates also EC behavior in humans is not clear yet.
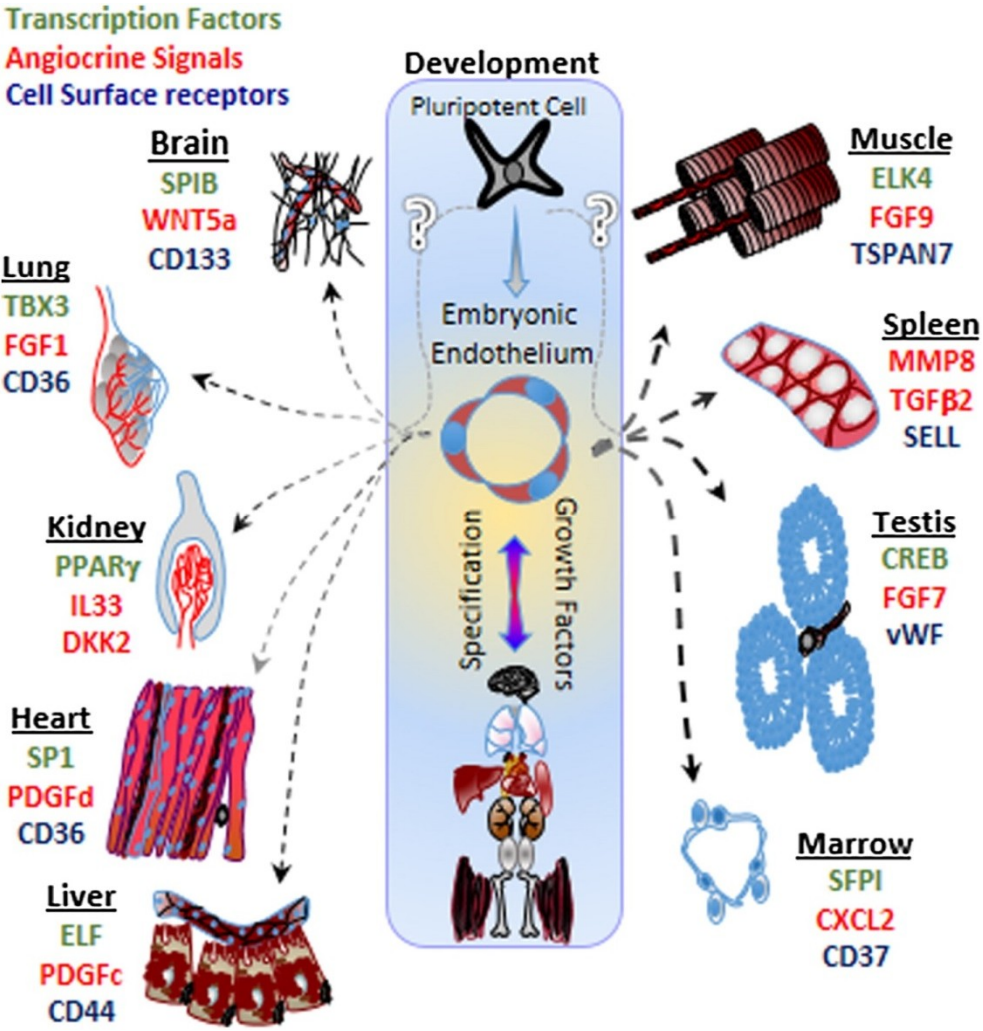
(From: Nolan et al. Molecular Signatures of Tissue-Specific Microvascular Endothelial Cell Heterogeneity in Organ Maintenance and Regeneration)

Fig7: Molecular Signatures of Tissue-Specific microvascular endothelial cell heterogeneity

Relative to human endothelia few studies are present in literature all of them relative to in vitro 2D studies evidencing the lack of research in this field (90-92).

Another function attributable to tissue specific EC in that their expression of unique trophic angiocrine factors supporting the regeneration of stem and progenitor cells after tissue damages and homeostasis in healthy tissues. Thus, sinusoidal ECs in the bone marrow are involved in hematopoiesis (93). Furthermore, lung but not liver ECs supported alveolar regeneration (94) and in the liver the regeneration after 70% partial hepatectomy is likely due to sinusoidal EC specific expression (95). These results suggest that the microvascular EC within each organ may be programmed to provide the needed angiocrine and metabolic demands of each specific tissue.

The past three decades evidenced the key roles of endothelial cells metastatic progression leading to a poor prognosis for the patient (96, 97). In fact Cancer cell cells growth rely heavily on blood vessels to obtain nutrients and eliminate waste derived metabolism. It has been already demonstrated the ability of cancer cells to manipulate endothelial cells by using intricate signaling mechanisms educating endothelial cells to support cancer growth (98). Recently, in this field Strilic *et al.* provide compelling evidence suggesting the presence of intricate signaling interactions between migrating tumor cells in the circulation and the endothelium lining blood vessels that promote extravasation into tissue and subsequent metastasis formation (96). The Strilic's group demonstrated the existence of specific signals originating from cancer cells which induce lung endothelial cells necroptosis, a type of cell-death program (99). The necroptosis process seemed to be responsible of enhanced extravasation resulting in increased number of metastasis in mice.

In this context, E‑selectin is induced by inflammatory microenvironment but is not normally expressed on ECs. This event can be generated by cancer cells themselves or cancer cell-associated leukocytes. In fact, cancer cells induce E‑selectin

expression on the endothelium of the liver after few hours from their injection *in vivo*, and this likely occurs by tumour-recruited macrophages secretions and by resident liver macrophages, the Kupffer cells (100).

All together these findings support the evidence that since organ-specific endothelial cell types establish vessels boundaries in each organ it could be possible that cancer cells exploit different and adapted approach to take advantage of different endothelia behaviors to generate organ-specific metastasis.

Once breached the barrier formed by the endothelium cancer cells to generate overt metastases must grow in the secondary organ site often called "niche" (Fig8).
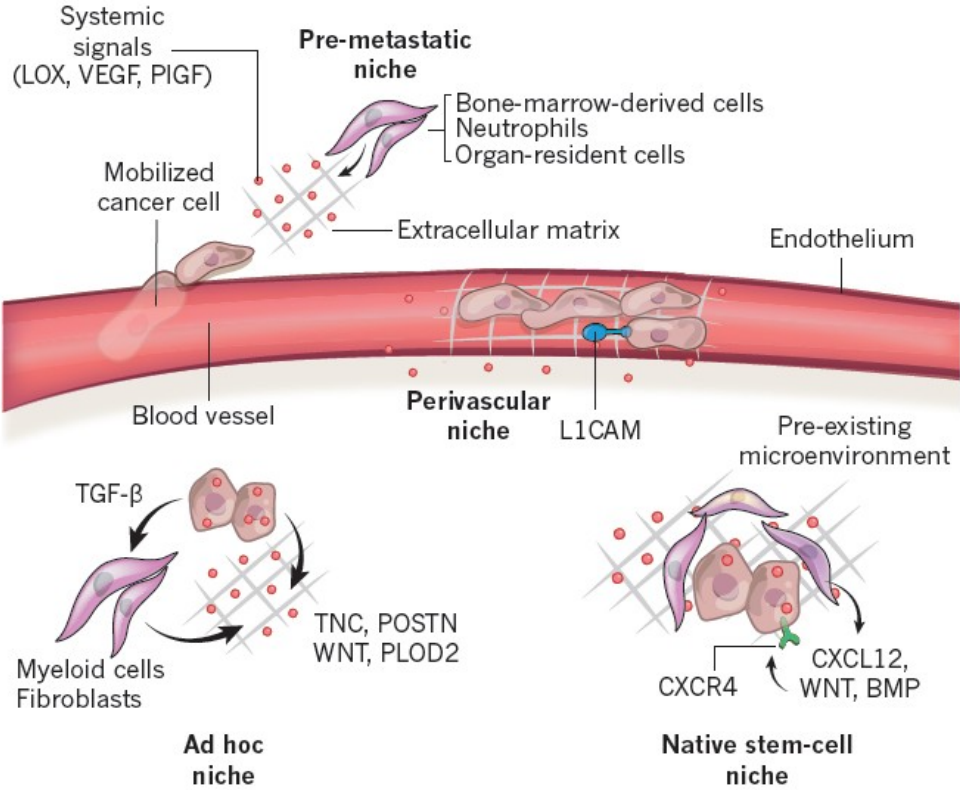
(From: Massagué et al. Metastatic colonization by circulating tumour cells)

Fig8: Metastatic niches. Cancer cells that infiltrate distant tissues survive and retain their stem-cell potential by locating themselves in supportive niches, which are akin to the niches that support normal adult stem cells. A number of different niches have been proposed. Pre-metastatic niches form before the arrival of cancer cells by systemic signals from the primary tumor that recruit supportive stromal cells. Perivascular niches support cancer cells that spread over the capillary basement membrane after extravasation. The cancer cells remain close to cells of the endothelium and their paracrine factors. Ad hoc niches are established by the secretory products of cancer cells and act in an autocrine manner or recruit stromal components as sources of supportive signals. Native stem-cell niches of the host tissue are often invaded by the infiltrating cancer cells, which allows the cells to occupy directly a supportive microenvironment. The location or composition of these niches can overlap.

Supportive niche is not immediately available at the time of extravasation for cancer cells and for these reasons most of these cells will die or enter in dormancy state (101).

For cancer cells every distant soil is deadly, thus the most welcoming soils in the body is represented by the primary tumor itself in a dangerous process called "self-seeding" which could lead to the amplification of the most aggressive cancer-cell clones (102, 103).

Cancer cells in the new microenvironment are particularly vulnerable to immune surveillance. Tumors contain many inflammatory cells such as macrophages and neutrophils. These inflammatory cells can be either pro or anti supportive functions in cancer growth, and progression of tumors depending on tumor stage. Furthermore, macrophages in the secondary organ site, may attract cancer cells towards blood vessels through epidermal growth factor (EGF) and tumor necrosis factor 1α (TNF1α) secretion which regulate the retraction of endothelial junctions, thus facilitating cancer cell trans-endothelial migration (TEM). More in detail, tumor associated macrophages (TAMs) are known to provide a number of key functions required for tumor growth (104, 105).

In addition it has been evidenced that primary tumors is able to secrete systemic signals influencing the microenvironment of distant organs by creating pre-metastatic niches before the arrival of CTCs training immune and stromal cells (106).

The specific immune-cell composition of secondary organs influence the organ's susceptibility to overt metastasis. Indeed, chronic inflammation fosters cancer progression modulating tumor responses to anticancer therapies (34). Since, immunity is the major defense against metastasis advances in immunotherapy, obtained impressive results in diverse metastatic tumor types, especially the ones employing immune checkpoint inhibitors (107, 108).

In summary, the dynamic combination of priming signals from the tumor stroma, the type of CTC clusters, the interaction within the blood vessels, the circulatory patterns structure of target-organ and cancer-cell-origin contribute to the metastatic formation in specific organs.

Experimental Models for Cancer Research: focus on microfluidic approach

Noteworthy, organ specificity of cancer dissemination and extravasation seems to be strictly coupled because specific chemo-attractant molecules are secreted by organ-specific stromal cells. Furthermore, positive interactions with circulating non cancer cells, e.g., platelets, neutrophils and macrophages, promote cancer cell trans-endothelial migration into surrounding tissues (64).

While in vivo or in vitro model do not fully replicate the complexity of factors that induce metastasis in humans, numerous studies have been aimed to investigate cancer cell invasion, migration, and interactions with the environment, which comprise different stages of cancer metastasis. However, although the overall metastatic mechanisms have been widely investigated, the cellular and molecular interactions related with extravasation are still poorly understood. Thus, in order to enhance the effectiveness of new drugs, it rises the necessity to understand the

precise mechanism on which extravasation lies. Extravasation involves a cascade of events consisting of:

- Tumor cell arrest during vascular adhesion resulting in dynamic contacts that generate cytoskeletal modifications in both cancer cells and endothelium
- Tumor cell trans-endothelial migration (TEM) consisting in cancer cell breaching the endothelial barrier
- Invasion into the surrounding matrix beyond circulation representing the secondary organ site.

Extravasation mechanism is still to be elucidated since most data are derived from low-resolution studies and endpoint assays which not accurately estimate tumor cells extravasation, in fact these studies have been performed through the analyses of secondary tumor formation in animal models.

The direct observation of single tumor cell during arrest and subsequent trans-endothelial migration across endothelial wall in tightly controlled and physiologically relevant microenvironments will lead to important insights about the extravasation mechanisms. For these reasons, microfluidic approaches could be exploited to provide new advanced tools allowing the analysis of not discernible events in traditional models (Fig9).

In vivo mouse models of extravasation do not allow for high-resolution visualization of single extravasating cells and they are not well suited to perform reproducible parametric studies (59). Beyond ethical issues, time-consuming and expensive set up, in vivo studies exhibit species-related differences from human physiological mechanisms. Moreover, chick embryo models and experimental zebrafish provides improved imaging quality, in shorter times, however, as well as

mice they lack many human organs since they are evolutionary far from humans (109, 110).

Ex vivo studies allow for easier and higher resolution imaging than in vivo and typically employ entire organ or biopsy cultures but they are affected by tissue degradation.

Although, in vitro models such as the Boyden chamber trans-well assays are limited in their physiological relevance, they provide a simple method for cell migration studies but do not allow real time study of the entire extravasation cascade. In vitro studies provide higher power in imaging resolution, controlled cellular composition exclusively from human origin but they are not suitable for long-term studies and they lack physiological and structural relevance. Significant disparities in cell response and drug sensitivity are due to 2D culture which fail to recapitulate the tissue 3D environment of human organs (111, 112).

Human organs are characterized by 3D complex structures, multicellular components, cell–cell direct contact, cell-ECM interactions, as well as biomechanical stimulation which could be mimicked through in vitro 3D assays providing a more reliable tool for breaking through research (113).
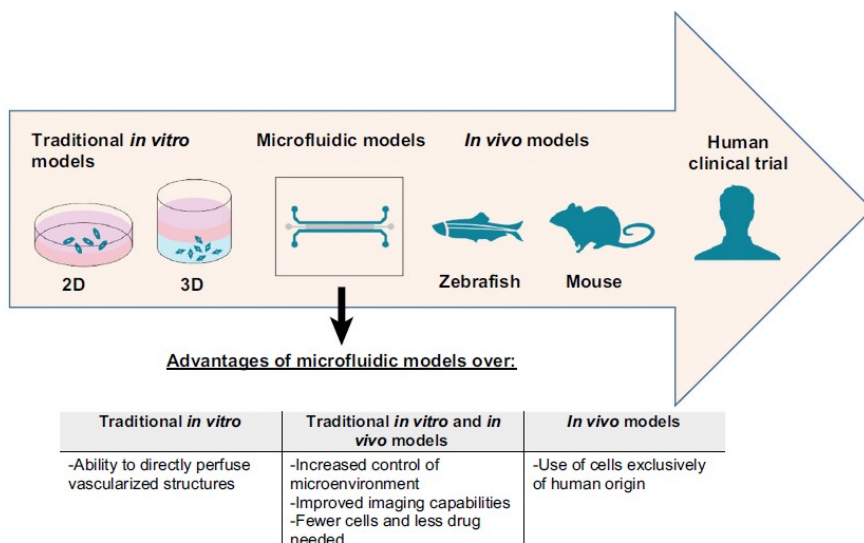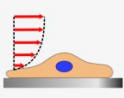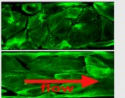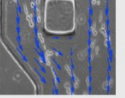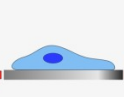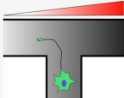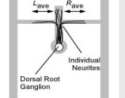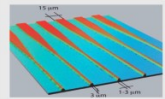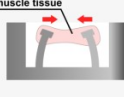
(From: Boussommier-Calleja et al. Microfluidics: A New Tool for Modeling Cancer–Immune Interactions)

Fig.9 Microfluidic Models as a Compromise between Traditional In Vitro and In Vivo Models. The figure shows the different in vitro versus in vivo models available for studying biological processes and testing drugs before clinical human trials in order of increasing physiological relevance.

Reliable extravasation studies have been impeded by the complexity of the phenomena underlying cancer interaction with surrounding cells composing the vascular niche and a lack of adequate experimental models including organ specificity and functional microvasculature (114). With the advent of microfluidics came the capability to control experimental conditions that contribute to cell response analyses in more physiological environments, and also to observe that response through real time high resolution imaging. Indeed, microfluidics systems are powerful in replicating the intricate metastatic environment and will be potential to analyze cancer cells interactions within the extravasation niche.

Microfluidics overcomes some of the technical issues of standard models, providing a biochemically and biophysically controlled 3D microenvironment coupled with high-resolution real-time imaging for studying tumor progression. In addition, microfluidic techniques offer unique advantages for modeling the metastatic microenvironment allowing improvements in analyses which will give insight in elucidating circulating tumor cells tropism to colonize distant specific supportive niches in the host tissue. Through microfluidic approach it would be possible to strictly control experimental parameters such as shear stress, interstitial flow, cell stretching, matrix stiffness and confinement and to perform force measurement (Fig10).

(From: Polacheck et al. Microfluidic platforms for mechanobiology)

Fig.10 Microfluidic techniques have been developed to investigate the biological behaviors of cells and tissues in response to various mechanical stimuli. Schematics (left) and the pictures (right) of microfluidic devices developed to study the effect of mechanical stimuli are shown along with typical biological responses to each stimulus. (a) Fluid flow through confined channels imparts shear stress on cells cultured within microfluidic devices. (b) Applying a fluid pressure gradient across a hydrogel allows the investigation of the effect of interstitial flow on cell migration and alignment. (c) By incorporating flexible substrates into microfluidic platforms, devices have been developed to study the effect of mechanical stretch on the cells cultured on the deformable substrate. (d) Gradients in stiffness of a substrate within a microfluidic device were used to study the effect of stiffness gradient on axon outgrowth. (e) A microfluidic system was used to study the effect of geometric confinement on axon outgrowth. (f) Devices have been developed to measure force generated by mechanically active cells and tissues.

Up to date, microfluidic studies have modeled EMT and migration in 3D matrix (115). Other studies through microfluidic technique it has been shown that human mammary fibroblasts induce the acquisition of invasiveness phenotype by breast cancer cells leading to collagen remodeling (116). Furthermore, microfluidic experiments have demonstrated that in both normoxic and hypoxic environment that increase in metastatic potential lead to a more cancer cell ability in migration (117). In terms of interactions between cancer and endothelium, a key element in the tumor niche, previous microfluidic models provided new tools to study intra and extravasation however, endothelial monolayer resembling the flat endothelial trans-well structure were not suitable for reliable results in physiologically relevant environment (118, 119). Recently, micro-vascular networks have been generated inducing self-assembly vasculogenesis (120-122) representing a more physiologically and structural relevant environment in which to study cancer and endothelial interactions. In addition, taking advantage from these new tool improvements in physiological relevance, it could be possible to simulate the real circulation flowing circulating elements with cancer cells in the generated microvascular networks.

Advantages and drawbacks of micro and macro models

Improving the effectiveness of human drug responses predictions is crucial to reducing costly failures in clinical trials to improve the number of therapies which will be translated from the bench to the bed side. Recent advances in cell biology, microfabrication and microfluidics have enabled the development of micro-engineered models of the functional units of human organs called organs-on-chips that could provide the basis for preclinical assays with greater predictive power. These models provide new opportunities for the application of organ-on-chip technologies in a range of areas in preclinical drug discovery, such as target identification and validation, target-based screening, and phenotypic screening

evidencing the emerging drug discovery opportunities enabled by organs-on-chips. In this context, significant advances have been made in the last few years in the development of microscale in vitro models generating highly controlled, multicellular microenvironments. However, the extremely low number of cells sets a key limitation to perform genomic, transcriptomic and proteomic analyses. For this reason, multiple studies have tried to combine the advantages offered by microscale systems, e.g. highly controlled microenvironment, high resolution imaging, with the slightly larger scale of the so-called meso-scale models (123). These millimeter-scale systems better reproduce the natural architecture and functionality of basic physiological units of specific tissues, while still maintaining the possibility to easily tune the biochemical and biophysical stimuli provided to the tissue construct. Overall, these models represent the natural bridge between microscale systems and in vivo studies. Indeed, the combined application of both microscale and mesoscale models perfectly complements results from in vivo studies allowing to obtain a broader perspective on specific biological events such as cancer metastases.

Many works reported the study of metastatic progression in 3D models (124, 125) however they lack the possibility to analyze cancer microenvironment interaction in a physiological vascularized organ-specific reliable model.

In fact one of the major challenge in the development of functional engineered meso-scale tissues is the formation of vascular networks which provide nutrients and remove waste products [jain]. Noteworthy, the generation of vascularized macro-scale constructs represents a key factor for the design of advanced in vitro models that can be used to study complex biological phenomena including the metastatic dissemination of cancer cells (126).

Several approaches have been developed in the last years to create complex vascular structures within meso-scale systems. Three dimensional networks of sacrificial carbohydrate glasses were designed by Miller et al. for the generation of hollow cylindrical networks lined by ECs (Fig11) (127). Microtissue molding

approaches were adopted to develop 3D constructs containing highly aligned "cords" of ECs (Fig11) (128).
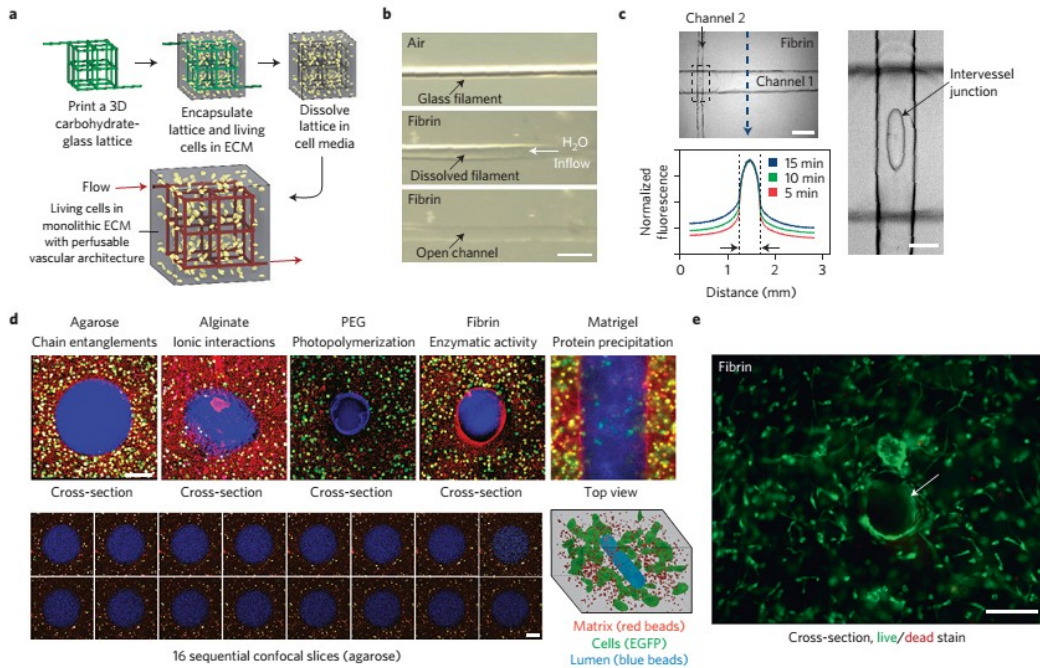
(From: Miller et al. Rapid casting of patterned vascular networks for perfusable engineered three-dimensional tissue.

Fig11: Monolithic tissue construct containing patterned vascular architectures and living cells. (a) Schematic overview. An open, interconnected, self-supporting carbohydrate glass lattice is 3D printed to serve as the sacrificial element for the casting of vascular architectures. The process yields a tissue construct with a vascular architecture that matches the original lattice. (b) A single carbohydrate glass fiber is encapsulated in a fibrin gel (top). Following ECM crosslinking (middle). Removal of the filament yields an open perfusable channel in the fibrin gel (bottom). (c) A fibrin gel with patterned interconnected channels of different diameters supports convective and diffusive transport of a fluorescent dextran injected into the channel network (upper left). Line plot of normalized fluorescence across the gel and channel (blue arrow) shows a sinusoidal profile in the channel. Enlargement of the dotted box region shows an oval intervessel junction between the two perpendicular channels (right). (d) Cells expressing EGFP were encapsulated in a variety of ECM materials then imaged to visualize

the matrix (red beads), cells (green) and the perfusable vascular lumen (blue beads) shown schematically (bottom right). (e) Representative cross-section image of HUVEC and 10T1/2 co-cultures in fibrin gel stained with a fluorescent Live/Dead assay (green, Calcein AM; red, Ethidium Homodimer). Cells survive and spread near open cylindrical channels (highlighted with white arrow). Scale bar = 200 μm.

These systems were subsequently employed to demonstrate the functionality of engineered vascularized tissue, including the liver. A key aspect of these novel microfabricated constructs is that their application spans from the development of clinically relevant implantable tissues to the analysis of biological process such as cancer metastases. For instance, these systems could be applied to replicate the interaction between a specific vascularized tissue and cancer cells and deeply investigate the molecular mechanisms underlying the metastatic dissemination for the design of more effective therapeutics.

References

1. Anonymous (Estimated Incidence, Mortality and Prevalence Worldwide in 2012.

2. Bersini S & Moretti M (2015) 3D functional and perfusable microvascular networks for organotypic microfluidic models. *Journal of materials science. Materials in medicine* 26(5):180.

3. Labelle M, Begum S, & Hynes RO (2014) Platelets guide the formation of early metastatic niches. *Proc Natl Acad Sci U S A* 111(30):E3053-3061.

4. Nguyen DX, Bos PD, & Massague J (2009) Metastasis: from dissemination to organ-specific colonization. *Nat Rev Cancer* 9(4):274-284.

5. Giampieri S*, et al.* (2009) Localized and reversible TGFbeta signalling switches breast cancer cells from cohesive to single cell motility. *Nat Cell Biol* 11(11):1287-1296.

6. Friedl P, Wolf K, von Andrian UH, & Harms G (2007) Biological second and third harmonic generation microscopy. *Current protocols in cell biology* Chapter 4:Unit 4 15.

7. Haeger A, Wolf K, Zegers MM, & Friedl P (2015) Collective cell migration: guidance principles and hierarchies. *Trends in cell biology* 25(9):556-566.

8. Ilina O & Friedl P (2009) Mechanisms of collective cell migration at a glance. *J Cell Sci* 122(Pt 18):3203-3208.

9. Friedl P & Gilmour D (2009) Collective cell migration in morphogenesis, regeneration and cancer. *Nature reviews. Molecular cell biology* 10(7):445-457.

10. Roh-Johnson M*, et al.* (2014) Macrophage contact induces RhoA GTPase signaling to trigger tumor cell intravasation. *Oncogene* 33(33):4203-4212.

11. Tabassum DP & Polyak K (2015) Tumorigenesis: it takes a village. *Nat Rev Cancer* 15(8):473-483.

12. Calbo J, *et al.* (2011) A functional role for tumor cell heterogeneity in a mouse model of small cell lung cancer. *Cancer Cell* 19(2):244-256.

13. Gundem G, *et al.* (2015) The evolutionary history of lethal metastatic prostate cancer. *Nature* 520(7547):353-357.

14. Aceto N, *et al.* (2014) Circulating tumor cell clusters are oligoclonal precursors of breast cancer metastasis. *Cell* 158(5):1110-1122.

15. Thiery JP, Acloque H, Huang RY, & Nieto MA (2009) Epithelial-mesenchymal transitions in development and disease. *Cell* 139(5):871-890.

16. Tam WL & Weinberg RA (2013) The epigenetics of epithelial-mesenchymal plasticity in cancer. *Nature medicine* 19(11):1438-1449.

17. Fischer KR, *et al.* (2015) Epithelial-to-mesenchymal transition is not required for lung metastasis but contributes to chemoresistance. *Nature* 527(7579):472-476.

18. Reymond N, d'Agua BB, & Ridley AJ (2013) Crossing the endothelial barrier during metastasis. *Nat Rev Cancer* 13(12):858-870.

19. Weis SM & Cheresh DA (2011) alphaV integrins in angiogenesis and cancer. *Cold Spring Harbor perspectives in medicine* 1(1):a006478.

20. Cristofanilli M, *et al.* (2004) Circulating tumor cells, disease progression, and survival in metastatic breast cancer. *The New England journal of medicine* 351(8):781-791.

21. Labelle M & Hynes RO (2012) The initial hours of metastasis: the importance of cooperative host-tumor cell interactions during hematogenous dissemination. *Cancer discovery* 2(12):1091-1099.

22. Labelle M, Begum S, & Hynes RO (2011) Direct signaling between platelets and cancer cells induces an epithelial-mesenchymal-like transition and promotes metastasis. *Cancer Cell* 20(5):576-590.

23. Schumacher D, Strilic B, Sivaraj KK, Wettschureck N, & Offermanns S (2013) Platelet-derived nucleotides promote tumor-cell transendothelial migration and metastasis via P2Y2 receptor. *Cancer Cell* 24(1):130-137.

24. Gay LJ & Felding-Habermann B (2011) Contribution of platelets to tumour metastasis. *Nat Rev Cancer* 11(2):123-134.

25. Stegner D, Dutting S, & Nieswandt B (2014) Mechanistic explanation for platelet contribution to cancer metastasis. *Thrombosis research* 133 Suppl 2:S149-157.

26. Schubert P, Coupland D, Culibrk B, Goodrich RP, & Devine DV (2013) Riboflavin and ultraviolet light treatment of platelets triggers p38MAPK signaling: inhibition significantly improves in vitro platelet quality after pathogen reduction treatment. *Transfusion* 53(12):3164-3173.

27. Timar J, *et al.* (2005) Platelet-mimicry of cancer cells: epiphenomenon with clinical significance. *Oncology* 69(3):185-201.

28. Hanahan D & Weinberg RA (2011) Hallmarks of cancer: the next generation. *Cell* 144(5):646-674.

29. Galdiero MR, *et al.* (2013) Tumor associated macrophages and neutrophils in cancer. *Immunobiology* 218(11):1402-1410.

30. Galdiero MR, Garlanda C, Jaillon S, Marone G, & Mantovani A (2013) Tumor associated macrophages and neutrophils in tumor progression. *J Cell Physiol* 228(7):1404-1412.

31. Coussens LM & Werb Z (2002) Inflammation and cancer. *Nature* 420(6917):860-867.

32. Swierczak A, Mouchemore KA, Hamilton JA, & Anderson RL (2015) Neutrophils: important contributors to tumor progression and metastasis. *Cancer metastasis reviews* 34(4):735-751.

33. Kondo M, Kato H, Yoshikawa T, & Sugino S (1986) Treatment of cancer ascites by intraperitoneal administration of a streptococcal preparation OK-432 with fresh human complement--role of complement-derived chemotactic factor to neutrophils. *International journal of immunopharmacology* 8(7):715-721.

34. Liang W & Ferrara N (2016) The Complex Role of Neutrophils in Tumor Angiogenesis and Metastasis. *Cancer immunology research* 4(2):83-91.

35. Mantovani A (2009) The yin-yang of tumor-associated neutrophils. *Cancer Cell* 16(3):173-174.

36. Mishalian I*, et al.* (2013) Tumor-associated neutrophils (TAN) develop pro-tumorigenic properties during tumor progression. *Cancer immunology, immunotherapy : CII* 62(11):1745-1756.

37. Dranoff G & Fearon D (2013) Tumour immunology. *Current opinion in immunology* 25(2):189-191.

38. Nozawa H, Chiu C, & Hanahan D (2006) Infiltrating neutrophils mediate the initial angiogenic switch in a mouse model of multistage carcinogenesis. *Proc Natl Acad Sci U S A* 103(33):12493-12498.

39. Huang S*, et al.* (2002) Fully humanized neutralizing antibodies to interleukin-8 (ABX-IL8) inhibit angiogenesis, tumor growth, and metastasis of human melanoma. *Am J Pathol* 161(1):125-134.

40. Laubli H, Spanaus KS, & Borsig L (2009) Selectin-mediated activation of endothelial cells induces expression of CCL5 and promotes metastasis through recruitment of monocytes. *Blood* 114(20):4583-4591.

41. Guidotti LG*, et al.* (2015) Immunosurveillance of the liver by intravascular effector CD8(+) T cells. *Cell* 161(3):486-500.

42. Ley K, Laudanna C, Cybulsky MI, & Nourshargh S (2007) Getting to the site of inflammation: the leukocyte adhesion cascade updated. *Nature reviews. Immunology* 7(9):678-689.

43. Stoletov K*, et al.* (2010) Visualizing extravasation dynamics of metastatic tumor cells. *J Cell Sci* 123(Pt 13):2332-2341.

44. Kienast Y*, et al.* (2010) Real-time imaging reveals the single steps of brain metastasis formation. *Nature medicine* 16(1):116-122.

45. Ito S, *et al.* (2001) Real-time observation of micrometastasis formation in the living mouse liver using a green fluorescent protein gene-tagged rat tongue carcinoma cell line. *Int J Cancer* 93(2):212-217.

46. Dejana E & Vestweber D (2013) The role of VE-cadherin in vascular morphogenesis and permeability control. *Progress in molecular biology and translational science* 116:119-144.

47. Dejana E & Giampietro C (2012) Vascular endothelial-cadherin and vascular stability. *Curr Opin Hematol* 19(3):218-223.

48. Gavard J & Gutkind JS (2006) VEGF controls endothelial-cell permeability by promoting the beta-arrestin-dependent endocytosis of VE-cadherin. *Nat Cell Biol* 8(11):1223-1234.

49. Ngok SP, *et al.* (2012) VEGF and Angiopoietin-1 exert opposing effects on cell junctions by regulating the Rho GEF Syx. *J Cell Biol* 199(7):1103-1115.

50. Gavard J & Gutkind JS (2008) VE-cadherin and claudin-5: it takes two to tango. *Nat Cell Biol* 10(8):883-885.

51. Le Guelte A, Dwyer J, & Gavard J (2011) Jumping the barrier: VE-cadherin, VEGF and other angiogenic modifiers in cancer. *Biology of the cell* 103(12):593-605.

52. Desgrosellier JS & Cheresh DA (2010) Integrins in cancer: biological implications and therapeutic opportunities. *Nat Rev Cancer* 10(1):9-22.

53. Askari JA, Buckley PA, Mould AP, & Humphries MJ (2009) Linking integrin conformation to function. *J Cell Sci* 122(Pt 2):165-170.

54. Shibue T & Weinberg RA (2009) Integrin beta1-focal adhesion kinase signaling directs the proliferation of metastatic cancer cells disseminated in the lungs. *Proc Natl Acad Sci U S A* 106(25):10290-10295.

55. Reymond N, *et al.* (2012) Cdc42 promotes transendothelial migration of cancer cells through beta1 integrin. *J Cell Biol* 199(4):653-668.

56. Felding-Habermann B, *et al.* (2001) Integrin activation controls metastasis in human breast cancer. *Proc Natl Acad Sci U S A* 98(4):1853-1858.

57. Barthel SR, *et al.* (2013) Definition of molecular determinants of prostate cancer cell bone extravasation. *Cancer Res* 73(2):942-952.

58. Cserni G, *et al.* (2008) Variations in sentinel node isolated tumour cells/micrometastasis and non-sentinel node involvement rates according to different interpretations of the TNM definitions. *Eur J Cancer* 44(15):2185-2191.

59. Al-Mehdi AB, *et al.* (2000) Intravascular origin of metastasis from the proliferation of endothelium-attached tumor cells: a new model for metastasis. *Nature medicine* 6(1):100-102.

60. Kaplon J, *et al.* (2013) A key role for mitochondrial gatekeeper pyruvate dehydrogenase in oncogene-induced senescence. *Nature* 498(7452):109-112.

61. Joyce JA & Pollard JW (2009) Microenvironmental regulation of metastasis. *Nat Rev Cancer* 9(4):239-252.

62. Chambers AF, *et al.* (2001) Critical steps in hematogenous metastasis: an overview. *Surgical oncology clinics of North America* 10(2):243-255, vii.

63. Luzzi KJ, *et al.* (1998) Multistep nature of metastatic inefficiency: dormancy of solitary cells after successful extravasation and limited survival of early micrometastases. *Am J Pathol* 153(3):865-873.

64. Valastyan S & Weinberg RA (2011) Tumor metastasis: molecular insights and evolving paradigms. *Cell* 147(2):275-292.

65. Weiss L (1990) Metastatic inefficiency. *Advances in cancer research* 54:159-211.

66. Chambers AF, MacDonald IC, Schmidt EE, Morris VL, & Groom AC (2000) Clinical targets for anti-metastasis therapy. *Advances in cancer research* 79:91-121.

67. Chambers AF, Groom AC, & MacDonald IC (2002) Dissemination and growth of cancer cells in metastatic sites. *Nat Rev Cancer* 2(8):563-572.

68. Steeg PS (2012) Perspective: The right trials. *Nature* 485(7400):S58-59.

69. Bernards R & Weinberg RA (2002) A progression puzzle. *Nature* 418(6900):823.

70. Hoover HC, Jr. & Ketcham AS (1975) Metastasis of metastases. *American journal of surgery* 130(4):405-411.

71. Bersini S*, et al.* (2016) Cell-microenvironment interactions and architectures in microvascular systems. *Biotechnol Adv* 34(6):1113-1130.

72. Hiratsuka S, Watanabe A, Aburatani H, & Maru Y (2006) Tumour-mediated upregulation of chemoattractants and recruitment of myeloid cells predetermines lung metastasis. *Nat Cell Biol* 8(12):1369-1375.

73. Psaila B & Lyden D (2009) The metastatic niche: adapting the foreign soil. *Nat Rev Cancer* 9(4):285-293.

74. Psaila B, Kaplan RN, Port ER, & Lyden D (2006) Priming the 'soil' for breast cancer metastasis: the pre-metastatic niche. *Breast disease* 26:65-74.

75. Kaplan RN, Psaila B, & Lyden D (2006) Bone marrow cells in the 'pre-metastatic niche': within bone and beyond. *Cancer metastasis reviews* 25(4):521-529.

76. Pegram MD, Konecny G, & Slamon DJ (2000) The molecular and cellular biology of HER2/neu gene amplification/overexpression and the clinical development of herceptin (trastuzumab) therapy for breast cancer. *Cancer treatment and research* 103:57-75.

77. Hughes PE, Caenepeel S, & Wu LC (2016) Targeted Therapy and Checkpoint Immunotherapy Combinations for the Treatment of Cancer. *Trends in immunology* 37(7):462-476.

78. Weitz J*, et al.* (1998) Dissemination of tumor cells in patients undergoing surgery for colorectal cancer. *Clin Cancer Res* 4(2):343-348.

79. Paget G (1889) Remarks on a Case of Alternate Partial Anaesthesia. *British medical journal* 1(1462):1-3.

80. Fidler IJ (2003) The pathogenesis of cancer metastasis: the 'seed and soil' hypothesis revisited. *Nat Rev Cancer* 3(6):453-458.

81. Radinsky R (1995) Modulation of tumor cell gene expression and phenotype by the organ-specific metastatic environment. *Cancer metastasis reviews* 14(4):323-338.

82. Fidler IJ (1995) Modulation of the organ microenvironment for treatment of cancer metastasis. *Journal of the National Cancer Institute* 87(21):1588-1592.

83. Zetter BR (1990) The cellular basis of site-specific tumor metastasis. *The New England journal of medicine* 322(9):605-612.

84. Orr FW & Wang HH (2001) Tumor cell interactions with the microvasculature: a rate-limiting step in metastasis. *Surgical oncology clinics of North America* 10(2):357-381, ix-x.

85. Aird WC (2007) Phenotypic heterogeneity of the endothelium: I. Structure, function, and mechanisms. *Circulation research* 100(2):158-173.

86. Rubin LL & Staddon JM (1999) The cell biology of the blood-brain barrier. *Annual review of neuroscience* 22:11-28.

87. Churg J & Grishman E (1975) Ultrastructure of glomerular disease: a review. *Kidney international* 7(4):254-261.

88. Budczies J*, et al.* (2015) The landscape of metastatic progression patterns across major human cancers. *Oncotarget* 6(1):570-583.

89. Aird WC (2007) Phenotypic heterogeneity of the endothelium: II. Representative vascular beds. *Circulation research* 100(2):174-190.

90. Borsum T, Hagen I, Henriksen T, & Carlander B (1982) Alterations in the protein composition and surface structure of human endothelial cells during growth in primary culture. *Atherosclerosis* 44(3):367-378.

91. Molema G (2010) Heterogeneity in endothelial responsiveness to cytokines, molecular causes, and pharmacological consequences. *Seminars in thrombosis and hemostasis* 36(3):246-264.

92. Muller AM, Hermanns MI, Cronen C, & Kirkpatrick CJ (2002) Comparative study of adhesion molecule expression in cultured human macro- and microvascular endothelial cells. *Experimental and molecular pathology* 73(3):171-180.

93. Butler JM*, et al.* (2010) Endothelial cells are essential for the self-renewal and repopulation of Notch-dependent hematopoietic stem cells. *Cell Stem Cell* 6(3):251-264.

94. Ding BS*, et al.* (2011) Endothelial-derived angiocrine signals induce and sustain regenerative lung alveolarization. *Cell* 147(3):539-553.

95. Ding BS*, et al.* (2010) Inductive angiocrine signals from sinusoidal endothelium are required for liver regeneration. *Nature* 468(7321):310-315.

96. Strilic B*, et al.* (2016) Tumour-cell-induced endothelial cell necroptosis via death receptor 6 promotes metastasis. *Nature* 536(7615):215-218.

97. Ferrara N (2009) Vascular endothelial growth factor. *Arterioscler Thromb Vasc Biol* 29(6):789-791.

98. Gupta GP*, et al.* (2007) Mediators of vascular remodelling co-opted for sequential steps in lung metastasis. *Nature* 446(7137):765-770.

99. Pasparakis M & Vandenabeele P (2015) Necroptosis and its role in inflammation. *Nature* 517(7534):311-320.

100. Auguste P*, et al.* (2007) The host inflammatory response promotes liver metastasis by increasing tumor cell arrest and extravasation. *Am J Pathol* 170(5):1781-1792.

101. Ghajar CM*, et al.* (2013) The perivascular niche regulates breast tumour dormancy. *Nat Cell Biol* 15(7):807-817.

102. Kim MY*, et al*. (2009) Tumor self-seeding by circulating cancer cells. *Cell* 139(7):1315-1326.

103. Massague J & Obenauf AC (2016) Metastatic colonization by circulating tumour cells. *Nature* 529(7586):298-306.

104. Pollard JW (2004) Tumour-educated macrophages promote tumour progression and metastasis. *Nat Rev Cancer* 4(1):71-78.

105. Allavena P, Sica A, Solinas G, Porta C, & Mantovani A (2008) The inflammatory micro-environment in tumor progression: the role of tumor-associated macrophages. *Critical reviews in oncology/hematology* 66(1):1-9.

106. McAllister SS & Weinberg RA (2014) The tumour-induced systemic environment as a critical regulator of cancer progression and metastasis. *Nat Cell Biol* 16(8):717-727.

107. Postow MA*, et al.* (2015) Nivolumab and ipilimumab versus ipilimumab in untreated melanoma. *The New England journal of medicine* 372(21):2006-2017.

108. Sharma P & Allison JP (2015) Immune checkpoint targeting in cancer therapy: toward combination strategies with curative potential. *Cell* 161(2):205-214.

109. Konantz M*, et al.* (2012) Zebrafish xenografts as a tool for in vivo studies on human cancer. *Annals of the New York Academy of Sciences* 1266:124-137.

110. Berens EB, Sharif GM, Wellstein A, & Glasgow E (2016) Testing the Vascular Invasive Ability of Cancer Cells in Zebrafish (Danio Rerio). *J Vis Exp* (117).

111. Kimlin L, Kassis J, & Virador V (2013) 3D in vitro tissue models and their potential for drug screening. *Expert opinion on drug discovery* 8(12):1455-1466.

112. Kimlin LC, Casagrande G, & Virador VM (2013) In vitro three-dimensional (3D) models in cancer research: an update. *Mol Carcinog* 52(3):167-182.

113. Huh D, Hamilton GA, & Ingber DE (2011) From 3D cell culture to organs-on-chips. *Trends in cell biology* 21(12):745-754.

114. Bersini S, Jeon JS, Moretti M, & Kamm RD (2014) In vitro models of the metastatic cascade: from local invasion to extravasation. *Drug Discov Today* 19(6):735-742.

115. Kuo CT*, et al.* (2014) Modeling of cancer metastasis and drug resistance via biomimetic nano-cilia and microfluidics. *Biomaterials* 35(5):1562-1571.

116. Sung KE*, et al.* (2011) Transition to invasion in breast cancer: a microfluidic in vitro model enables examination of spatial and temporal effects. *Integr Biol (Camb)* 3(4):439-450.

117. Acosta MA*, et al.* (2014) A microfluidic device to study cancer metastasis under chronic and intermittent hypoxia. *Biomicrofluidics* 8(5):054117.

118. Jeon JS, Zervantonakis IK, Chung S, Kamm RD, & Charest JL (2013) In vitro model of tumor cell extravasation. *PLoS One* 8(2):e56910.

119. Bersini S*, et al.* (2014) A microfluidic 3D in vitro model for specificity of breast cancer metastasis to bone. *Biomaterials* 35(8):2454-2461.

120. Jeon JS*, et al.* (2014) Generation of 3D functional microvascular networks with human mesenchymal stem cells in microfluidic systems. *Integr Biol (Camb)* 6(5):555-563.

121. Moya ML, Hsu YH, Lee AP, Hughes CC, & George SC (2013) In vitro perfused human capillary networks. *Tissue Eng Part C Methods* 19(9):730-737.

122. Whisler JA, Chen MB, & Kamm RD (2014) Control of perfusable microvascular network morphology using a multiculture microfluidic system. *Tissue Eng Part C Methods* 20(7):543-552.

123. Bersini S*, et al.* (2016) Human in vitro 3D co-culture model to engineer vascularized bone-mimicking tissues combining computational tools and statistical experimental approach. *Biomaterials* 76:157-172.

124. Mastro AM & Vogler EA (2009) A three-dimensional osteogenic tissue model for the study of metastatic tumor cell interactions with bone. *Cancer Res* 69(10):4097-4100.

125. Villasante A, Marturano-Kruik A, & Vunjak-Novakovic G (2014) Bioengineered human tumor within a bone niche. *Biomaterials* 35(22):5785-5794.

126. Chaffer CL & Weinberg RA (2011) A perspective on cancer cell metastasis. *Science* 331(6024):1559-1564.

127. Miller JS*, et al.* (2012) Rapid casting of patterned vascular networks for perfusable engineered three-dimensional tissues. *Nature materials* 11(9):768-774.

128. Baranski JD*, et al.* (2013) Geometric control of vascular networks to enhance engineered tissue integration and function. *Proc Natl Acad Sci U S A* 110(19):7586-7591.

Relevance and focus of my project

Metastasis is responsible of more than 90% of cancer related mortality in patients with solid tumors. Metastasis is a complex process involving a cascade of tight interconnected steps dependent by the secondary organ type and by the characteristic of primary tumor. Scientists have always taken advantage of the aid of models of different nature, among which animal models or in vitro models to analyze biological phenomena. In particular, the landscape of *in vitro* models offers several alternatives. It is possible to choose from standard models of 2D cultures that represent the majority of the studies especially in the past until you reach to the most recent 3D models of co-cultures of different cell types together.

Unfortunately, standard 2D *in vitro* and *in vivo* models do not represent complete valuable tools to study the intricate process peculiar of human metastatic dissemination largely dependent by an intricate plethora of mechanical and biochemical stimuli which are generated in the metastatic niche. Furthermore, the majority of these models does not include nor the 3D structure of cell interactions neither all the components of tumor microenvironment such as resident organotypic cells, immune cells and functional and structured vasculature.

The skeleton is the most common secondary site of metastasis and in turn, bone cancer is the major responsible of death making the primary disease no longer curable with actual therapies. Bone metastases related symptoms are bone pain, hypercalcemia, fracture, and spinal cord compression, causing a progressive decline in the quality of life leading to death. Bone metastases are the natural consequence of many primary tumors progression, such as breast, lung and prostate cancer.

Despite progress in the field, many questions remain about the mechanisms driving organ-specific metastasis and in the establishment of the rate-limiting steps of

metastasis itself. The answers to these important questions will lead to groundbreaking improvements in patient diagnostics and anti-metastatic therapies.

For these reasons, the goal of my PhD period was to contribute to the understanding of the molecular and cellular biology regulating the metastatic niche through the generation and exploitation of novel advanced 3D vascularized organ-specific human model.

Particularly, I have pursued my objectives through the generation and application of 3D advanced vascularized organ-specific models, which represents a breakthrough in current in vitro cancer related research bridging the gap between in vivo animal models and human body. More in detail, micro (µm scale) and macroscale (mm/cm scale) organ-specific models have been engineered and exploited to investigate cancer cell interaction with the organ specific vascular niche in metastasis context. Indeed, the generation of both micro and macro models in parallel will provide additional advantages. Particularly, by the side of micro-models all the advantages provided from microfluidic approach, by contrast, from the perspective of macro-systems, beyond more relevant tissue scale, it rises the possibility to perform proteomic and transcriptomic analyses on retrieved cells and media after the culture.

In particular, 3D vascularized organ-specific micro-environment, such as bone and muscle, has been engineered through a tuned approach leading to the progressive addition to the 3D co-culture of all the cells composing the physiological target organ. Generated models have been characterized demonstrating both the expression of peculiar markers of bone and muscle resident cells and the functionality of engineered vasculature in terms of physiological permeability and perfusion. In addition it has been demonstrated that the belonging organ influences, not only the physical parameters of a vascular network but also endothelial gene expression leading to the definition of organ-specific endothelia. Furthermore, it is evident that the peculiar 3D structure and properties of networks and their respective dynamic remodeling it is due to perivascular cells, such as pericytes,

fibroblasts and tissue resident cells suggesting the requirement of complete models to study the complexity of cell-cell, cell-matrix interactions in metastatic cascade.

The interaction with the vascular niche during metastatic progression has been recognized as one of the most important steps contributing in the definition of aggressiveness of cancer cells leading to extravasation and subsequent colonization of secondary organs. Extravasation the process through which cancer cell migrate from inside the circulatory system to the target organ breaching endothelial barrier, have been already described in its steps in literature with the aim to identify new targets for treatments. However, up to date, no significant techniques are available to researchers which allow to study in single cell detail each step independently from the previous one.

More in detail, extravasation could be dissected in three main steps including vascular adhesion, trans-endothelial migration and early invasion. Being these steps very attractive for the development of anti-metastatic therapies rises the needed to closely understand the lying mechanism driving this events which are far to be elucidated.

Despite integrin signaling has been already associated with metastatization, however since their large and complex signaling pathway contributing to vital signaling pathways in healthy tissue they could not be very suitable as targets for new treatments challenging metastasis. In this context, I studied the integrin downstream pathway leading to cytoskeletal remodeling which is largely involved in extravasation, the focal adhesion signaling. More in detail, focal adhesion pathway role in all specific steps of extravasation has been dissected by means of 3D microvasculature embedded in tuned microfluidic models allowing single cell extravasation analysis. In particular, the importance of the axis CDK-5/TLN-1/FAK in extravasation steps has been elucidated.

A major focus on immune cells including platelets, neutrophils and macrophages and their effects on extravasation has been considered in the analyses of cancer cell interaction within the vascular niche engineered microenvironments. In particular,

interrogating co-culture of platelet-neutrophils and cancer in engineered microvasculature a new mechanism of action of the anticoagulant drug eptifibatide in extravasation context has been clarified. In fact, beyond the well known effect on platelets activation this molecule is able to block extravasation of metastatic breast cancer cell tightening endothelial junction decreasing both SRC phosphorylation and VE-cadherin recruitment to the nucleus.

The successful development of organ-specific vascularized humanized models in which to study cancer progression in a physiologically relevant environment, will pave the way to the generation of reliable results to give insights in cancer biology. Finally, taking into account the limitations and the advantages of each type of study, these results added constructively with in vivo data will be an excellent starting point for new anti-metastatic therapy.

Chapter1

In vitro co-culture models of breast cancer metastatic progression towards bone

From: C. Arrigoni, S. Bersini, M. Gilardi and M. Moretti

Around 70% of patients with advanced breast cancer present skeletal metastases, which cause pain, pathological fractures and an overall decrease of patient quality and expectancy of life [1]. Despite significant advances in the cure of breast cancer, secondary skeletal lesions remain an unsolved issue and available specific therapies directed against bone metastases do not significantly increase patient survival as compared to standard chemotherapy [2]. In this scenario it becomes evident how new effective therapies are needed, counteracting the development of secondary tumors. The spreading of hematogenous metastases is a complex, multistep process, originating with the acquisition of an aggressive, mesenchymal-like phenotype by a subpopulation of cells in the primary tumor, which enters the vasculature, becoming circulating tumor cells (CTC), and reaches the target organ, transported by the bloodstream [3]. CTC can then arrest on the endothelium, transmigrate through it (extravasation) and colonize the target organ [4]. Why the bone represents an attractive site for breast cancer metastases is still a matter of

debate, and extensive literature exists investigating the mechanisms underlying the preferential metastatization of breast cancer to bone [5,6].

Researchers exploited complimentary methodologies in the effort to elucidate molecular events driving the metastatic spread and *in vivo* models represent the most used tool to gain insights into cancer progression [7]. However, even if *in vivo* models present unquestionable advantages, primarily the recapitulation of the metastatic process in a full, living organism, they also begin to show important limitations, regarding differences in biological mechanisms due to differences between species [8], low control on experimental variables and scarce resolution of applicable analytical methodologies [9]. On the other hand, even if they are a simplified representation of cancer complexity, *in vitro* models can represent a powerful tool to complement *in vivo* studies, allowing a thorough dissection of molecular mechanisms, in highly controlled conditions, possibly using only human cells and allowing to apply single-cell resolution analytical methodologies [10].

Historically, the first examples of *in vitro* cancer models were represented by bi-dimensional cultures of immortalized cancer cell lines [11], used as a simple testing method to screen the ability of candidate drugs to stop cancer cell growth [12]. However, in recent years, the role of the microenvironment in cancer progression received increasing attention, since several studies demonstrated that the reciprocal crosstalk between cancer cells and host cells governs cancer cell behavior, also in the context of metastatic cascade [13]. Thus, as a mean to model the interactions between cancer and host cells, co-culture systems have been proposed, ranging from bi-dimensional, indirect co-cultures [14] up to the more recent systems based on complex 3D environments embedding multiple cell types [15]. The simplest co-culture model is represented by the use of conditioned medium: the two cell populations are cultured separately and the culture medium of one population is collected and used to feed the other cell population (Fig1a). The main disadvantage of this system is the impossibility to study the bi-directional crosstalk among

cancer and bone cells, since only soluble factors released in the medium from one population have effects over the other population.
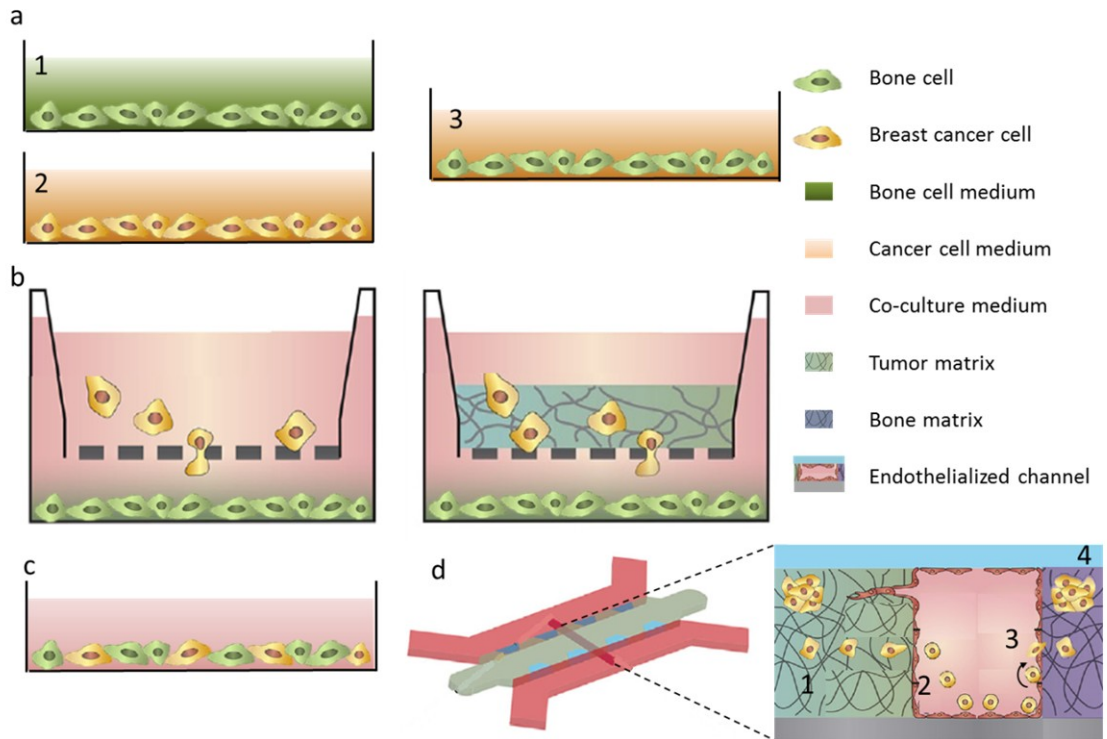
Fig1: Schematics of different co-culture methods. (a) conditioned medium culture. Culture medium from population (2) is used to culture population (1), originating an indirect, monodirectional co-culture system (3). (b) left: Transwell co-culture: population (1) is seeded in the bottom of a culture dish and population (2) is cultured on a porous insert, allowing the exchange of soluble factors, migration of cells through the membrane but without contact between the two populations. Right: transwell can also be used to measure invasion, by coating the porous membrane with a layer of a protein matrix. (c) 2D direct co-culture system, in which the two populations are mixed and seeded on the bottom of a culture plate, with a shared medium. (d) an example of advanced co-culture systems, allowing to recapitulate (1) the initial migration of cells from the primary tumor, (2) intravasation, (3) adhesion and extravasation through the endothelium and (4) growth of the metastasis[14].

To overcome this limitation, Transwell systems have been developed, allowing the simultaneous culture of two different cell types sharing the same culture medium but without direct contact (Fig1b). In Transwell assays, one cell population is seeded on the bottom of a culture plate and the other is seeded over a porous membrane, allowing cell migration in the lower compartment. Reciprocal, paracrine interactions between cells can be studied with this widely used technique, mainly in the context of chemotactic migration. Furthermore, to study cell invasion, the porous membrane can be coated with a layer of a protein gel which is degraded by invading cells that can successively migrate through the membrane (Fig1b). However, heterotypic interactions caused by direct contact between cancer cells and bone cells are not present, thus researchers exploit also direct co-culture systems (Fig1c). These traditional 2D models have been extensively used to investigate molecular mechanisms at the basis of cancer metastasis, however they are limited by the simplifications introduced, being the cancer environment characterized by three-dimensionality, presence of multiple cells and of biophysical stimuli [14]. Thus, to more closely replicate the cancer environment, advanced *in vitro* systems have been recently developed, implementing three-dimensionality, structural organization of host cells and presence of flow (Fig1d). Yet, these models are still in their initial stages of development and in the majority of cases articles only report descriptive results, for the validation of the model itself, rather than the investigation of biological mechanisms [16,17].

In this context our review will focus on the main biological findings obtained with the application of co-culture models between breast cancer cells and bone cells, to highlight the contribution of engineered *in vitro* models to the comprehension of bone metastatic process. We searched in PubMed for "breast cancer bone metasta* AND (co-culture OR coculture)", limiting the citations to the last ten years. The resulting papers were categorized following the stage of metastatic cascade studied in the paper. We refer the reader to recent excellent reviews for comprehensive

descriptions of *in vivo* models for breast cancer bone metastases [18] and models based on bone slices [19].

1.1 Early steps of metastatic dissemination

In vitro models involving the co-culture between breast cancer cells (BCCs) and bone cells have been exploited to study the mechanisms driving the metastatic process since the very initial events. As stated in the introduction, the metastatic spreading of a tumor begins with the acquisition of an aggressive phenotype by a subset of cells which allows them to detach from the primary tumor and migrate towards a secondary organ (Fig2 [3]).
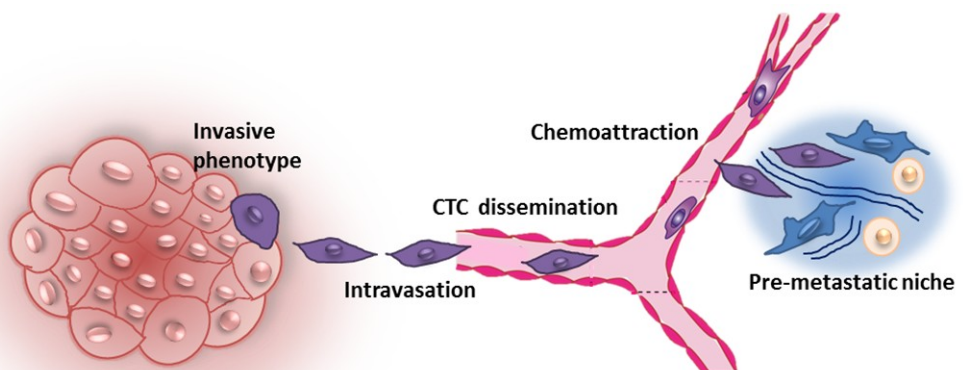
Fig2: Schematic of the initial phases of metastatic dissemination. A subset of cells of the primary tumor acquires an aggressive phenotype and can detach from the tumor, entering the vasculature. Circulating tumor cells are subjected to chemotactic attraction towards favorable microenvironments called pre-metastatic niches, where they can extravasate and start to form a secondary tumor. [3].

Cancer is a very heterogeneous disease, and several subtypes of breast cancers can be defined, with different tendencies to form metastases into bone [20]. The identification of markers that can predict if a tumor is likely to form bone

metastases is then fundamental for the classification of patients based on metastatic risk. One of the features that varies between different types of breast cancer is the response of the tumor to estrogen, that is defined by the presence and type of estrogen receptors (ER-α or ER-β) on tumor cells. To investigate a possible link between the hormone receptor status of the primary tumor and its tendency to form metastases in the bone, *in vitro* co-culture models between BCC lines with different estrogen receptor types and bone cells have been proposed [21,22].

In particular, Sasser and co-workers [21] demonstrated by means of direct co-culture, that bone marrow stromal cells (BMSCs) can induce the acquisition of a more aggressive phenotype in ER-α positive BCCs (MCF-7). Thanks to the *in vitro* model, which allowed to use both human derived and mouse derived BMSCs, it was possible to demonstrate that IL-6 produced by human, but not from mouse, derived BMSCs was able to induce phosphorylation of STAT-3 and subsequently to increase the growth rate of MCF-7, discovering a specific mechanism underlying the higher bone metastatic potential demonstrated in advanced ER-α positive tumors [23]. On the other hand, it has been demonstrated that ER-α, but not ER-β, positive cells in co-culture with bone cells increased their expression of osteopontin, indicating the acquisition of an osteo-mimetic phenotype, which can also be related to the probability of metastasizing to the bone [22]. In the same study, genomic analysis of the two different BCCs subtypes after co-culture was carried out to evidence estrogen responsive genes which can dictate a more aggressive phenotype. Among others, the genes that were more expressed in ER-α and ER-β positive BCCs were Muc-1 and MacMarks, known to be related to cell-cell and cell-matrix adhesion [24], and to cell adhesion and spreading [25] respectively. It can be concluded that the expression of a specific hormone receptor subtype influences the expression of genes involved in the in the early detachment of BCCs from primary tumor and in the acquisition of a phenotype more prone to

metastasize to bone, thus representing potential prognostic markers to identify high-risk patients.

Apart from these few examples of direct co-culture between breast cancer and bone cells, the majority of works investigating early steps of metastatic spreading focus on the chemotactic attraction exerted by bone cells over BCCs. Preferential chemotactic migration towards bone of BCCs is mainly orchestrated by soluble factors released by the bone cells [26], thus an indirect co-colture model is more suitable to dissect such paracrine effects. In this context, the system most used is represented by Transwell, together with Boyden chambers and conditioned medium assays.

Transwell assays can be used to measure both BCCs migration and invasion. To quantify the latter phenomenon, the transwell porous membrane is coated with a layer of matrix that can be degraded by the proteolytic action of BCCs [14]. This approach has been used in the work of Pohorelic and colleagues [27], investigating the role of Src kinase in BCCs migration and invasion in the bone. Several BCCs lines were compared, both in co-culture with bone derived cells and in control conditions, showing that the more aggressive MDA-MB-231 line and co-cultured BCCs compared to respective BCCs in control conditions showed an higher Src kinase-specific activity. Furthermore, the inhibition of Src by a specific inhibitor and by siRNA decreased BCCs migration towards bone cells. Interestingly, BCCs invasion was not modified by Src inhibition and was not different between BCCs cultured with bone cells or with control fibroblasts, suggesting that BCCs invasion is less influenced by the surrounding microenvironment as compared to migration, which is instead greatly influenced by chemoattractants produced by bone cells [26].

One of the major mechanisms underlying the chemotactic attraction of breast cancer cells towards bone has been identified in the CXCR-4/CXCL-12 axis [28],

also critical for other bone-metastasizing tumors as prostate cancer [29]. CXCL-12 (also called Stromal cell-Derived Factor 1, SDF-1) is a well-known chemokine secreted by stromal cells playing a key role in hematopoiesis, driving the homing of hematopoietic stem cells (HSCs) into the bone marrow niche [30]. To clarify upstream pathways involved in the chemotactic migration driven by this chemokine, Guo and coworkers [31] established a Transwell indirect co-culture system between two lines of BCCs (the more invasive MDA-MB-231 and the less aggressive MCF-7) and a bone-like cell line (MG63). They showed that BMP-4 transduced BCCs lines migrated more and showed increased expression of CXCR-4. Furthermore, they found an increased expression of CXCL-12 on co-cultured MG63. When an inhibitory factor for BMP-4 was added to the co-cultures, migration of breast cancer cells was decreased and their CXCR-4 expression downregulated, demonstrating that BMP-4 acted as an activator of the CXCR-4/CXCL-12 pathway. Another work [32] confirmed the central role of the same pathway in the chemotactic migration of BCCs towards bone-like cells, demonstrating how the protein Kisspeptin-10, known to inhibit metastasis of different cancer types as melanoma and breast cancer [33], negatively regulated the expression of CXCR-4 and consequently decreased MCF-7 migration towards MG63 bone cells. The CXCR-4/CXCL-12 axis seems to be regulated also through estrogen receptors. Indeed, it has been demonstrated [34] that the addition of an ER-β receptor agonist to three different estrogen responsive BCCs lines, indirectly co-cultured with MG63, caused a decrease in their migration and in CXCR-4 expression. Thus, the results of the study suggested that the selective activation of ER-β receptors led to reduced metastatic potential of BCCs.

Another cytokine that has been involved in the chemotactic migration of BCCs towards bone is CCL-2 (also called Monocyte Chemotactic Protein, MCP-1), known to regulate the attraction of various immune cells to inflammation sites and to activate monocytes [35]. CCL-2 is secreted by several cell types and it has been

shown that BMSCs differentiating towards osteoblasts produced increasing amounts of the protein as osteodifferentiation advances [36]. Furthermore, when BCCs were put in indirect co-culture with osteo-differentiated BMSCs their migration rate increased, and the effect was partly abolished by the addition of a CCL-2 monoclonal antibody, suggesting an important role of this cytokine in BCC migration. Further evidences confirming the potential role of MCP-1 as chemoattractant come from the study of Bussard and co-workers [37]. Although the study presented come limitations due to the use of mouse bone derived cells co-cultured with human cancer cells, it however confirmed how soluble factors (among which MCP-1 and IL6) produced by bone cells are chemotactic for BCCs and that the cross-talk between BCCs and bone cells alters the production of molecules by bone cells.

This concept of dynamic and reciprocal interactions between BCCs and bone cells has been recently resumed in the theory of pre-metastatic niches [38]. In this view, tumor cells guide the formation of a pre-metastatic niche by secreting a plethora of cytokines and growth factors that in turns promote mobilization and recruitment of BMSCs towards future metastatic sites, to create a favorable environment for tumor cell engrafting. To study such a complex phenomenon, recent studies have been published, based on indirect co-culture models, aiming at identifying key molecules, cells and ECM proteins which constitute the target niche in the bone marrow [39,40].

ECM proteins have been indicated as important factors determining tumor cell behavior [41] and, among them, tenascin W has attracted special interest due to its abundant presence in the niche of osteoblastic progenitors [42]. To study the potential involvement of tenascin W in the establishment of a pre-metastatic niche, BCCs were co-cultured in a transwell system with BMSCs, and BCCs migration, expression of tenascin W and its transcriptional regulation were analyzed [39]. It

has been found that BCCs in co-culture (both direct and indirect) with BMSCs induced the expression of tenascin W in BMSCs, and this effect was mediated by soluble substances secreted by BCCs. On the contrary, BMSCs did not elicit the production of tenascin W in BCCs, highlighting how the role of this molecule is restricted to the metastatic microenvironment. To discover what soluble factors released by BCCs caused the production of tenascin W, a transcriptional regulation analysis was performed, allowing to demonstrate that TGF- β1 secreted by BCCs induced SMAD-4 dependent transcription of tenascin W gene in BMSCs. To confirm that TGF- β1was regulating the protein production, TGF- β1 receptors on BMSCs were blocked, decreasing tenascin W production. As further indication of the importance of this ECM protein specifically for the metastatic bone niche, the researchers demonstrate how the conditioned medium from a line of BCCs preferentially metastasizing to bone (MDA-MB231-1833) increased the production of tenascin W in BMSCs as compared to the conditioned medium from a parental BCC line (MDA-MB231). Beside increasing the production of tenascin W, TGF-β 1 has been demonstrated to foster the generation of pre-metastatic niches in the bone marrow also through different mechanisms. Wobus and co-workers [40] recently reported that TGF-β1 produced by BCCs can alter the gene expression profile and, consequently, the secretion of key molecules by BMSCs, and in particular, exposition of BMSCs to medium conditioned by BCCs decreased the production of CXCL-12 by BMSCs. The addition of a monoclonal antibody against TGF- β1 completely restored CXCL-12 production by BMSCs. Since, as already stated, CXCL-12 is involved in the homing of HSCs in the bone marrow, a decreased production of the chemokine can alter the balance between circulating and resident HSCs. Indeed, in the peripheral blood of patients with breast cancer a higher number of HSCs were found, suggesting how tumor cells can hijack physiological mechanisms that assure stromal support to stem cells, to create a favorable microenvironment which will facilitate their homing in the target organ.

Despite the relevant findings obtained with co-culture models, it has to be evidenced that further improvements are possible, to facilitate the translation towards effective clinical treatments. In particular, the study of early events originating BCCs bone metastases could be more relevant if obtained in the context of a 3D tumor model. Furthermore, the presence of flow in chemotaxis assays could better replicate the *in vivo* BCCs behavior. Finally, in the majority of cited co-culture systems only two cell types are co-cultured, while the presence of several other cell types (endothelial cells, osteoclasts) can add a substantial contribution to the observed mechanism.

1.2 Breast cancer cell extravasation to bone – *In vitro* modeling of key mechanisms

The extravasation step of the metastatic cascade represents the last key event before the invasion of secondary tissues and the establishment of micrometastases. Cancer cells flowing into the bloodstream can become physically trapped within small capillaries or they can roll and adhere on the endothelium. In the latter scenario, the initial attachment is mediated by endothelial selectins and cancer cell counter-receptors, while subsequent stable interactions with the endothelium involve the active role of integrins and other receptors including CD-44 and mucins [4]. Then, cancer cells transmigrate through the endothelial wall in a process which is often mediated by organ-specific cytokines which attract cancer cells [43].

Several *in vitro* modeling approaches characterized by a different level of complexity can be adopted to recapitulate the process of cancer cell extravasation. These ones span from traditional transwell assays to recent microfluidic systems which can mimic transendothelial migration through either endothelial monolayers or physiological-like microvessels [15]. Surprisingly, only a few *in vitro* models have specifically analyzed the mechanisms driving BCCs extravasation to bone tissues.

Corcoran and co-authors employed transwells with a double layer of BMSCs and bone marrow endothelial cells (ECs) to study the signaling promoting the extravasation of BCCs with different levels of metastatic potential. In particular, a lower number of transmigration events was detected without BMSCs and this reduction was higher for BCCs with low metastatic potential (T47D and MCF-7 vs. MDA-231), suggesting that BMSCs can differentially modulate extravasation according to the invasive ability of cancer cells. Specific BCCs express surface-bound SDF-1α and the chemokine receptor CXCR-4, whose knock-down (KD) was demonstrated to influence both adhesion and transmigration. In addition, the authors found that Tac-1 KD, which is associated with reduced expression of both SDF-1α and CXCR-4 was able to impair adhesion and transmigration and that re-expression of CXCR-4 (but not SDF-1α) in Tac-1 KD cells partly (MDA-231) or completely (TD47) restored BCC ability to migrate through the endothelial monolayer [44]. Despite this model represented one of the first attempt to analyze the mechanisms driving organ-specific metastases of BCCs to bone, it did not allow to reproduce the complete process of cancer cell flow, attachment, transmigration and colonization of the bone. Furthermore, transwell assays do not allow to real-time monitor adhesion/transmigration events nor to control the biochemical/biophysical stimulation of the local microenvironment.

Microfluidic models allow to overcome these limitations, thus representing promising tools to analyze the molecular mechanisms driving BCCs extravasation. Recently, our group has developed two microfluidic models to study BCCs transmigration/colonization of a bone-mimicking microenvironment generated with hydrogel-laden osteo-differentiated BMSCs. In the first simplified model, microfluidic channels containing BMSCs embedded in a collagen matrix were endothelialized and MDA-231 were flowed through these biomimetic microvessels, showing a preferential transmigration towards the bone-like matrix compared to empty collagen matrix. More in detail, it was demonstrated that the

CXCL-5-CXCR-2 signaling axis was involved in the extravasation process, since gradients of CXCL-5 generated through the microfluidic device were able to attract BCCs to control acellular matrices, while antibodies blocking CXCR-2 significantly reduced BCCs transmigration towards bone-mimicking microenvironments. Interestingly, the addition of CXCL-5 not only affected BCCs transmigration but also their migration distance once extravasated [45]. Despite this system represented the first microfluidic model mimicking the organ-specificity of BCCs metastases to bone, it did not fully recapitulate the transmigration of cancer cells through capillary-like vessels nor the effects of physiological flows. Microvascular networks were then developed within fibrin matrices containing osteo-differentiated BMSCs and mural-like BMSCs which wrapped around microvessels (Fig3, upper panel). BCCs (BOKL, bone seeking clone of MDA-231) were then infused into the perfusable microvessels and extravasated towards the bone-mimicking microenvironment while a control muscle-mimicking matrix was not able to attract cancer cells. Several molecules can be involved in the anti-metastatic features characterizing the skeletal muscle. In particular, the muscle-secreted adenosine was demonstrated to reduce bone metastases *in vivo* through interaction with the A3 adenosine receptor, which is expressed by BCCs [46], despite its role in extravasation was not previously clarified. Surprisingly, the addition of adenosine was able to reduce BCCs extravasation to the bone-mimicking microenvironment, despite increasing vascular permeability. Conversely, blocking the A3 adenosine receptor (PSB-10 antagonist) on BCCs injected in the muscle-mimicking microenvironment increased BCCs transmigration. These data clearly demonstrated that muscle secreted adenosine was able to impair BCCs extravasation but also showed how endothelial permeability was not the key factor driving extravasation [47].
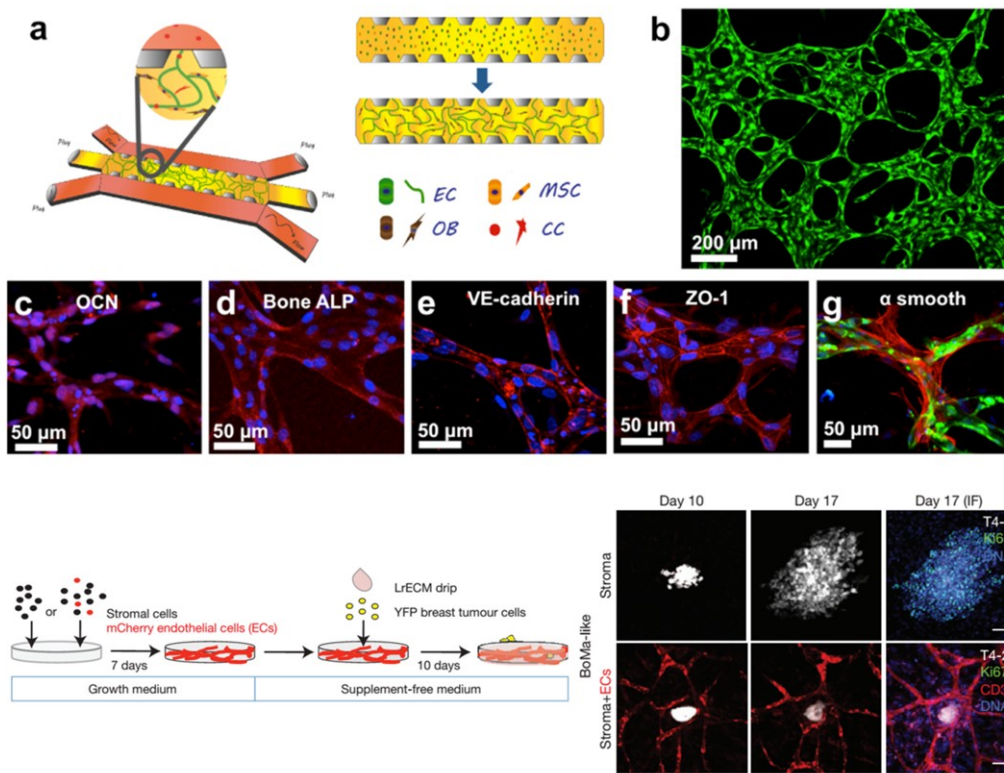
Fig3: Upper panel: *in vitro* **modeling of cancer cell extravasation and early invasion. (a) Microfluidic model of breast cancer cell (BCCs) extravasation towards a bone-mimicking microenvironment containing mesenchymal stem cells (BMSCs) and osteo-differentiated BMSCs (OBs). (b) Perfusable microvascular networks (green) allowing cancer cell flow, adhesion and trapping within capillary-like structures. (c-g) Representative figures showing expression of bone and vascular specific markers (red), namely osteocalcin (OCN, (c), bone alkaline phosphatase (ALP, (d)), vascular endothelial (VE)-cadherin (e), zonula occludens (ZO)-1 (f) and alpha smooth muscle actin (g). Endothelial cells (ECs): green. Nuclei: blue. Lower panel: engineered model for the study of the effect of microvasculature on BCCs dormancy. BMSCs were seeded alone (stroma) or in co-culture with ECs (microvasculature niche). BCCs were seeded onto stroma or microvasculature niche and laminin rich ECM (LrECM) was deposited to create a 3D environment for cancer cell study. YFP: yellow fluorescent protein. (j) T4-2 BCCs seeded on bone marrow (BoMa)-like stroma (scale bar: 100 μm) or BoMa-like stroma + ECs (scale bar: 50 μm) showing how the presence of microvasculature significantly reduced the presence of Ki-67 positive cells and induced a dormant state. T4-2 cells: white. Ki67: green. CD31: red. Nuclei: blue.**

65

1.3 Bone tissue colonization

From early invasion to cancer cell dormancy

Once extravasated, cancer cells must adapt to the local microenvironment and tune its features through bi-directional interactions with organ-specific cells. The bone tissue is particularly rich in cytokines, hormones and growth factors, whose release can be conditioned by the interaction with BCCs, hence promoting the progression of metastases [49].

Rajski and co-authors developed a simple co-culture model to study the cross-talk between BCCs and osteoblasts with the aim to find a correlation between the gene signature of these heterotypic co-cultures and the expression profile of human tumors *in vivo*. In particular, the authors found that IL-6 mRNA was significantly higher in MDA-231-osteoblast co-cultures compared to the sum of the two mono-cultures. IL-6 is a cytokine involved in a wide set of processes including cell proliferation, angiogenesis and inflammation. When compared to human samples, the presence of IL-6 was positively correlated with bone metastases and a lower metastasis-free survival at 10 years [50].

Another example of the interaction between bone cells and BCCs was reported by D'Ambrosio and Fatatis, who investigated how osteoblasts can modulate the calcium signaling in BCCs. Cells are generally characterized by low cytosolic calcium levels while deregulation of this condition may drive to cytotoxicity and cell death. The authors exposed low (MDA-468) and high (MDA-231) metastatic cancer cells to ATP, which induces an increase in intracellular calcium followed by a plateau. The behavior of highly metastatic BCCs was divided in groups characterized by high or low plateau levels of intracellular calcium. The authors found that co-cultures of BCCs and osteoblasts promoted a shift towards low plateau responses but the removal of osteoblasts reverted cancer cell behavior. Thus, the presence of osteoblasts tunes the calcium signaling in BCCs protecting

them from conditions of cellular stress. Interestingly, similar results to those obtained with osteoblast co-cultures were shown by treatment with histone deacetylase, demonstrating that osteoblasts reversibly mediate calcium signaling in metastatic cancer cells through this enzyme [51].

It is important to highlight that cancer cell invasion of the local microenvironment does not represent an effective and straightforward process. Indeed, most extravasated cancer cells do not survive in the newly colonized microenvironment and the rate of cancer cells able to induce the formation of stable macrometastases is extremely low [52]. Disseminated tumor cells often survive in the secondary tissue in a condition of cell-cycle arrest named cellular dormancy [53].

A striking example of cellular dormancy model was developed by Ghajar and co-authors, who hypothesized that ECs and the basement membrane could be responsible for the generation of a dormant niche. ECs and BMSCs were co-cultured to generate a primitive microvasculature and BCCs were subsequently seeded on their top, finding that the presence of ECs significantly reduced the growth of BCCs including T4-2, MCF-7 and MDA-231, as shown in Figure 3, middle panel. Significantly, cancer cells associated with a stable microvasculature were characterized by a dormant state and perivascular thrombospondin (TSP-1) was responsible for this condition. Conversely, TSP-1 was downregulated at neovascular tips, which were generally associated with proliferating BCCs. Furthermore, networks with higher number of tip cells and branch points showed higher expression of active transforming growth factor (TGF)-β1, while stalk cells preferentially expressed latent TGF-β1 [48].

Similar results were found by Marlow and colleagues, who developed 3D co-cultures models of inhibitory niches (osteoblasts, mesenchymal and endothelial cells) or supportive niches (bone marrow stromal cells and BCCs, Figure 3, lower panel). Noteworthy, BCCs were able to re-start proliferating once extracted from

the inhibitory niche. These results show that dormancy can be directly modulated by the local microenvironment, while specific cancer cell signaling pathways can be inhibited to block cellular dormancy (e.g. p38 MAPK or TGF-β) [53]. Zhou et al. also reported that co-cultures of BCCs and BMSCs induced cancer cell dormancy with more cells entering the G0 or G1 phase compared to the S phase. This dormant state seems to be promoted by BMSCs secreted SDF-1α, which alters Tac-1 expression and reduces neurokinin receptor 1 (NKR1) [54]. Noteworthy, Tac-1 KD was previously shown to reduce BCC extravasation suggesting that the same gene can be involved in different steps of the metastatic cascade [44]. Ono and colleagues extended the established paradigm that BCCs-BMSCs co-cultures induce cancer cell dormancy, demonstrating that co-cultures significantly reduce the expression of stem-like markers, cell invasion (matrigel assay) and sensitivity to chemotherapeutics. A key finding of this study was the identification of the same effects when BCCs were cultured with BMSC secreted exosomes. In particular, the authors demonstrated that miR-23b was transferred to BCCs leading to the suppression of MARCK-5, which is involved in cell motility and cell cycling [55]. The transfer of miRNA from bone marrow stromal cells to colonizing BCCs is emerging as a key aspect of cellular dormancy. Indeed, miRNA 127, 197, 222 and 223 were transferred from the bone marrow stroma to BCCs through gap junctions leading to reduced CXCL-12 and impaired cancer cell proliferation [56]. Noteworthy, Lim and co-authors confirmed that miRNA transferred through exosomes contribute to the dormant state, despite their effect is less pronounced compared to the gap junction communication system [56].

Metastasis growth and formation of osteolytic lesions

Up to now it is not clear why, even after several years, BCCs exit from the dormant state and start to grow, originating an overt metastasis. Recently, bone remodeling cytokines produced in inflammatory processes consequent to traumatic events have been indicated as potential activators of dormant metastatic cells [57]. With a 3D

co-culture model between the dormant BCCs line MDA-MB-231BRMS1 and fetal osteoblasts MC3T3-E1, the authors demonstrated that dormant BCCs did not proliferate in co-culture until TNF-β and IL-α were added, suggesting that modifications in the bone microenvironment due to inflammatory cytokines may regulate the insurgence of latent bone metastases.

Once rescued from the dormant state, BCCs are known to promote osteolytic bone metastases through the establishment of "vicious cycles" (amplifying feedback loops) which induce continuous bone resorption and release of pro-tumorigenic factors [58,59] (Figure 4). Beyond the well studied RANKL-RANK-OPG pathway [59] which will be discussed in a separate section, other signaling programs are involved in the formation of an osteolytic milieu. Morrison and colleagues characterized through co-cultures (direct contact, transwell, conditioned medium) of BCCs (MDA-1833) and osteoblasts which osteoclast independent features are critical for bone metastases [60]. The authors found a significant increase in matrix metalloprotease (MMP)-13 mRNA production by osteoblasts when co-cultured with BCCs. The presence of MMP-13 was shown to increase the level of CCL-2, platelet derived growth factor (PDGF)-C and serum amyloid A3 apoliprotein SAA3, which can promote monocyte recruitment and osteoclast differentiation. Hence, BCCs produce factors such as SAA3 that induce osteoblast secretion of MMP-13, which in turn activates the inducers of MMP-13 stimulating additional MMP-13 production and the generation of a vicious cycle (Fig4a).

Beside the creation of a proteolytic milieu, BCCs interfere with bone homeostasis by altering the balance of resident bone cells differentiation, as widely reported in the literature for osteoclasts but less characterized for osteoblasts (Fig4b). In this context, Chen and coworkers focused on β -catenin, which plays a key role in skeletogenesis and post-natal bone regeneration, and investigated its potential involvement in the regulation of osteoblasts and osteoclasts differentiation [61].

Using a direct co-culture between murine BCCs and murine osteoblasts or osteoclasts, the authors observed that β -catenin was upregulated in bone metastatic BCCs (TM40D-MB) as compared to parental BCCs, and inactivation of -catenin in the bone metastatic line inhibited osteoblast differentiation while increasing osteoclast differentiation. Furthermore, inhibition of β-catenin increased osteolytic bone resorption *in vivo*, even if BCCs overexpressing β -catenin induced a slight increment of osteoblast differentiation only *in vitro*, however confirming an involvement of β-catenin in regulating osteoblastic differentiation within metastatic bone environment. Another emerging factor involved in the BCCs alteration of osteoblasts differentiation has been identified in Galectin-3, a tumor-secreted sugar-binding protein, which can activate Notch signaling, involved in embryonic development, differentiation and proliferation [62]. The authors co-cultured breast cancer BT-549 with human fetal osteoblasts, demonstrating an inhibition in osteoblast differentiation as compared to controls. More in detail, they found a down-regulation of the expression of osteoblast differentiation markers such as ALPL, COL1A1, RUNX2, SP7, IBSP, and BGLAP due to Galectin-3 secreted by BCCs, which accelerated Notch1 cleavage and activation in a sugar-dependent manner.
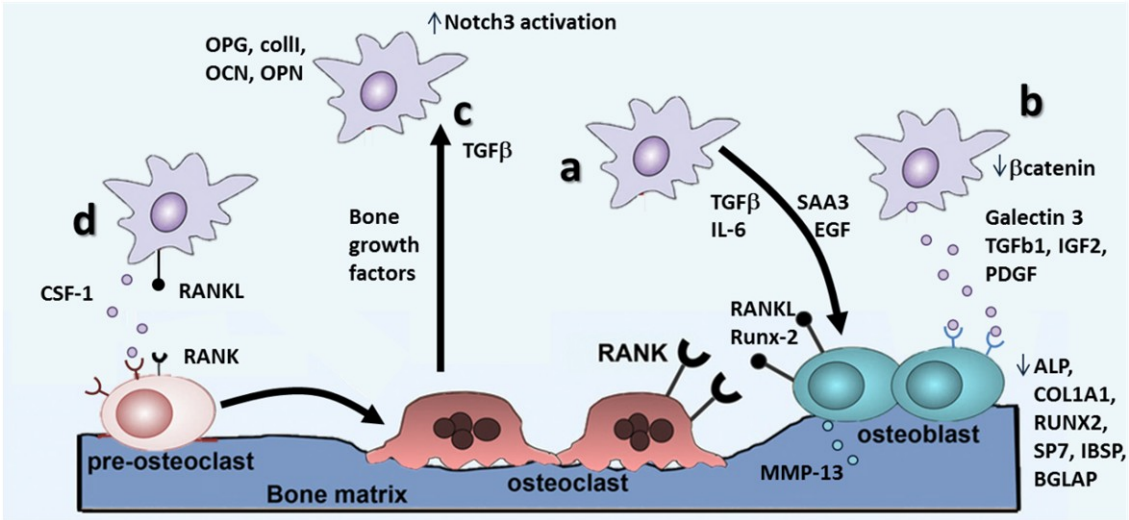
Fig4: Mechanisms involved in the establishment of osteolytic bone metastases. (a) effects of BCCs on bone resorption mediated by osteoblasts: molecules secreted by BCCs (TGF-β, IL-6, EGF) have been shown to activate osteoblasts to produce MMP-13 that degrades bone matrix and RANKL and RUNX-2, which stimulate osteoclasts to resorb bone. (b) direct effects of BCCs on osteoblasts differentiation: molecules secreted by BCCs (galectin-3 and TGF-β 1, IGF-2, PDGF) and BCCs expressed proteins (β-catenin) have been shown to regulate osteoblastic differentiation (affecting the expression of specific osteoblastic markers such as ALP, RUNX-2) through different pathways. (c) effects of molecules released by bone cells on BCCs: crosstalk between bone and cancer cells has been shown to promote an osteomimetic phenotype in BCCs (increasing the expression of typical bone markers such as osteocalcin OCN, osteopontin OPN) and TGF-β released by bone cells has been shown to activate Notch3 signaling and to promote BCCs growth. (d) direct effects of BCCs on osteoclastic differentiation: molecules secreted (CSF-1) or expressed (RANKL) by BCCs have been demonstrated to promote differentiation and activation of osteoclastic precursors towards mature osteoclasts.

Other studies evidenced the importance of Notch signaling in the establishment of BCCs bone metastases, elucidating the role of osteoblast derived TGF- β 1 in Notch3 signaling activation in cancer cells ([63], Fig4c). The authors performed direct and Transwell co-culture of bone marrow osteoblasts with the human BCCs line MDA-MET (a bone seeking clone derived from MDA-MB231), demonstrating that both direct contact and secreted factors from osteoblasts induced a two-fold increase in tumor cells of the expression of Notch3, as well as Notch3 ligand Jagged1. Furthermore, through the soft agar assay they demonstrated that Notch3 silencing affects osteoblast-induced anchorage independent growth in cancer cells. Finally, they identified osteoblast secreted TGFβ-1 as the regulator of the over expression of Notch3 in BCCs. TGF-β has been involved also in the regulation of bone cell differentiation, since it has been reported that TGF-β produced by MDA-MB-231 BCCs inhibited MC3T3-E1 osteoblasts differentiation, morphology, actin stress fiber pattern and reduced focal adhesion plaques. Using neutralizing antibodies against platelet derived growth factor (PDGF) and insulin-like growth factor II (IGF-II) in conditioned medium from MDA-MB 231, focal adhesion

plaques and actin stress fiber formation were restored in co-cultured MC3T3-E1 osteoblasts. Furthermore, they evidenced that these cytokines activate signaling pathways as PI3Kinase and Rac, highlighting potential molecules that can be targeted to restore bone homeostasis altered by breast cancer metastases. Recently, TGF- β has been also indicated as a mediator of the pro-metastatic activity of Integrin –β like1 (ITGBL1) in BCCs [64]. The authors characterized the role of ITGBL1 in bone metastatic process, by knocking down and overexpressing the molecule in BCCs lines and monitoring cell migratory potential with a Transwell assay. Results of the work demonstrated that expression of ITGBL1 regulated the migration of BCCs towards bone cells and knock down of ITGBL1 downregulated bone-related genes in BCCs, indicating a reversal of osteomimetic phenotype and a consequent decrease of bone-metastatic potential. Furthermore, overexpression of ITGBL1 in BCCs increased the production of osteoclast stimulating factors, as confirmed by the increased maturation of murine osteoclast precursors cultured in the presence of medium conditioned by BCCs. When a blocker of the TGF-β SMAD signaling pathway was used, all the effects of ITGBL1 overexpression were suppressed, suggesting that the TGF β signaling pathway mediates the role of ITGBL1 in breast cancer bone metastasis.

The RANKL/RANK/OPG pathway

Beside suppressing osteoblasts differentiation, BCCs have been shown to enhance osteoclast differentiation, switching bone homeostasis towards resorption [58] (Fig4a and 4d). Osteoblasts derive from mesenchymal stem cells and are recognized as the main sources of factors regulating osteoclasts formation including receptor activator of NF-kB ligand (RANKL), macrophage colony-stimulating factor (M-CSF), osteoprotegerin (OPG) [65] and monocyte chemoattractant protein 1 (MCP-1) [35]. M-CSF regulates osteoclast precursors in terms of proliferation, survival, and differentiation [66], while MCP-1 was showed to stimulate osteoclast fusion and activity [67]. RANKL is the key mediator for

osteoclast fusion, differentiation and activation [68] while OPG is the soluble decoy receptor able to block the interaction of RANKL with its receptor RANK expressed on osteoclasts [69]. All these players strictly regulate bone resorption/deposition balance making them attractive as therapeutic targets.

To analyze the incidence of soluble mediators secreted by BCCs on osteoclast from human origin in terms of maturation (Figure 4d), an indirect co-culture model was setup [70]. The authors reported that MDA-MB- 231 secreted CSF-1 and BCCs conditioned medium increased osteoclastic differentiation. To investigate if this phenomenon was CSF-1 dependent, they analyzed the capacity of 5H4 (an anti CSF-1 antibody) to impair BCCs ability to promote osteoclast differentiation and activation, evaluated by TRAP assay. Furthermore, the effects on osteoclasts differentiation of zoledronate, (a third-generation bisphosphonate) and Denosumab (a human anti-RANKL antibody) were investigated. The treatment with both 5H4 and Denosumab reduced osteoclast differentiation and survival while the exposition to zoledronate induced osteoclast apoptosis. Furthermore, BCCs induced resistance to zoledronate and increased sensitivity to 5H4 in cancer-induced-osteoclasts as compared to osteoclasts differentiated with factors. Direct co-culture models have been widely used, in particular to study the direct effects of BCCs on osteoclasts [71], with the aim to determine if MCF-7 BCCs could induce monocytes differentiation towards osteoclasts. The authors identified RANKL as the effector of BCCs promoted osteoclasts differentiation, and, in particular, the RANKL trans-membrane isoform, expressed by BCCs, produced an effect on monocytes differentiation, while the soluble form played a minor role, only in early differentiation steps. As a further confirmation that also BCCs express RANKL, another study reported that the direct co-culture with bone cells induced RANKL expression in BCCs [72]. In particular, the authors studied BCCs (BOKL, a bone seeking clone derived from MDA-MB231) gene expression after direct and indirect co-culture with human BMSCs differentiated toward osteoblastic lineage. The co-

cultures were digested and FACS sorted to obtain separated populations and PCR analyses performed on the sorted populations, evidencing a significant increment in the RANKL/OPG ratio only in BCCs after direct co culture, suggesting a key role of heterotypic cell interactions. This fundamental role of heterotypic junctions between BCCs and bone cells in the establishment of bone metastases has been elucidated also in a recent article [73], showing how BCCs expressing E-cadherin form adherent junctions with osteogenic cells, mainly expressing N-cadherin in a 3D co-culture model. The authors demonstrated that heterotypic adherent junctions between cancer cells and osteoblasts or BMSCs (but not with osteoclasts) were necessary to activate mTOR pathway in BCCs and, consequently, to elicit a proliferative response of cancer cells in the bone microenvironment, which was completely abolished if the formation of junctions was inhibited.

Beside the activation of osteoclast differentiation mediated by RANKL, BCCs also stimulate osteoblasts to secrete osteoclast-stimulating factors. Zhao and coworkers [74] investigated how BCCs promoted the production of osteoblast-derived factors stimulating osteoclastogenesis and moreover, they studied the effects of Calcitonin gene-related peptide (CGRP) on co-cultures between MDA-MB 231 BCCs and MG63 human osteoblast-like cell line. The authors demonstrated that interactions between MDA-MB-231 and MG63 did not affect the survival of osteoblasts, but BCCs caused osteolytic lesions by inducing the up-regulation in MG63 of RUNX-2, an essential factor for osteoblast differentiation which however also mediates osteoclast activation. Furthermore, they showed that CGRP has an opposite effect than that of BCCs, increasing osteoblasts formation and inhibiting osteolysis through the regulation of RANKL and OPG ratio. RANKL expression in osteoblasts can be also induced by Interleukin-6 (IL-6) secreted by BCCs. Indeed, IL-6 expression in serum has been linked with poor prognosis in cancer patients. To better investigate the role of IL-6 in the crosstalk between BCCs and osteoblasts, Zheng and coworkers [75] analyzed if RANKL released by KUSA-O

or primary osteoblasts directly induced IL-6 expression in MDA-MB231, using a direct co-culture system. Firstly, they discovered that RANKL from osteoblasts up-regulated secretion of IL-6 by BCCs. Secreted IL-6 in turns induced BCCs RANK expression which sensitized the tumor cells to RANKL released from the bone microenvironment and thus alimented a positive loop. The confirmation that this auto-amplifying cross-talk was involved in bone metastases was also validated *in vivo*, highlighting how RANKL and IL-6 are important regulators of direct paracrine and autocrine signaling in bone resorption, leading to increased proliferation of BCCs within bone metastatic environment. An alternative mechanism by which BCCs stimulate osteoblasts to produce osteoclasts stimulating factors has been identified in Epidermal growth factor (EGF) signaling [76]. EGF and related receptors are implicated in the most important signaling pathways in tissue development and cancer biology and have been also linked to bone homeostasis. Using a co-culture system composed by murine osteoclasts precursors and MC3T3-E1 murine osteoblasts in which BCCs (MDA-MB231) can be also added, the authors evidenced that EGF-like ligands stimulate osteoclasts differentiation. Since osteoclasts do not express functional EGF receptors, the enhanced osteoclastogenesis could be explained by an indirect effect, mediated by osteoblasts, further confirmed by culturing pre-osteoclasts in medium conditioned by EGF treated osteoblasts. Furthermore, EGF-like ligands on osteoblasts decreased OPG expression and increased the secretion of monocyte chemoattractant protein 1 (MCP1), factors known to stimulate osteoclastogenesis. To elucidate a possible role of EGF signaling in bone metastasis, the secretion of EGF-like ligands was measured in BCCs, finding a high expression of EGF-like ligands, at least at mRNA level. Taken together these results evidence that BCCs cross-talk with osteoblasts increases osteoclastogenesis through EGF signaling pathway, amplifying the release of bone-matrix trapped factors, which finally fosters tumor growth triggering and feeding the vicious cycle.

While it is well known that an increased RANKL/OPG ratio shift bone homeostasis towards osteoclastogenesis, less is known about the role of OPG in BCCs. In this context, a peculiar result has been reported by Kapoor and colleagues [77]. They indeed showed that MDA-231, MDA 435, MDA-MET, and MDA-231/K BCCs line expressed OPG and its level was directly correlated with metastatic potential and specific bone homing. Furthermore, they highlighted the expression of other bone-related markers in BCCs including type I collagen, osteocalcin, osteopontin, and RUNX-2, suggesting that cancer cells can acquire an osteomimetic phenotype. However, the higher expression of OPG in more bone-metastatic cells was not correlated to an higher expression of other bone-markers, suggesting that OPG expression was not merely a consequence of enhanced osteomimicry but that it had a key role in the metastatic process.

Step of Metastatic Dissemination	Mechanism Studied	Type of In Vitro Model Used	Molecules Involved	References
Early steps of bone metastasis	Acquisition of bone-aggressive phenotype	2D direct co-culture	IL-6 ER-α, ER-β	[21] [22]
	Chemotactic migration	Transwell	Src-kinase CXCR-4/CXCL-12 CCL-2	[26] [31,32,34] [36,37]
	Pre-metastatic niche	Transwell, conditioned medium	Tenascin W TGF-β1, CXCL-12	[39] [40]
Extravasation	Transedothelial migration	Transwell	SDF-1α, CXCR-4, Tac-1	[44]
		Microfluidic	CXCR-2/CXCL-5, adenosine	[45,47]
Bone colonization	Early invasion	2D direct co-culture	IL-6 Ca^{2+}	[50] [51]
	Dormancy	3D direct co-culture	TSP-1, TGF-β, p38	[50,53]
		2D direct co-culture	Tac-1, NRK-1 miRNAs from BMCs	[54] [55,56]
	Cancer cell growth in the bone	2D and 3D direct co-culture	ILα, TNF-β E-cadh, N-cadh	[57] [73]
	Interaction with osteoblasts	2D direct co-culture	MMP-13 β-catenin	[60] [61]
		Transwell, 2D direct co-culture	Galectin-3, Notch, TGF-β	[62,63]
	Osteoclast maturation	Conditioned medium	Integrin β1, TGF-β CSF-1	[64] [70]
		2D and 3D direct co-culture	RANKL/RANK, CGRP, IL-6 EGF, MCP-1 OPG	[71,72,74,75] [76] [77]

Table 1. Summary of the different molecules involved in breast cancer bone metastasis, discovered with the application of different in vitro models.

1.4 Conclusions

In conclusion, the application of *in vitro* co-culture models allowed to discover fundamental molecular mechanisms driving specific steps of the metastatic progression of breast cancer to bone (summarized in Table 1), thanks to the possibility to accurately control applied environmental conditions and thus to dissect the effects of distinct variables, an approach not applicable within *in vivo* models. Furthermore, the exploitation of high-resolution imaging and quantitative techniques assures a deep insight into molecular and cellular mechanisms. However, traditional co-culture models are severely limited by the over-simplifications of the system, sometimes leading to scarce translation into a real clinical benefit. Aiming to overcome this critical issue, advanced *in vitro* devices are needed, which could better recapitulate key hallmarks of the metastatic cascade. A fundamental characteristic is the three dimensionality of the *in vivo* environment which has been shown to be a key regulator of cell behavior [78] and thus would likely play a role also in the metastatic spreading of BCCs to bone. Furthermore, to study CTC arrest on endothelium and extravasation it is essential to recreate a vascular system similar to physiological capillaries, such as recently described in millimeter-scale engineered bone models [79,80]. A perfusable microvascular network could also allow the inclusion of blood cellular components, which have been indicated as key players for CTC survival in the blood stream and adhesion to endothelium [81,82]. Finally, striking evidence is mounting against the use of cancer cell lines, which have been started to be considered too dissimilar from heterogeneous real tumors and thus fostered the research of alternative cellular sources [83]. In this context, the generation of *in vitro* tumor models based on patient-derived cells could provide an invaluable contribution, allowing to investigate the effects of tumor inter-individual heterogeneity on the bone metastatic progression, achieving a significant progress in the field of personalized medicine.

References

1.   Coleman, R.E. Skeletal complications of malignancy. *Cancer* **1997**, *80*, 1588-1594.

2.   Kroep, J.R.; Charehbili, A.; Coleman, R.E.; Aft, R.L.; Hasegawa, Y.; Winter, M.C.; Weilbaecher, K.; Akazawa, K.; Hinsley, S.; Putter, H*., et al.* Effects of neoadjuvant chemotherapy with or without zoledronic acid on pathological response: A meta-analysis of randomised trials. *European journal of cancer* **2016**, *54*, 57-63.

3.   Chaffer, C.L.; Weinberg, R.A. A perspective on cancer cell metastasis. *Science* **2011**, *331*, 1559-1564.

4.   Reymond, N.; d'Agua, B.B.; Ridley, A.J. Crossing the endothelial barrier during metastasis. *Nature reviews. Cancer* **2013**, *13*, 858-870.

5.   Fazilaty, H.; Mehdipour, P. Genetics of breast cancer bone metastasis: A sequential multistep pattern. *Clinical & experimental metastasis* **2014**, *31*, 595-612.

6.   Futakuchi, M.; Fukamachi, K.; Suzui, M. Heterogeneity of tumor cells in the bone microenvironment: Mechanisms and therapeutic targets for bone metastasis of prostate or breast cancer. *Advanced drug delivery reviews* **2016**, *99*, 206-211.

7.   Simmons, J.K.; Hildreth, B.E., 3rd; Supsavhad, W.; Elshafae, S.M.; Hassan, B.B.; Dirksen, W.P.; Toribio, R.E.; Rosol, T.J. Animal models of bone metastasis. *Veterinary pathology* **2015**, *52*, 827-841.

8.   Yin, S.; Fan, Y.; Zhang, H.; Zhao, Z.; Hao, Y.; Li, J.; Sun, C.; Yang, J.; Yang, Z.; Yang, X*., et al.* Differential tgfbeta pathway targeting by mir-122

in humans and mice affects liver cancer metastasis. *Nature communications* **2016**, *7*, 11012.

9.   Evans, J.P.; Sutton, P.A.; Winiarski, B.K.; Fenwick, S.W.; Malik, H.Z.; Vimalachandran, D.; Tweedle, E.M.; Costello, E.; Palmer, D.H.; Park, B.K.*, et al.* From mice to men: Murine models of colorectal cancer for use in translational research. *Critical reviews in oncology/hematology* **2016**, *98*, 94-105.

10.   Shologu, N.; Szegezdi, E.; Lowery, A.; Kerin, M.; Pandit, A.; Zeugolis, D.I. Recreating complex pathophysiologies in vitro with extracellular matrix surrogates for anticancer therapeutics screening. *Drug discovery today* **2016**.

11.   Sanford, K.K.; Barker, B.E.; Woods, M.W.; Parshad, R.; Law, L.W. Search for "indicators" of neoplastic conversion in vitro. *Journal of the National Cancer Institute* **1967**, *39*, 705-733.

12.   Haskell, C.M.; Sullivan, A. Comparative survival in tissue culture of normal and neoplastic human cells exposed to adriamycin. *Cancer research* **1974**, *34*, 2991-2994.

13.   Junttila, M.R.; de Sauvage, F.J. Influence of tumour micro-environment heterogeneity on therapeutic response. *Nature* **2013**, *501*, 346-354.

14.   Katt, M.E.; Placone, A.L.; Wong, A.D.; Xu, Z.S.; Searson, P.C. In vitro tumor models: Advantages, disadvantages, variables, and selecting the right platform. *Frontiers in bioengineering and biotechnology* **2016**, *4*, 12.

15.   Bersini, S.; Jeon, J.S.; Moretti, M.; Kamm, R.D. In vitro models of the metastatic cascade: From local invasion to extravasation. *Drug discovery today* **2014**, *19*, 735-742.

16. Krishnan, V.; Vogler, E.A.; Sosnoski, D.M.; Mastro, A.M. In vitro mimics of bone remodeling and the vicious cycle of cancer in bone. *Journal of cellular physiology* **2014**, *229*, 453-462.

17. Holen, I.; Nutter, F.; Wilkinson, J.M.; Evans, C.A.; Avgoustou, P.; Ottewell, P.D. Human breast cancer bone metastasis in vitro and in vivo: A novel 3d model system for studies of tumour cell-bone cell interactions. *Clinical & experimental metastasis* **2015**, *32*, 689-702.

18. Horas, K.; Zheng, Y.; Zhou, H.; Seibel, M.J. Animal models for breast cancer metastasis to bone: Opportunities and limitations. *Cancer investigation* **2015**, *33*, 459-468.

19. Taubenberger, A.V. In vitro microenvironments to study breast cancer bone colonisation. *Advanced drug delivery reviews* **2014**, *79-80*, 135-144.

20. Hess, K.R.; Pusztai, L.; Buzdar, A.U.; Hortobagyi, G.N. Estrogen receptors and distinct patterns of breast cancer relapse. *Breast cancer research and treatment* **2003**, *78*, 105-118.

21. Sasser, A.K.; Sullivan, N.J.; Studebaker, A.W.; Hendey, L.F.; Axel, A.E.; Hall, B.M. Interleukin-6 is a potent growth factor for er-alpha-positive human breast cancer. *FASEB journal : official publication of the Federation of American Societies for Experimental Biology* **2007**, *21*, 3763-3770.

22. Wang, J.; Jarrett, J.; Huang, C.C.; Satcher, R.L., Jr.; Levenson, A.S. Identification of estrogen-responsive genes involved in breast cancer metastases to the bone. *Clinical & experimental metastasis* **2007**, *24*, 411-422.

23. Koenders, P.G.; Beex, L.V.; Langens, R.; Kloppenborg, P.W.; Smals, A.G.; Benraad, T.J. Steroid hormone receptor activity of primary human breast

cancer and pattern of first metastasis. The breast cancer study group. *Breast cancer research and treatment* **1991**, *18*, 27-32.

24. Wesseling, J.; van der Valk, S.W.; Hilkens, J. A mechanism for inhibition of e-cadherin-mediated cell-cell adhesion by the membrane-associated mucin episialin/muc1. *Molecular biology of the cell* **1996**, *7*, 565-577.

25. Yue, L.; Bao, Z.; Li, J. Expression of macmarcks restores cell adhesion to icam-1-coated surface. *Cell adhesion and communication* **2000**, *7*, 359-366.

26. Cooper, C.R.; Sikes, R.A.; Nicholson, B.E.; Sun, Y.X.; Pienta, K.J.; Taichman, R.S. Cancer cells homing to bone: The significance of chemotaxis and cell adhesion. *Cancer treatment and research* **2004**, *118*, 291-309.

27. Pohorelic, B.; Singh, R.; Parkin, S.; Koro, K.; Yang, A.D.; Egan, C.; Magliocco, A. Role of src in breast cancer cell migration and invasion in a breast cell/bone-derived cell microenvironment. *Breast cancer research and treatment* **2012**, *133*, 201-214.

28. Burger, J.A.; Kipps, T.J. Cxcr4: A key receptor in the crosstalk between tumor cells and their microenvironment. *Blood* **2006**, *107*, 1761-1767.

29. Uygur, B.; Wu, W.S. Slug promotes prostate cancer cell migration and invasion via cxcr4/cxcl12 axis. *Molecular cancer* **2011**, *10*, 139.

30. Nagasawa, T. Cxcl12/sdf-1 and cxcr4. *Frontiers in immunology* **2015**, *6*, 301.

31. Guo, D.; Huang, J.; Gong, J. Bone morphogenetic protein 4 (bmp4) is required for migration and invasion of breast cancer. *Molecular and cellular biochemistry* **2012**, *363*, 179-190.

32. Olbrich, T.; Ziegler, E.; Turk, G.; Schubert, A.; Emons, G.; Grundker, C. Kisspeptin-10 inhibits bone-directed migration of gpr54-positive breast cancer cells: Evidence for a dose-window effect. *Gynecologic oncology* **2010**, *119*, 571-578.

33. Makri, A.; Pissimissis, N.; Lembessis, P.; Polychronakos, C.; Koutsilieris, M. The kisspeptin (kiss-1)/gpr54 system in cancer biology. *Cancer treatment reviews* **2008**, *34*, 682-692.

34. Hinsche, O.; Girgert, R.; Emons, G.; Grundker, C. Estrogen receptor beta selective agonists reduce invasiveness of triple-negative breast cancer cells. *International journal of oncology* **2015**, *46*, 878-884.

35. Marriott, I.; Gray, D.L.; Rati, D.M.; Fowler, V.G., Jr.; Stryjewski, M.E.; Levin, L.S.; Hudson, M.C.; Bost, K.L. Osteoblasts produce monocyte chemoattractant protein-1 in a murine model of staphylococcus aureus osteomyelitis and infected human bone tissue. *Bone* **2005**, *37*, 504-512.

36. Molloy, A.P.; Martin, F.T.; Dwyer, R.M.; Griffin, T.P.; Murphy, M.; Barry, F.P.; O'Brien, T.; Kerin, M.J. Mesenchymal stem cell secretion of chemokines during differentiation into osteoblasts, and their potential role in mediating interactions with breast cancer cells. *International journal of cancer* **2009**, *124*, 326-332.

37. Bussard, K.M.; Venzon, D.J.; Mastro, A.M. Osteoblasts are a major source of inflammatory cytokines in the tumor microenvironment of bone metastatic breast cancer. *Journal of cellular biochemistry* **2010**, *111*, 1138-1148.

38. Sceneay, J.; Smyth, M.J.; Moller, A. The pre-metastatic niche: Finding common ground. *Cancer metastasis reviews* **2013**, *32*, 449-464.

39. Chiovaro, F.; Martina, E.; Bottos, A.; Scherberich, A.; Hynes, N.E.; Chiquet-Ehrismann, R. Transcriptional regulation of tenascin-w by tgf-beta signaling in the bone metastatic niche of breast cancer cells. *International journal of cancer* **2015**, *137*, 1842-1854.

40. Wobus, M.; List, C.; Dittrich, T.; Dhawan, A.; Duryagina, R.; Arabanian, L.S.; Kast, K.; Wimberger, P.; Stiehler, M.; Hofbauer, L.C*., et al.* Breast carcinoma cells modulate the chemoattractive activity of human bone marrow-derived mesenchymal stromal cells by interfering with cxcl12. *International journal of cancer* **2015**, *136*, 44-54.

41. Oskarsson, T.; Massague, J. Extracellular matrix players in metastatic niches. *The EMBO journal* **2012**, *31*, 254-256.

42. Scherberich, A.; Tucker, R.P.; Samandari, E.; Brown-Luedi, M.; Martin, D.; Chiquet-Ehrismann, R. Murine tenascin-w: A novel mammalian tenascin expressed in kidney and at sites of bone and smooth muscle development. *Journal of cell science* **2004**, *117*, 571-581.

43. Massague, J.; Obenauf, A.C. Metastatic colonization by circulating tumour cells. *Nature* **2016**, *529*, 298-306.

44. Corcoran, K.E.; Trzaska, K.A.; Fernandes, H.; Bryan, M.; Taborga, M.; Srinivas, V.; Packman, K.; Patel, P.S.; Rameshwar, P. Mesenchymal stem cells in early entry of breast cancer into bone marrow. *PloS one* **2008**, *3*, e2563.

45. Bersini, S.; Jeon, J.S.; Dubini, G.; Arrigoni, C.; Chung, S.; Charest, J.L.; Moretti, M.; Kamm, R.D. A microfluidic 3d in vitro model for specificity of breast cancer metastasis to bone. *Biomaterials* **2014**, *35*, 2454-2461.

46. Varani, K.; Vincenzi, F.; Targa, M.; Paradiso, B.; Parrilli, A.; Fini, M.; Lanza, G.; Borea, P.A. The stimulation of a(3) adenosine receptors reduces bone-residing breast cancer in a rat preclinical model. *European journal of cancer* **2013**, *49*, 482-491.

47. Jeon, J.S.; Bersini, S.; Gilardi, M.; Dubini, G.; Charest, J.L.; Moretti, M.; Kamm, R.D. Human 3d vascularized organotypic microfluidic assays to study breast cancer cell extravasation. *Proceedings of the National Academy of Sciences of the United States of America* **2015**, *112*, 214-219.

48. Ghajar, C.M.; Peinado, H.; Mori, H.; Matei, I.R.; Evason, K.J.; Brazier, H.; Almeida, D.; Koller, A.; Hajjar, K.A.; Stainier, D.Y*., et al.* The perivascular niche regulates breast tumour dormancy. *Nature cell biology* **2013**, *15*, 807-817.

49. Kingsley, L.A.; Fournier, P.G.; Chirgwin, J.M.; Guise, T.A. Molecular biology of bone metastasis. *Molecular cancer therapeutics* **2007**, *6*, 2609-2617.

50. Rajski, M.; Vogel, B.; Baty, F.; Rochlitz, C.; Buess, M. Global gene expression analysis of the interaction between cancer cells and osteoblasts to predict bone metastasis in breast cancer. *PloS one* **2012**, *7*, e29743.

51. D'Ambrosio, J.; Fatatis, A. Osteoblasts modulate ca2+ signaling in bone-metastatic prostate and breast cancer cells. *Clinical & experimental metastasis* **2009**, *26*, 955-964.

52. Valastyan, S.; Weinberg, R.A. Tumor metastasis: Molecular insights and evolving paradigms. *Cell* **2011**, *147*, 275-292.

53. Marlow, R.; Honeth, G.; Lombardi, S.; Cariati, M.; Hessey, S.; Pipili, A.; Mariotti, V.; Buchupalli, B.; Foster, K.; Bonnet, D*., et al.* A novel model of

dormancy for bone metastatic breast cancer cells. *Cancer research* **2013**, *73*, 6886-6899.

54. Zhou, Y.; Zuo, D.; Wang, M.; Zhang, Y.; Yu, M.; Yang, J.; Yao, Z. Effect of truncated neurokinin-1 receptor expression changes on the interaction between human breast cancer and bone marrow-derived mesenchymal stem cells. *Genes to cells : devoted to molecular & cellular mechanisms* **2014**, *19*, 676-691.

55. Ono, M.; Kosaka, N.; Tominaga, N.; Yoshioka, Y.; Takeshita, F.; Takahashi, R.U.; Yoshida, M.; Tsuda, H.; Tamura, K.; Ochiya, T. Exosomes from bone marrow mesenchymal stem cells contain a microrna that promotes dormancy in metastatic breast cancer cells. *Science signaling* **2014**, *7*, ra63.

56. Lim, P.K.; Bliss, S.A.; Patel, S.A.; Taborga, M.; Dave, M.A.; Gregory, L.A.; Greco, S.J.; Bryan, M.; Patel, P.S.; Rameshwar, P. Gap junction-mediated import of microrna from bone marrow stromal cells can elicit cell cycle quiescence in breast cancer cells. *Cancer research* **2011**, *71*, 1550-1560.

57. Sosnoski, D.M.; Norgard, R.J.; Grove, C.D.; Foster, S.J.; Mastro, A.M. Dormancy and growth of metastatic breast cancer cells in a bone-like microenvironment. *Clinical & experimental metastasis* **2015**, *32*, 335-344.

58. Chen, Y.C.; Sosnoski, D.M.; Mastro, A.M. Breast cancer metastasis to the bone: Mechanisms of bone loss. *Breast cancer research : BCR* **2010**, *12*, 215.

59. Canon, J.; Bryant, R.; Roudier, M.; Branstetter, D.G.; Dougall, W.C. Rankl inhibition combined with tamoxifen treatment increases anti-tumor efficacy and prevents tumor-induced bone destruction in an estrogen receptor-

positive breast cancer bone metastasis model. *Breast cancer research and treatment* **2012**, *135*, 771-780.

60.   Morrison, C.; Mancini, S.; Cipollone, J.; Kappelhoff, R.; Roskelley, C.; Overall, C. Microarray and proteomic analysis of breast cancer cell and osteoblast co-cultures: Role of osteoblast matrix metalloproteinase (mmp)-13 in bone metastasis. *J Biol Chem* **2011**, *286*, 34271-34285.

61.   Chen, Y.; Shi, H.Y.; Stock, S.R.; Stern, P.H.; Zhang, M. Regulation of breast cancer-induced bone lesions by beta-catenin protein signaling. *The Journal of biological chemistry* **2011**, *286*, 42575-42584.

62.   Nakajima, K.; Kho, D.H.; Yanagawa, T.; Harazono, Y.; Gao, X.; Hogan, V.; Raz, A. Galectin-3 inhibits osteoblast differentiation through notch signaling. *Neoplasia* **2014**, *16*, 939-949.

63.   Zhang, Z.; Wang, H.; Ikeda, S.; Fahey, F.; Bielenberg, D.; Smits, P.; Hauschka, P.V. Notch3 in human breast cancer cell lines regulates osteoblast-cancer cell interactions and osteolytic bone metastasis. *The American journal of pathology* **2010**, *177*, 1459-1469.

64.   Li, X.Q.; Du, X.; Li, D.M.; Kong, P.Z.; Sun, Y.; Liu, P.F.; Wang, Q.S.; Feng, Y.M. Itgbl1 is a runx2 transcriptional target and promotes breast cancer bone metastasis by activating the tgfbeta signaling pathway. *Cancer research* **2015**, *75*, 3302-3313.

65.   Takahashi, N.; Maeda, K.; Ishihara, A.; Uehara, S.; Kobayashi, Y. Regulatory mechanism of osteoclastogenesis by rankl and wnt signals. *Frontiers in bioscience* **2011**, *16*, 21-30.

66. Yao, G.Q.; Sun, B.H.; Weir, E.C.; Insogna, K.L. A role for cell-surface csf-1 in osteoblast-mediated osteoclastogenesis. *Calcified tissue international* **2002**, *70*, 339-346.

67. Kim, M.S.; Day, C.J.; Morrison, N.A. Mcp-1 is induced by receptor activator of nuclear factor-{kappa}b ligand, promotes human osteoclast fusion, and rescues granulocyte macrophage colony-stimulating factor suppression of osteoclast formation. *The Journal of biological chemistry* **2005**, *280*, 16163-16169.

68. Yasuda, H.; Shima, N.; Nakagawa, N.; Yamaguchi, K.; Kinosaki, M.; Mochizuki, S.; Tomoyasu, A.; Yano, K.; Goto, M.; Murakami, A*., et al.* Osteoclast differentiation factor is a ligand for osteoprotegerin/osteoclastogenesis-inhibitory factor and is identical to trance/rankl. *Proceedings of the National Academy of Sciences of the United States of America* **1998**, *95*, 3597-3602.

69. Shalhoub, V.; Faust, J.; Boyle, W.J.; Dunstan, C.R.; Kelley, M.; Kaufman, S.; Scully, S.; Van, G.; Lacey, D.L. Osteoprotegerin and osteoprotegerin ligand effects on osteoclast formation from human peripheral blood mononuclear cell precursors. *Journal of cellular biochemistry* **1999**, *72*, 251-261.

70. Liverani, C.; Mercatali, L.; Spadazzi, C.; La Manna, F.; De Vita, A.; Riva, N.; Calpona, S.; Ricci, M.; Bongiovanni, A.; Gunelli, E*., et al.* Csf-1 blockade impairs breast cancer osteoclastogenic potential in co-culture systems. *Bone* **2014**, *66*, 214-222.

71. Nicolin, V.; Bortul, R.; Bareggi, R.; Baldini, G.; Martinelli, B.; Narducci, P. Breast adenocarcinoma mcf-7 cell line induces spontaneous

osteoclastogenesis via a rank-ligand-dependent pathway. *Acta histochemica* **2008**, *110*, 388-396.

72. Arrigoni, C.; De Luca, P.; Gilardi, M.; Previdi, S.; Broggini, M.; Moretti, M. Direct but not indirect co-culture with osteogenically differentiated human bone marrow stromal cells increases rankl/opg ratio in human breast cancer cells generating bone metastases. *Molecular cancer* **2014**, *13*, 238.

73. Wang, H.; Yu, C.; Gao, X.; Welte, T.; Muscarella, A.M.; Tian, L.; Zhao, H.; Zhao, Z.; Du, S.; Tao, J*., et al.* The osteogenic niche promotes early-stage bone colonization of disseminated breast cancer cells. *Cancer cell* **2015**, *27*, 193-210.

74. Zhao, H.; Ning, L.L.; Wang, Z.Y.; Li, H.T.; Qiao, D.; Yao, Y.; Qin, H.L. Calcitonin gene-related peptide inhibits osteolytic factors induced by osteoblast in co-culture system with breast cancer. *Cell biochemistry and biophysics* **2014**, *70*, 1097-1104.

75. Zheng, Y.; Chow, S.O.; Boernert, K.; Basel, D.; Mikuscheva, A.; Kim, S.; Fong-Yee, C.; Trivedi, T.; Buttgereit, F.; Sutherland, R.L*., et al*. Direct crosstalk between cancer and osteoblast lineage cells fuels metastatic growth in bone via auto-amplification of il-6 and rankl signaling pathways. *Journal of bone and mineral research : the official journal of the American Society for Bone and Mineral Research* **2014**, *29*, 1938-1949.

76. Zhu, J.; Jia, X.; Xiao, G.; Kang, Y.; Partridge, N.C.; Qin, L. Egf-like ligands stimulate osteoclastogenesis by regulating expression of osteoclast regulatory factors by osteoblasts: Implications for osteolytic bone metastases. *The Journal of biological chemistry* **2007**, *282*, 26656-26664.

77.   Kapoor, P.; Suva, L.J.; Welch, D.R.; Donahue, H.J. Osteoprotegrin and the bone homing and colonization potential of breast cancer cells. *Journal of cellular biochemistry* **2008**, *103*, 30-41.

78.   Schwartz, M.A.; Chen, C.S. Cell biology. Deconstructing dimensionality. *Science* **2013**, *339*, 402-404.

79.   Bersini, S.; Gilardi, M.; Arrigoni, C.; Talo, G.; Zamai, M.; Zagra, L.; Caiolfa, V.; Moretti, M. Human in vitro 3d co-culture model to engineer vascularized bone-mimicking tissues combining computational tools and statistical experimental approach. *Biomaterials* **2016**, *76*, 157-172.

80.   Bongio, M.; Lopa, S.; Gilardi, M.; Bersini, S.; Moretti, M. A 3d vascularized bone remodeling model combining osteoblasts and osteoclasts in a cap nanoparticle-enriched matrix. *Nanomedicine* **2016**, *11*, 1073-1091.

81.   Labelle, M.; Begum, S.; Hynes, R.O. Platelets guide the formation of early metastatic niches. *Proceedings of the National Academy of Sciences of the United States of America* **2014**, *111*, E3053-3061.

82.   Spiegel, A.; Brooks, M.W.; Houshyar, S.; Reinhardt, F.; Ardolino, M.; Fessler, E.; Chen, M.B.; Krall, J.A.; DeCock, J.; Zervantonakis, I.K*., et al.* Neutrophils suppress intraluminal nk cell-mediated tumor cell clearance and enhance extravasation of disseminated carcinoma cells. *Cancer discovery* **2016**, *6*, 630-649.

83.   Whittle, J.R.; Lewis, M.T.; Lindeman, G.J.; Visvader, J.E. Patient-derived xenograft models of breast cancer and their predictive power. *Breast cancer research : BCR* **2015**, *17*, 17.

Chapter2

Direct but not indirect co-culture with osteogenically differentiated human bone marrow stromal cells increases RANKL/OPG ratio in human breast cancer cells generating bone metastases

From: C. Arrigoni, P. De Luca, M. Gilardi, S. Previdi, M. Broggini and M. Moretti

2.1 Introduction

Bone metastases arise in nearly 70% of patients with advanced breast cancer, indicating bone as a favorable microenvironment for metastases, which onset dramatically alters physiological bone turnover, leading to bone lysis. It has been reported[1] that this can be caused by the up-regulation of RANKL to OPG ratio, causing an increased osteoclastogenesis[2], although the mechanisms inducing RANKL/OPG modification are not clear[1, 3].

Recently, interactions between metastatic cells and metastatic niche cells have been indicated as potential drivers of the metastatic process[4]. Thus, to understand the cross-talk between metastatic breast cancer cells and bone microenvironment, many in vitro co-culture models have been established[5-10]. The majority of

these[5, 6] involve human tumor cells cultured with mouse osteoblasts, but osteoblasts from different species have different characteristics[11] and mechanisms underlying metastasis formation can be diverse between mouse and human[12]. Moreover, while some studies reported the culture of human tumor cells in conditioned medium from human bone cells, highlighting only soluble factors effects[7, 8], only a few works[9, 10] implemented direct contact between human tumor and bone cells. However, gene expression analyses on individual cell populations have not always been performed[9].

Our work was thus aimed at investigating, by means of direct co-culture, the interactions between a line of fluorescently tagged bone metastatic human breast cancer cells, MDA-MB231-BO-KL (BOKL) and a bone microenvironment represented by osteo-differentiated primary human bone marrow stromal cells (BMSCs), in terms of modifications on RANKL/RANK/OPG expression, cell proliferation and migration.

2.2 Materials and methods

2.2.1 BMSCs isolation, differentiation and characterization

BMSCs from 3 patients undergoing hip surgery after informed consent were isolated by centrifugation at 510g for 10 minutes and incubated in complete medium (α-MEM, 10% FBS, 100 U/ml Penicillin, 100 ug/ml Streptomycin, 1% HEPES, b-FGF 5ng/ml). Non-adherent cells were removed after 6 days and medium was changed twice a week until confluence. To induce osteo-differentiation, BMSCs were seeded at 3000 cells/cm^2 in complete medium for 3 days. Osteogenic medium (OM) was successively added for 14 days: DMEM with 10% FBS, 1% HEPES, 1% sodium pyruvate, 100 U/ml Penicillin, 100 ug/ml Streptomycin, 2mM L-Glutamine, 0.15mM Ascorbic Acid-2P, 10mM β-glycerophosphate, 10nM Cholecalciferol, 10nM Dexhametasone, as already

reported[15]. Medium was changed every 3-4 days. BMSCs osteodifferentiation level was characterized through Alkaline Phosphatase (ALP) assay, Alizarin red staining and calcium quantification by means of a commercial kit (RANDOX). Osteogenic marker expression (osteopontin, osteocalcin and RUNX-2) was determined with Real time PCR compared to a human fetal lung fibroblasts cell line (MRC-5) and to primary human osteoblasts, also derived from hip surgery patients.

2.2.2 Tumor and fibroblast-like cell lines culture

MDA-MB-231-BO, a bone metastatic breast cancer cell line derived from MDA-MB-231has been developed[14] and kindly provided by Professor T. Yoneda (University of texas Health Science Cancer at San Antonio, USA). MDA-MB-231-BO cells have been transfected with Katushka plasmid (Evrogen), encoding for a red fluorescent protein and with PGL3-Luc plasmid, encoding for Firefly Luciferase enzyme. Clones expressing high levels of Katushka have been isolated by FACS and one of these (BOKL) was used in subsequent experiments. BOKL were cultured in growth medium (GM): DMEM with 10% FBS, 1% Penicillin/Streptomycin and 2mM L-Glutamine. MRC-5 fibroblasts were grown in EMEM with 10% FBS, 1% Penicillin/Streptomycin and 2mM L-Glutamine.

2.2.3 Co-culture between BMSCs or MRC-5 and BOKL

To study the effect of direct contact of tumor cells (BOKL) on bone-like cells (osteo-differentiated BMSCs) or MRC-5, five different experimental conditions were compared:

1. **BOKL in direct co-culture with osteo-differentiated BMSCs (BOKL co-culture BMSCs):** After BMSCs osteo-differentiation for 14 days, BOKL (5000 cells/cm^2) were seeded on the BMSCs monolayer. BOKL adhered to BMSCs and both cell types were cultured in GM for 3 days.

2. **BOKL in conditioned medium from osteo-differentiated BMSCs (BOKL CM BMSCs):** After BMSCs osteo-differentiation for 14 days, osteogenic medium was removed; GM was then added for 24h to obtain conditioned medium (CM) from osteo-differentiated BMSCs. BOKL were seeded in a multiwell at 5000 cells/cm^2 and cultured in 100% CM for 3 days.

3. **BOKL in co-culture with MRC-5 (BOKL co-culture MRC-5):** MRC-5 were kept in culture until confluence, then BOKL (5000 cells/cm^2) were seeded on the MRC-5 monolayer and GM was added for 3 days.

4. **BOKL in conditioned medium from MRC-5 (BOKL CM MRC-5):** After MRC-5 culture until confluence, MRC-5 culture medium was removed and fresh medium was added for 24h to obtain conditioned medium (CM) from MRC-5. BOKL were seeded in a multiwell at 5000 cells/cm^2 and cultured in 100% CM for 3 days.

5. **BOKL control:** As a control condition, BOKL were seeded at 5000 cells/cm^2 in a multiwell and cultured for 3 days in GM.

2.2.4 Gene expression analysis

After direct co-culture between BOKL and osteo-differentiated BMSCs or MRC-5, cells were enzymatically digested for 15 minutes with collagenase I (15 mg/ml) and for 15 minutes with trypsin-EDTA 0.05% at 37°C, under gentle agitation. Cells were then re-suspended in FACS buffer and subjected to FACS sorting, to obtain two separated populations.

Total RNA was isolated from individual cell populations using SV total RNA (Promega) and reverse transcribed (High-capacity cDNA archive kit - Applied Biosystem). Gene expression was assessed in relative quantitative RT-PCR with taqman® probes (Applied Biosystem) for the target genes RANK (Hs00187192_m1), RANKL (Hs00243522_m1), OPG (Hs00900358_m1), CDH11

(Hs00901475_m1), RUNX2 (HS00231692_m1). As housekeeping gene human cyclofillin (4326316E-1101014) was used.

To exclude that modifications in gene expression were due to the above reported separation procedure and not to co-culture, data were normalized to appropriate controls. Gene expression levels of cells after co-culture were normalized respective to cells grown in GM and then subjected to the same enzymatic digestion and sorting procedure (control 1). For cells grown in CM, gene expression was instead normalized to BOKL control (control 2).

2.2.5 Cell proliferation

BOKL were seeded 5000/cm^2 and grown for 3 days in the four different experimental conditions. After detachment with trypsin-EDTA 0.05%, cells were counted by an automated image-based Cell Counter, equipped with fluorescence filters (TALI$^®$, LifeTechnologies), which allowed us to quantify separately red fluorescent BOKL and non-fluorescent BMSCs or fibroblasts.

2.2.6 Time lapse analysis

To monitor BOKL migration in the different experimental conditions, time lapse analysis was performed over 3 days, capturing an image every 15 minutes. A total of 10404 images were analyzed, specifically 9 fields for each of the four experimental conditions, 289 images for each field. ImageJ software-Manual Tracking tool was applied to measure the displacement of each cell between two consecutive images. To establish the existence of a preferential direction in cell migration, index of directionality $P=A1/A2$[25] was calculated, whereby A2 is the sum of distances traveled by each cell through all the 289 images whereas A1 is the distance, calculated for each cell, between the initial position (first image) and the final one (last image). P values near 0 indicate a random movement, whereas higher P values indicate a preferential migration.

To quantify cell clusterization at the end of the co-culture, the image at 72h time point was analyzed, counting cells. Clusters were defined as groups of at least 4 cells in direct contact, a definition already adopted for micro-metastases[24]. Cluster number was normalized to total cell number, to exclude the possible effect of cell proliferation.

2.2.7 Statistical analysis

All statistical analyses were performed with Prism5. ANOVA followed by Bonferroni post-hoc test was used to detect significant differences between groups. Level of significance was set at $p < 0.05$.

2.3 Results and discussion

2.3.1 Direct contact with bone-like cells induced RANKL/OPG up-regulation in metastatic cells

To investigate whether specific direct contact between bone and tumor cells is involved in RANKL/OPG ratio modifications, we compared gene expression of BOKL after 3 days of direct co-culture with osteo-differentiated BMSCs (co-culture BMSCs) with that of BOKL cultured in conditioned medium from osteo-differentiated BMSCs (CM BMSCs) and that of BOKL in direct or indirect co-culture with fibroblasts, non osteogenic cells (co-culture MRC-5, CM MRC-5). Based on literature data showing that cell populations with equivalent capacity to form bone metastasis also share equal expression of genes related to bone invasion and metastasis[13], we chose to use a single bone seeking clone[14], with equivalent bone metastatic potential as compared to other bone seeking clones[13]. BMSCs were harvested from 3 patients undergoing hip surgery, after informed consent, and were differentiated in osteogenic medium (OM), as described[15].

BOKL and BMSCs after direct co-culture with BMSCs or MRC-5 were retrieved by enzymatic digestion and separated by FACS sorting. To exclude modifications in gene expression caused by the separation procedure, gene expression levels were normalized respective to those of BOKL grown in GM and then subjected to the same separation procedure (control 1). CM for indirect co-culture was harvested from the same BMSCs and MRC-5 used in direct co-cultures and gene expression of BOKL in CM was normalized respective to BOKL grown in GM (control 2). All materials and methods are described in Additional file 1: Supplementary materials and methods.

Results of PCR analyses showed a strong and statistically significant upregulation (13 fold, $p < 0.05$) of RANKL in BOKL co-culture BMSCs as compared to control1 but not in BOKL CM BMSCs and BOKL CM MRC-5 (Fig. 1A, $p < 0.05$ and $p < 0.01$, respectively). A small increase (not statistically significant) in RANKL was observed in BOKL co-culture MRC-5 where a siginificant upregulation of OPG was found (Fig. 1A), differently from all other conditions. Altogheter our results show that RANKL/OPG ratio (a more useful indicator of effectively available RANKL) in BOKL co-culture BMSCs is 7 fold increased (Fig. 1B) relative to control, and significantly higher ($p < 0.01$) than all other conditions, where no increase was found, demonstrating that direct, specific contact between tumor and bone cells can modify RANKL/OPG ratio. This suggests that among other factors hypothesized in the literature[1], heterotypic interactions between metastatic and bone cells can be involved in RANKL/OPG imbalance.

We demonstrated a specific activation of RANKL/OPG and not a generalized change in gene expression, since CDH11, known to be highly expressed in bone-seeking clones[16], and RANKL receptor RANK were not significantly modified in BOKL after direct or indirect co-cultures (Fig1A). We also analyzed gene expression of BMSCs after direct co-culture and we found that average value of RANKL and osteogenic differentiation markers expression did not significantly differ between osteo-differentiated BMSCs before and after direct co-culture.

However, 1 out of 3 patients derived osteo-differentiated BMSCs (patient2) showed a 4-fold RANKL up regulation after direct co-culture, due to the high biological variability of primary human cells (Fig1C,D). RANK expression was instead significantly upregulated in BMSCs after co-culture with tumor cells (Fig. 1C, p<0.01 as compared to BMSCs before co-culture), differently from MRC-5, which showed no expression of RANK before or after co-culture (data not shown), confirming a specific activation of the RANKL/OPG/RANK pathway caused by the crosstalk between tumor cells and bone microenvironment.

The separation of metastatic cells from bone-like cells was based on fluorescent labeling of cells before co-culture, giving a particular reliability to our results. Another study analyzed gene expression of tumor cells in direct co-culture with BMSCs[10], separating the two cell populations on the basis of epithelial markers expression. It is however known that highly aggressive breast cancer cells in co-culture with BMSCs can undergo epithelial-to-mesenchymal transition[17], causing a loss of epithelial markers and consequently affecting cell separation reliability.
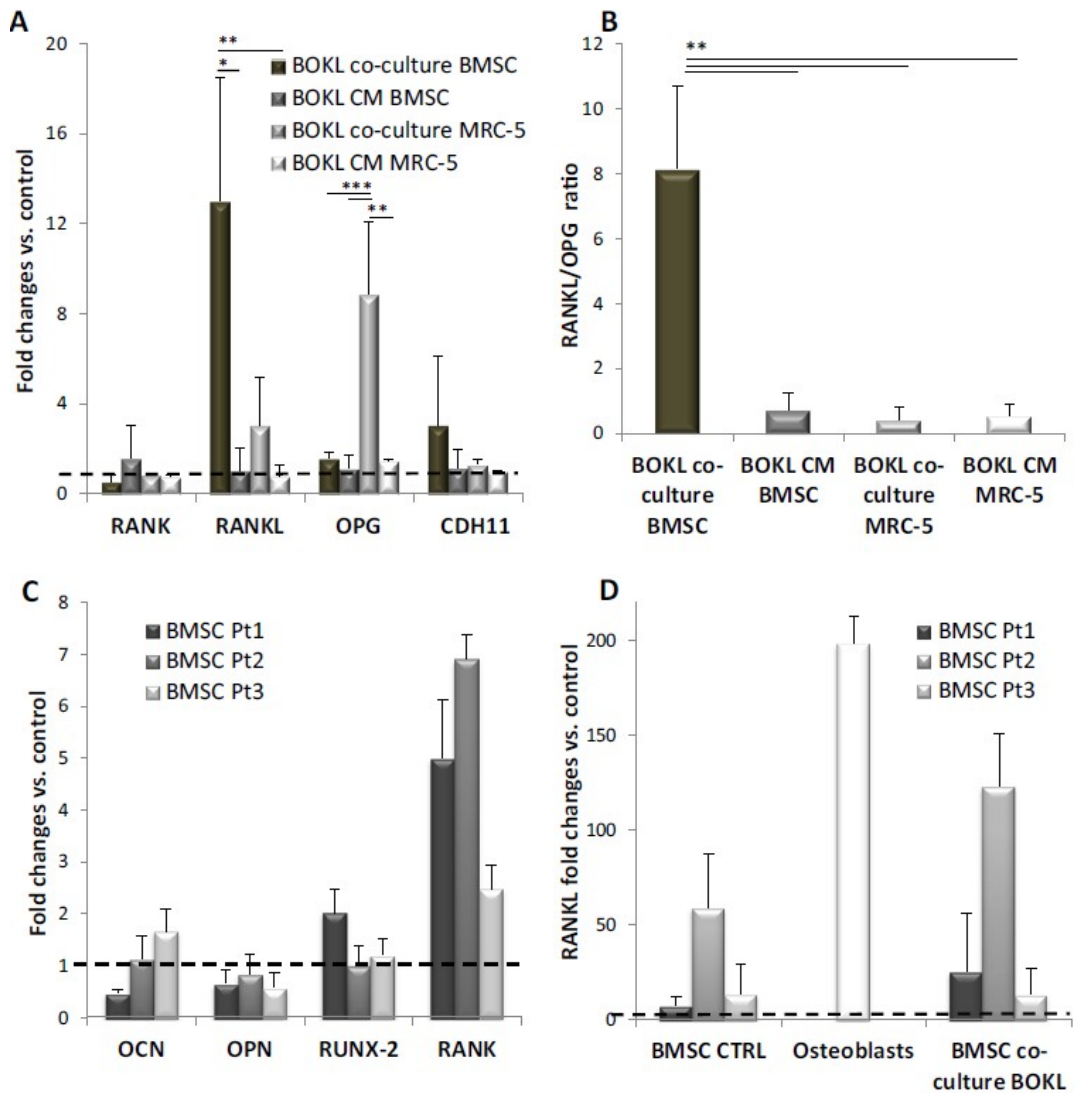
Fig1: Gene expression of BOKL and BMSCs from different patients cultured for 3 days in direct contact. (A) Expression of genes related to RANK/RANKL/OPG pathway and CDH11 in BOKL after direct co-culture with osteo-differentiated BMSCs (BOKL co-culture BMSC) compared with BOKL cultured in medium conditioned by the same osteo-differentiated BMSCs (BOKL CM BMSC), with BOKL after direct co-culture with fibroblasts (BOKL co-culture MRC-5) and with BOKL cultured in medium conditioned by the same fibroblasts (BOKL CM MRC-5). *: p < 0.05, **: p < 0.01 and ***: p < 0.001. Fold changes were calculated respective to control 1 or 2 (expression set to 1, dotted line). Control 1: BOKL grown in GM and subjected to enzymatic digestion and FACS sorting, used for BOKL from

both direct co-cultures, control 2: BOKL grown in GM, used for BOKL in both CMs. (B) RANKL/OPG ratio, for BOKL after direct co-culture with BMSCs and fibroblasts (BOKL co-culture BMSC and BOKL co-culture MRC-5) and in BOKL cultured in medium conditioned by BMSCs and fibroblasts (BOKL CM BMSC and BOKL CM MRC-5). **: $p < 0.01$. (C) Gene expression of osteocalcin (OCN), osteopontin (OPN), RUNX-2 and RANK in BMSCs from three different patients (Pt1, Pt2, Pt3) after direct
co-culture with BOKL. Fold changes were calculated respective to the same BMSCs before co-culture expression value set to 1, dotted line). (D) RANKL expression of BMSCs before (BMSC CTRL) and after direct co-culture (BMSCs co-culture BOKL), relative to three different patients, compared to that of osteoblasts. Fold changes were calculated respective to fibroblasts (expression set to 1, dotted line). All error bars represent standard deviations of at least three different experiments.

2.3.2 Direct co-colture effects on BOKL aggregation, migration and proliferation

With the aim to analyze effects of direct contact between bone-like cells and BOKL on aggregation, migration and proliferation, time lapse analyses were performed, revealing an evident BOKL aggregation in direct co-culture with osteo-differentiated BMSCs, not noticeable in the other conditions, as shown in fluorescence images (Fig2A,B,C,D). This phenomenon resembled cell filing, already described in pathological tissues bearing metastases[5]. Interestingly, BOKL clustering did not occur in co-culture with MRC-5, suggesting that this can represent a specific effect of the direct contact with bone cells. Cluster number normalized to total cell number was indeed significantly higher in BOKL co-culture BMSCs, as compared to other conditions ($p<0.001$, Fig.2E). We observed a preferential direction of cell migration in direct co-culture as compared to culture with CM or GM ($p<0.01$, Fig.2F), probably due to cell contact guidance[18] and not to specific characteristics of cells that composed the monolayer, being this effect evident also in co-culture with MRC-5. Fig.2G reports the quantification of BOKL proliferation in the different conditions, showing no significant differences between BOKL co-culture BMSCs and BOKL CM BMSCs. BOKL grown in

100% CM did not show a lower degree of proliferation as compared to control 2, indicating that CM can support BOKL growth. On the other hand, BOKL in contact with fibroblasts showed a significantly higher (p<0.001) proliferation, accordingly to literature results showing how the release of specific factors (such as interleukin-6) by fibroblasts can increase the growth of breast cancer cells[19].
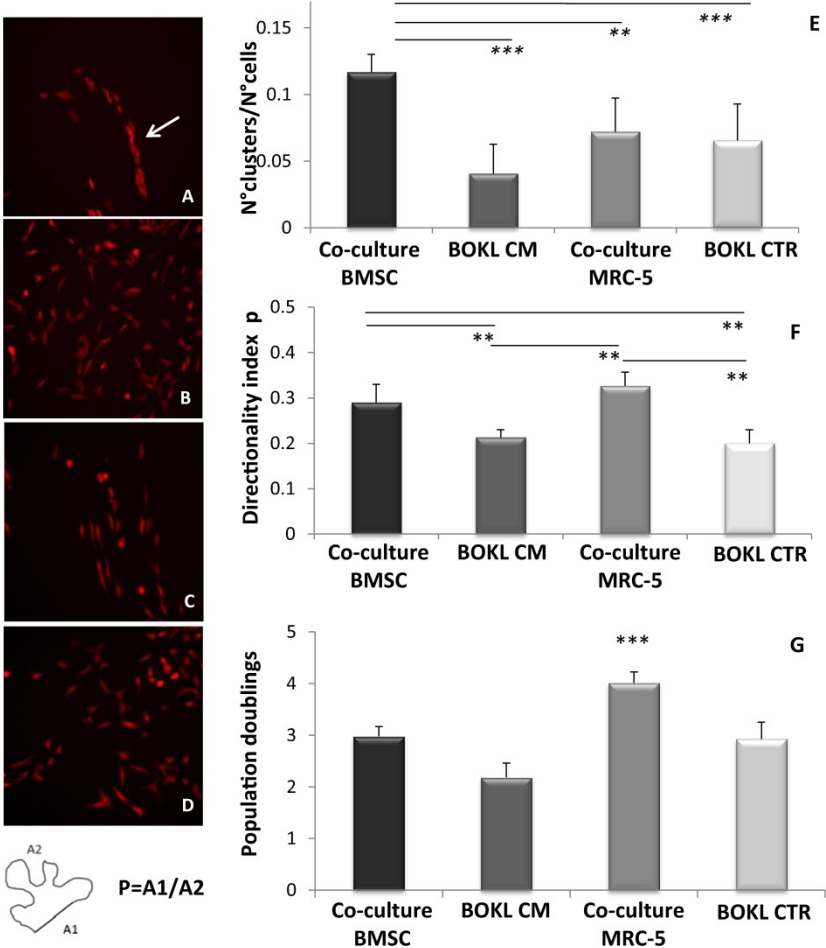
Fig2: Cell migration, aggregation and proliferation in different conditions. Fluorescence images of: (A) BOKL in direct co-culture with BMSCs (arrow indicates a cell cluster), (B) BOKL cultured in CM BMSCs, (C) BOKL in co-culture with MRC-5 and (D) BOKL in GM. All the images have been taken after 3 days of culture. (E) Quantification of the cell aggregation, expressed as the average number of clusters normalized per total cell number. Clusters were defined as groups of at least four cells in contact, as already reported for

micrometastasis [20]. ***: p < 0.001, **p < 0.01 vs. other conditions. (F) Quantification of the directionality of the cell movement, expressed as index P. P is defined as A1/A2, where A1 is the distance between the position of the cell in the last image and that in the first. A2 is the sum of distances travelled by the cell in all the images [21]. Values of P near 1 indicate a directional movement. **: p < 0.01 vs. other conditions. (G) Proliferation of BOKL after 3 days of direct co-culture with BMSCs or MRC-5 and after 3 days in culture with conditioned medium from BMSCs (CM) or control medium (CTR), ***: p < 0.001. All error bars represent standard deviations of at least three different experiments.

2.3.3 Characterization of bone-like microenvironment

To establish a bone-like environment we differentiated BMSCs for 14 days in osteogenic medium, having previous surveys and literature data[20] established that it allowed to achieve adequate osteo-differentiation. However, considering the time-dependence of differentiation markers expression and the different effects reported on tumor cells co-cultured with variously differentiated bone cells[6], we determined the osteodifferentiation degree of BMSCs used in our experiments with reference to both terminally differentiated osteoblasts and MRC-5. We characterized BMSCs osteodifferentiation through Alkaline Phosphatase (ALP) assay, Alizarin red staining and calcium quantification. Moreover, expression of both early (RUNX-2) and late osteogenic markers (osteopontin and osteocalcin)[21], was determined. After 14 days in osteogenic medium, BMSCs from all the 3 different donors showed positive Alizarin red staining (Fig3A), demonstrating the presence of calcium deposits.Their quantification demonstrated significantly higher calcium levels in BMSCs as compared to MRC-5 ($p<0.001$, Fig1_SupplementaryA). ALP activity, index of initial osteogenic commitment of cells, normalized to total protein content, was detectable in all the 3 patients at comparable levels as shown in Fig1_SupplementaryB. Moreover, the expression of osteogenic markers osteopontin, osteocalcin and RUNX-2 was significantly up-regulated in osteo-differentiated BMSCs as compared to MRC-5. Osteopontin and

osteocalcin expression was significantly lower than in primary osteoblasts (p<0.05) whereas expression of RUNX-2 was comparable (Fig.3B).
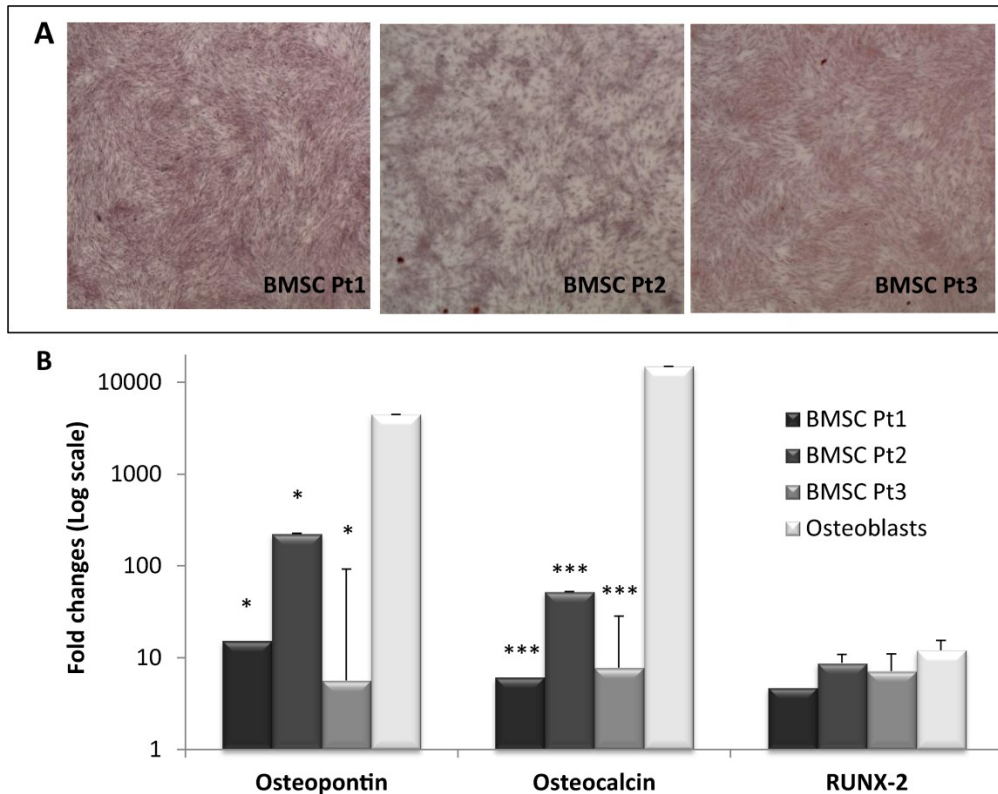
Fig3: Characterization of the bone-like microenvironment. Characterization of the osteo-differentiation level of BMSCs from three different patients cultured for 14 days in osteogenic medium (DMEM additioned with 10% FBS, 1% HEPES, 1% pen strep, 15 mM ascorbic acid, 10 mM β −glycerophosphate, 10 nM dexamethasone, 10nM cholecalciferol). (A) Alizarin red staining for the three different BMSCs populations; (B) Expression
of typical osteoblastic markers, normalized to MRC-5 expression (set to 1) and also quantified in RNA deriving directly from human bone samples (osteoblasts). *: p < 0.05, ***: p < 0.001 as compared to osteoblasts expression. All error bars represent standard deviations of at least three different experiments.

In conclusion, our simple co-culture model allowed to obtain results otherwise not possible to achieve in *in vivo* experiments, whereby it would be impossible to sort, separate and analyze the cell populations involved in the metastatic process. In particular, we demonstrated for the first time that direct but not indirect co-culture between human tumor cells and primary bone-like cells induced a significant up-regulation of RANKL/OPG expression in bone metastatic cells, suggesting an important role of direct contact in the bone metastatic process. This is in line with the reported clinical expression, determined by immunohistochemistry, of RANKL in human bone metastases[22, 23]. Furthermore, although we do not yet have a mechanistic explanation, upregulation of RANKL/OPG ratio and BOKL clustering observed only in direct co-culture with osteo-differentiated BMSCs and not in culture with conditioned medium or in direct co-culture with fibroblasts, further support the hypothesis that heterotypic cell interactions between tumor cells and bone cells can have a key role in the establishment of bone metastases.

References

1. *Dougall WC:* **Molecular pathways: osteoclast-dependent and osteoclast-independent roles of the RANKL/RANK/OPG pathway in tumorigenesis and metastasis.** *Clin Cancer Res 2012,* **18:***326-335.*

2. *Hofbauer LC, Schoppet M:* **Clinical implications of the osteoprotegerin/RANKL/RANK system for bone and vascular diseases.** *JAMA : the journal of the American Medical Association 2004,* **292:***490-495.*

3. *Canon JR, Roudier M, Bryant R, Morony S, Stolina M, Kostenuik PJ, Dougall WC:* **Inhibition of RANKL blocks skeletal tumor progression and improves survival in a mouse model of breast cancer bone metastasis.** *Clin Exp Metastasis 2008,* **25:***119-129.*

4. *Chaffer CL, Weinberg RA:* **A Perspective on Cancer Cell Metastasis.** *Science 2011,* **331:***1559-1564.*

5. *Krishnan V, Shuman LA, Sosnoski DM, Dhurjati R, Vogler EA, Mastro AM:* **Dynamic interaction between breast cancer cells and osteoblastic tissue: Comparison of Two- and Three-dimensional cultures.** *Journal of Cellular Physiology 2011,* **226:***2150-2158.*

6. *Giunciuglio D, Cai T, Filanti C, Manduca P, Albini A:* **Effect of osteoblast supernatants on cancer cell migration and invasion.** *Cancer Lett 1995,* **97:***69-74.*

7. *Pohorelic B, Singh R, Parkin S, Koro K, Yang AD, Egan C, Magliocco A:* **Role of Src in breast cancer cell migration and invasion in a breast cell/bone-derived cell microenvironment.** *Breast Cancer Res Treat 2012,* **133:***201-214.*

8. *Hsu YL, Hou MF, Kuo PL, Huang YF, Tsai EM:* **Breast tumor-associated osteoblast-derived CXCL5 increases cancer progression by ERK/MSK1/Elk-1/snail signaling pathway.** *Oncogene 2013,* **32:***4436-4447.*

9.   Rajski M, Vogel B, Baty F, Rochlitz C, Buess M: **Global gene expression analysis of the interaction between cancer cells and osteoblasts to predict bone metastasis in breast cancer.** *PLoS One 2012, **7**:e29743.*

10.   Molloy AP, Martin FT, Dwyer RM, Griffin TP, Murphy M, Barry FP, O'Brien T, Kerin MJ: **Mesenchymal stem cell secretion of chemokines during differentiation into osteoblasts, and their potential role in mediating interactions with breast cancer cells.** *International Journal of Cancer 2009, **124**:326-332.*

11.   Czekanska EM, Stoddart MJ, Richards RG, Hayes JS: **In search of an osteoblast cell model for in vitro research.** *Eur Cell Mater 2012, **24**:1-17.*

12.   Borowsky AD: **Choosing a mouse model: experimental biology in context--the utility and limitations of mouse models of breast cancer.** *Cold Spring Harb Perspect Biol 2011, **3**:a009670.*

13.   Kang Y, Siegel PM, Shu W, Drobnjak M, Kakonen SM, Cordón-Cardo C, Guise TA, Massagué J: **A multigenic program mediating breast cancer metastasis to bone.** *Cancer Cell 2003, **3**:537-549.*

14.   Yoneda T, Williams PJ, Hiraga T, Niewolna M, Nishimura R: **A bone-seeking clone exhibits different biological properties from the MDA-MB-231 parental human breast cancer cells and a brain-seeking clone in vivo and in vitro.** *J Bone Miner Res 2001, **16**:1486-1495.*

15.   Lopa S, Mercuri D, Colombini A, De Conti G, Segatti F, Zagra L, Moretti M: **Orthopedic bioactive implants: Hydrogel enrichment of macroporous titanium for the delivery of mesenchymal stem cells and strontium.** *J Biomed Mater Res A 2013.*

16.   Tamura D, Hiraga T, Myoui A, Yoshikawa H, Yoneda T: **Cadherin-11-mediated interactions with bone marrow stromal/osteoblastic cells support selective colonization of breast cancer cells in bone.** Int J Oncol 2008, **33:**17-24.

17.   Foroni C, Broggini M, Generali D, Damia G: **Epithelial-mesenchymal transition and breast cancer: role, molecular mechanisms and clinical impact.** Cancer Treat Rev 2012, **38:**689-697.

18.   Leong MC, Vedula SR, Lim CT, Ladoux B: **Geometrical constraints and physical crowding direct collective migration of fibroblasts.** Commun Integr Biol 2013, **6:**e23197.

19.   Studebaker AW, Storci G, Werbeck JL, Sansone P, Sasser AK, Tavolari S, Huang T, Chan MW, Marini FC, Rosol TJ, et al: **Fibroblasts isolated from common sites of breast cancer metastasis enhance cancer cell growth rates and invasiveness in an interleukin-6-dependent manner.** Cancer Res 2008, **68:**9087-9095.

20.   Birmingham E, Niebur GL, McHugh PE, Shaw G, Barry FP, McNamara LM: **Osteogenic differentiation of mesenchymal stem cells is regulated by osteocyte and osteoblast cells in a simplified bone niche.** Eur Cell Mater 2012, **23:**13-27.

21.   Long MW: **Osteogenesis and bone-marrow-derived cells.** Blood Cells Mol Dis 2001, **27:**677-690.

22.   Brown JM, Corey E, Lee ZD, True LD, Yun TJ, Tondravi M, Vessella RL: **Osteoprotegerin and rank ligand expression in prostate cancer.** Urology 2001, **57:**611-616.

23.   Peng X, Guo W, Ren T, Lou Z, Lu X, Zhang S, Lu Q, Sun Y: **Differential expression of the RANKL/RANK/OPG system is associated with bone metastasis in human non-small cell lung cancer.** *PLoS One 2013,* **8:***e58361.*

24.   Cserni G, Bianchi S, Vezzosi V, van Diest P, van Deurzen C, Sejben I, Regitnig P, Asslaber M, Foschini MP, Sapino A, et al: **Variations in sentinel node isolated tumour cells/micrometastasis and non-sentinel node involvement rates according to different interpretations of the TNM definitions.** *Eur J Cancer 2008,* **44:***2185-2191.*

25.   Maheshwari G, Lauffenburger DA: **Deconstructing (and reconstructing) cell migration.** *Microsc Res Tech 1998,* **43:***358-368.*

Supplementary information

FigS1: Confirmation of osteo-differentiation of BMSCs. (A) Quantification of calcium deposits for BMSCs from three different patients. ***: p < 0.001, compared to fibroblasts. (B) Quantification of ALP activity, normalized to the total protein content. All error bars represent standard deviations of at least three different experiments.
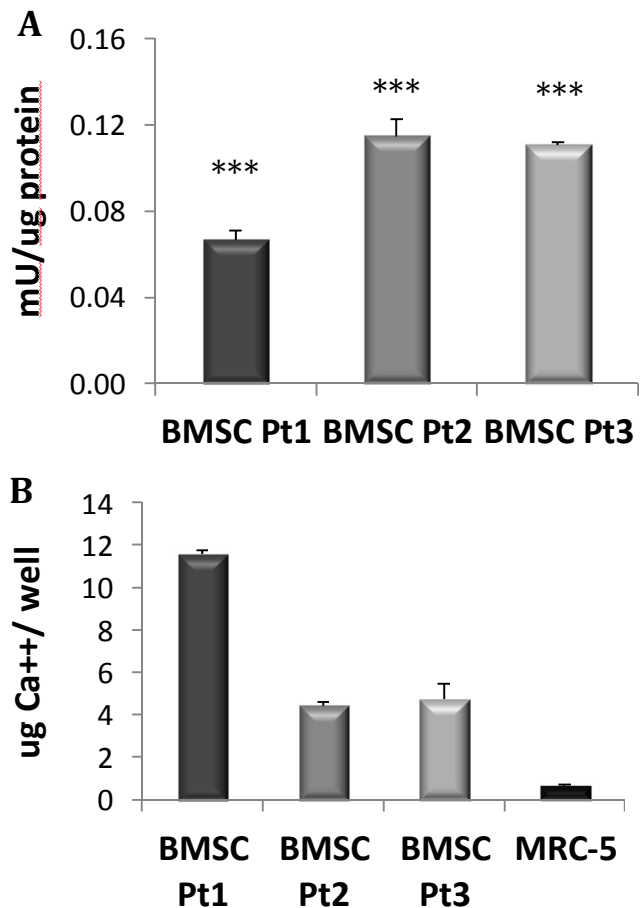
Chapter 3

Human 3D Vascularized Organotypic Microfluidic Assays to Study Breast Cancer Cell Extravasation

*From: *JS Jeon, *S. Bersini, M. Gilardi, G. Dubini, JL Charest, M. Moretti, RD Kamm,*
equally contributing authors

3.1 Introduction

Dissemination of cancer cells from a primary tumor to secondary loci represents the leading cause of cancer-related mortality [1]. Despite significant advances in diagnostics and therapy, most of the available treatments are not effective, since the disseminated cells are resistant to conventional agents [2, 3]. Invasion and metastatization are complex and multistep processes guided by a wide spectrum of genetic and biochemical determinants [4]. A key aspect of metastases is reflected in the interactions between specific cancer cell types and different secondary organs. While circulatory patterns and flow rates may play some role in cancer cell dissemination, it appears that the organ-specificity of metastases is primary due to the cross-talk between specific cancer cells and biologically unique

tissues – the seed-and-soil paradigm [3]. For example, breast and prostate cancers are known to frequently metastasize to bone [5] with 70% of advanced breast cancer patients affected by skeletal metastases, leading to high rates of morbidity and mortality [6]. Moreover, it has been recently demonstrated that breast cancer cells can reseed from bone to other sites including the breast, further emphasizing the key role of the bone microenvironment in the metastatic process [7].

Metastasis organ-specificity and extravasation appear to be tightly coupled since specific chemo-attractant molecules are secreted by organ-specific stromal cells [8]. Furthermore, positive interactions with circulating non-cancer cells, e.g. platelets, leukocytes and monocytes/macrophages promote cancer cell trans-endothelial migration into surrounding tissues [9].

In vivo and *ex vivo* studies have been performed to investigate cancer cell extravasation in mouse models through liver sinusoids and pulmonary circulation [10], or in zebrafish embryos [11]. Recently, Schumacher and colleagues have shown the influence of platelet-secreted nucleotides playing a crucial role in the trans-endothelial migration of cancer cells in the lung of mouse models [12]. *In vivo* models have been developed to study breast cancer metastases to bone by means of intravenous or direct skeletal injection of breast cancer cells in mice [13]. Although *in vivo* models play an essential role in replicating physiological conditions, they lack the possibility to analyze highly specific interactions between human cancer cells, human blood vessels and tissues, and they are not well suited to perform reproducible parametric studies. To remedy this, several *in vitro* models have been developed to analyze cell migration mechanisms and particularly the invasive potential of cancer cells [14]. However, these models are often highly simplified, such as the Boyden chamber or wound assays [15], which fail to allow the analysis of complex cell-cell and cell-matrix interactions, are

limited in their capability to tightly control the local microenvironment, and offer only limited imaging.

Microfluidics overcomes some of the technical limitations of traditional assays [16] allowing the study of cancer metastases under biochemically and biophysically controlled 3D microenvironments coupled with high resolution real time imaging [17]. Various microfluidic models have been developed for studying tumor angiogenesis [18], transition to invasion [19], intravasation [20], the role of interstitial flow [21] and matrix stiffness [22] on cancer cell migration, adhesion [23] and extravasation [24, 25]. Recently, the Kamm group presented a microfluidic model to investigate the specificity of breast cancer metastasis to bone, providing quantitative data on cancer cell extravasation rate and reproducing the effects of the CXCL5-CXCR2 interaction between bone cells and metastatic breast cancer cells observed *in vivo* [26] (Chapter 2). However, in that system, the vascular wall was represented by an endothelial monolayer on the side of a central gel region. With the recent attempts in inducing vasculogenesis [27-30], vascular networks have been generated inside the gel region either by co-culture with human lung fibroblasts in separate gel regions or by interstitial flow. Despite the tremendous advances in modeling angiogenesis and vasculogenesis, these models have not previously been used to study metastasis organ-specificity and investigate the role human organ-specific microenvironments.

This chapter presents a novel organ-specific human 3D microfluidic model that enables the study of human metastatic breast cancer cell extravasation within a perfusable human microvascularized bone-mimicking (BMi) microenvironment. The resulting model represents a functional human quad-culture in which breast cancer cells flow into, adhere to and metastasize through human microvascular networks. These networks are supported by primary human bone marrow-derived mesenchymal stem cells (hBM-MSCs) that have undergone phenotypical transition

toward the smooth muscle cell lineage, embedded in a BMi microenvironment with homogeneously distributed osteo-differentiated (OD) primary hBM-MSCs.

3.2 Materials and methods

3.2.1 Microfluidic system

The microfluidic system contains a 1.3 mm wide central hydrogel region flanked by two lateral media channels, as previously used for other studies [27]. The microfabrication process of the device was documented in detail for other configurations [26]. Briefly, the microfluidic device was fabricated with poly-dimethyl-siloxane (PDMS, Silgard 184, Dow-Chemical) using soft lithography techniques from patterned SU-8 silicon wafers. Inlet and outlet ports were created with biopsy punches and a cover glass was bonded to the PDMS after 60 s oxygen plasma treatment to generate 200 μm deep microchannels. A thrombin solution (4 U/mL) was used to resuspend cells and 10 μL aliquots were mixed with 10 μL fibrinogen solution (5 mg/mL) to create a fibrin gel. After gelation, media channels were filled with cell culture medium and microfluidic devices were cultured for 4 days. The two channels system enabled easy access to the hydrogel region for cancer cell extravasation studies under static or dynamic conditions.

3.2.2 Cell culture and cell selection

Bone marrow aspirates were collected from patients undergoing hip arthroplasty and selected by plastic adherence through an optimized protocol [31]. hBM-MSCs of passage 4 were cultured in growth medium prepared with alpha-minimum essential medium (αMEM; Invitrogen) with non-essential amino acids, sodium pyruvate and L-glutamine, 10% fetal bovine serum (FBS; Invitrogen), biological buffer and antibiotics. hBM-MSCs were differentiated toward the osteo-lineage by

culturing in osteo-differentiating medium containing L-ascorbic acid, β-glycerophosphate, cholecalciferol and dexamethasone for at least 2 weeks [26]. Green fluorescent protein (GFP)-transfected human umbilical vein endothelial cells (HUVECs) were commercially obtained (Angio-Proteomie) and cultured in endothelial growth medium with full supplements (EGM-2MV bullet kit; Lonza). Prior to seeding, collagenase type I (Gibco) solution (15 mg/mL) was applied for 20 min on an orbital shaker to dissolve the osteo-matrix; next, cells were trypsinized for 10 min. HUVECs at passage 6 were suspended at 2×10^7 cells/mL in EGM-2MV + thrombin (4 U/mL) and combined with OD and non-differentiated hBM-MSC suspension (10:1 ratio, 4×10^5 cells/mL) in hBM-MSC growth medium + thrombin (4 U/mL). The final suspension was mixed with fibrinogen solution (5 mg/mL) at 1:1 ratio for a few seconds and inserted into the gel channel to complete the seeding. Polymerization occurred in ~15 min within humidity boxes at room temperature. Both lateral channels of the microfluidic devices were then filled with EGM-2MV supplemented with 50 ng/mL vascular endothelial growth factor (VEGF) (Peprotech). After day 2, the culture medium was replaced with EGM-2MV supplemented with 50 ng/mL VEGF and 100 ng/mL angiopoietin-1 (Ang-1) (Peprotech). The katushka-expressing bone seeking clone (BOKL) of the MDA-MB-231 metastatic breast cancer cells enabled live cell imaging via confocal microscopy. The generation of microvascular networks required 3 days of culture in EGM-2MV supplemented with VEGF+Ang-1.

Cancer cell lines were cultured in Dulbecco's Modified Eagle Medium (DMEM; Sigma) with 10% FBS (Invitrogen) and antibiotics. Cancer cells were seeded at day 4 introducing 100 μl of 400,000 cells/mL cell suspension in a single channel. EGM-2MV+VEGF+Ang-1 medium was then added to both channels. As a control, microvascular networks composed of HUVEC alone were generated and the extravasation ability of cancer cells was quantified as described below. A distinct microenvironment was created by culturing endothelial cells, non-differentiated hBM-MSCs and the myoblast cell line C2C12 (ATCC) in the central gel region.

C2C12 myoblasts were seeded at half of the cell density applied for OD hBM-MSCs because of their higher proliferation rate, which could lead to overpopulation, gel retraction and microvasculature disruption [32, 33].

Finally, mammary epithelial cell line (MCF-10A) extravasation was tested within a BMi microenvironment and compared to metastatic BOKL. The medium was replaced every 24 h, and all cultures were kept in a humidified incubator at 37°C and 5% CO_2. For supplementary experiments, the macrophage cell line RAW264.7 (ATCC) was also used. Macrophages were homogeneously dispersed within the fibrin gel at a final cell density of 25,000 cells/mL while keeping fixed the cell density of the other populations. Myoblast and macrophage cell lines were cultured in standard DMEM (Sigma) with 10% FBS (Invitrogen) and antibiotics.

3.2.3 Immunofluorescent staining and image acquisition

All devices were washed with phosphate buffered saline (PBS; Invitrogen), fixed with 4% paraformaldehyde (PFA) for 15 min and permeabilized with 0.1% Triton-X 100 solution for 5 min at room temperature. Samples were treated with 5% bovine serum albumin (BSA) + 3% goat serum solution for at least 3 h at 4°C before incubation with primary antibody. Mouse polyclonal alpha smooth muscle actin (α-SMA) antibody (abcam, dilution 1:100), rabbit polyclonal vascular endothelial (VE)-cadherin antibody (abcam, dilution 1:100), mouse polyclonal zonula occludens (ZO)-1 antibody (Invitrogen, dilution 1:100), rabbit polyclonal osteocalcin antibody (BTI, dilution 1:50) and mouse monoclonal bone alkaline phosphatase (abcam, dilution 1:40) were used for staining. Red fluorescently-labeled secondary antibodies (Invitrogen) were used at 1:200 dilution (Invitrogen). Cell nuclei were stained with 4'6-Diamidino-2-Phenylindole (DAPI;5 mg/mL; Invitrogen) at 1:500 dilution, and F-actin filaments were stained with AlexaFluor633 phalloidin (Invitrogen) at 1:100 dilution. All images were captured

using a confocal microscope (Olympus IX81) and processed with Imaris software (Bitplane Scientific Software).

3.2.4 Addition of adenosine and antagonist for adenosine receptor

Additional experiments were performed to test the role of the muscle-secreted molecule adenosine as anti-metastatic agent. Adenosine (R&D Systems) was diluted at a final concentration of 10 µM and added to BMi microfluidic devices for 24 h before cancer cell addition. Cancer cells were pre-incubated with adenosine 4 h before the seeding. Extravasation events were monitored in presence of adenosine. Furthermore, in order to confirm presence and effect of adenosine within C2C12 myoblast conditioned matrices, the highly specific A_3 adenosine receptor (A_3AR) antagonist (PSB-10, R&D Systems) at 10 µM was introduced to the microfluidic devices for 24 h before cancer cell addition, and cancer cells were pre-incubated with A_3AR for 4 h before injection. Extravasation events were monitored in presence of A_3AR antagonist.

Live/Dead assays were performed to analyze the effect of adenosine by diluting 1 µL fluorescein diacetate (FDA, green; Sigma-Aldrich) and 3.5 µL propidium iodide (PI, red; Sigma-Aldrich) in 1 mL PBS. Samples were incubated for 5 min, washed with PBS and observed through confocal microscopy.

3.2.5 Flow experiments

Flow was produced in the microvascular network by withdrawing medium from one channel outlet at a rate of 1, 3 or 5 µl/min using a syringe pump. Medium was supplemented from a reservoir (P1000 pipette tip) connected to the opposite channel, plugging the other 2 outlets to enforce flow through the microvascular network. While the syringe pump was withdrawing the medium, a rough estimate of the flow velocity in the microvascular network was obtained by adding 3 µm

microspheres to the perfusion medium and measuring the distances they travelled between frames. The measured velocity values (distance travelled between frames by microspheres times the frame rate) for randomly selected microspheres were averaged to estimate the mean velocity of the medium flowing across the microvascular network. Then, the mean wall shear stress applied to the microvascular network was calculated assuming Hagen-Poiseuille flow in cylindrical pipe:

$$\tau = \frac{8\mu v}{D}$$

where τ is the wall shear stress, μ the viscosity of medium, D the average diameter of the vessel, and v the average velocity of the medium flowing through the microvascular network.

The flow was maintained for 14 h in order to precondition the microvascular network before the addition of the cancer cell suspension, re-applied 30 min after cancer cell seeding and then imaged for 7.5 h during extravasation.

3.2.6 Metrics for extravasation

Microfluidic devices were live imaged through confocal microscopy after the addition of cancer cell suspension into the system. Each cell localized within the microvascular network and identified by cancer cell katushka signal was tracked to check whether the cell had indeed extravasated by the end of the live imaging process (8 h). The percentage of cells that had extravasated was determined for each region of interest (ROI) and the percentages were averaged to get a final value for each condition. The dimensions of the ROI were 1405 μm x 1124 μm x 200 μm (height).

3.2.7 Permeability measurements

Permeability of the microvascular network was measured as described previously [27]. Briefly, the medium was first aspirated from the system. Then, 40 µL fluorescent dextran (70 kDa, red, Invitrogen) was dissolved in endothelial growth medium to a final concentration of 25 µg/mL and then added to 2 reservoirs of the opposite media channels (Supplementary Fig. 4.3a). Permeability was measured by quantifying the average intensity at the initial and final time points analyzing a ROI including both the microvessel and the surrounding extracellular matrix (ECM). Permeability values were calculated with the following formula with the assumption that the vessels were roughly circular in cross section [27]:

$$P_D = \frac{1}{I_i - I_b} \left(\frac{I_f - I_i}{\Delta t} \right) \times \frac{d}{4}$$

where I_b, I_i, and I_f are the background, initial and final average intensities, Δt is the time interval between images and d is the diameter of the imaged microvessel.

3.2.8 Adenosine treatment: effect on breast cancer cell viability

Live/Dead assay and 3-(4,5-dimethylthiazol-2-yl)-2,5-diphenyltetrazolium bromide (MTT) assay were performed to analyze breast cancer cell viability after adenosine treatment (10 µM). According to the experimental protocol followed during microfluidic experiments, breast cancer cells were incubated either with BOKL medium+10 µM adenosine for 4 h (simulating BOKL pre-treatment before injection) or EGM-2MV+10 µM adenosine for 12 h (simulating the whole BOKL incubation period considering pre-treatment and microfluidic assay).

3.2.9 A3 adenosine receptor (A₃AR) expression

The A_3AR has been recently identified as a promising target for anti-metastatic treatments and several agonists have been developed to inhibit cancer cell growth and proliferation [34, 35]. Rabbit monoclonal A_3AR antibody (Santa Cruz, 1:50) was used for staining. Immunofluorescent images were obtained for different breast cancer cell lines including 1833, BOKL and MDA-MB-231 (Fig. 4.3a and Supplementary Fig. 4.7c and d). Additional tests were performed with HUVECs (Supplementary Fig. 4.7a) and hBM-MSC (Supplementary Fig. 4.7b).

3.2.10 Adenosine expression within the C2C12 conditioned microenvironment

Immunofluorescence and mass spectrometry analyses were performed to investigate the ability of the C2C12 conditioned microenvironment to secrete adenosine and influence cancer cell extravasation. Endothelial cells, hBM-MSCs and C2C12 were seeded in a flask with the same cell ratios used in the microfluidic model and conditioned with the same media during co-culture. Cell supernatants were collected and filtered through standard 0.22 µm filters, diluted 1:100 in H_2O+CH_3CN (45:55 ratio) and injected in the mass spectrometer (Esquire 3000 plus ESI Ion trap LC/MS^n System, Bruker Daltonik, Bremen, Germany) at a flow-rate of 4 L/min, operated in the positive-ion MS mode. A potential of 4.5 kV was applied to the capillary. A drying gas flow rate was set to 5 L/min while the nebulizer pressure was equal to 10 psi. Nitrogen was used as both nebulizing gas and drying gas. The dry temperature was set to 250 °C. Control infusion was performed with adenosine standards dissolved in H_2O+CH_3CN (45:55 ratio) to reach a final concentration of 0.1 µM and 1 µM.

In order to provide additional data confirming adenosine secretion by the tri-culture system, we carried out immunofluorescent staining for the CD73 marker, which catalyzes the conversion of adenosine monophosphate (AMP) to adenosine. The expression of this marker was assessed in a HUVECs+hBM-MSCs+C2C12 tri-culture conditioned with the same media used for microfluidic experiments.

3.2.11 Cancer cell migration distance

Cancer cell migratory behavior after extravasation was monitored for specific conditions. Imaris software (Bitplane Scientific Software) was used to track the time-dependent migration of katushka-expressing breast cancer cells and measure the distance between extravasation point location and final cell position. Cancer cell extravasation distance was quantified averaging data obtained from each specific condition as a single group.

3.2.12 Statistics

All extravasation percentages are reported as averages ± standard error of the mean (SEM). Measurements are obtained from a minimum of 10 ROIs from 3 or more independent devices while all permeability values are averages of 5 (min) to 7 (max) measurements from 2 (min) to 4 (max) independent devices. Measurements were compared using unpaired Student's t-test. Statistical tests were performed with SigmaPlot12. All tests with $p<0.05$ (*) and $p<0.005$ (***) were assumed statistically significant.

3.3 Results

3.3.1 Generation of functional 3D microvascular networks within a BMi microenvironment

This chapter reports an *in vitro* platform that enables the study of organ-specific human breast cancer cell extravasation into a human BMi microenvironment through a functional, perfusable 3D microvascular network. Primary hBM-MSCs were obtained from patients undergoing hip arthroplasty under written informed consent. A tri-culture of primary hBM-MSCs, OD primary hBM-MSCs (14 days differentiation in osteogenic medium prior to seeding, according to a previously optimized protocol [26]) and primary GFP HUVECs was embedded in a fibrin gel to generate a microvascular network enclosed in a BMi matrix characterized by actively secreting OD cells, which create naturally-formed molecular gradients affecting both microvasculature and cancer cells. The microfluidic model used in this study consists of a microfluidic device containing a microvascular network employed to conduct organ-specific extravasation experiments (Fig4.1a). Functional microvascular networks, characterized by anastomoses with the lateral media channels, were formed over 4 days (Fig4.1b), at which time, breast cancer cells were introduced and extravasation events were monitored during the next 8 h. Formation of functional microvascular networks within a BMi microenvironment was characterized by the expression of specific bone markers, i.e. osteocalcin and bone alkaline phosphatase (Fig4.1c and d and Supplementary Fig4.4), and vascular markers, i.e. VE-cadherin and (ZO)-1 (Fig4.1e and f), and α-SMA (Fig4.1g). Primary hBM-MSCs cultured with HUVECs showed a phenotypic adaptation toward a mural cell lineage, as demonstrated by positive α-SMA immunofluorescent staining, and wrapped around patent microvessels. Furthermore, the presence of endothelial cell-cell adherens and tight junctions

represents a key factor for the development of effective extravasation models: the immunofluorescent staining demonstrates the existence of mature vessel walls with well-formed cell-cell junctions. The microvascular network, characterized by complex interconnections and continuous hollow lumens (Supplementary Fig 4.3a), was embedded in a BMi microenvironment with primary OD hBM-MSCs secreting bone proteins such as osteocalcin and bone alkaline phosphatase (Fig4.1c and d). It was previously demonstrated OD hBM-MSCs secreted osteopontin as well as osteonectin, and generated calcium deposits within 3D matrices [26].

Endothelial cells displayed morphological features similar to *in vivo* vasculatures, such as an elongated shape aligned with microvessel axes (Supplementary Fig 4.3b), in contrast to the random alignment exhibited by endothelial monolayers or endothelialized microchannels in the absence of flow [36]. Finally, fluorescent microspheres (3 µm and 10 µm diameter) were perfused through the system showing patent microvessels.
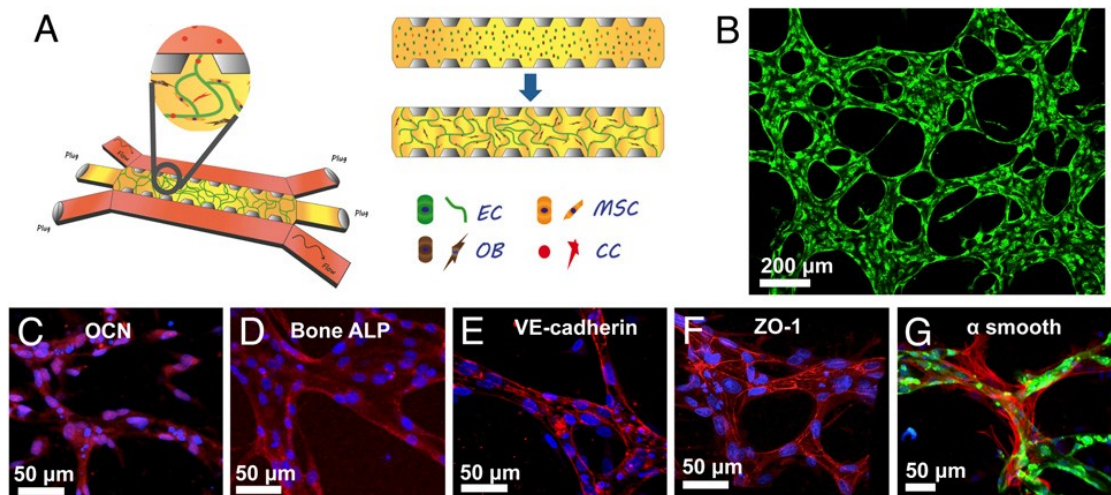

Fig4.1: Characterization of the extravasation model. (a) Two side media channels allow addition of cancer cells, biochemical factors, and flow across the vasculature formed in the gel channel. Endothelial cells (ECs), mesenchymal stem cells (MSCs), and osteoblast-differentiated cells (OBs) are initially seeded in the gel. ECs form vasculature over time, while

MSCs and OBs create a BMi microenvironment. Cancer cells introduced in the vessel extravasate into the organ-mimicking cell-enriched gel. (b) The microvascular network is characterized by highly branched structures, which allow cancer cell rolling/adhesion or physical entrapment. Establishment of BMi microenvironment is shown by staining for osteocalcin (OCN, red, (c) and bone alkaline phosphatase (ALP, red, (d)). Formation of vasculature is confirmed by staining for adherens junctions (VE-cadherin, red, (e)) and tight junctions (ZO-1, red, (f)). Differentiation of hBM-MSCs to mural cell lineage is indicated by immunofluorescent staining of α-smooth muscle actin (α-SMA, red, (g)). HUVECs (green). DAPI (nucleus, blue).

3.3.2 Cancer cell extravasation in a BMi microenvironment

A perfusable microvascular network generated via a vasculogenesis-like process from endothelial cells suspended in gel solution within the microfluidic device was used to model the extravasation process of breast cancer cells toward a BMi microenvironment (Fig4.1b). BOKL metastatic breast cancer cells flowed into the microvascular network, rolled on and adhered to the endothelium or became physically trapped, and subsequently spread, extended filopodia through intercellular junctions into the local microenvironment, and finally invaded the ECM (Fig4.2a and b). Cancer cells transmigrated through the endothelium into the matrices engineered to mimic three different microenvironments: bone, muscle, and acellular collagen matrix (Fig4.2e). Extravasation rates of the cancer cells in the BMi microenvironment were significantly higher compared to the other conditions such as the microenvironment conditioned with the myoblast cell line C2C12, mimicking a muscle microenvironment, or control matrix without any cells. BOKL average extravasation rate was $56.5 \pm 4.8\%$ in the presence of OD hBM-MSCs, compared to $8.2 \pm 2.3\%$ with C2C12 myoblasts and $14.7 \pm 3.6\%$ without stromal cell addition (control matrix) (Fig4.2c). The average extravasation rate within the BMi microenvironment was then 3.8-fold higher than without stromal cell addition, which is higher compared to previous work (Chapter 2)

analyzing the extravasation of cancer cells through a simple and less physiologically relevant endothelial monolayer (2.06). It is noteworthy that the presence of actively secreting mural cell-like hBM-MSCs that enabled the generation of a more *in vivo*-like microenvironment could have also played a role in the increased extravasation ratio. No significant differences were quantified comparing cancer cell migratory behavior in BMi microenvironments and control matrices.

Vessel permeability was quantified by analyzing 70 kDa dextran diffusion through the microvascular wall and compared among experimental conditions (Supplementary Fig4.3a). Permeability values were significantly higher in BMi microfluidic devices $(4.12 \pm 0.75) \cdot 10^{-6}$ cm/s compared to control matrices $(0.89 \pm 0.31) \cdot 10^{-6}$ cm/s (Fig4.2d). Finally, the highest permeability values were found in the presence of C2C12 myoblasts $(8.37 \pm 1.53) \cdot 10^{-6}$) cm/s, resulting in a 2.0-fold increase compared to the BMi systems (Fig4.2d). It is surprising that the most leaky environment C2C12 gave rise to the lowest extravasation rate. This demonstrates that permeability is only one of multiple factors affecting extravasation.
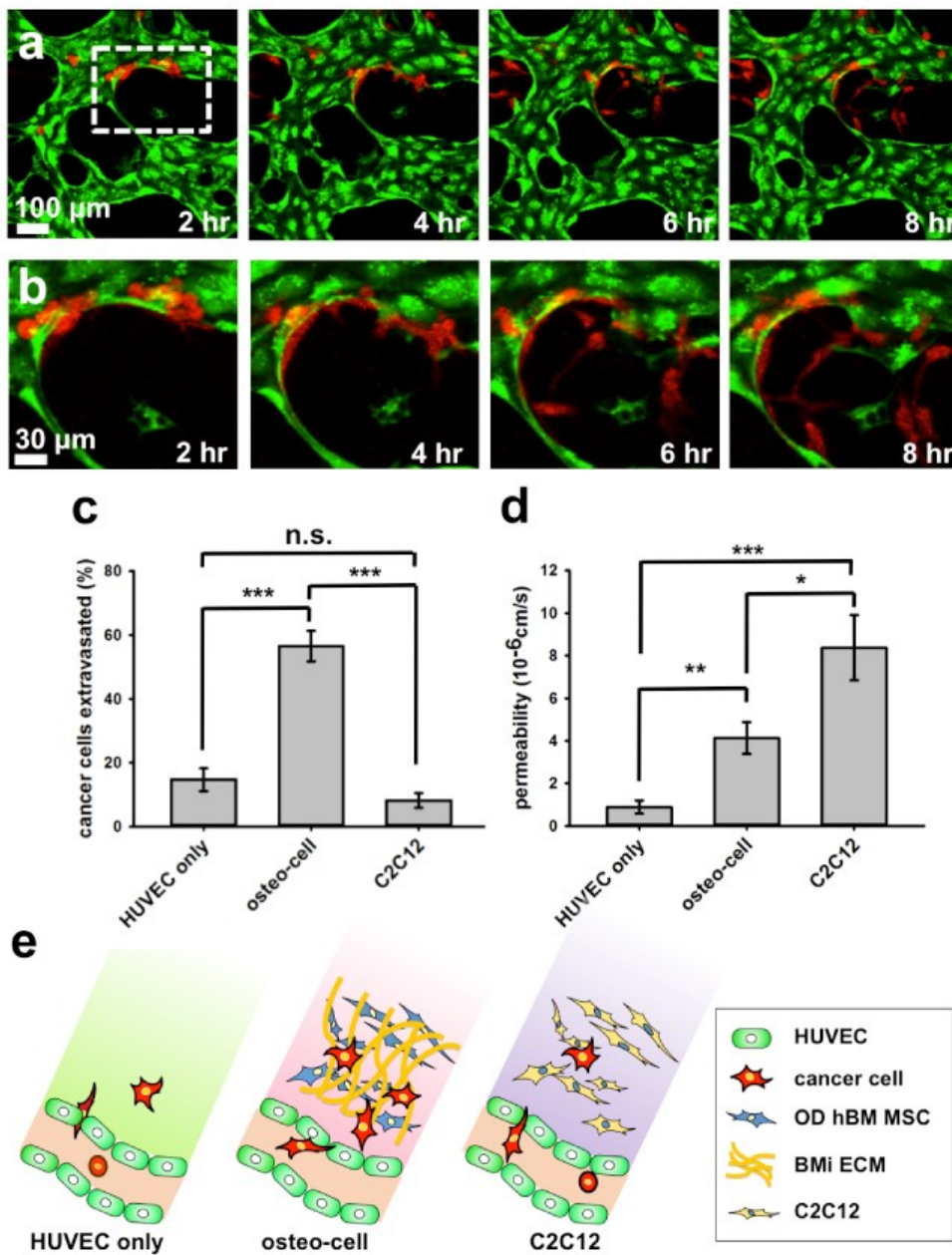
Fig4.2: Cancer cell extravasation. (a) Extravasation of cancer cells (red) introduced into the vascular network (HUVECs, green) is monitored in real time. (b) Magnified images of white dotted box in (a) show extravasation of cancer cells. (c) Percent of cancer cells extravasated vary significantly among the vascular networks embedded in different microenvironments, i.e. acellular and bone or muscle-mimicking microenvironment, respectively. (d) Permeability

values increased when cells are added to mimic the two organ-specific microenvironments compared to HUVEC only condition. (e) Schematic of HUVEC only, osteo-cell and C2C12 cell added systems. HUVECs are shown as green cells that form vessel, osteo-cells are blue colored cells and secrete bone matrix as shown in yellow, and C2C12 cells are depicted as yellow cells. Cancer cells are colored in red and seen both in the vessels as well as extravasated out in the surrounding matrix.

The capability of the assay to distinguish between the extravasation potentials of different cell types and cellular environments was explored. First, an inflammatory model was set up with the addition of a macrophage cell line. RAW264.7 macrophages were homogeneously dispersed within the fibrin gel. The average extravasation rate within macrophage conditioned BMi microenvironment was significantly higher (32.4 ± 4.3%) compared to matrices without addition of stromal cells (14.7 ± 3.6%) but lower with respect to standard BMi microenvironment (56.5 ± 4.8%) (Supplementary Fig4.1a). The promising nature of these data was confirmed by microvessel permeability values, which were higher $((6.77± 1.56)·10^{-6}$ cm/s) in presence of macrophages compared to BMi matrices $((4.12 ± 0.75)·10^{-6}$ cm/s) (Supplementary Fig4.1b). Substantial clinical and experimental evidences indicate a key role of macrophages in multiple steps of the metastatic cascade. Based on previous experiments performed in the Kamm group on cancer cell intravasation [20], it can be suggested the increased microvasculature permeability could be due to the macrophage secretion of the inflammatory cytokine tumor necrosis factor-alpha (TNF-α). However, it is known that TNF-α inhibits osteoblast differentiation and bone-specific protein expression, particularly osteocalcin, while inducing osteoclastogenesis [37-39]. Then, it is possible to speculate the macrophage-secreted TNF-α could have conditioned the BMi microenvironment, limiting the pro-metastatic effect induced by OD cell secretome. However, further analyses are required to in-depth investigate specific role and impact of macrophages and particularly macrophage-secreted TNF-α on breast cancer bone metastases. Control experiments were performed introducing

non-metastatic mammary epithelial cells (MCF-10A) within the BMi microenvironment. MCF-10A extravasation rate was significantly lower ($5.2 \pm 2.5\%$) compared to BOKL ($56.5 \pm 4.8\%$) (Supplementary Fig4.2), thus demonstrating the specificity of the interaction between metastatic cancer cells and a BMi microenvironment.

3.3.3 The role of adenosine in cancer cell extravasation

As striking differences were found between cancer cell extravasation within BMi and muscle-mimicking microenvironments, it was investigated which factors secreted by muscle might be responsible. It is reported that the skeletal muscle microenvironment reduces cancer cell tumorigenity and elicits paracrine-mediated cytotoxic and cytostatic effects on metastatic cancer cells [40]. In particular, several studies identified the A_3AR, which is expressed by multiple cancer cell types [41], as key in the anti-metastatic and protective effect of skeletal muscle cells [42]. Before investigating the role of A_3AR in extravasation, it was first demonstrated through immunofluorescence that BOKL introduced in the system expressed the A_3AR (Fig. 4.3a). Then, the A_3AR antagonist PSB-10 was introduced within C2C12 containing microfluidic devices (Fig4.3h) and pre-incubated cancer cells with A_3AR prior to seeding [43, 44]. With the addition of the antagonist, cancer cell extravasation rate significantly increased ($32.4 \pm 7.7\%$) compared to non-treated C2C12 matrices ($8.2 \pm 2.3\%$) (Fig4.3e), while microvessel permeability was not significantly affected (($7.4 \pm 2.61) \cdot 10^{-6}$cm/s vs.($8.04 \pm 1.72) \cdot 10^{-6}$ cm/s) (Fig4.3g). These data indirectly demonstrate the presence of C2C12-secreted adenosine in the system as well as the protective role of this molecule against cancer metastases.
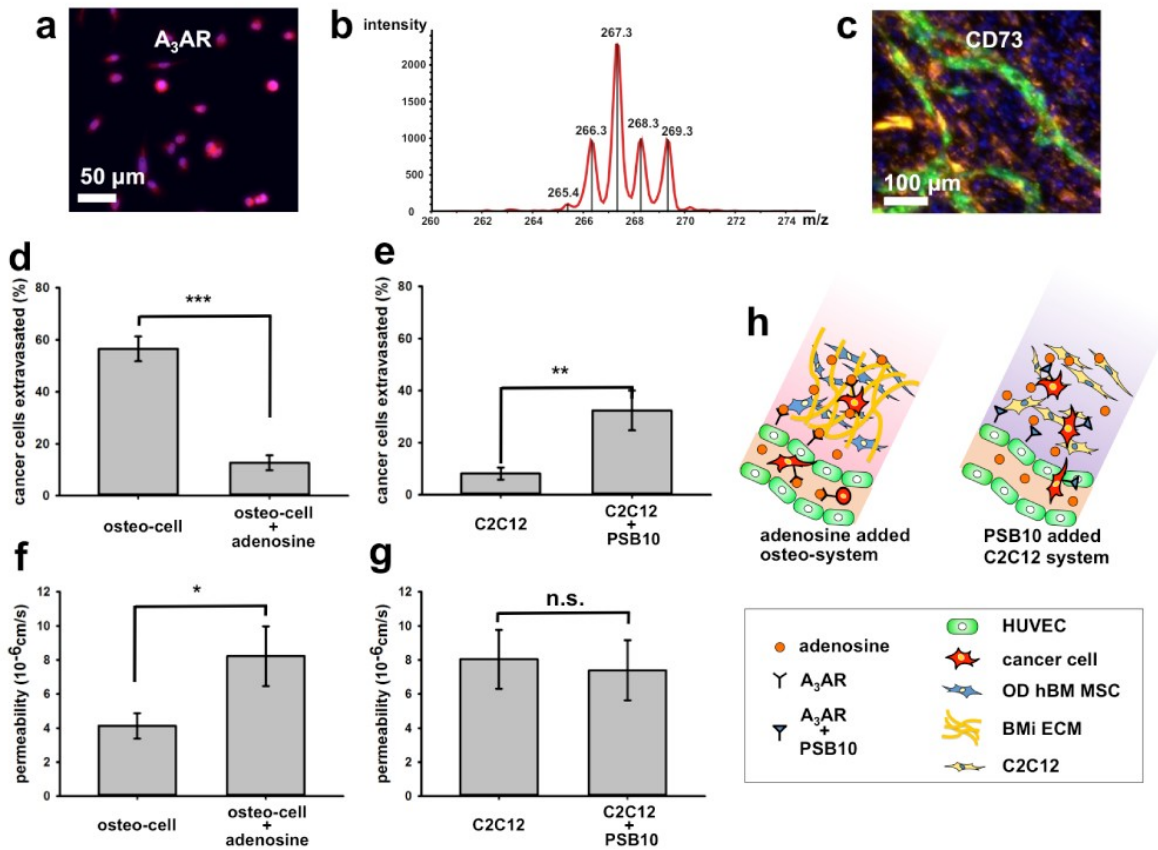
Fig4.3: Percent of cancer cell extravasation and vascular permeability in bone and muscle-mimicking microenvironment with addition of stimulating or blocking molecules. Cancer cells express the A_3 adenosine receptor (a) while C2C12 embedded matrices secrete adenosine as shown by mass spectrometry data (268 m/z peak) (b) and CD73 immunofluorescent staining (c). Percentage of cancer cells that extravasate (d) and permeability of the vasculature (f) in the BMi microenvironment with OD hBM-MSCSs, with and without adenosine. Extravasation rate decreased significantly with addition of adenosine while the permeability increased with adenosine. Percentage of cancer cells that extravasate (e) and permeability of the vasculature (g) in the muscle-mimicking microenvironment with C2C12 cells, with and without PSB10. While blocking of A_3AR with the addition of PSB10 did not alter the permeability of the vasculature, cancer cell extravasation rate increased significantly. (h) Schematic of osteo-cell and C2C12 cell added systems with adenosine, A_3 adenosine receptor and its antagonist PSB10.

Mass spectrometry analyses performed on cell culture supernatants provided further evidence of adenosine secretion by the C2C12 conditioned microenvironment (Fig4.3b and Supplementary Fig4.8) while immunofluorescence staining demonstrated the expression of the adenosine converter CD73 (Fig4.3c), which catalyzes the conversion of adenosine monophosphate (AMP) to adenosine [45].

Supported by collected results with untreated or conditioned (A_3AR antagonist) C2C12 microenvironments, the role of adenosine on cancer cell extravasation within a BMi microenvironment was investigated using the present model as drug screening platform (Fig4.3h). The presence of adenosine significantly reduced cancer cell extravasation ($12.7 \pm 2.8\%$) compared to the untreated BMi microenvironment ($56.5 \pm 4.8\%$) (Fig4.3d). Furthermore, a dramatic increase was found in microvasculature permeability (($8.22 \pm 1.76) \cdot 10^{-6}$ cm/s) compared to BMi control ($4.12 \pm 0.75) \cdot 10^{-6}$cm/s) (Fig4.3f). It is interesting to note that treating BMi microenvironments with adenosine led to extravasation rate and permeability values comparable to C2C12 conditioned matrices, suggesting this molecule could be theoretically used to tune a specific microenvironment with anti-metastatic properties. Finally, Live/Dead and MTT assays were performed at different time points on cancer cells treated with adenosine, confirming that the A_3AR antagonist action in reducing extravasation was not due to a cytotoxic effect on BOKL (Supplementary Fig4.5 and 4.6).

3.3.4 Flow experiments: effect of shear stress on microvasculature and cancer cell extravasation

Since extravasation normally occurs during blood flow, the effects on microvascular networks conditioned by physiological levels of shear stress were

subsequently examined. In these experiments, microvascular networks were pre-conditioned with flow overnight before cancer cell seeding and analyzed the effects of flow on extravasation and microvessel permeability. A flow rate of 2 μl/min was set in the channel which resulted in an average velocity in the vasculature of 220 μm/s and a wall shear stress of 0.25 dyne/cm [46].

Cancer cell extravasation within the flow conditioned BMi microenvironment occurred at a rate of 38.6 ± 4.8% (Fig4.4a), significantly lower than under static conditions (56.5 ± 4.8%). Microvessel permeability decreased 2.4-fold, compared to static conditions ((1.72 ± 0.53)·10^{-6} cm/s compared to (4.12 ± 0.75)·10^{-6} cm/s) (Fig4.4b). Endothelial cells exposed to a laminar flow were characterized by an elongated morphology and a clear actin filament alignment in the flow direction with compelling stress fibers at cell-cell junctions (Fig4.4e (flow) and d (static control), Supplementary Fig4.3b), thus displaying morphological features resembling *in vivo* microvessels [47]. Finally, it is worth noting that flow conditioned breast cancer cells migrated further into the surrounding matrix (33.7 ± 4.3 μm) compared to static experiments (23.3 ± 2.7 μm) (Fig4.4c).

Several works have recently shown that when endothelial cells are subjected to laminar flow shear stress, trans-endothelial electrical resistance increases, microvasculature permeability decreases, actin filaments become more aligned, and cytoskeletal tension and intercellular forces between endothelial cells increase compared to static conditions. Moreover, a significant over-expression has been highlighted for β-catenin (adherens junctions) and ZO-1 (tight junctions), with respect to disturbed flow or static conditions [48, 49].
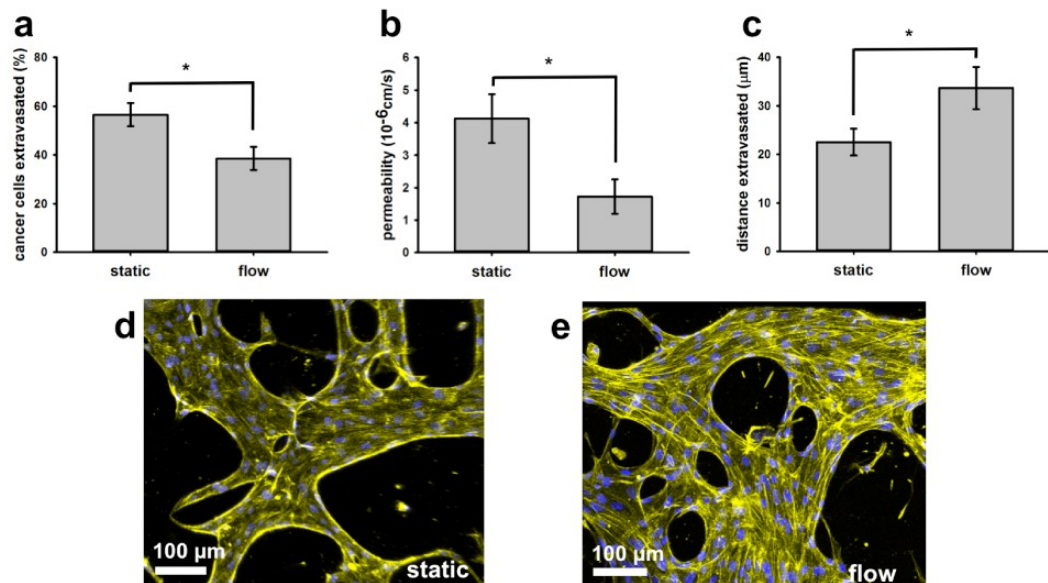
Fig4.4: Cancer cell extravasation and endothelial cell (EC) permeability change in the presence of flow through the vasculature. Extravasation of cancer cells (a) and permeability of the vasculature (b) decreased significantly with the addition of flow. (c) Extravasated cancer cells migrated further in the flow condition versus the static condition. Actin (yellow) within ECs in static condition (d) and under conditions when flow was added in the vasculature (e). DAPI (nucleus, blue).

Overall, these studies suggest that exposure of endothelial cells to controlled, laminar flows results in cell-cell junction tightening with a corresponding decrease in vasculature permeability. These findings agree with collected results showing decreased microvessel permeability due to flow shear stress in the same BMi microenvironment. It is likely that the reduced extravasation rate within the flow conditioned BMi microenvironment could be due to enhanced endothelial cell intercellular forces and cell-cell junction tightening. Furthermore, it could be speculated the presence of an interstitial flow within the BMi matrix during flow conditioned experiments could partially explain the increased migration distance shown by breast cancer cells compared to static controls, as previously demonstrated by several studies highlighting the link between flow induced

mechanical stimulation and cell migration [21]. Reported data demonstrate that generation of a more physiological microenvironment with the addition of endothelial wall shear stress can dramatically affect extravasation potential, which could have critical implications on drug screening tests and *in vitro* model development. It is noteworthy to emphasize that, in addition to endothelial cell pre-conditioning, the employed platform enables real time monitoring of cancer cell extravasation under flow, thus allowing the *in situ* analysis of extravasation in the microenvironment where both endothelial and cancer cells are exposed to physiological stimuli.

3.4 Discussion

A novel organ-specific 3D microfluidic model was created to study human breast cancer cell extravasation into an actively secreting BMi microenvironment generated with OD hBM-MSCs through perfusable human microvascular networks composed of endothelial and mural-like cells. The relevance of the present work lies in the application of a complex model to investigate and subsequently tune a specific step of the metastatic cascade within different organ-specific microenvironments with implications for the screening of new therapeutics. The efficacy and potentiality of the present microfluidic model go beyond the established role of adenosine as a promising anti-cancer molecule to specifically demonstrate its involvement in the extravasation process.

The microfluidic model presented is based on the co-culture of endothelial and hBM-MSC derived mural cells to create physiologically relevant highly branched structures, characterized by reduced microvessel diameter and increased branch number compared to microvascular networks made of endothelial cell alone [27]. Particularly, this model overcomes some of the limitations of previously developed elegant models which showed impaired perfusability when supportive stromal cells

were added to the system [28]. It is known that a wide panel of molecules is involved in vessel wall and network maturation including vascular endothelial growth factor (VEGF), platelet derived growth factor (PDGF-B) and members of the transforming growth factor (TGF-β) family. Moreover, it is reported that angiopoietin-1 (Ang-1) represents a key molecule in vessel stabilization and could play a role in the recruitment of mesenchymal cells [50]. As previously demonstrated (Chapter 3), the addition of Ang-1 within HUVEC+hBM-MSC co-cultures significantly induces mesenchymal cell expression of common markers displayed by mural cells, e.g. α-SMA, SM22α and NG-2 [27], which contribute to network stabilization. Taken together, these findings provide evidence that the combination of endothelial-mesenchymal stem cell co-culture and the external addition of stabilizing molecules promote the generation of functional microvascular networks, which represent a suitable model to study cancer cell extravasation within an actively secreting BMi microenvironment.

Cancer cell extravasation rates were significantly higher in the BMi microenvironment compared to control matrices without stromal cells or muscle-mimicking microenvironments. While the higher permeability in the BMi microenvironment is likely due to a combination of factors, it may also contribute to the increase in extravasation. Indeed, matrix-specific cell-secreted chemokines can both generate molecular gradients affecting cancer cell transendothelial migration [51] and alter endothelial permeability [52]. Of particular note is the increase in microvasculature permeability when adenosine is added. It has been reported that adenosine can interact with endothelial cells expressing A_2B adenosine receptors, promoting the release of pro-angiogenic factors including VEGF and interleukin-8, which could lead to the increased permeability [53]. While A_2B adenosine receptors are preferentially expressed by human microvascular endothelial cells compared to HUVECs, the external addition of adenosine in the BMi microenvironment played a role in the increased microvessel permeability compared to untreated matrices, in spite of reducing cancer cell

extravasation. These data highlight the fact that permeability represents only one of the key factors driving cancer cell extravasation. C2C12-secreted adenosine could also partially explain permeability differences detected comparing no stromal cell addition, BMi microenvironment and C2C12 conditioned matrices. Finally, the presence of high values of microvessel permeability with the addition of the A_3AR antagonist within C2C12 embedded microenvironments, which are comparable to data obtained with untreated C2C12 matrices, suggests the A_3AR antagonist did not adversely affect the mechanical properties of the endothelium, confirming previous studies demonstrating low expression levels of A_3AR by endothelial cells [53]. However, the addition of the antagonist did promote an increase in the extravasation rate compared to untreated microenvironments, suggesting a specific interaction with cancer cells. Indeed, it should also be considered the A_3AR antagonist could have affected endothelial cell secretory activity or the expression of surface markers contributing to cancer cell adhesion/extravasation, thus leading to increased extravasation rates.

In conclusion, an organ-specific vascularized 3D microfluidic model was created to study human breast cancer cell extravasation into an actively secreting human BMi microenvironment through perfusable human microvascular networks composed of endothelial and mural-like cells. It was found clear evidence of the seed (breast cancer cells) and soil (BMi microenvironment) coupling and provided quantitative results regarding the anti-metastatic and protective role played by skeletal muscle cells. Particularly, it was demonstrated the effectiveness of the model as a drug screening assay, being able to investigate both the effects of A_3AR antagonist on cancer cell extravasation in a C2C12 myoblast conditioned matrix and the anti-metastatic role of adenosine in a human BMi microenvironment, thus overcoming limitations of traditional *in vitro* models. These assays pave the way to a new generation of 3D *in vitro* models capable of bridging highly specific human *in vitro* cultures with physiological *in vivo* conditions, to foster a more effective screening of tailored anti-cancer therapies in the context of personalized medicine and

promote the study of key molecular pathways involved in cancer biology in controlled, organ-specific, physiological-like conditions.

References

[1] Valastyan S, Weinberg RA. Tumor metastasis: molecular insights and evolving paradigms. Cell. 2011;147:275-92.

[2] Chambers AF, Groom AC, MacDonald IC. Dissemination and growth of cancer cells in metastatic sites. Nat Rev Cancer. 2002;2:563-72.

[3] Fidler IJ. The pathogenesis of cancer metastasis: the 'seed and soil' hypothesis revisited. Nat Rev Cancer. 2003;3:453-8.

[4] Hanahan D, Weinberg RA. Hallmarks of cancer: the next generation. Cell. 2011;144:646-74.

[5] Bussard KM, Gay CV, Mastro AM. The bone microenvironment in metastasis; what is special about bone? Cancer Metastasis Rev. 2008;27:41-55.

[6] Coleman RE. Bone cancer in 2011: Prevention and treatment of bone metastases. Nat Rev Clin Oncol. 2012;9:76-8.

[7] Kim MY, Oskarsson T, Acharyya S, Nguyen DX, Zhang XH, Norton L, et al. Tumor self-seeding by circulating cancer cells. Cell. 2009;139:1315-26.

[8] Nguyen DX, Bos PD, Massague J. Metastasis: from dissemination to organ-specific colonization. Nat Rev Cancer. 2009;9:274-84.

[9] Reymond N, Borda d'Agua B, Ridley AJ. Crossing the endothelial barrier during metastasis. Nature Reviews Cancer. 2013;13:13.

[10] Al-Mehdi AB, Tozawa K, Fisher AB, Shientag L, Lee A, Muschel RJ. Intravascular origin of metastasis from the proliferation of endothelium-attached tumor cells: a new model for metastasis. Nat Med. 2000;6:100-2.

[11] Stoletov K, Kato H, Zardouzian E, Kelber J, Yang J, Shattil S, et al. Visualizing extravasation dynamics of metastatic tumor cells. J Cell Sci. 2010;123:2332-41.

[12] Schumacher D, Strilic B, Sivaraj KK, Wettschureck N, Offermanns S. Platelet-derived nucleotides promote tumor-cell transendothelial migration and metastasis via P2Y2 receptor. Cancer Cell. 2013;24:130-7.

[13] Kuperwasser C, Dessain S, Bierbaum BE, Garnet D, Sperandio K, Gauvin GP, et al. A mouse model of human breast cancer metastasis to human bone. Cancer Res. 2005;65:6130-8.

[14] Lauffenburger DA, Horwitz AF. Cell migration: a physically integrated molecular process. Cell. 1996;84:359-69.

[15] Simpson KJ, Selfors LM, Bui J, Reynolds A, Leake D, Khvorova A, et al. Identification of genes that regulate epithelial cell migration using an siRNA screening approach. Nat Cell Biol. 2008;10:1027-38.

[16] Bersini S, Jeon JS, Moretti M, Kamm RD. In vitro models of the metastatic cascade: from local invasion to extravasation. Drug Discov Today. 2013.

[17] Shin Y, Han S, Jeon JS, Yamamoto K, Zervantonakis IK, Sudo R, et al. Microfluidic assay for simultaneous culture of multiple cell types on surfaces or within hydrogels. Nat Protoc. 2012;7:1247-59.

[18] Vickerman V, Kamm RD. Mechanism of a flow-gated angiogenesis switch: early signaling events at cell-matrix and cell-cell junctions. Integr Biol (Camb). 2012;4:863-74.

[19] Sung KE, Yang N, Pehlke C, Keely PJ, Eliceiri KW, Friedl A, et al. Transition to invasion in breast cancer: a microfluidic in vitro model enables examination of spatial and temporal effects. Integr Biol (Camb). 2011;3:439-50.

[20] Zervantonakis IK, Hughes-Alford SK, Charest JL, Condeelis JS, Gertler FB, Kamm RD. Three-dimensional microfluidic model for tumor cell intravasation and endothelial barrier function. Proc Natl Acad Sci U S A. 2012;109:13515-20.

[21] Polacheck WJ, Charest JL, Kamm RD. Interstitial flow influences direction of tumor cell migration through competing mechanisms. Proc Natl Acad Sci U S A. 2011;108:11115-20.

[22] Pathak A, Kumar S. Independent regulation of tumor cell migration by matrix stiffness and confinement. Proc Natl Acad Sci U S A. 2012;109:10334-9.

[23] Song JW, Cavnar SP, Walker AC, Luker KE, Gupta M, Tung YC, et al. Microfluidic endothelium for studying the intravascular adhesion of metastatic breast cancer cells. PLoS One. 2009;4:e5756.

[24] Jeon JS, Zervantonakis IK, Chung S, Kamm RD, Charest JL. In vitro model of tumor cell extravasation. PLoS One. 2013;8:e56910.

[25] Zhang Q, Liu T, Qin J. A microfluidic-based device for study of transendothelial invasion of tumor aggregates in realtime. Lab Chip. 2012;12:2837-42.

[26] Bersini S, Jeon JS, Dubini G, Arrigoni C, Chung S, Charest JL, et al. A microfluidic 3D in vitro model for specificity of breast cancer metastasis to bone. Biomaterials. 2014;35:2454-61.

[27] Jeon JS, Bersini S, Whisler JA, Chen MB, Dubini G, Charest JL, et al. Generation of 3D functional microvascular networks with human mesenchymal stem cells in microfluidic systems. Integr Biol (Camb). 2014.

[28] Kim S, Lee H, Chung M, Jeon NL. Engineering of functional, perfusable 3D microvascular networks on a chip. Lab Chip. 2013;13:1489-500.

[29] Moya ML, Hsu YH, Lee AP, Hughes CC, George SC. In Vitro Perfused Human Capillary Networks. Tissue Eng Part C Methods. 2013.

[30] Whisler JA, Chen MB, Kamm RD. Control of perfusable microvascular network morphology using a multiculture microfluidic system. Tissue Eng Part C Methods. 2014;20:543-52.

[31] Lopa S, Mercuri D, Colombini A, De Conti G, Segatti F, Zagra L, et al. Orthopedic bioactive implants: Hydrogel enrichment of macroporous titanium for the delivery of mesenchymal stem cells and strontium. J Biomed Mater Res A. 2013.

[32] Evans CE, Ng K, Allen J, Gallimore P. Modulation of cell phenotype in human osteoblast-like cells by the simian virus 40. J Orthop Res. 1995;13:317-24.

[33] Pisani DF, Cabane C, Derijard B, Dechesne CA. The topoisomerase 1-interacting protein BTBD1 is essential for muscle cell differentiation. Cell Death Differ. 2004;11:1157-65.

[34] Bar-Yehuda S, Barer F, Volfsson L, Fishman P. Resistance of muscle to tumor metastases: a role for a3 adenosine receptor agonists. Neoplasia. 2001;3:125-31.

[35] Lu J, Pierron A, Ravid K. An adenosine analogue, IB-MECA, down-regulates estrogen receptor alpha and suppresses human breast cancer cell proliferation. Cancer research. 2003;63:6413-23.

[36] Chrobak KM, Potter DR, Tien J. Formation of perfused, functional microvascular tubes in vitro. Microvasc Res. 2006;71:185-96.

[37] Abbas S, Zhang YH, Clohisy JC, Abu-Amer Y. Tumor necrosis factor-alpha inhibits pre-osteoblast differentiation through its type-1 receptor. Cytokine. 2003;22:33-41.

[38] Gilbert L, He X, Farmer P, Boden S, Kozlowski M, Rubin J, et al. Inhibition of osteoblast differentiation by tumor necrosis factor-alpha. Endocrinology. 2000;141:3956-64.

[39] Nanes MS. Tumor necrosis factor-alpha: molecular and cellular mechanisms in skeletal pathology. Gene. 2003;321:1-15.

[40] Parlakian A, Gomaa I, Solly S, Arandel L, Mahale A, Born G, et al. Skeletal muscle phenotypically converts and selectively inhibits metastatic cells in mice. PLoS One. 2010;5:e9299.

[41] Madi L, Ochaion A, Rath-Wolfson L, Bar-Yehuda S, Erlanger A, Ohana G, et al. The A3 adenosine receptor is highly expressed in tumor versus normal cells: potential target for tumor growth inhibition. Clin Cancer Res. 2004;10:4472-9.

[42] Fishman P, Bar-Yehuda S, Ohana G, Barer F, Ochaion A, Erlanger A, et al. An agonist to the A3 adenosine receptor inhibits colon carcinoma growth in mice via modulation of GSK-3 beta and NF-kappa B. Oncogene. 2004;23:2465-71.

[43] Muller CE. Medicinal chemistry of adenosine A3 receptor ligands. Curr Top Med Chem. 2003;3:445-62.

[44] Polycarpou E, Meira LB, Carrington S, Tyrrell E, Modjtahedi H, Carew MA. Resveratrol 3-O-D-glucuronide and resveratrol 4'-O-D-glucuronide inhibit colon cancer cell growth: evidence for a role of A3 adenosine receptors, cyclin D1 depletion, and G1 cell cycle arrest. Mol Nutr Food Res. 2013;57:1708-17.

[45] Regateiro FS, Cobbold SP, Waldmann H. CD73 and adenosine generation in the creation of regulatory microenvironments. Clin Exp Immunol. 2013;171:1-7.

[46] Evani SJ, Prabhu RG, Gnanaruban V, Finol EA, Ramasubramanian AK. Monocytes mediate metastatic breast tumor cell adhesion to endothelium under flow. FASEB J. 2013;27:3017-29.

[47] He P, Adamson RH. Visualization of endothelial clefts and nuclei in living microvessels with combined reflectance and fluorescence confocal microscopy. Microcirculation. 1995;2:267-76.

[48] Colgan OC, Ferguson G, Collins NT, Murphy RP, Meade G, Cahill PA, et al. Regulation of bovine brain microvascular endothelial tight junction assembly and barrier function by laminar shear stress. Am J Physiol Heart Circ Physiol. 2007;292:H3190-7.

[49] Ting LH, Jahn JR, Jung JI, Shuman BR, Feghhi S, Han SJ, et al. Flow mechanotransduction regulates traction forces, intercellular forces, and adherens junctions. Am J Physiol Heart Circ Physiol. 2012;302:H2220-9.

[50] Jain RK. Molecular regulation of vessel maturation. Nat Med. 2003;9:685-93.

[51] Hsu YL, Hou MF, Kuo PL, Huang YF, Tsai EM. Breast tumor-associated osteoblast-derived CXCL5 increases cancer progression by ERK/MSK1/Elk-1/Snail signaling pathway. Oncogene. 2012.

[52] Borsig L, Wolf MJ, Roblek M, Lorentzen A, Heikenwalder M. Inflammatory chemokines and metastasis-tracing the accessory. Oncogene. 2013.

[53] Feoktistov I, Goldstein AE, Ryzhov S, Zeng D, Belardinelli L, Voyno-Yasenetskaya T, et al. Differential expression of adenosine receptors in human endothelial cells: role of A2B receptors in angiogenic factor regulation. Circ Res. 2002;90:531-8.

Supplementary information
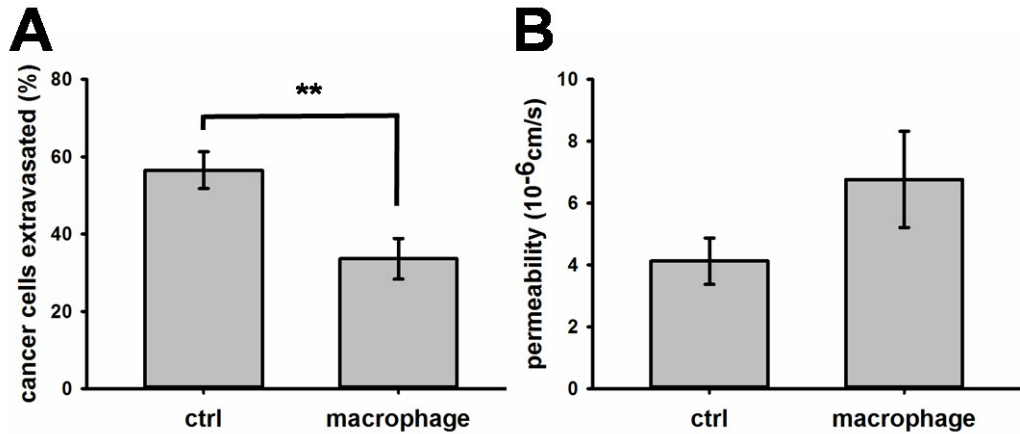
Fig4.S1: Cancer cell extravasation and endothelium permeability in the presence of macrophages. The addition of macrophages in the BMi microenvironment significantly reduced cancer cell extravasation (A) despite an increase in the endothelium permeability (B). This effect could be due to macrophage-secreted TNF-α which could affect both primary OD hBM-MSC secretion and endothelial barrier function.
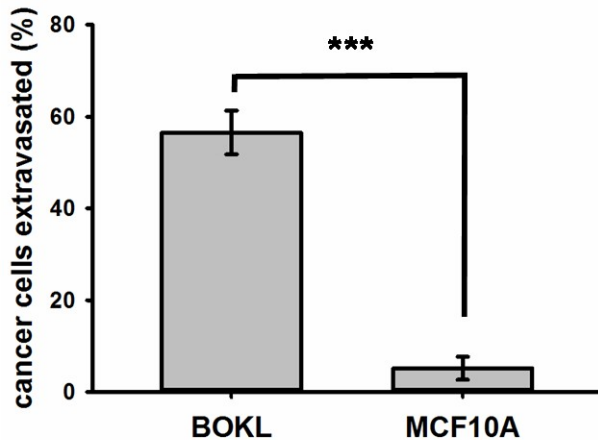
Fig4.S2: MCF-10A extravasation. Control experiments were performed to quantify the extravasation ability of non-metastatic mammary epithelial cells MCF-10A in the BMi microenvironment. Average extravasation rate was significantly lower (5.2 ± 2.5%) compared to metastatic bone seeking clone (BOKL) of the MDA-MB-231 metastatic breast cancer cells

(56.5 ± 4.8%), thus confirming the specific interaction between cancer cells and OD hBM-MSCs.
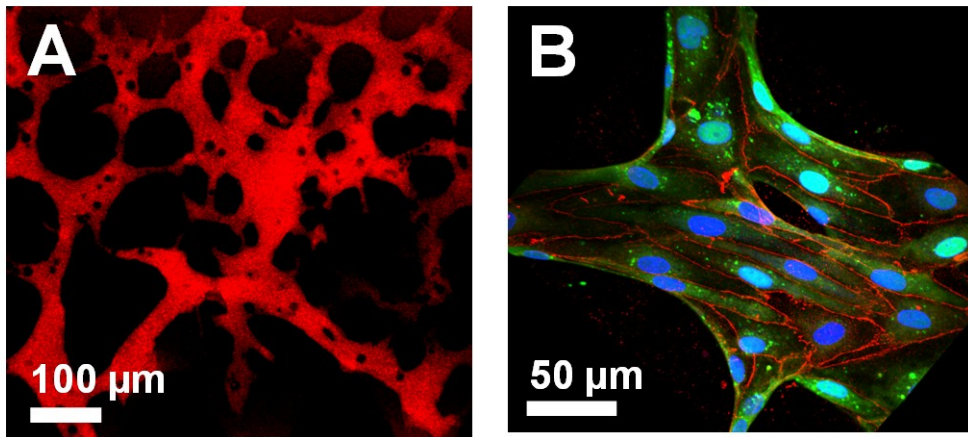
Fig4.S3: Dextran diffusive permeability. (A) Permeability of the microvascular network for each condition was measured injecting 70 kDa red fluorescent dextran and quantifying the average intensity at the initial and final time points within a region of interest including both microvessels and surrounding ECM. (B) Micrograph showing the alignment of endothelial cells (green) resulting from flow through the network. DAPI (nucleus, blue). ZO-1 (tight junctions, red).
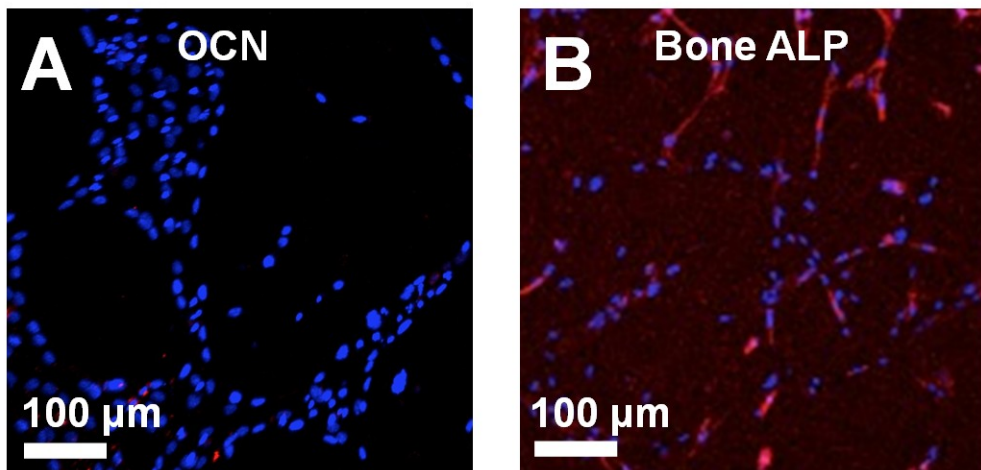
Fig4.S4: Immunofluorescent staining of OCN and bone alkaline phosphatase control. Control experiments were performed to check the organ-specific expression of OCN and bone alkaline phosphatase within the BMi microenvironment. Immunofluorescent stainings revealed the

total absence of OCN (A) and a significantly lower level of bone alkaline phosphatase (B) in matrices without OD hBM-MSCs. OCN and bone alkaline phosphatase are shown in red, cell nuclei appear blue (DAPI).
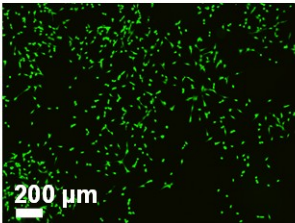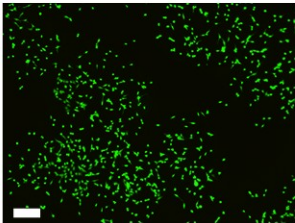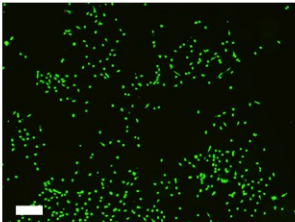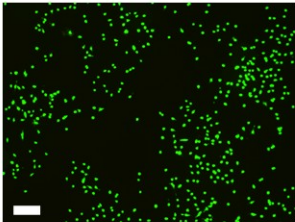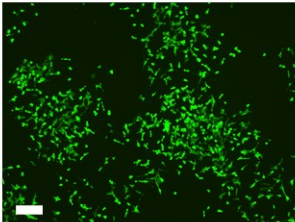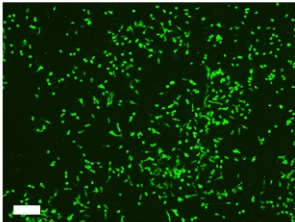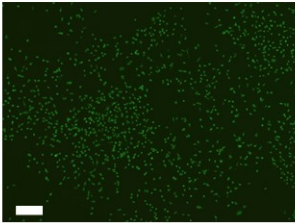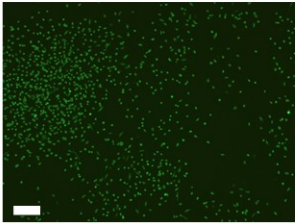
hours	adenosine	control
24		
48		
72		
96		

Fig4.S5: Breast cancer cell viability after the adenosine treatment. Breast cancer cells were incubated for 24 h with cancer cell medium+10 µM adenosine and Live/Dead assays were performed after 24 h, 48 h, 72 h and 96 h. Most of cells appeared viable at all time points with no significant differences between adenosine treated samples and controls.
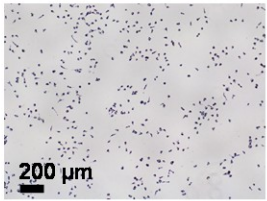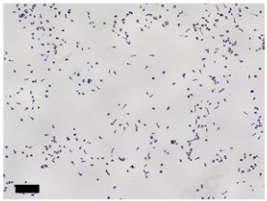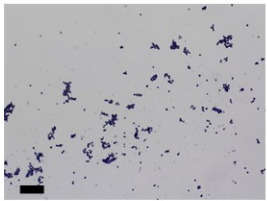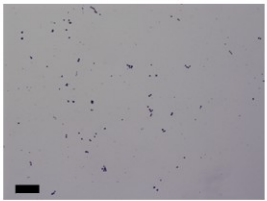
hours	adenosine	control
4	200 µm	
12		

Fig4.S6: Breast cancer cell metabolic activity after the adenosine treatment. Breast cancer cells were incubated either with cancer cell medium+10 µM adenosine for 4 h (simulating cancer cell pre-treatment before injection) or EGM-2MV+10 µM adenosine for 12 h (simulating the whole cancer cell incubation period considering both pre-treatment and microfluidic assay). Cells appear metabolically active (purple staining) without differences between adenosine treated samples and controls, as shown MTT assay.
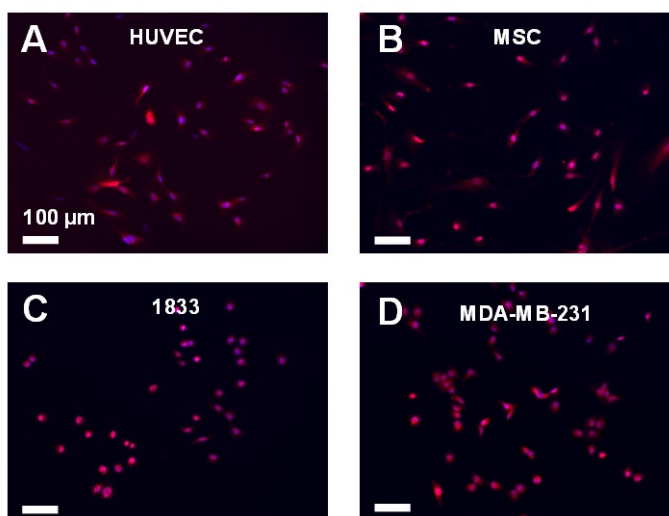
Fig4.S7: Breast cancer cell A_3AR expression. Immunofluorescent staining of A_3AR (red) on HUVECs (A), hBM-MSCs) (B), and different breast cancer cell lines including 1833 and MDA-MB-231 (C and D, respectively). DAPI (nucleus, blue).
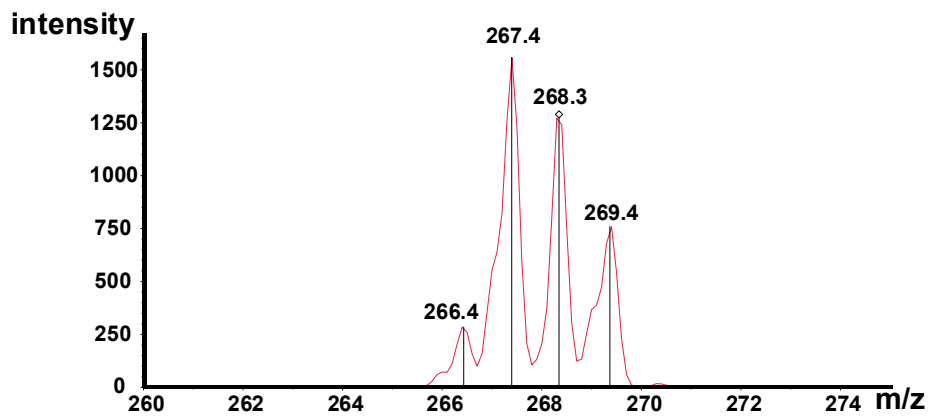
Fig4.S8: Adenosine expression within the C2C12 conditioned microenvironment. Mass spectrometry analysis of an adenosine standard (0.1 µM). A comparable level of adenosine (268 m/z peak) was detected within C2C12 embedding co-cultures (Fig4.3b).

Chapter 4

Human in vitro 3D co-culture model to engineer vascularized bone-mimicking tissues combining computational tools and statistical experimental approach

From: S. Bersini, M. Gilardi, C. Arrigoni, G. Talo, M. Zamai, L. Zagra, V. Caiolfa, M. Moretti

4.1 Introduction

A major challenge in the development of functional and clinically relevant engineered tissue constructs is the formation of long-lasting vascular networks for oxygen and nutrient supply as well as metabolic byproduct removal [1]. Due to the slow rate of neovessel growth (about 200 μm/day) [2, 3], the functionality of implanted substitutes relies on the pre-vascularization of the engineered tissues [4]. Noteworthy, the generation of vascularized constructs represents also a key factor for the design of advanced in vitro models that can be used to study complex biological phenomena involving the interaction with a functional endothelium, e.g. the metastatic spread of cancer cells from the primary tumor to secondary loci

[5, 6] or the lymphocyte homing towards diseased tissues [7]. Indeed, despite significant advances in microfluidic in vitro models generating biochemically and biophysically controlled, multicellular microenvironments where cell-cell and cell-matrix interactions can be tuned and quantified [8], size limitations do not allow to fully recapitulate the effects of biological processes occurring within thick and more physiological tissue constructs, including oxygen and nutrient transport. In addition, the extremely low number of cells sets a key limitation to perform genomic, transcriptomic and proteomic analyses.

Several strategies have been optimized in the last years to develop complex vascular networks, including microtissue molding [9], angiogenesis-based methods inducing capillary sprouting from vascular explants or coated microspheres [10, 11], cell sheet engineering [12, 13] and interfacial polyelectrolyte complexation [14]. Moreover, sacrificial templates made of alginate, carbohydrate glasses or agarose fibers have been successfully employed [15-17].

Compared to other approaches, vasculogenesis-based techniques allow to reproduce complex, highly branched and interconnected vascular networks through the self assembly of homogeneously distributed endothelial cells (ECs), thus mimicking the *de novo* morphogenesis of capillary vessels occurring during development. We previously developed a 3D microfluidic model based on the co-culture of ECs and mesenchymal stem cells (MSCs) to study the role of heterotypic cell-cell contact and the effect of different biomolecules, i.e. angiopoietin (Ang)-1 and transforming growth factor (TGF)-β1 [18], on microvascular network features and mural cell recruitment [19]. Khademhosseini group tested the effect of multiple gelatin methacrylate concentrations and hydrogel crosslinking degrees on vascular network development, demonstrating functional anastomoses of the tissue constructs with the host circulatory system [20]. Vasculogenesis-based techniques have been employed by Sung group to develop 3D cellular spheroids embedding ECs and MSCs, which were successfully implanted in mice to treat severe

hindlimb ischemia [21, 22]. Since vascularization is a critical process regulated by the synergic contribution of multiple factors, it is critical to analyze the specific role of each experimental parameter involved. However, these systems did not take into account the oxygen and nutrient distribution within the tissue construct and did not analyze the specific influence that different experimental variables, such as cell density and cell ratio, could have on the structural properties of the network, including length and branching. Understanding the main regulators of microvascular network features would be critical to design customized systems, according to the specific application. It is known that the cross-talk between ECs and osteo-cells is critical for the generation of vascularized bone tissues [23], while matrix stiffness and composition affect both vascular network development [24] and osteogenic differentiation [25]. In this context, the generation of functional vascularized bone models represents a key issue for both tissue regeneration purposes and the elucidation of the molecular mechanisms involved in bone-vascularization and osteogenesis [25-27].

Despite vascularized bone models have been reported, they generally analyze the effect of one or two experimental parameters, e.g. cell culture medium, endothelial/stromal cell ratio and matrix composition, on vascularization, calcium deposition and bone-specific marker expression within the engineered constructs [23, 28, 29]. These models did not focus on the synergic effect of multiple parameters and did not quantify the impact of their variation on the system. In addition, vascular network features were analyzed in terms of total network length (n.l.) or network area (n.a.) [10, 30], rarely taking into account the potential importance of other parameters, such as number and length of vascular trees [31].

Improving current vascularization strategies of organ-specific tissues lies on a deeper understanding of the interplay among key factors driving microvascular network generation and stabilization. Reliable platforms are necessary to high-throughput screen and compare different experimental conditions through the

combination of cellular, structural and genetic analyses. In this framework, our goals were (1) to design a human 3D mesoscale vascular model by combining the advantages of microscale and traditional tissue engineered macroscale systems to develop capillary networks within organ-specific matrices under controlled and tunable conditions; (2) to employ this model to screen a wide set of experimental conditions and analyze how the combination of multiple parameters can affect EC self-assembly into physiological microvascular networks within a bone-mimicking environment.

To reach our goals we employed computational simulations to predict the oxygen level of hydrogel-based systems embedded within 3D structures and we analyzed microvascular network features by means of custom image processing algorithms. Noteworthy, a key point of the present study is represented by the application of the Design of Experiment (DoE) approach, which allows to quantitatively and reliably analyze with a statistical method a wide set of experimental conditions, thus identifying synergic effects that cannot be highlighted by semi-quantitative studies based on standard statistical methods [32]. In addition, we demonstrated the presence of a bone-specific environment and compared the structure of different matrices and their evolution during network development. More than 200 samples corresponding to 35 selected experimental conditions were analyzed. This allowed us to identify key relationships between cell ratio and tissue geometry or cell ratio and cell culture medium, demonstrating that our model would represent a reliable platform to screen and compare different experimental conditions through the combination of cellular, structural and genetic analyses.

4.2 Materials and methods

3D masks were designed through computational simulations to mimic hypoxic and normoxic conditions. Pre-polymerized hydrogels embedding cell suspensions were

encased in the 3D masks and the formation and evolution of microvascular networks were daily monitored. Microvascular network features including total network length/area and vascular branch number/length were quantified. The DoE approach was applied to study the combined effects of five different classes of experimental parameters which could potentially affect the generation of vascular networks. Particularly, absolute number of ECs, cell ratio between ECs and stromal cells, culture medium, tissue construct thickness and oxygen distribution, and hydrogel composition were investigated (Fig1).
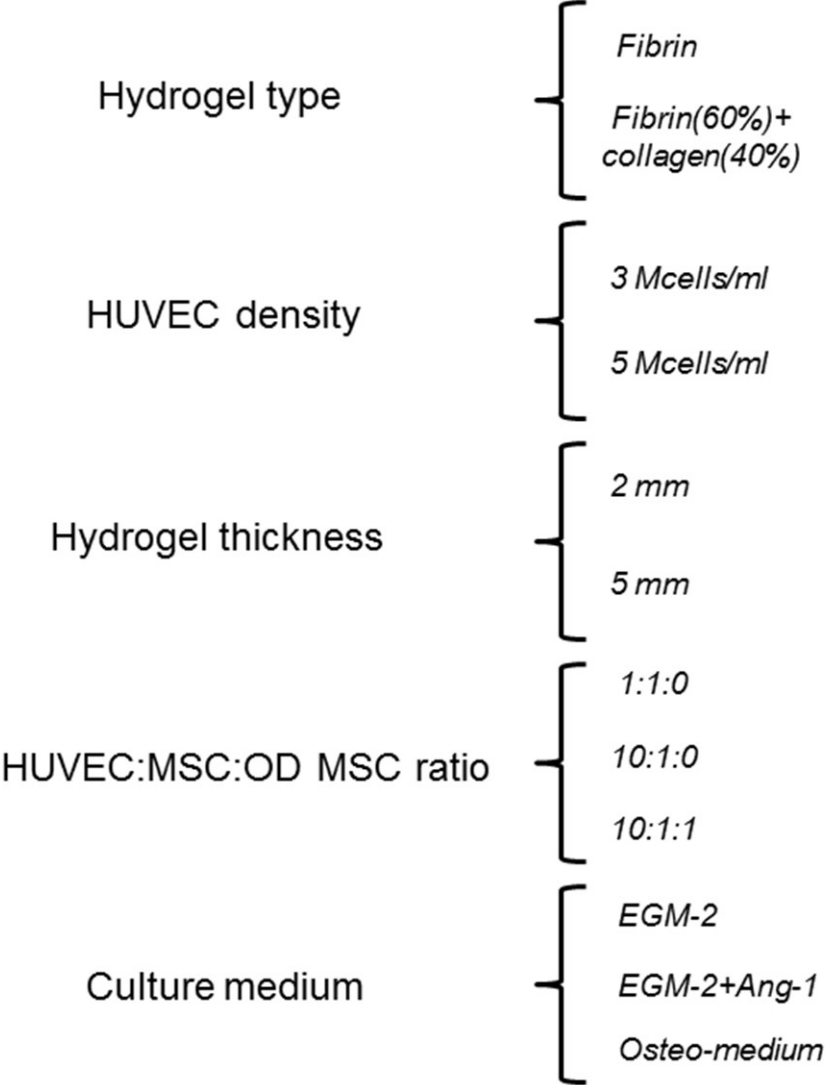
Fig1: Experimental parameters analyzed in the model: hydrogel type, HUVEC absolute density, hydrogel thickness, HUVEC/MSC/OD MSC ratio and culture medium. Osteomedium means a 1:1 mix of (EGM-2+Ang-1) and osteo-differentiating medium. HUVEC: human umbilical vein endothelial cell. OD MSC: osteo-differentiated mesenchymal stem cell.

4.2.1 Computational simulations and mask design

Cell constructs were embedded within poly-methyl-methacrylate (PMMA) cages with two open windows to allow an easy hydrogel filling and recovering. PMMA was selected for optical transparency and control of oxygen diffusion. PMMA masks were designed through a computer assisted design (CAD) software (Rhinoceros, Robert McNeel and Associates), laser cut, bonded to 100 μm thick glass coverslips with a acetoxy curing silicone glue) and sterilized with 70% ethanol. The oxygen distribution within cell constructs was assessed through 3D computational simulations; particularly, two different PMMA masks were designed to mimic two experimental conditions, i.e. highly oxygenated ($2\times2\times2$ mm^3 mask) and hypoxic environment ($2\times2\times5$ mm^3 mask). Computational simulations were performed using a finite element method (FEM) software (COMSOL Multiphysics 4.0; AB, Sweden). Cell constructs were modeled with a numerical grid consisting of 125,000 ($2\times2\times2$ mm^3 mask) and 300,000 ($2\times2\times5$ mm^3 mask) hexahedral elements. The oxygen diffusion coefficient was assumed in the range $2\text{-}3\times10^{-9}$ m^2/s (adapted from 3 mg/ml fibrin gels) [33]. The oxygen consumption rate was assumed to be 0.1188 μmol/(Mcells×h) and 0.0794 μmol/(Mcells×h) for MSCs [34] and human umbilical vein endothelial cells (HUVECs) [35], respectively. A Michaelis-Menten kinetics was considered, assuming a Michaelis constant of 0.0105 mol/m^3 and 0.00055 mol/m^3 for MSCs [34] and HUVECs [35], respectively. Zero mass flux conditions were imposed on the lateral surfaces of cell constructs while atmospheric oxygen level was assumed at the two cage openings (2×2 mm^2). Computational simulations were performed considering representative experimental conditions. Different cell ratios between ECs and MSCs (1:1 and

10:1) were assumed. Furthermore, 2 mm thick tissue constructs were simulated embedding 5 Mcells/ml HUVECs while oxygen diffusion within 5 mm masks was computed considering 3 Mcells/ml HUVECs.

4.2.2 Cell culture and hydrogel preparation

Primary green fluorescent protein (GFP)-transfected HUVECs were commercially obtained (Angio-Proteomie), cultured in endothelial growth medium EGM-2 (Lonza) and used at passage 6. MSCs were harvested from patients undergoing hip surgery after informed consent and isolated following already described protocols [19]. Cells were collected from three different donors, expanded, pooled and used at passage 5. Osteo-differentiated (OD) MSCs were obtained by culturing in osteo-differentiating medium containing L-ascorbic acid, β-glycerophosphate, cholecalciferol and dexamethasone for at least two weeks [36]. Prior to seeding, collagenase type I (Gibco) solution (15 mg/ml) was applied for 20 min on an orbital shaker to dissolve the matrix produced by OD MSCs; next, cells were trypsinized for 10 min. Two different hydrogels were prepared, namely 2.5 mg/ml fibrin gel and 2.5 mg/ml collagen type I (40%)-fibrin (60%) gel (hereinafter named fibrin+collagen). For fibrin gel preparation, human fibrinogen (Sigma) was diluted in Phosphate Buffered Saline (PBS) to a concentration of 5 mg/ml. Human thrombin at 500 IU/ml (Tisseel®, Baxter) was diluted in a solution of 1.1% NaCl and 2 mM $CaCl_2$ to a concentration of 100 IU/ml. The obtained solution was finally diluted in EGM-2 to a final concentration of 4 IU/ml. HUVECs were suspended in thrombin solution (4 IU/ml) at 20 Mcells/ml (for 5 Mcells/ml final cell density) or 12 Mcells/ml (for 3 Mcells/ml final cell density) and 1:1 mixed with an MSC suspension in thrombin solution (4 IU/ml) at 20 Mcells/ml or 12 Mcells/ml for 1:1 cell ratio, and with an MSC or MSC+OD MSC suspension at 2 Mcells/ml or 1.2 Mcells/ml for 10:1 or 10:1:1 cell ratios, according to the specific experimental condition. Particularly, MSCs and OD MSCs were 1:1 diluted before

mixing with HUVECs. The resulting cell suspension was 1:1 mixed with 5 mg/ml fibrinogen and left polymerizing for 20 min at room temperature within humid chambers to obtain a 2.5 mg/ml fibrin gel. Regarding mixed collagen+fibrin hydrogels, collagen type I (BD Biosciences) solution (4 mg/ml) with PBS (Gibco) and NaOH was prepared and 1:1 mixed with 6 mg/ml fibrinogen solution; next, cell suspensions (according to the experimental conditions) prepared in thrombin solution (4 IU/ml) were 1:1 mixed with the collagen/fibrinogen preparation to get a final concentration of 2.5 mg/ml (1.0 mg/ml collagen gel and 1.5 mg/ml fibrin gel). Hydrogels were left polymerizing at 37° within humid chambers and cultured until day 14. The medium was changed every 3-4 days. No supplements (100 ng/ml Ang-1) nor combination of EGM-2 and osteo-differentiating medium were applied until the first media change.

4.2.3 The DoE approach

A statistical software (JMP, SAS Institute Inc.) was used to define the minimum set of experiments to be performed in order to identify the best parameter combination for the generation of a physiologically-like vascular networks (Table 1).

Total network length, average branch number, average tree length (average of the total length of each vascular structure identified in each region of interest (ROI)) and network area (percentage of each ROI occupied by the vascular network) were analyzed for each experimental condition. These parameters, commonly employed to quantify and compare the main features of vascular networks [10, 30, 31], were provided as inputs to the statistical software to determine the best experimental condition (Fig2). A desirability coefficient (0:1) was generated to rate each experimental condition (combination of EC number, cell ratio, culture medium, mask geometry, gel type) according to the output parameters (total network length, average branch number, average tree length and network area) [37]. For example,

the combination of experimental parameters determining the maximum value of total network length was associated with a desirability coefficient equal to 1, while the remaining combinations were accordingly coupled with values in the range 0-1. The overall desirability coefficient for a specific combination of experimental conditions was then represented by the product of the desirability coefficients extracted for each input parameter.

Table 1. Analyzed conditions

	Hydrogel type	HUVEC density	Hydrogel thickness	HUVEC : MSCs : OD MSCs ratio	Culture medium
	Fibrin (-) Fibrin+collagen (+)	3M cells/ml (-) 5M cells/ml (+)	2 mm (-) 5 mm (+)	1 : 1 : 0 (-) 10 : 1 : 0 (*) 10 : 1 : 1 (+)	EGM-2 (-) EGM-2+Ang-1 (*) Osteo-medium (+)
1	-	-	-	*	+
2	-	-	-	-	-
3	-	-	-	+	-
4	-	-	-	*	*
5	-	-	+	+	+
6	-	-	+	-	-
7	-	-	+	-	+
8	-	-	+	+	*
9	-	-	-	*	-
10	-	+	-	*	-
11	-	+	-	+	*
12	-	+	-	-	*
13	-	+	-	*	+
14	-	+	-	+	+
15	-	+	+	+	-
16	-	+	+	-	*
17	-	+	+	*	*
18	+	-	-	*	-
19	+	-	-	+	*
20	+	-	-	-	*
21	+	-	-	*	+
22	+	-	-	-	+
23	+	-	+	*	*
24	+	-	+	+	*
25	+	-	+	-	-
26	+	-	+	+	+
27	+	+	-	-	+
28	+	+	-	*	*
29	+	+	-	-	-
30	+	+	-	+	-
31	+	+	+	-	*
32	+	+	+	*	+
33	+	+	+	+	-
34	+	+	+	+	+
35	+	+	+	*	-

Table 1. Experimental conditions resulting from the combination of different gel type, HUVEC density, EC/stromal cell ratio, culture medium and tissue construct thickness. Osteo-medium means a 1:1 mix of (EGM-2+Ang-1) and osteo-differentiating medium.
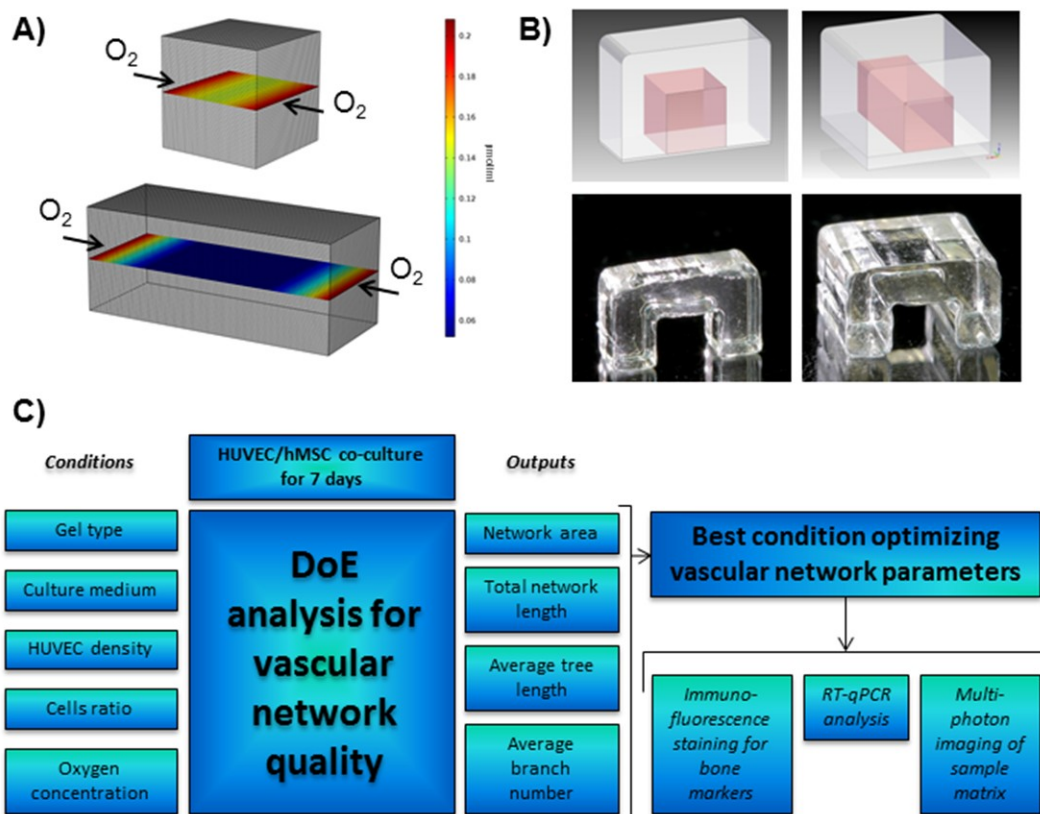
Fig2: The DoE approach. Computational simulations of oxygen concentration within two tissue constructs characterized by different gel thickness. The critical value of oxygen concentration was assumed equal to 0.052 μmol/ml (A). 3D PMMA masks were designed according to computational simulations through a CAD software. The external cage appears in grey while the gel is represented in light red. 3D masks captured with a digital camera(Canon 500D, Canon Macro Lens EF 100 mm) (B).Schematic representing the whole experimental process and the main variables considered in the framework of the DoE approach. Multiple inputs (EC density, cell ratio, culture medium, gel type and geometry of the mask) were considered to generate vascular networks which were rated in terms of network area, total network length, average tree length and average branch number. The best parameter combination was then tested to analyze the surrounding bone-mimicking environment by means of immunofluorescent staining and qRT-PCR for bone-specific and vascular markers, and multi-photon imaging to quantify and compare structural properties of the matrix (C).

4.2.4 Image analysis and quantification

Samples were daily imaged through an epifluorescence microscope (Olympus IX71) and vascular parameters quantified at day 7 for each experimental condition. Multiple network parameters were investigated, as reported above. At least three ROIs ($600 \times 600 \mu m^2$) were analyzed for each sample and at least three samples were always considered for each condition. Moreover, $2 \times 2 \times 5$ mm^3 samples were imaged and quantified by distinguishing outer and inner regions, thus trying to investigate potential differences due to high-low oxygen levels, as predicted by computational simulations. Particularly, a minimum of two ROIs were considered both for outer and inner regions. Fluorescence images were analyzed using Fiji software (http://fiji.sc/Fiji), harnessing the endothelial cell GFP signal. Images were pre-processed to subtract the background (rolling ball radius: 10), enhance the contrast (0.4% saturation), and filter noise (application of "despeckle" algorithm and "gaussian blur" filter (sigma: 1.5)). Then, pre-processed images were converted to a binary format by applying the "triangle" threshold method. Finally, 2D skeletonize data were noise filtered applying a 25 µm threshold value to remove image artifacts (Fig3A). The second harmonic generation (SHG) and GFP-HUVEC fluorescence images were acquired on a Zeiss 780 multi-lines confocal system coupled to a MaiTai (Spectraphysics) tunable multiphoton laser. After removing the glass coverslip, samples were placed in a plastic dish and covered with PBS. Images were acquired at room temperature using an upright Axio Examiner Z.1 scope equipped with a dipping 20x Plan Apochromat NA 1.0 DIC 0,17 M27 75 mm objective. The excitation was set at 800 nm and the emission was collected through 2 spectral hybrid detectors set at 387-410 nm (channel 1) and 509-580 nm (channel 2). The scan area was 425x425x313 (X,Y,Z) µm^3 with a pixels dwell time of 0.79 µs. The same system was used for tile scan z-stacks to acquire sections of 3,400x3,400x313 µm^3. In this case the GFP-HUVECs were excited with an argon

laser at 488 nm with a pixel dwell time of 0,79 µs. Emission was collected with a spectral detector set at 509-580nm. Scan area was 1,024x1,024 pixels and the stitching of 8 stacks/sample was carried out using the Zen 2011 version software and applying a 5% pixel overlap. These images were used to quantify the 3D volume occupied by vascular networks within representative samples (Imaris, Bitplane). Particularly, vessel branch volumes were normalized to the total volume of the sample and color-coded as large continuous branches (green), medium size branches (purple) and small size branches (light blue) (Fig. 3B).
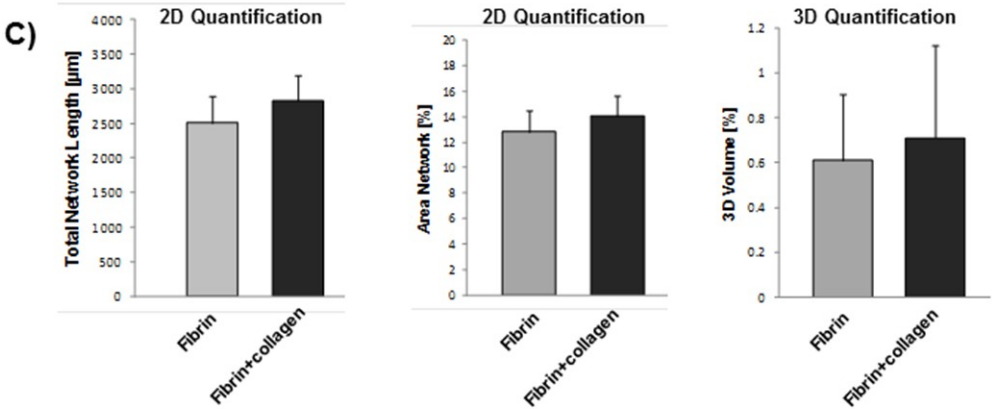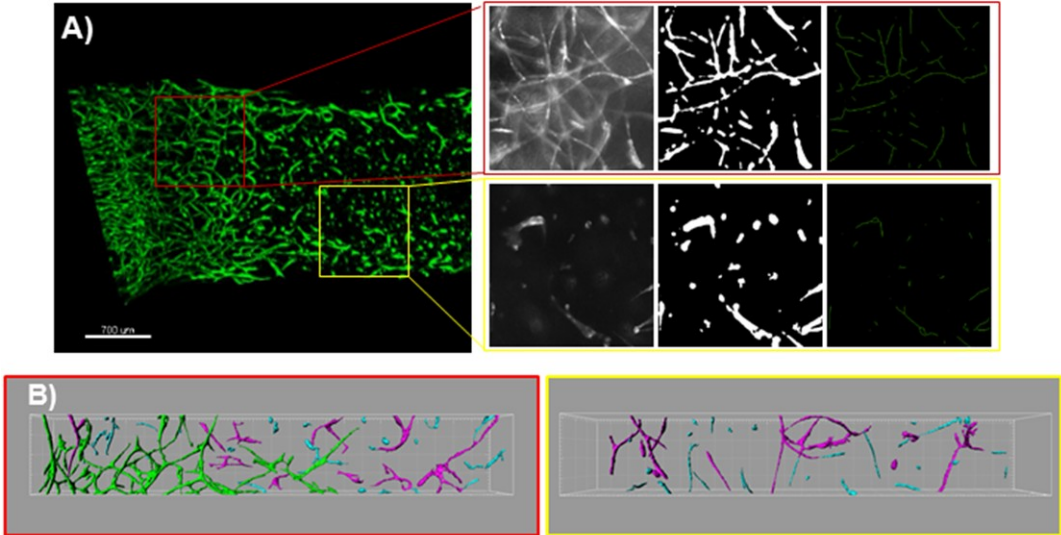
Fig3: Image processing and quantification of vascular network parameters.3D confocal reconstruction of a 5 mm thick tissue construct characterized by a 1:1 ratio between ECs (green) and MSCs (Z-stack series for 3D rendering were collected with a Leica TCS SP8 X equipped with super continuum excitation source and hybrid detectors). Representative fluorescent images of specific areas of the vascular network within outer and inner regions of the tissue construct. Fluorescent images were noise-filtered and converted in binary format. A skeletonization algorithm was applied to extract main features of the vascular network, including total network length, average tree length and average branch number (A). Representative 3D segmentation analysis of the vessel network, showing clear differences between outer (left) and inner (right) regions of 5 mm tissue constructs characterized by a 1:1 cell ratio. Large continuous branches (green), medium size branches (purple), small size branches (light blue). Stitched z-stacks were first filtered to reduce the background by applying a 2% threshold of the maximum intensity, then a filter of 1.5×10^4 voxels was applied to discard small aggregates and single cells from analysis. Vessel branch volumes were normalized to the total volume occupied in the imaged sample and color-coded according to a three-level log-scale of volumes (B). Comparison between 2D and 3D quantification of microvascular networks: fibrin+collagen tissue constructs showed superior total network length and network area (2D quantification) compared to fibrin hydrogels. Accordingly, microvascular networks occupied larger volumes within fibrin+collagen samples compared to fibrin tissue constructs (3D quantification) (C).

4.2.5 Immunofluorescent staining

Immunofluorescent staining for alpha smooth muscle actin (α□SMA) (mouse anti-human, abcam, 1:60), osteonectin (rabbit anti-human, SantaCruz, 1:60) and osteopontin (rabbit anti-human, abcam, 1:100) was performed on whole samples. Hydrogels were extruded from the PMMA masks, fixed in 4% paraformaldehyde for 30 min ($2 \times 2 \times 2$ mm^3) or 1 h ($2 \times 2 \times 5$ mm^3)and rinsed with PBS. Samples were then permeabilized with 0.1% Triton X-100 (Sigma) for 10 min and subsequently treated with 2% bovine serum albumine (BSA) (Sigma) overnight to avoid unspecific binding. Next, primary antibodies diluted in PBS were incubated at 4°C

for 24 h. Then, primary antibodies were removed and samples twice rinsed with PBS. A solution containing secondary antibody (goat anti-rabbit, AlexaFluor 568, LifeTechnologies, 1:200 dilution or goat anti-mouse, AlexaFluor 568, Santa Cruz Biotechnologies, 1:200 dilution) and 4'6-Diamidino-2-Phenylindole (DAPI, 300 nM final concentration) in PBS was added to the samples and incubated at 4°C for 24 h. Finally, samples were twice rinsed in PBS and observed under a confocal microscope (Leica TCS-SP5).

4.2.6 Gel digestion and cell sorting

The 3D gel containing the co-culture was digested after seven days by an enzyme mixture at 37 °C under stirring. The enzyme mixture was composed of collagenase I (Worthington) 7.5 mg/ml and nattokinase (JBSL-USA) 50 U/ml. Subsequently, the different cell populations were sorted as previously performed in other studies [38]. Briefly, the cell suspension was incubated with biotinylated monoclonal anti-CD31 (abcam) for 10 minutes under stirring at 4°C. After washing, 25 μL of activated streptavidin-coupled dynabeads (Life Technologies) were added to the cell suspension and let interact for 20 minutes at 4°C under stirring. Following interaction with the magnet (DynaMag-5 Magnet, Life Technologies), ECs were removed from the suspension by binding through the anti-CD31-dynabeads and purified MSCs were harvested from the supernatant. Then, MSCs were used for genetic analysis to determine the expression of osteogenic and vascular markers.

4.2.7 Gene expression analysis

Total MSC RNA from frozen cultured cells (7 days co-culture) was purified with RNeasy Mini kit (Qiagen). Obtained RNA was spectrophotometrically quantified by the use of Nanodrop (Thermo Scientific) and cDNA was prepared using the iScript cDNA Synthesis Kit (Bio-Rad Laboratories). The amplifications were

performed in thermo cycler (Bio-Rad). Gene expression of selected markers was analyzed by quantitative reverse transcription polymerase chain reaction (qRT-PCR) by the use of StepOne Plus (Life Technologies).The reaction mixture for qRT-PCR was composed of TaqMan® Universal PCR Master Mix and TaqMan Assays-on-Demand™ Gene expression probes (Life Technologies). A sample containing 28.56 ng cDNA was loaded for each well and used as a template for the qRT-PCR, which was performed in 20 µl reaction mixture. Three replicates were analyzed for each experimental group. The gene expression of selected markers was normalized to the housekeeping gene glyceraldehyde-3-phosphate dehydrogenase (GAPDH), using the comparative $\Delta\Delta C_T$ method [39]. The following probes were employed: GAPDH (Hs99999905_m1, housekeeping gene), α-SMA (ACTA-2, Hs00426835_g1, mural cell marker), osteocalcin (BGLAP, Hs001587814_g1, bone marker), osteonectin (SPARC, Hs00234160_m1, bone marker) and osteopontin (SPP1, Hs00959010_m1, bone marker).

4.2.8 Statistical analysis

Analysis of variance (ANOVA) and unpaired Student's *t*-test were performed with Prism Graph Pad software. ANOVA was followed by Bonferroni post-hoc test to determine significant differences between groups. Differences were considered significant for $p < 0.05$ (*), $p < 0.01$ (**) and $p < 0.005$ (***). Results are presented as mean ± standard deviation. Vascular network parameters were analyzed considering at least n=3 samples per experimental condition. qRT-PCR experiments were performed pooling at least n=10 samples per experimental condition.

4.3 Results and discussion

4.3.1 Validation of the model

The development of 3D human vascularized bone models is critical to study the molecular and cellular interactions occurring in the bone microenvironment [32]. In this context, our group has recently developed microfluidic models [36, 40] to analyze the metastatic spread of specific cancer cell types towards the bone [41, 42]. However, the limited thickness of microfluidic devices does not allow to reproduce the structural complexity and hierarchical organization characterizing physiological tissues, neither their biological consequences, e.g. oxygen and nutrient diffusion within thick tissues.

In this project, we performed computational simulations to design two different conditions mimicking a highly oxygenated and a hypoxic environment. The $2\times2\times2$ mm^3 mask was characterized by a minimum oxygen level of 0.142 µmol/ml, which is significantly higher compared to the threshold value commonly considered for cell survival (0.052 µmol/ml, corresponding to 38 mmHg) (Fig2A) [43]. Conversely, $2\times2\times5$ mm^3 constructs showed extremely low (< 1%) oxygen levels in the core regions, with a threshold distance of about 1 mm from the outer face of the hydrogel defining the critical depth for cell survival (0.052 µmol/ml) (Fig2A). Interestingly, samples characterized by 10:1 EC/MSC cell ratio resulted in high oxygen levels (0.091 µmol/ml minimum) within the whole 5 mm thick tissue constructs, being significantly different compared to 5 mm thick samples characterized by 1:1 ratio.

The model here described allowed us to screen 35 experimental conditions preparing more than 200 samples. It is easy to tune and responsive to changes, it provides highly reproducible results and requires just basic training in order to be employed by any kind of user with cell culture skills. In addition, it allows simple

and effective recovery of the samples for qRT-PCR analyses and it could be employed for the study of other vascularized tissues, and for disease modeling and drug screening. Tissue constructs were successfully embedded within PMMA/glass masks and were cultured for up to 12-14 days. Vascular networks were generated throughout all experimental conditions, despite significant differences were detected when key experimental parameters were modified. The application of 1:1 EC/MSC cell ratio determined thin, highly interconnected microvessels, while 10:1 or 10:1:1 ratios were characterized by large cell clusters, which gradually remodeled into tiny capillaries at day 7. Consistently with computational simulations, clear differences were observed comparing the inner and outer regions of 5 mm thick tissue constructs with 1:1 cell ratio (Fig3B), demonstrating oxygen diffusion/consumption did play a role in vascular network development.

2D and 3D quantifications were performed at the same time. More in detail, 2D fluorescent images were used to quantify key network parameters such as total network length and network area. We detected higher values of total network length and network area within fibrin+collagen samples compared to fibrin tissue constructs (2,828 ± 361 μm vs. 2,510 ± 391 μm (n.l.) and 14.0 ± 1.6% vs. 12.8 ± 1.7% (n.a.), respectively). These data captured from 2D fluorescent images highlight 11.2% difference in terms of network length and 8.6% difference in terms of network area between the two matrices. 3D quantifications were carried on analyzing the total volume occupied by vascular structures reconstructed from 3D confocal images (slice thickness: 1 μm, ROI: 2,400×400 μm^2 with a minimum of 205 slices). Noteworthy, results obtained from 3D confocal reconstructions performed on the same experimental groups, i.e. fibrin+collagen and fibrin tissue constructs, showed 14.1% difference in terms of occupied volume. This demonstrated to be consistent with results observed from 2D quantifications (11.2% difference (n.l.) and 8.6% difference (n.a.)) (Fig3C) and allowed us to perform the analysis of microvascular networks through a 2D image-based

strategy, which was characterized by reduced acquisition time and image post-processing, compared to 3D analyses.

4.3.2 Generation and characterization of 3D interconnected vascular networks within bone-mimicking environment

4.3.2.1 Application of the model and identification of the optimal experimental parameter combination

Several studies investigated the role of single experimental parameters on vascularization and/or osteogenesis, such as culture medium, endothelial-stromal cell ratio or supporting biomaterial, despite they did not provide a comprehensive analysis of their synergic effect [23, 29, 32, 44]. Hence, a specific aim of the present work was to analyze the combined effect of a broad panel of experimental conditions through the application of a statistical method, i.e. the DoE approach, which minimizes the number of tests to be performed. A desirability coefficient (0:1) allowed us to rate each experimental condition.

The whole set of 35 experimental conditions tested through our high-throughput system promoted the generation of vascular networks (FigS1), although we were able to highlight that the combination of 3 Mcells/ml ECs, 10:1 EC/MSC cell ratio, 1:1 mixture of (EGM-2+Ang-1) and osteo-medium (hereinafter referred as to "osteo-medium"), $2\times2\times5$ mm^3 masks and 2.5 mg/ml fibrin+collagen hydrogels determined the highest desirability score, which was equal to 0.73 (Fig4A). The statistical method we employed allowed us to analyze experimental conditions obtained through the modification of each single parameter characterizing the ideal combination and quantify the effect of this change in terms of desirability coefficient. Particularly, we found that desirability coefficient differences with the optimal condition due to the use of fibrin gel or 1:1 ratio (0.67 score) were mainly dependent on the reduced average tree length (0.73) (Fig4B and 4C).

Since we found that the introduction of an osteogenic medium was critical to promote the best vascularization, we hypothesized that the presence of OD MSCs could represent a key parameter to get a vascularized bone construct, providing pro-angiogenic cues comparable to those ones present within an osteogenic medium. We quantified vascular network differences comparing the desirability coefficient of the previously discussed best parameter combination with the one obtained with the introduction of osteo-cells. Particularly, the generation of vascularized tissue constructs with a fixed 10:1:1 EC/MSC/ODMSC cell ratio determined a change in the optimal parameter combination predicted by the statistical software, due to the introduction of a standard EGM-2 culture medium instead of an osteo-medium to optimize the desirability coefficient. This one decreased from 0.73 (previously identified overall best condition) to 0.58, indicating a general lower quality of the vascular network. This results show that the paracrine effect of osteogenic factors but not the direct contact with OD MSCs was critical to promote the generation of physiologically-like microvascular networks.
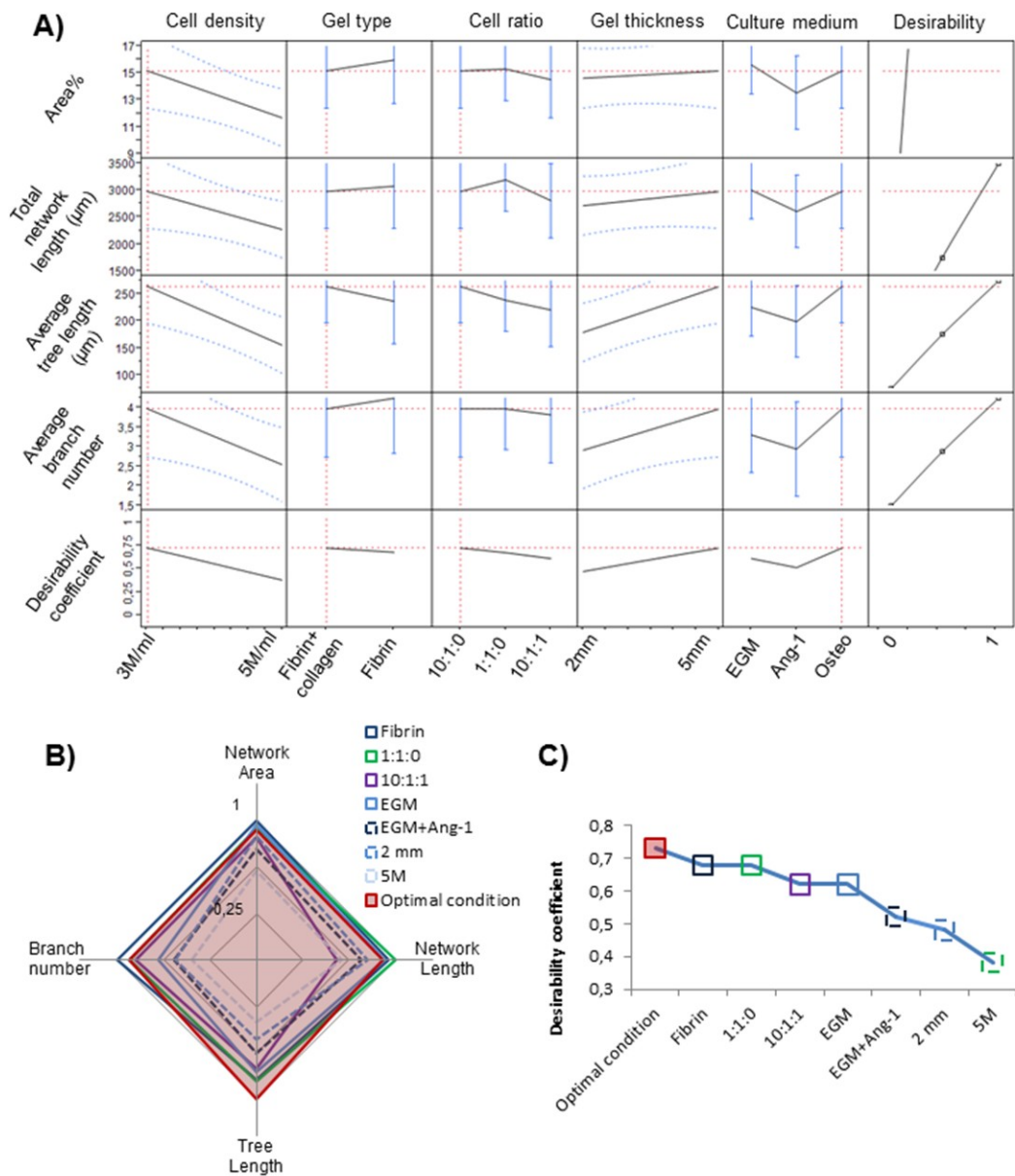
Fig4: Identification of the optimal parameter combination for the generation of vascular networks within bone-mimicking tissues. Vascular networks were analyzed and compared in terms of network area, total network length, average tree length and average branch number. A desirability coefficient was computed to rate each specific parameter combination and identify the optimal vascular network. The DoE approach allows to fix a specific input parameter (EC density, cell ratio, culture medium, gel type and geometry of the mask) and dynamically predict the optimal combination of the remaining parameters to get the best

vascular networks. At the same time, it is possible to maximize a specific output parameter (e.g. total network length) and identify the best parameter combination to obtain vascular networks with that specific feature. Data are shown as average values with 95% confidence interval of the mean (A).Radar graph comparing the overall best parameter combination (3 Mcells/ml ECs, 10:1 EC/MSC cell ratio, osteo-medium, 2×2×5 mm³ masks and 2.5 mg/ml fibrin+collagen hydrogels) and experimental conditions characterized by a single parameter change. Despite other conditions obtained with the introduction of 1:1 EC/MSC cell ratio or fibrin gel resulted in similar total network length or network area, the overall best combination was characterized by a superior average tree length. Data were normalized according to the highest value of network area, network length, tree length and branch number quantified among selected conditions (B). Desirability coefficient trend among experimental conditions presented in B). It appears clear that the introduction of 5 Mcells/ml ECs, 2 mm thick constructs or the addition of Ang-1medium determined a dramatic decrease in the desirability coefficient (C).

4.3.2.2 Effect of culture medium composition, EC density and EC/stromal cell ratio

In addition to the overall desirability coefficient, which allowed us to identify the optimal experimental condition, we independently analyzed the specific role of single parameters or combinations of two of them. It was found that osteo-medium resulted in significantly higher values of total network length ($2{,}821 \pm 241$ μm) and network area ($14.4 \pm 0.8\%$) compared to EGM-2+Ang-1 (hereinafter referred as to Ang-1 medium) ($2{,}507 \pm 169$ μm (n.l.) and $12.8 \pm 0.8\%$ (n.a.)) (Fig5A). Kolbe and colleagues analyzed a panel of seven media for cell culture including pure endothelial growth medium, pure osteogenic medium and pure endothelial or osteogenic media with particular combinations of supplements, e.g. endothelial growth medium supplemented with the osteogenic factor β-glycerophosphate. The authors found that co-cultures of outgrowth ECs and bone marrow MSCs in endothelial growth medium generated more vessel-like structures after 2 weeks and promoted the expression of pro-angiogenic factors and smooth muscle cell markers compared to pure osteogenic medium. Particularly, no clear vessel structures were

detected with the addition of osteogenic medium with or without endothelial supplements [28]. Conversely, it is interesting to highlight that our results showed the combination of endothelial and osteogenic media was critical to develop interconnected vascular networks, resulting in even superior network parameters when compared with Ang-1 medium supplemented tissue constructs. This is in agreement with previous findings by the Vunjak-Novakovic group, which showed the addition of pure endothelial growth medium followed by a 1:1 mixture of endothelial/osteogenic medium was critical to promote the generation of both capillary-like structures and bone-like tissue [32]. However, despite focusing on culture medium composition and effects of sequential induction of osteogenesis and vasculogenesis, the authors did not take into account the role of endothelial/stromal cell ratio, absolute number of endothelial cells or oxygen distribution [32]. Ma and co-authors co-cultured ECs and osteoblasts focusing on multiple cell ratios and culture media and identified a 1:1 ratio within osteogenic medium as the best parameter combination to get both osteogenesis and vascularization, despite mineralization seemed to represent the most critical factor in their work [44]. Conversely, the present study demonstrated the 10:1 cell ratio provided the best outcomes when coupled with 3 Mcells/ml ECs, osteo-medium, $2\times2\times5$ mm^3 masks and 2.5 mg/ml collagen+fibrin hydrogels. Looking in detail at data representing the effect of single parameters or combinations of two parameters, we found a significant interaction between cell ratio and culture medium. For example, the 1:1 cell ratio provided the highest total network length when coupled with osteo-medium(3,151 ± 142 μm (1:1), 2,536 ± 442 μm (10:1) and 2,531 ± 329 μm (10:1:1)), despite no significant differences among cell ratios were detected in the network area with the same culture medium (14.8 ± 0.9% (1:1), 13.4 ± 2.5% (10:1) and 13.7 ± 1.6% (10:1:1)) (Fig5B). Conversely, the same cell ratio determined the lowest value of network area in the EGM-2 condition (12.4 ± 1.0%), despite no differences in terms of network area when compared with the other cell ratios in the same culture medium (14.3 ± 1.5% (10:1) and 15.0 ±

1.2% (10:1:1)) (Fig5B). It is noteworthy to highlight these results could be extremely useful to design vascular networks with desired features, i.e. high total network length or network area, according to the specific requirements of a particular model.

Another significant interaction was found between culture medium and EC density. Particularly, 5Mcells/ml seeding density resulted in superior total network length when coupled with Ang-1 medium (2,694 ± 272 μm vs. 2,368 ± 212 μm) while 3Mcells/ml provided the highest value of network area (3.2 ± 1.0% vs. 2.2 ± 0.1%) and network length (2,993 ± 55 μm vs. 2,496 ± 126 μm) when tissue constructs were supplemented with osteo-medium (Fig5C). Previously reported studies [32, 44] employed fixed cell densities to screen for the optimal culture media or identify the best EC/stromal cell ratio. However, it would have been interesting to combine the wide set of tested cell ratios with different values of EC densities or culture medium in order to identify potential correlations among these parameters. Indeed, despite a limited set of combinations was analyzed in the present study, it appears clear how changing EC density and culture medium could allow to tune specific properties of the vasculature, as well as generate different local microenvironments, since both ECs and MSCs could secrete different factors or express specific endothelial/osteogenic markers.

4.3.2.3 Effect of hydrogel composition

Specific studies focused on the specific role of cell ratio and gel composition on vascular network development [29, 45, 46]. Particularly, Rao and colleagues found that vasculogenesis was significantly decreased with the highest tested endothelial/mesenchymal stem cell ratio (5:1) and that vessel formation was promoted by gradually increasing the fibrin content within multiple fibrin+collagen composite materials, although fibrin(60%)+collagen(40%) hydrogels and pure

fibrin material exhibited the same degree of vascularization. Moreover, the authors showed an inverse correlation between matrix stiffness and vascular network formation. Our data show that fibrin(60%)+collagen(40%) gels provided significantly higher values of total network length (2,828± 361 µm vs. 2,510 ± 391 µm), average tree length (169 ± 54 µm vs. 132 ± 30 µm), network area (14.0 ± 1.6% vs. 12.8 ± 1.7%) and average branch number (2.8 ± 0.6 vs. 2.4 ± 0.4) (Fig5D). Thus, these results not only confirm the presence of collagen could induce a positive effect on vascular network development, but also extend previously reported data on the effects of gel composition on vascularization which highlighted the absence of significant differences between pure fibrin and composite materials.

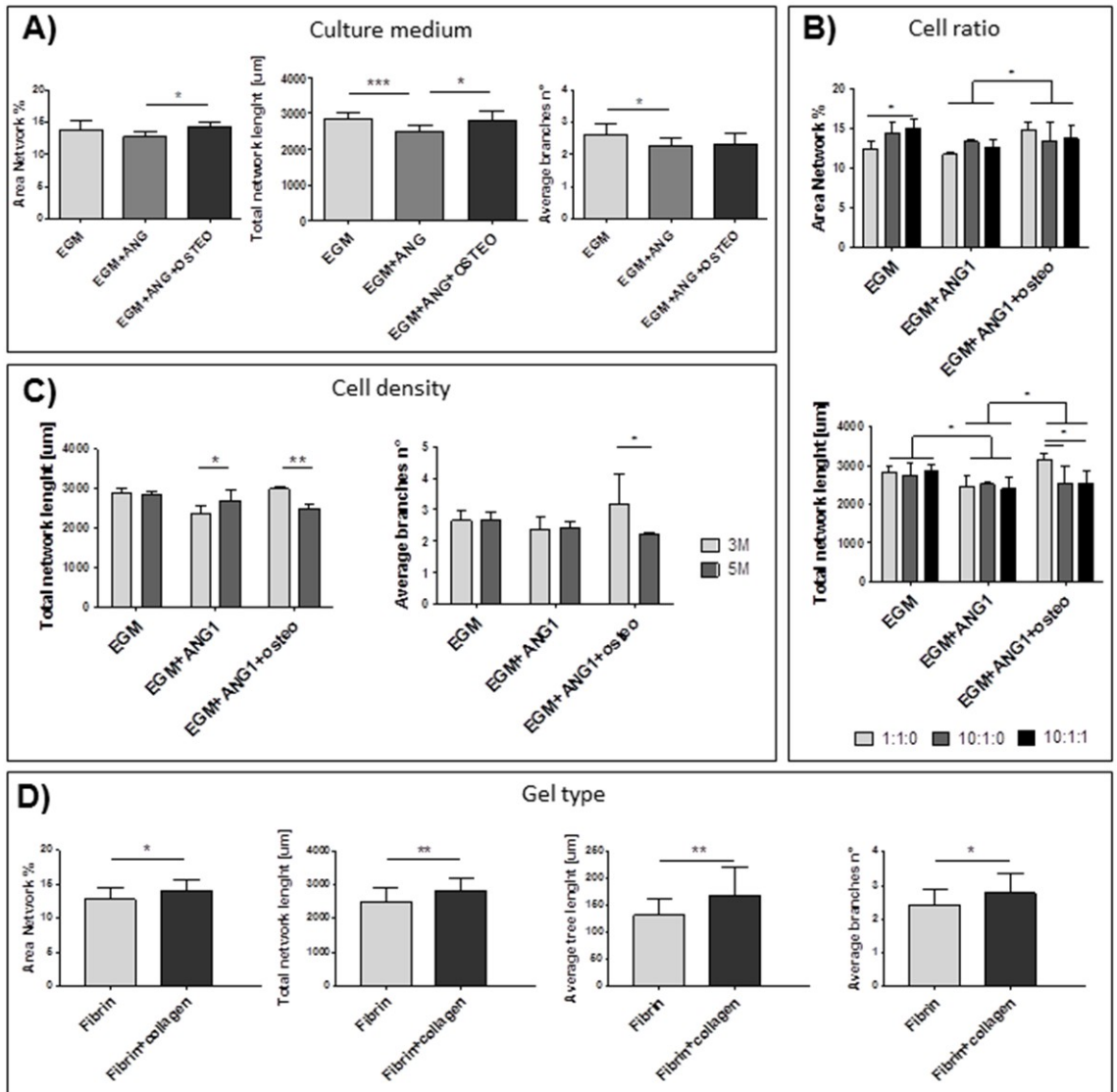Fig5: Effect of single parameters on vascular network development. The effect of gel type (A) and culture medium (B) was analyzed averaging all the experimental conditions characterized by that specific parameter. The effect of EC/stromal cell ratio (C) and EC density (D) was dependent on the selected culture medium, demonstrating the interplay between different parameters in the generation of vascular networks.

4.3.2.4 Effect of oxygen distribution

Significant correlations were found between oxygen diffusion computational simulations and experimental tests. Indeed, computational simulations predicted the presence of hypoxic areas within the core regions of $2\times2\times5$ mm^3 tissue constructs with 1:1 mixed ECs and MSCs at both 3 and 5 Mcells/ml (Fig6A). Conversely, simulations showed the oxygen concentration was above the critical threshold within 5 mm thick tissue constructs characterized by 10:1 cell ratio (Fig6A). In vitro experiments confirmed the geometry of the mask and the oxygen level did play a role in the vascular network development. Particularly, clear differences were detected in terms of total network length and network area between 2 mm thick masks (2,966 $\pm$ 282 μm (n.l.) and 13.2 $\pm$ 1.3% (n.a.)) and the inner region of 5 mm thick masks (1,179 $\pm$ 584 μm (n.l.) and 7.8 $\pm$ 2.0% (n.a.)), as well as between inner (1,179 $\pm$ 584 μm (n.l.) and 7.8 $\pm$ 2.0% (n.a.)) and outer (3,719 $\pm$ 734 μm (n.l.) and 16.1 $\pm$ 2.5% (n.a.)) regions of 5 mm thick tissue constructs with 1:1 cell ratio (Fig6B). No statistical differences were shown between internal and external regions of 5 mm thick masks in presence of 10:1 cell ratio in terms of total network length (2,337 $\pm$ 509 μm vs. 2,901 $\pm$ 366 μm), network area(12.9 $\pm$ 2.9% vs. 14.9 $\pm$ 1.7%) and average branch number (3.1 $\pm$ 0.1 vs. 2.5 $\pm$ 0.5) (Fig6B). Noteworthy, the average tree length was higher within the inner core of 5 mm thick tissue constructs compared to 2 mm thick masks (187 $\pm$ 38 μm vs. 128 $\pm$ 19 μm) in presence of 10:1 cell ratio (Fig. 6B). Conversely, a statistical difference was detected between inner and outer regions of 5 mm tissue constructs, averaging all samples with both 3 and 5 Mcells/ml EC density (Fig6B).Overall, these results demonstrate the 10:1 combination of ECs and MSCs resulted in the most homogeneous distribution of vascular structures within 5 mm thick tissue constructs, without significant differences compared to the other geometry. Moreover, collected data show a correlation between tissue construct

oxygenation and vascular network development, despite the role and mechanism of action of hypoxia in sprouting angiogenesis or cell differentiation is not totally clarified in the literature [35, 47-49]. Indeed, several molecules including reactive oxygen species (ROS) have been implicated with vessel formation through both hypoxia-inducible factor 1-alpha (HIFα)-independent and HIFα-dependent pathways [35]. It is likely that impaired vascular development within the inner core of 5 mm thick tissue constructs with 1:1 cell ratio can be due to the extremely low oxygen level (<1%), which induced EC death or migration towards external regions characterized by higher oxygen and/or nutrient availability. Particularly, an ideal line identifying regions with impaired vascular structures could be defined about 1 mm apart from the oxygenated outer faces of the hydrogel (FigS2A), in agreement with computational simulations highlighting a threshold distance close to 1 mm to identify the critical oxygen level for cell survival. Subsequently, ECs self assembled intomicrovessel-like structures within the outer regions and started sprouting towards the core of the gel following the oxygen gradient [50], despite not able to generate continuous, highly branched vascular networks compared to vascular trees obtained with other cell ratios within the same mask geometry. No dead cells were detected after 7 days within either external or internal regions (FigS2A and B). Nuclear fluorescent staining of tissue constructs characterized by 1:1 cell ratio within 5 mm thick masks was performed to clarify MSC localization. Interestingly, despite EC inhomogeneous distribution comparing inner and outer regions, MSCs well dispersed throughout the whole tissue construct (FigS3), thus demonstrating the effect of oxygen concentration was more pronounced on ECs rather than MSCs.
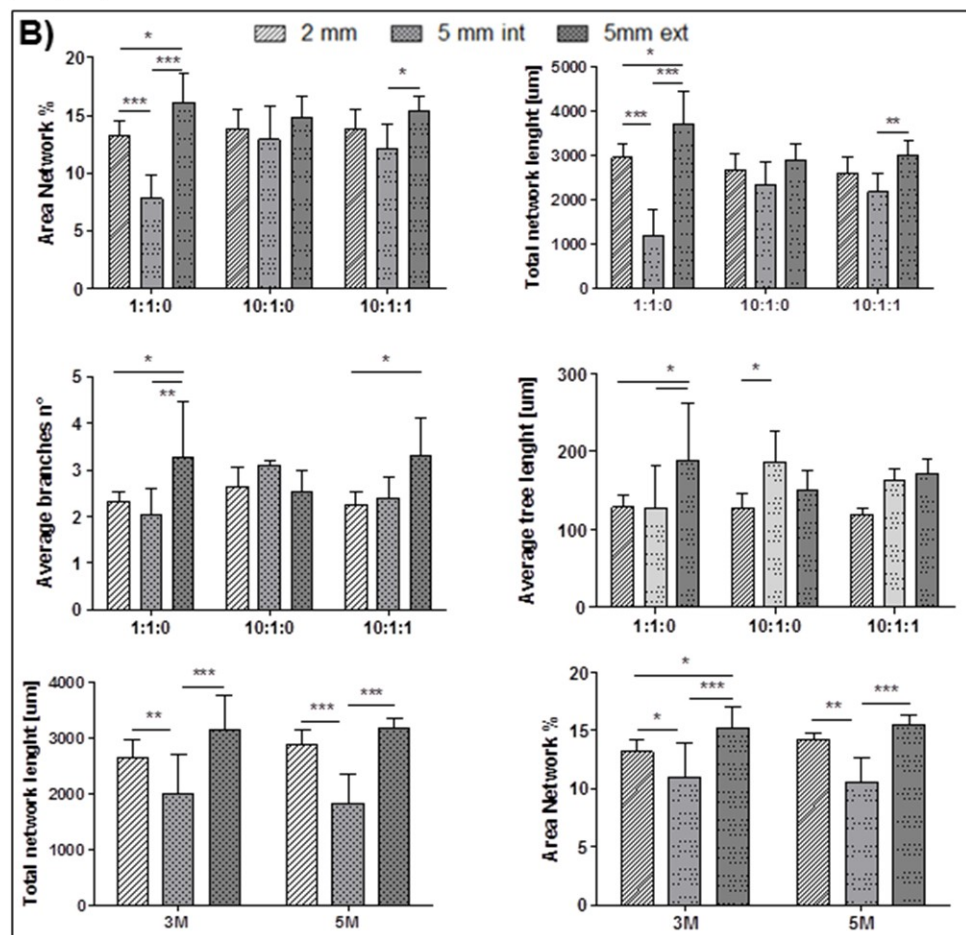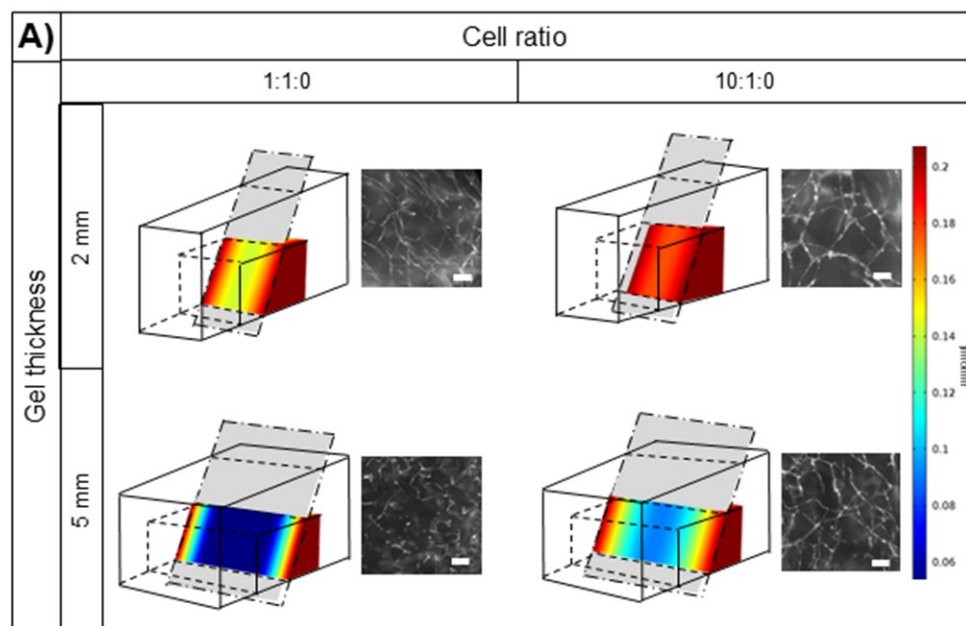
Fig6: Effect of gel thickness. Computational simulations were performed to quantify oxygen concentration within tissue constructs characterized by different thickness (2 mm vs. 5 mm) or EC/MSC cell ratios (1:1 vs. 10:1). Computational results were confirmed by experimental data showing a strong correlation between oxygen availability and generation of vascular networks. Scale bar: 50 µm (A). Quantification of vascular network differences comparing 2 mm thick tissue constructs and inner/outer regions of 5 mm thick gels. Quantified differences were dependent on EC/stromal cell ratio and EC density, showing a correlation between these two parameters and gel thickness (B).

4.3.3 Characterization of the optimal tissue through vascular and bone-specific markers

The optimal tissue constructs (3 Mcells/ml ECs, 10:1 EC/MSC cell ratio, osteo-medium, $2 \times 2 \times 5$ mm^3 masks and 2.5 mg/ml fibrin+collagen hydrogels) were characterized by means of immunofluorescent staining and qRT-PCR to analyze the expression of vascular, i.e. α-SMA by mural-like differentiated MSCs, and bone-specific markers, i.e. osteocalcin (BGLAP), osteonectin (SPARC) and osteopontin (SPP1) by MSCs. Immunofluorescent staining revealed the presence of α-SMA+ supportive mural-like cells concentrically wrapping around microvessel-like structures (Fig7A). Noteworthy, MSCs were homogeneously distributed within the composite gel and constitutively expressed bone-specific markers such as osteonectin (Fig7B) and osteopontin (Fig7C). Moreover, hollow lumens were clearly detected within the whole gel suggesting that these tissue engineered constructs could anastomose with a host vasculature (Fig7D and E). Genetic analyses demonstrated a significantly higher expression of α-SMA (2.72 fold increase), SPARC (1.93 fold increase) and BGLAP (5.19 fold increase) compared to control conditions characterized by the same parameter combination of the best vascular condition but supplemented with standard EGM-2 (Fig7F). However, no differences were detected regarding the expression of the late bone marker SPP1.This could be explained considering SPP1 appears to be related to more

mature bone tissues. Overall, these results demonstrate the presence of Ang-1 and osteo-medium positively influence MSC differentiation towards both a mural-like and a bone-like phenotype. Particularly, the positive role of Ang-1 in promoting vascular network stabilization and α-SMA expression by differentiated MSCs co-cultured with ECs confirms our previous results obtained through a microfluidic model [19]. At the same time, the role of osteo-medium as a positive regulator of MSC osteo-differentiation is in agreement with previous 3D co-culture studies [23, 32].

176
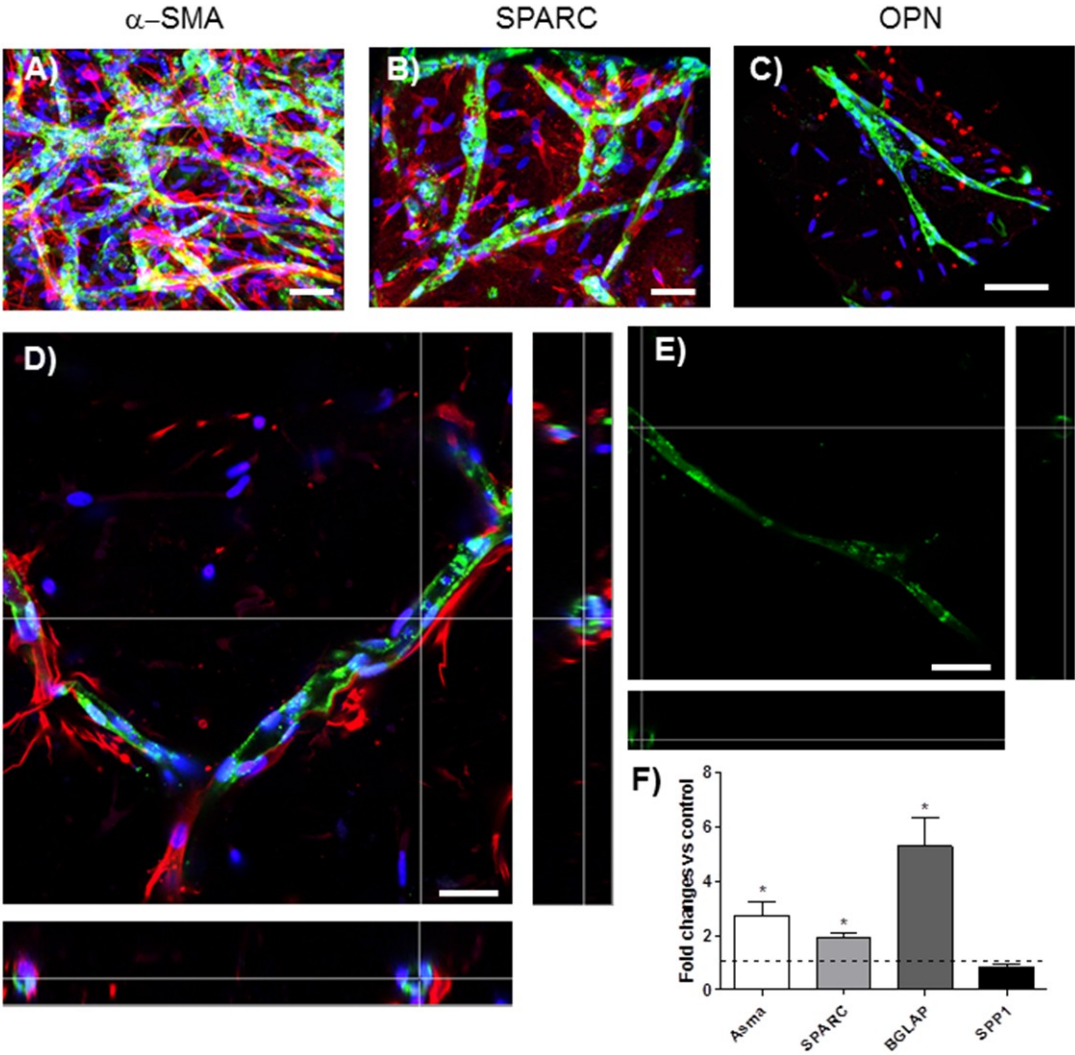
Fig7: Characterization of the vascularized bone-mimicking environment. Immunofluorescent staining of vascular (α-SMA (A), red) and bone-specific markers (SPARC (B), red; OPN (C), red) within the optimal tissue construct identified through the DoE approach (3 Mcells/ml ECs, 10:1 EC/MSC cell ratio, osteo-medium, 2×2×5 mm^3 masks and 2.5 mg/ml collagen+fibrin hydrogels). Hollow microvessels were clearly detected throughout the whole gel thickness (D and E). Green: ECs. Blue: nuclei (DAPI). qRT-PCR showed the expression of α-SMA and bone-specific markers as SPARC and BGLAP (osteocalcin) was significantly enhanced comparing the optimal experimental condition and control samples supplemented with standard EGM-2. No differences were quantified in terms of SPP1, which represents a late expressed bone-specific marker (F). Scale bars: 50 μm.

4.3.4 Extracellular matrix (ECM) remodeling

It is known that mechanical properties of the local microenvironment can influence cell function and differentiation [51]. Particularly, EC migration, elongation and assembly into tubular structures during microvascular network development are affected by matrix composition and stiffness [46]. On the other side ECs locally remodel the ECM, increasing the concentration of the collagen matrix around lumens or sprouts. In particular, it is thought that ECs generate traction forces which remodel the ECM, thus driving cell migration and promoting the generation of complex microvascular networks [52-54].

In the present study we coupled the analysis of microvascular network features (total network length and area, average branch number and average tree length) with the qualitative study of the ECM structure (Fig8 and 9A), specifically focusing on the differences between hydrogel compositions and on the dynamic evolution of the local microenvironment during in vitro culture. A multi-photon and confocal system was used to image GFP labeled ECs and detect the second harmonic generation (SHG), which allows to visualize the distribution of collagen within tissue constructs. Fibrin+collagen hydrogels were generally characterized at T_1 (day 1) by a dense network of isotropically distributed collagen microfibers (Fig8A). No clear differences were detected comparing inner and outer regions of 5

mm thick tissue constructs at this time point. At day 7 of culture (T_7) collagen microfibers appeared concentrated around vessels and between bifurcating structures (Fig8B). This is in agreement with Lee and colleagues, which showed increased collagen fiber density around sprouting microvessels and the perimeter of lumenal structures [54]. In addition, ECs promoted the development of holes and tunnels within the collagen matrix (Fig9B and C, white arrows), in agreement with Hanjaya-Putra and colleagues, which showed matrix remodeling close to invading ECs. These tunnels were generally located behind invading ECs and provided vascular guidance for the generation of microvessel structures.
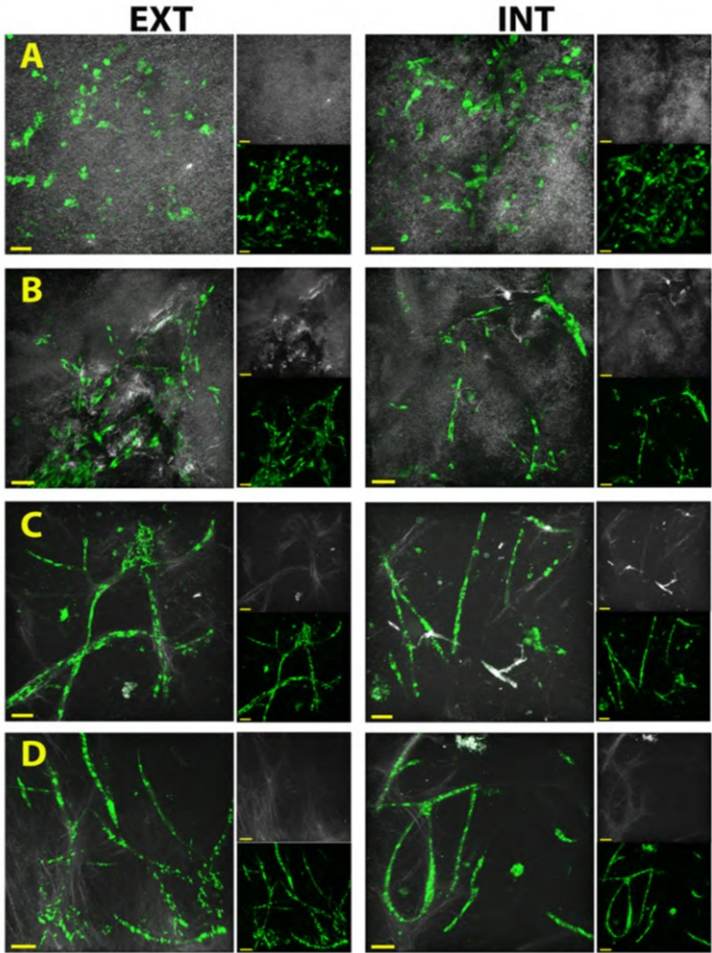
Fig8: Examples of SHG and GFP-HUVEC merged images depicting the organization of the matrix (gray) and of the microvasculature (green). Snapshots of the sample top-view were taken from the 3-D rendering of z-stacks. SHG and GFP images are also shown on the right inside of each sample. Dynamic evolution of the matrix structure between day 1 (A) and day 7 (B) within fibrin+collagen tissue constructs with 10:1 ECs/MSC cell ratio. Cells remodel the 3D matrix, with collagen microfibers concentrated around bifurcating vascular structures. Comparison between fibrin hydrogels characterized by 10:1 (C) and 1:1 (D) ECs/MSC cell ratio. Collagen microfibers can be visualized around the vessels after 7 days of culture, suggesting the presence of a basement membrane. More collagen microfibers are found in the 1:1 sample (D) than in the sample with 10:1 ECs/MSC cell ratio (C). EXT: peripheral regions, INT: central region of the gels. Scale bars: 50 μm.

Compared to fibrin+collagen tissue constructs, fibrin only hydrogels clearly highlighted the presence of cell secreted collagen deposits which seemed wrapping microvascular networks. This fact demonstrated that embedded cells were able to produce collagenous proteins typical of both ECM and basal membrane. In addition, it seems that collagen microfibers preferentially localized in the outer regions of 5 mm thick samples, characterized by higher vessel densities compared to the core regions (Fig8C and D). Then, it is possible that both ECs and MSCs close to microvessel structures secreted collagen (FigS4). Indeed, it is known that heterotypic direct contacts between ECs and MSCs induce MSC differentiation toward a mural-like phenotype [19] and that these supporting cells actively contribute to the deposition of a basal membrane [55]. On the other side, it seemed that MSCs alone (e.g. within the core region of 5 mm thick samples characterized by 1:1 ratio, as discussed in Section 3.2.3 and showed in FigS3) were less prone to secrete collagen. This is also evident from hydrogel regions where less microvascular structures were detected (Fig8C and D). Finally, it seems more collagen was present within 1:1 fibrin hydrogels compared to 10:1 fibrin samples, probably due to the presence of more MSCs (Fig8D).

Our model is able to recapitulate the process of ECM remodeling during vascular network development and suggest that the interaction between ECs and supporting mural cells can influence collagen secretion and organization.
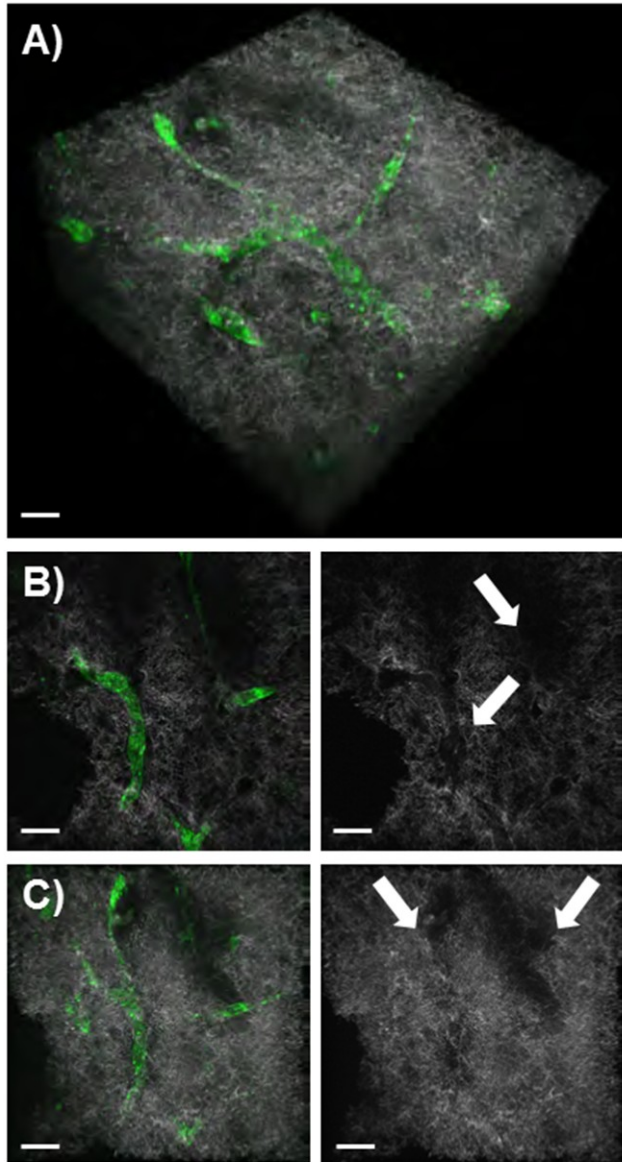
Fig9: ECM structure. ECs (green) embedded within a 3D matrix of collagen microfibers (SHG, white) (A). Cells remodel the local microenvironment generating tunnels and holes (white arrows) (B and C). Scale bars: 50 μm.

4.4 Conclusions

We have presented a reliable and reproducible model to develop human 3D vascular networks within organotypic environments under controlled and tunable experimental conditions. We have applied this model to analyze the synergistic effect of five different classes of parameters affecting vascular network development that were not previously combined in a single, comprehensive analysis. We have screened 35 experimental conditions and identified the combination of 3 Mcells/ml ECs, 10:1 EC/MSC cell ratio, osteo-medium, 2×2×5 mm^3 masks and 2.5 mg/ml fibrin(60%)+collagen(40%) hydrogels as the optimal protocol to generate bone-mimicking pre-vascularized matrices characterized by patent microvessels. Vascular networks were characterized by mural-like cells concentrically wrapping hollow microvessels, which were successfully embedded within a bone-mimicking matrix generated by bone marrow MSCs expressing bone-specific proteins, as confirmed by immunofluorescence and qRT-PCR.

The model is easy-to-use and could be employed by anyone with basic cell culture skills. We have demonstrated it is possible to isolate specific cellular populations and perform genetic analyses to characterize specific marker expression. Then, the present system could be employed to develop disease models, perform drug screening tests or investigate vascular biology issues.

Concluding, we have developed an effective, versatile and inexpensive tool that could be employed to design human organ-specific vascularized macroscale tissues, showing that a statistical, experimental approach can be used to identify the optimal experimental protocol while minimizing the number of tests to be performed.

References

[1] Jain RK. Molecular regulation of vessel maturation. Nat Med. 2003;9:685-93.

[2] Ausprunk DH, Folkman J. Migration and proliferation of endothelial cells in preformed and newly formed blood vessels during tumor angiogenesis. Microvasc Res. 1977;14:53-65.

[3] Kearney JB, Kappas NC, Ellerstrom C, DiPaola FW, Bautch VL. The VEGF receptor flt-1 (VEGFR-1) is a positive modulator of vascular sprout formation and branching morphogenesis. Blood. 2004;103:4527-35.

[4] Fan H, Zeng X, Wang X, Zhu R, Pei G. Efficacy of prevascularization for segmental bone defect repair using beta-tricalcium phosphate scaffold in rhesus monkey. Biomaterials. 2014;35:7407-15.

[5] Bersini S, Moretti M. 3D functional and perfusable microvascular networks for organotypic microfluidic models. J Mater Sci Mater Med. 2015;26:180.

[6] Chaffer CL, Weinberg RA. A perspective on cancer cell metastasis. Science. 2011;331:1559-64.

[7] Guidotti LG, Inverso D, Sironi L, Di Lucia P, Fioravanti J, Ganzer L, et al. Immunosurveillance of the liver by intravascular effector CD8(+) T cells. Cell. 2015;161:486-500.

[8] Shin Y, Han S, Jeon JS, Yamamoto K, Zervantonakis IK, Sudo R, et al. Microfluidic assay for simultaneous culture of multiple cell types on surfaces or within hydrogels. Nat Protoc. 2012;7:1247-59.

[9] Baranski JD, Chaturvedi RR, Stevens KR, Eyckmans J, Carvalho B, Solorzano RD, et al. Geometric control of vascular networks to enhance engineered tissue integration and function. Proc Natl Acad Sci U S A. 2013;110:7586-91.

[10] Carrion B, Kong YP, Kaigler D, Putnam AJ. Bone marrow-derived mesenchymal stem cells enhance angiogenesis via their alpha6beta1 integrin receptor. Exp Cell Res. 2013;319:2964-76.

[11] Chiu LL, Montgomery M, Liang Y, Liu H, Radisic M. Perfusable branching microvessel bed for vascularization of engineered tissues. Proc Natl Acad Sci U S A. 2012;109:E3414-23.

[12] Sekine H, Shimizu T, Sakaguchi K, Dobashi I, Wada M, Yamato M, et al. In vitro fabrication of functional three-dimensional tissues with perfusable blood vessels. Nat Commun. 2013;4:1399.

[13] Tanaka N, Ota H, Fukumori K, Miyake J, Yamato M, Okano T. Micro-patterned cell-sheets fabricated with stamping-force-controlled micro-contact printing. Biomaterials. 2014;35:9802-10.

[14] Leong MF, Toh JK, Du C, Narayanan K, Lu HF, Lim TC, et al. Patterned prevascularised tissue constructs by assembly of polyelectrolyte hydrogel fibres. Nat Commun. 2013;4:2353.

[15] Bertassoni LE, Cecconi M, Manoharan V, Nikkhah M, Hjortnaes J, Cristino AL, et al. Hydrogel bioprinted microchannel networks for vascularization of tissue engineering constructs. Lab Chip. 2014;14:2202-11.

[16] Miller JS, Stevens KR, Yang MT, Baker BM, Nguyen DH, Cohen DM, et al. Rapid casting of patterned vascular networks for perfusable engineered three-dimensional tissues. Nat Mater. 2012;11:768-74.

[17] Wang XY, Jin ZH, Gan BW, Lv SW, Xie M, Huang WH. Engineering interconnected 3D vascular networks in hydrogels using molded sodium alginate lattice as the sacrificial template. Lab Chip. 2014;14:2709-16.

[18] Carmeliet P. Mechanisms of angiogenesis and arteriogenesis. Nat Med. 2000;6:389-95.

[19] Jeon JS, Bersini S, Whisler JA, Chen MB, Dubini G, Charest JL, et al. Generation of 3D functional microvascular networks with human mesenchymal stem cells in microfluidic systems. Integr Biol (Camb). 2014;6:555-63.

[20] Chen YC, Lin RZ, Qi H, Yang Y, Bae H, Melero-Martin JM, et al. Functional Human Vascular Network Generated in Photocrosslinkable Gelatin Methacrylate Hydrogels. Adv Funct Mater. 2012;22:2027-39.

[21] Chen DY, Wei HJ, Lin KJ, Huang CC, Wang CC, Wu CT, et al. Three-dimensional cell aggregates composed of HUVECs and cbMSCs for therapeutic neovascularization in a mouse model of hindlimb ischemia. Biomaterials. 2013;34:1995-2004.

[22] Lee WY, Tsai HW, Chiang JH, Hwang SM, Chen DY, Hsu LW, et al. Core-shell cell bodies composed of human cbMSCs and HUVECs for functional vasculogenesis. Biomaterials. 2011;32:8446-55.

[23] Correia C, Grayson W, Eton R, Gimble JM, Sousa RA, Reis RL, et al. Human adipose-derived cells can serve as a single-cell source for the in vitro cultivation of vascularized bone grafts. J Tissue Eng Regen Med. 2012.

[24] Rao RR, Ceccarelli J, Vigen ML, Gudur M, Singh R, Deng CX, et al. Effects of hydroxyapatite on endothelial network formation in collagen/fibrin composite hydrogels in vitro and in vivo. Acta Biomater. 2014.

[25] Tan S, Fang JY, Yang Z, Nimni ME, Han B. The synergetic effect of hydrogel stiffness and growth factor on osteogenic differentiation. Biomaterials. 2014;35:5294-306.

[26] Kusumbe AP, Ramasamy SK, Adams RH. Coupling of angiogenesis and osteogenesis by a specific vessel subtype in bone. Nature. 2014;507:323-8.

[27] Ramasamy SK, Kusumbe AP, Wang L, Adams RH. Endothelial Notch activity promotes angiogenesis and osteogenesis in bone. Nature. 2014;507:376-80.

[28] Kolbe M, Xiang Z, Dohle E, Tonak M, Kirkpatrick CJ, Fuchs S. Paracrine effects influenced by cell culture medium and consequences on microvessel-like structures in cocultures of mesenchymal stem cells and outgrowth endothelial cells. Tissue Eng Part A. 2011;17:2199-212.

[29] Rao RR, Peterson AW, Ceccarelli J, Putnam AJ, Stegemann JP. Matrix composition regulates three-dimensional network formation by endothelial cells and mesenchymal stem cells in collagen/fibrin materials. Angiogenesis. 2012;15:253-64.

[30] Thein-Han W, Xu HH. Prevascularization of a gas-foaming macroporous calcium phosphate cement scaffold via coculture of human umbilical vein endothelial cells and osteoblasts. Tissue Eng Part A. 2013;19:1675-85.

[31] Weinandy S, Laffar S, Unger RE, Flanagan TC, Loesel R, Kirkpatrick CJ, et al. Biofunctionalized Microfiber-Assisted Formation of Intrinsic Three-Dimensional Capillary-Like Structures. Tissue Eng Part A. 2014;20:1858-69.

[32] Correia C, Grayson WL, Park M, Hutton D, Zhou B, Guo XE, et al. In vitro model of vascularized bone: synergizing vascular development and osteogenesis. PLoS One. 2011;6:e28352.

[33] Colom A, Galgoczy R, Almendros I, Xaubet A, Farre R, Alcaraz J. Oxygen diffusion and consumption in extracellular matrix gels: Implications for designing three-dimensional cultures. J Biomed Mater Res A. 2013.

[34] Zhao F, Pathi P, Grayson W, Xing Q, Locke BR, Ma T. Effects of oxygen transport on 3-d human mesenchymal stem cell metabolic activity in perfusion and static cultures: experiments and mathematical model. Biotechnol Prog. 2005;21:1269-80.

[35] Abaci HE, Truitt R, Tan S, Gerecht S. Unforeseen decreases in dissolved oxygen levels affect tube formation kinetics in collagen gels. Am J Physiol Cell Physiol. 2011;301:C431-40.

[36] Bersini S, Jeon JS, Dubini G, Arrigoni C, Chung S, Charest JL, et al. A microfluidic 3D in vitro model for specificity of breast cancer metastasis to bone. Biomaterials. 2014;35:2454-61.

[37] Chen XC, Zhou L, Gupta S, Civoli F. Implementation of design of experiments (DOE) in the development and validation of a cell-based bioassay for the detection of anti-drug neutralizing antibodies in human serum. J Immunol Methods. 2012;376:32-45.

[38] Arrigoni C, De Luca P, Gilardi M, Previdi S, Broggini M, Moretti M. Direct but not indirect co-culture with osteogenically differentiated human bone marrow

stromal cells increases RANKL/OPG ratio in human breast cancer cells generating bone metastases. Mol Cancer. 2014;13:238.

[39] Livak KJ, Schmittgen TD. Analysis of relative gene expression data using real-time quantitative PCR and the 2(-Delta Delta C(T)) Method. Methods. 2001;25:402-8.

[40] Jeon JS, Bersini S, Gilardi M, Dubini G, Charest JL, Moretti M, et al. Human 3D vascularized organotypic microfluidic assays to study breast cancer cell extravasation. Proc Natl Acad Sci U S A. 2015;112:214-9.

[41] Bersini S, Jeon JS, Moretti M, Kamm RD. In vitro models of the metastatic cascade: from local invasion to extravasation. Drug Discov Today. 2013.

[42] Chambers AF, Groom AC, MacDonald IC. Dissemination and growth of cancer cells in metastatic sites. Nat Rev Cancer. 2002;2:563-72.

[43] Carreau A, El Hafny-Rahbi B, Matejuk A, Grillon C, Kieda C. Why is the partial oxygen pressure of human tissues a crucial parameter? Small molecules and hypoxia. J Cell Mol Med. 2011;15:1239-53.

[44] Ma J, van den Beucken JJ, Yang F, Both SK, Cui FZ, Pan J, et al. Coculture of osteoblasts and endothelial cells: optimization of culture medium and cell ratio. Tissue Eng Part C Methods. 2011;17:349-57.

[45] McLeod C, Higgins J, Miroshnikova Y, Liu R, Garrett A, Sarang-Sieminski AL. Microscopic matrix remodeling precedes endothelial morphological changes during capillary morphogenesis. J Biomech Eng. 2013;135:71002.

[46] Sieminski AL, Hebbel RP, Gooch KJ. The relative magnitudes of endothelial force generation and matrix stiffness modulate capillary morphogenesis in vitro. Exp Cell Res. 2004;297:574-84.

[47] Abaci HE, Shen YI, Tan S, Gerecht S. Recapitulating physiological and pathological shear stress and oxygen to model vasculature in health and disease. Sci Rep. 2014;4:4951.

[48] Pattappa G, Heywood HK, de Bruijn JD, Lee DA. The metabolism of human mesenchymal stem cells during proliferation and differentiation. J Cell Physiol. 2011;226:2562-70.

[49] Semenza GL. Regulation of physiological responses to continuous and intermittent hypoxia by hypoxia-inducible factor 1. Exp Physiol. 2006;91:803-6.

[50] Helmlinger G, Endo M, Ferrara N, Hlatky L, Jain RK. Formation of endothelial cell networks. Nature. 2000;405:139-41.

[51] Engler AJ, Sen S, Sweeney HL, Discher DE. Matrix elasticity directs stem cell lineage specification. Cell. 2006;126:677-89.

[52] Kniazeva E, Weidling JW, Singh R, Botvinick EL, Digman MA, Gratton E, et al. Quantification of local matrix deformations and mechanical properties during capillary morphogenesis in 3D. Integr Biol (Camb). 2012;4:431-9.

[53] Korff T, Augustin HG. Tensional forces in fibrillar extracellular matrices control directional capillary sprouting. J Cell Sci. 1999;112 (Pt 19):3249-58.

[54] Lee PF, Yeh AT, Bayless KJ. Nonlinear optical microscopy reveals invading endothelial cells anisotropically alter three-dimensional collagen matrices. Exp Cell Res. 2009;315:396-410.

[55] Armulik A, Abramsson A, Betsholtz C. Endothelial/pericyte interactions. Circ Res. 2005;97:512-23.
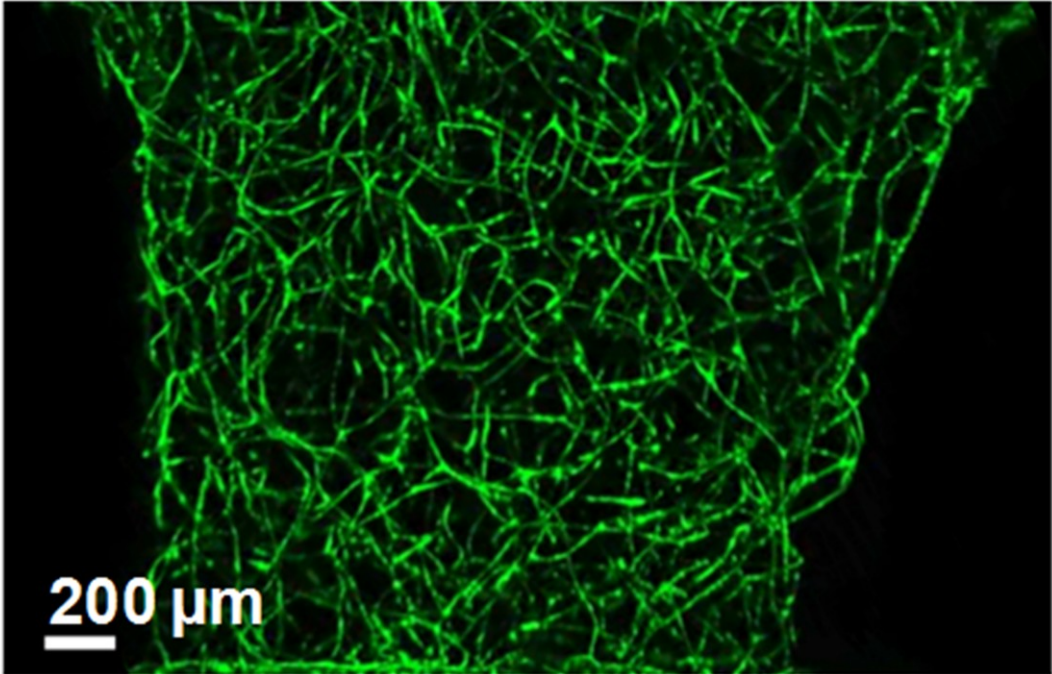
FigS1: 3D confocal reconstruction of a fully developed microvascular network. Z-stack series for 3D rendering were collected with a Leica TCS SP8 X equipped with super continuum excitation source and hybrid detectors.

Live&Dead
5 mm thickness – 1:1:0 cell ratio
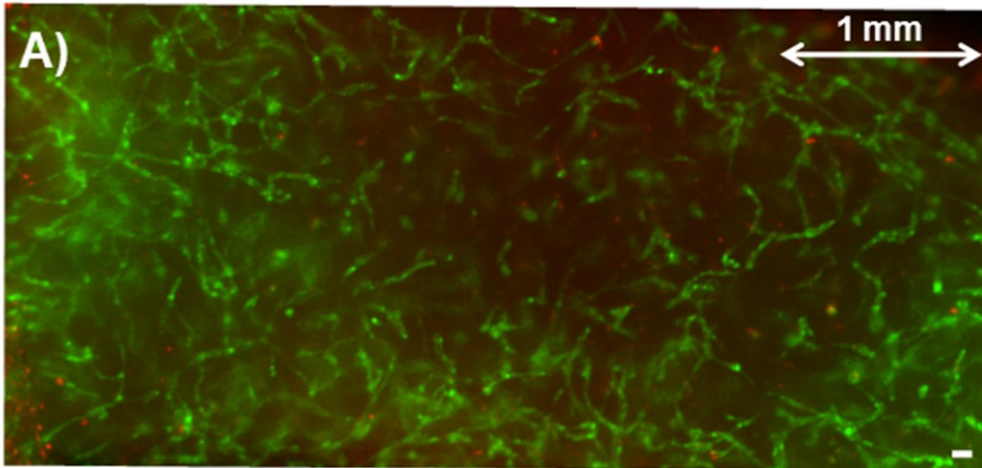
Live&Dead
5 mm thickness – 10:1:0 cell ratio
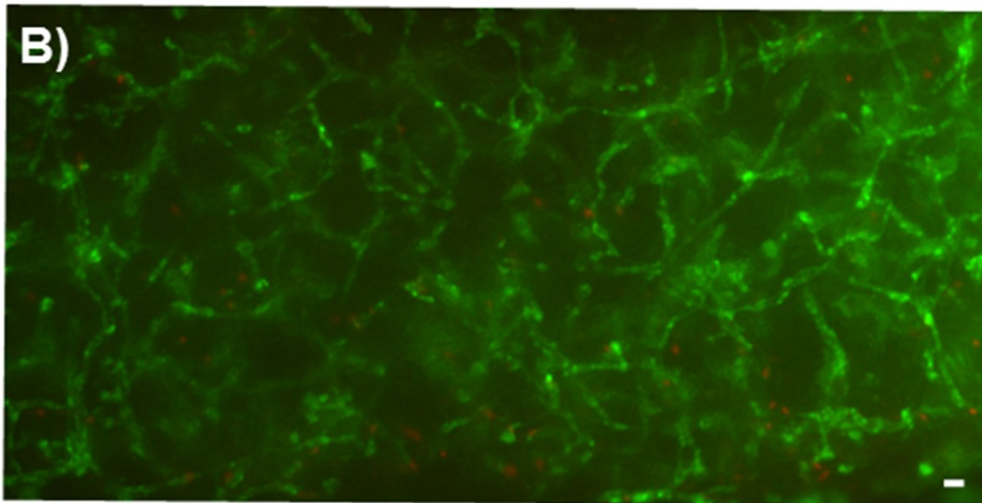
FigS2: Live&Dead assay showing a minimum number of dead cells was detected within 5 mm thick tissue constructs characterized by both 1:1 (A) and 10:1 (B) endothelial cell (EC)/MSCcell ratio. However, only 10:1 tissue constructs (B) were characterized by homogeneous EC distribution within the gel. Green: ECs. Red: dying cells stained with propidium iodide. Scale bars: 100 μm.

DAPI staining
5 mm thickness – 1:1 cell ratio
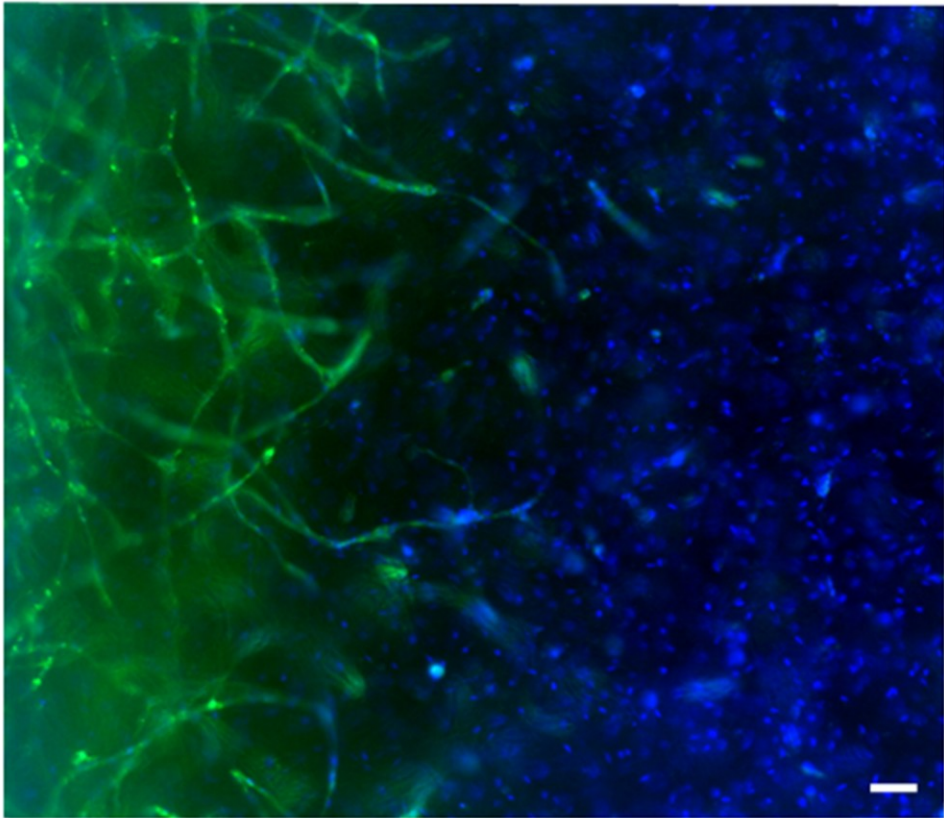
FigS3: Nuclear staining of 5 mm thick tissue constructs characterized by 1:1 endothelial cell (EC)/MSC cell ratio showing MSCs but not ECs were homogeneously distributed within the matrix. Green: ECs. Blue: nuclei (DAPI). Scale bar: 100 μm.

| SHG | EC-GFP | MERGED |
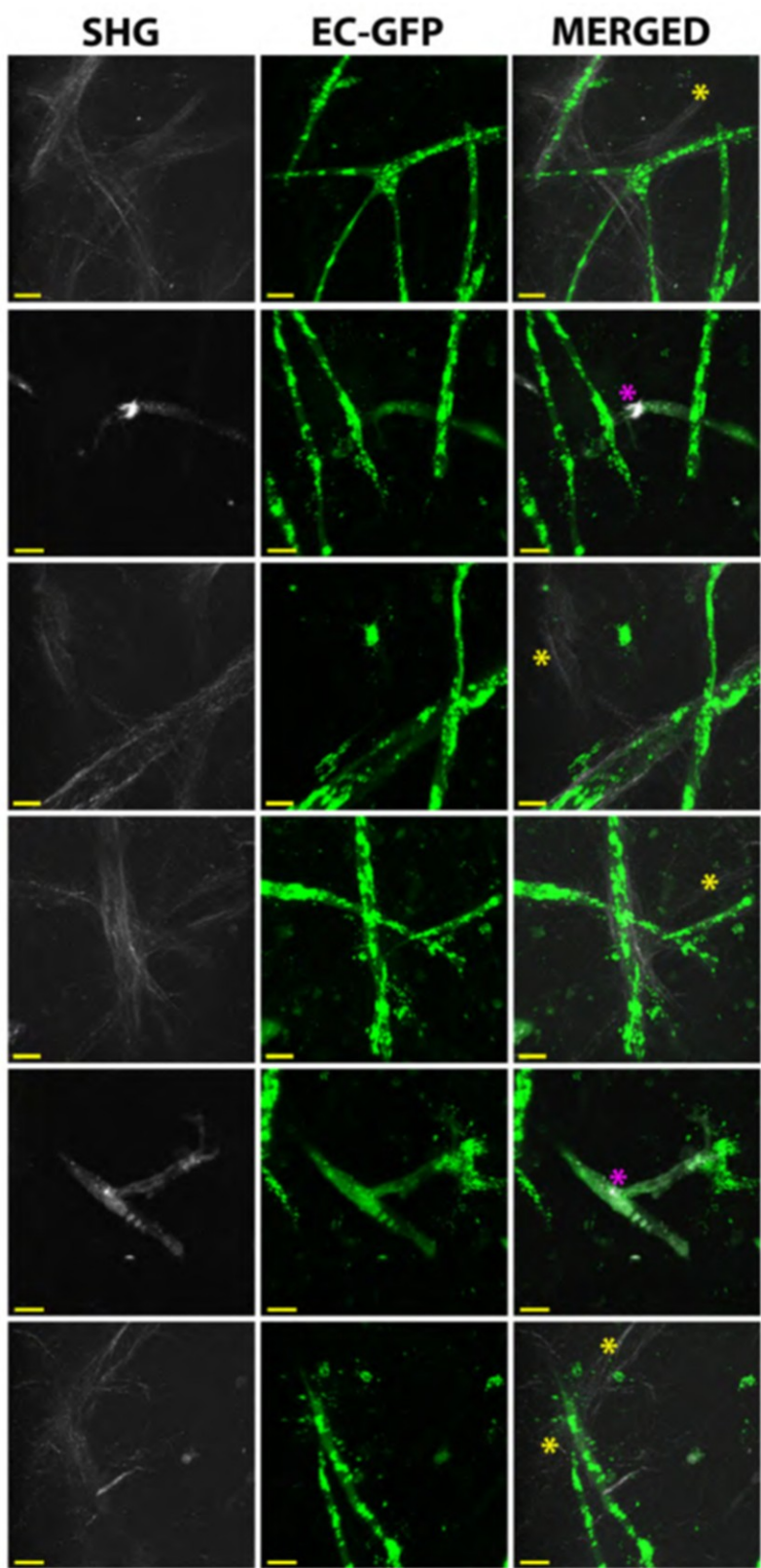
Fig. S4. Zoomed regions taken from samples shown in Fig. 8 illustrating the development of extracellular collagen microfibers. Very strong SHG signals were occasionally detected (pink asterisks) surrounding microvessels. Collagen microfibers were also detected in areas deprived of microvessels (yellow asterisks), an indication they might have been produced by the unlabeled stromal cells. Scale bars: 30 μm.

Movie S1. 3D confocal reconstruction of a hollow microvessel within the bone-mimicking matrix.

List of the most used abbreviations	
ECs	Endothelial cells
MSCs	Mesenchymal stem cells
OD MSCs	Osteo differentiated mesenchymal stem cells
DoE	Design of experiment
SHG	Second harmonic generation
n.l.	Network length
n.a.	Network area

Chapter 5

A 3D vascularized bone remodeling model combining osteoblasts and osteoclasts in a CaP nanoparticle-enriched matrix

From: M. Bongio, S. Lopa, M. Gilardi, S. Bersini, M. Moretti

5.1 Introduction

Bone remodeling is a dynamic process that relies on the delicate balance between bone resorption and formation [1, 2] and it is closely associated with angiogenesis [3]. In this scenario, osteoclasts, which are phagocytic multinucleated cells derived from circulating mononuclear cells [4], are capable of dissolving the minerals and breaking down the matrix, thereby leaving space for osteoblasts to deposit new bone, and to endothelial progenitors to form new blood vessels [5]. Conversely, blood vessel growth not only establishes local circulation in the newly synthesized bone, providing access to nutrients and oxygen, but also directly promotes bone formation [6]. In this context, mural cells, which have been shown to differentiate from bone marrow mesenchymal stem cells (BMSCs) upon the heterotypic contact with endothelial cells [7], play a key role in the regulation of vascular formation,

stabilization, remodeling, and function [8]. These premises indicate that endothelial cells, mural cells, osteoclasts, osteoblasts and their progenitors are functionally linked [9].

Because of the complexity of bone biology, owing to intricate heterogeneous cellular interactions, the study of bone remodeling in an in vivo setting still remains challenging and limits the predictive value regarding physiological and pathological processes [10]. A variety of in vitro models, recapitulating the essential properties of bone, have been developed by embedding human-derived cells in 3D systems, including hydrogels [7, 11-13], ceramics [14, 15] and composites [16, 17]. Nevertheless, very few studies have attempted to establish 3D vascularized bone models using more than two cell types for the study of cellular interactions in a bone-mimicking environment. Recently, we have developed in our laboratory different 3D MiniTissue models based on collagen and fibrin hydrogel constructs at the mm-scale [13, 18]. Specifically, we have shown that collagen/fibrin (Col/Fib) hydrogels are permissive to endothelial network formation when human umbilical vein endothelial cells (HUVECs) are cocultured with human BMSCs, serving both as vessel-stabilizing mural cells and osteo-differentiated cells [13]. The degree of microvascular network development resulted to be reliant on cell ratio, construct geometry, oxygen concentration within the constructs, and type of culture medium. Specifically, the coculture of HUVECs and BMSCs at a 10:1 ratio and the triculture of HUVECs, BMSCs, and osteo-differentiated BMSCs at a 10:1:1 ratio generated an homogeneous microvascular network in Col/Fib hydrogels of 2x2x5 mm^3, owing to an oxygen concentration above the critical threshold throughout the entire construct, as demonstrated by computational simulations.

Hydroxyapatite (HA) is the main constituent (~70% weight) of the mineral part of bone. This inorganic material, whose chemical formula is $Ca_{10}(PO_4)_6(OH)_2$, is mainly composed of calcium phosphate (CaP) and is continuously deposited and degraded by osteoblasts and osteoclasts, respectively, thereby modulating the

density, regeneration, and degradation of bones [19]. Several studies in the biomedical field have exploited HA as biomaterial and coating, thanks to its excellent biocompatibility and bioactivity [20]. The recently developed interest for nanotechnology has received a considerable attention for nanohydroxyapatite, which presents crystals in the range of 1 to 100 nm [21]. The nanodimensional and nanocrystalline forms of HA considerably increases the surface area (> 100 m^2/g) compared to their micron-sized counterparts (2-5 m^2/g) [22] and provide a better capability for the specific interactions with proteins [23, 24]. Previously, it has been shown that CaP nanoparticles (CaPn), homogeneously dispersed within synthetic polymer hydrogels, remarkably stimulated the osteogenic differentiation of encapsulated BMSCs compared to their plain analogs [25]. This phenomenon was attributed to the increase of matrix stiffness, which is known to guide the osteogenic lineage commitment of BMSCs [26, 27], and to the high specific surface area of CaPn that provided abundant nucleation sites for homologous CaP-on-CaP deposition, thereby accelerating the cellular mineralization. Also, it was reported that nano-sized HA has an inductive effect in the differentiation of the osteoclastic precursors [28]. Indeed, HA nanoparticles are able to up-regulate some intracellular signaling pathways involved in the osteoclastic process, including MEK, MAPKK, and JNK pathways [28]. Additionally, HA has been proved to have angiogenic potential. Namely, He et al. demonstrated that HA-containing composite scaffolds seeded with MSCs enhanced the expression of pro-angiogenic genes and the secretion of vascular endothelial growth factor (VEGF) to a significantly higher degree than HA-free scaffolds, leading to a more robust angiogenesis and bone formation [29, 30].

The research reported here aimed to develop an in vitro vascularized 3D MiniTissue bone remodeling model. Specifically, four cell types, including human umbilical endothelial cells (HUVECs), human BMSCs, and precursors of human osteoblasts (OBs) and osteoclasts (OCs), were embedded in Col/Fib hydrogels enriched with CaPn, closely resembling both the composition and dimensions of

the mineral phase of native bone. We first independently assessed angiogenesis with HUVECs and BMSCs, osteogenesis with OBs, and osteoclastogenesis with OCs on these Col/Fib hydrogels, either plain or enriched with CaPn. Eventually, we evaluated microvascular network formation and cell differentiation in tetraculture of these four cell types.
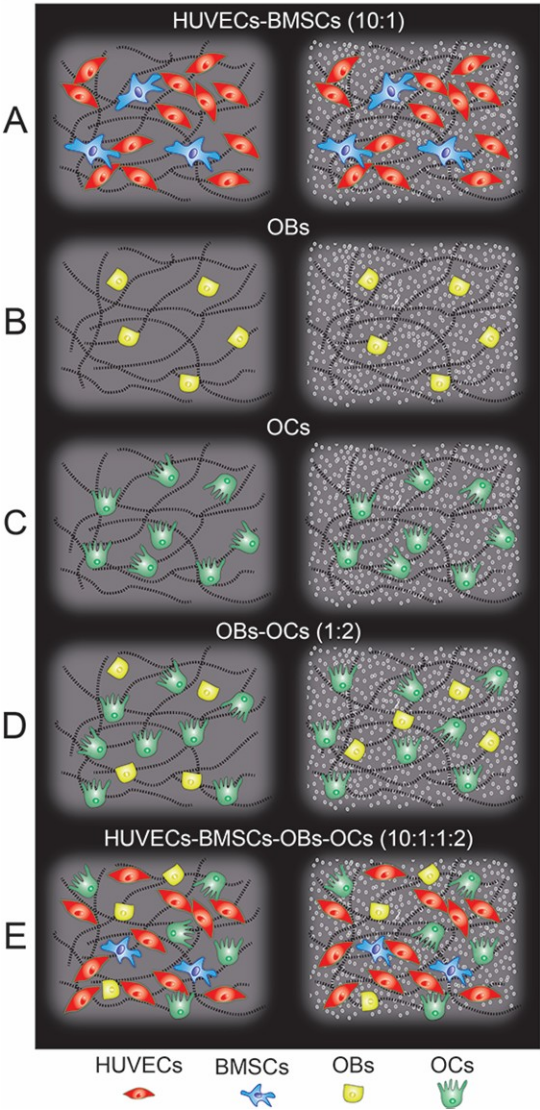
Fig1: Schematic drawing of cell culture combinations, including coculture of HUVECs and BMSCs (A), OBs and OCs both in monoculture (B and C, respectively) and coculture (D), and

tetraculture of HUVECs, BMSCs, OBs, and OCs (E) embedded in in plain and CaPn-enriched Col/Fib hydrogels. The ratio between cocultured cell types is indicated in brackets.

5.2 Materials & methods

5.2.1 Experimental overview

In the present study, we followed a step-by-step process for the development of a 3D vascularized bone remodeling model. First, we evaluated the potential cytotoxicity of Col/Fib hydrogels containing different concentrations of CaPn (0-10 mg/mL). Second, we identified the maximum concentration of CaPn able to not compromise microvessel formation in 3D scaffolds. To this end, HUVECs and BMSCs were embedded in Col/Fib hydrogels and vascular parameters were evaluated. Third, four culture conditions, including (1) coculture of BMSCs and HUVECs (Fig1A), (2) monoculture of OBs (Fig1B), (3) monoculture of OCs (Fig1C), and (4) coculture of OBs and OCs (Fig1D) were performed to assess cell viability and differentiation in both plain and CaPn-enriched Col/Fib hydrogels. Finally, all these cell populations were embedded in Col/Fib hydrogel composites (Fig1B), generating a tetraculture to study their interplay.

5.2.2 Synthesis of CaP nanoparticles

A stable suspension of homogeneously dispersed apatite nanoparticles at a concentration of 300 mg/mL, was prepared using a conventional wet-chemical precipitation method [25], according to the following reaction between calcium hydroxide and ortho-phosphoric acid (Ca/P=1.67):

$$5Ca(OH)_2 + 3H_3PO_4 \rightarrow Ca_5(PO_4)_3(OH) + 9H_2O$$
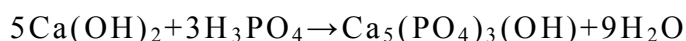
Briefly, 25 mL H_3PO_4 solution (3.56 M, Acros) was added dropwise at a rate of about 1-2 drops per second into 25 mL $Ca(OH)_2$ (5.92 M, Acros), under continuous stirring at 60 °C for 15-18 h. After aging, CaP nanoparticles were washed three times through centrifugation (2800 g, 2 min) and resuspension with deionized water at a concentration of 100 mg/mL. The stock CaPn suspension was then sterilized in a steel autoclave at 120°C during 20 minutes and the pH was adjusted to 7.4.

The resulting CaPn have been fully characterized in previous studies [25, 31, 32]. Specifically, X-ray diffraction (XRD) analysis showed that the prepared CaPn are crystalline, as revealed by sharp reflection peaks for apatite at 25.9° and 31.8°. Complementing Fourier-transform infrared spectroscopy (ATR–FTIR) confirmed the presence of apatitic phosphate by pronounced phosphate absorption peaks typical for apatitic CaP at 563, 600, 963 and 1027 cm^{-1}, and a hydroxyl absorption peak at 628 cm^{-1}. Transmission electron microscopy (TEM) images revealed needle-shaped CaPn with average diameter and length of 18±7 nm and 76±23 nm, respectively.

5.2.3 Cell isolation and pre-culture

5.2.3.1 Human bone marrow mesenchymal stem cells (BMSCs)

BMSCs, isolated from the bone marrow aspirate of 3 patients (2 males, 1 female, age range 45-66 years, average age 55±10 years) undergoing hip surgery after informed consent, were plated in complete medium composed of α-minimal essential medium (α-MEM, Life Technologies), 10% fetal bovine serum (FBS, Hyclone), 2 mM L-glutamine, 1 mM sodium pyruvate, 10 mM HEPES, 1 U/mL penicillin and 1 µg/mL streptomycin (all from Life Technologies), and 5 ng/mL b-FGF (Peprotech). Non-adherent cells were removed with subsequent medium change, and medium was refreshed every three days. At passage 3, cells were

stored in liquid nitrogen. BMSCs were either used undifferentiated, to support HUVECs in vessel formation (Fig1A and 1E), or differentiated into OBs (Fig1B, 1D, and 1E). When needed undifferentiated, cells were thawed and expanded for one additional passage in complete medium. When needed differentiated, BMSCs were thawed and pre-cultured for 7 days in osteoblastic medium consisting of DMEM (4.5 g/l glucose, Life Technologies), 10% FBS, 2 mM L-glutamine, 1 mM sodium pyruvate, 10 mM HEPES, 1 U/mL penicillin and 1 μg/mL streptomycin supplemented with 0.01 μM dexamethasone, 10 mM β-glycerophosphate, 10 nM cholecalciferol, 150 μM L-ascorbic acid-2-phosphate (all from Sigma Aldrich) [33, 34].

5.2.3.2 *Human umbilical vein endothelial cells (HUVECs)*

Red fluorescent protein (RFP) expressing HUVECs (Angio-Proteomie) were cultured in endothelial growth medium (EGM-2, Lonza) and used at passage 6.

5.2.3.3 *Peripheral blood mononuclear cells (PBMCs)*

PBMCs were isolated from human peripheral blood, obtained from 5 healthy donors (3 males, 2 females, age range 28-34 years, average age 30±3 years) after informed consent, by gradient centrifugation (Ficoll-Hypaque, GE Healthcare) at 900 g for 30 min. Then, PBMCs were pooled and washed twice with PBS (Life Technologies) centrifuging at 760 g for 10 min. PBMCs were plated (6×10^6 /cm^2) in α-MEM containing 20% FBS and 25 ng/mL M-CSF (Macrophage Colony-Stimulating Factor, Life Technologies). The following day, medium was refreshed to discard non-adherent cells. To obtain osteoclast precursor cells, adherent PBMCs were further cultured in α-MEM supplemented with 10% FBS, 2 mM glutamine, 1 mM sodium pyruvate, 10 mM HEPES, 1 U/mL penicillin and 1

µg/mL streptomycin, 25 ng/mL M-CSF, and 50 ng/mL RANK-L (Receptor Activator of NFKB-Ligand, Life Technologies) for 6 days.

5.2.4 Synthesis and cytotoxicity of cell-free hydrogels enriched with different concentrations of CaPn

Collagen type I and fibrinogen were combined at a mass ratio of 40/60 (final concentration 2.5 mg/mL), as previously described [13]. Collagen type 1 from rat tail (4 mg/mL) was prepared according to the manufacturer's instructions (CORNING®) and was enriched with the stock CaPn suspension to obtain the following concentrations of CaPn in the final gel volume: 0, 1.25, 2.5, 5, 7.5, and 10 mg/mL.

Human fibrinogen (Sigma Aldrich) was dissolved in PBS to a concentration of 6 mg/mL, filtered (0.2 µm) and mixed 1:1 with 4 mg/mL collagen type I either plain or enriched with CaPn. Subsequently, human thrombin (500 IU/mL, Tisseel®, Baxter) was diluted to 4 IU/mL in EGM-2, and mixed 1:1 with the collagen/fibrinogen solution. 150 µl of the polymer mixtures were quickly injected in a 96-well plates and incubated at 37 ºC for approximately 15 min to obtain hydrogel polymerization.

To evaluate the potential cytotoxicity of CaPn-enriched Col/Fib hydrogels, the MTT (3-(4,5-Dimethylthiazol-2-yl)-2,5-Diphenyltetrazolium Bromide, Sigma Aldrich) assay was performed. Briefly, BMSCs were seeded in 24-well plates (6 x 10^3/cm^2), where newly formed hydrogels were transferred the day after. 1 mL of complete medium was added to each well and changed every three days. At day 1 and 7, MTT working solution (600 µL, 0.5 mg/mL MTT in DMEM) was added to each well and the plates were incubated in the dark for 3 h at 37°C. Then, the MTT working solution was removed and 600 µL extracting solution (10% HCl 1N, 90% isopropanol) were added to each well. The absorbance was measured at 570 nm

using a VictorX3 plate reader (Perkin Elmer). Plain Col/Fib hydrogels were used as controls. All the experiments were carried out in triplicates.

5.2.5 Fabrication of cell-laden plain and CaPn-enriched Col/Fib hydrogels

At the day of the experiment, HUVECs, BMSCs and OBs were enzymatically detached with a trypsin-EDTA solution (Life Technologies). Differently, OCs were mechanically detached from the culture plates by gentle scraping in the presence of the enzyme-free Gibco® Cell Dissociation Buffer (Life Technologies).

To compare plain and CaPn-enriched Col/Fib hydrogels, two different collagen/fibrinogen solutions were prepared as described above: one CaPn-free solution for plain hydrogels and one solution enriched with CaPn to obtain a final concentration of 5 mg/mL CaPn in the hydrogel. Cell-laden Col/Fib hydrogels were prepared by resuspending cells in thrombin solution (4 IU/mL) and mixing 1:1 the cell suspension with either the plain or the CaPn-enriched collagen/fibrinogen solution. 32 µL of cell-laden polymer mixtures were quickly injected in custom U-shaped poly(methyl methacrylate) (PMMA) masks mounted on a glass slide [13] and incubated for 15 min at room temperature within humid chambers to allow hydrogel polymerization.

For the HUVEC-BMSC coculture, cells were mixed at a 10:1 ratio with a total final concentration of 2.475×10^6/mL (Fig1A), based on our recent study showing a superior microvascular network formation in Col/Fib constructs seeded with this cell ratio compared to constructs seeded with a number of BMSCs equal to the number of HUVECs (1:1 ratio) [13]. For the OB and OC monocultures, the final concentrations of OBs and OCs in the hydrogels were 0.225×10^6/mL and 0.450×10^6/mL, respectively (Fig1B and C). The same concentrations of OBs and OCs were used to prepare the OB-OC cocultures at a 1:2 ratio, resulting in a total concentration of 0.675×10^6 cells/mL (Fig1D). For the tetraculture systems,

HUVECs (2.25×10^6/mL), BMSCs (0.225×10^6/mL), OBs (0.225×10^6/mL), and OCs (0.450×10^6/mL) were combined at a 10:1:1:2 ratio (Fig1E).

Cell-laden Col/Fib hydrogels in PMMA masks were then transferred to 24-well plates and cultured in 1 mL EGM-2. At day 3, medium was replaced with EGM-2 and osteoblastic-osteoclastic medium (OB-OCM) at a ratio 1:1. OB-OCM was obtained by supplementing the osteoblastic medium with 25 ng/mL M-CSF and 50 ng/mL RANK-L. Hydrogels were cultured for 10 days and medium was changed two times a week. In addition to cell-laden hydrogels, cell-free hydrogels were prepared and cultured in EGM-2/OB-OCM. These samples were subjected to the same analyses in order to be used as control value (blank).

5.2.6 Characterization of microvessel formation

Microvascular network formation in Col/Fib hydrogels loaded with RFP-HUVECs was daily monitored through a fluorescence microscope (Olympus IX71). At day 10, samples were fixed for 1 hour in 4% neutral-buffered formalin and rinsed three times in PBS for confocal imaging (Leica TCS-SP5, Leica Microsystems). Two x-y-z fields at 10X magnification were acquired from 3 samples for each condition. Vascularization was quantified following a previously validated protocol [13]. Briefly, 3D projection images were filtered, converted to a binary format, and skeletonized using the Fiji image analysis software. Data were filtered applying a 25 μm threshold value to remove artifacts. Microvascular networks were analyzed in terms of average branch length and total network length, which was calculated as the product of branch number and average branch length.

5.2.7 Cell viability

The viability of OBs and OCs within monoculture hydrogel systems (Fig 1B and C) was determined at day 3 and 10, using LIVE/DEAD

Viability/Cytotoxicity Kit (Molecular Probes). For each condition, 3 samples were rinsed three times in PBS prior to incubation for 15 min at 37°C with 2 mM calcein-AM and 4 mM ethidium homodimer in PBS, which stain live and dead cells, respectively. After incubation, hydrogels were washed in PBS prior to evaluation through fluorescent microscopy.

5.2.8 Sample collection

Cell-free and cell-laden Col/Fib hydrogels, either plain or CaPn-enriched, were cultured for 3 or 10 days and then collected for subsequent analyses. Samples were rinsed in PBS, dissolved in 200 μL 0.1% Triton X-100 in aqueous solution for 1 h at 4°C under agitation, and then frozen at -80°C until analysis. Lysates prepared from samples cultured for 3 and 10 days were used for the quantification of DNA, ALP and/or TRAP activity depending on the experimental group.

5.2.9 DNA content

At the time of analyses, samples were subjected to three freeze-thaw cycles. DNA content was quantified using CyQuant kit (Invitrogen) according to the manufacturer's instructions. Briefly, samples were incubated with CyQuant working solution for 10 min at room temperature in the dark. The excitation of the solution at 480 nm and fluorescence measurement at 520 nm was performed using a VictorX3 plate reader. The values of cell-free hydrogels were subtracted from the values measured for the corresponding cell-laden hydrogels. For each experimental condition, 3 replicates per time point were analyzed.

5.2.10 Characterization of the osteoblastic cell response

The osteoblastic cell response within Col/Fib hydrogels was assessed through the quantification of Alkaline Phosphatase (ALP) enzymatic activity and cell-mediated mineralization.

5.2.10.1 ALP activity

ALP activity was determined in all OB-laden hydrogel systems by enzymatic assay. Briefly, sample lysates were incubated at 37°C for 1 hour with 1 mM p-nitrophenylphosphate (pNPP) in 100 mM diethanolamine and 0.5 mM $MgCl_2$ (pH 10.5) (all from Sigma Aldrich). A standard curve was prepared from solutions of 4-nitrophenol (range: 0-200 μM). Enzymatic reaction was stopped by adding 1.0 N NaOH. The absorbance was read at 405 nm using a VictorX3 plate reader. The absorbance measured for cell-laden hydrogels was adjusted with cell-free hydrogels and ALP activity values were normalized to the amount of DNA measured in the OB monoculture. For each experimental condition, 3 replicates per time point were analyzed.

5.2.10.2 Mineralization

Calcium quantification was performed in all OB-laden hydrogel systems. For each condition and time point, 3 samples were lysed in 200 μL 0.1% Triton X-100. Then, 200 μL 1.0 N acetic acid were added and samples were incubated on a shaker table overnight to dissolve mineral deposits. The standards (range: 0-100 μg/mL) were prepared using a $CaCl_2$ stock solution. 10 μL samples or standards were incubated with 300 μL of working solution containing o-cresolphtalein complexone (Sigma Aldrich). The absorbance was read at 570 nm using a

VictorX3 plate reader. To measure the calcium produced by cells, the values of cell-free hydrogels were subtracted from the values of the corresponding cell-laden hydrogels at each time point. Based on this, positive values are indicative of cell-mediated mineralization.

5.2.11 Characterization of the osteoclastic cell response

The osteoclastic cell response within Col/Fib hydrogels was determined through the quantification of Tartrate-Resistant Acid Phosphatase (TRAP) enzymatic activity and cell-mediated phosphate release.

5.2.11.1 TRAP activity

TRAP activity was measured in all OC-laden hydrogel systems based on a previously described protocol with minor modifications [35]. Briefly, sample lysates were incubated at 37°C for 1 hour in 100 mM Na acetate buffer containing 50 mM Na tartrate and 5 mM pNPP (pH 6.1) (all from Sigma Aldrich). A standard curve was prepared from solutions of 4-nitrophenol (range: 0-200 µM). The enzymatic reaction was stopped by adding 3.0 N NaOH and the absorbance was read at 405 nm using a VictorX3 plate reader. The absorbance measured for cell-laden hydrogels was adjusted with cell-free hydrogels, and TRAP activity values were normalized to the amount of DNA measured in the OC monoculture. For each experimental condition, 3 replicates per time point were analyzed.

Phosphate release in the culture medium

Prior to each medium refresh, the media were collected, centrifuged at 400 g for 5 min and the resulting supernatant were stored at -20°C. To evaluate the OC-mediated release of phosphate into the medium, the medium samples were thawed and assessed for phosphate levels using a colorimetric assay kit (Biovision Inc.). A standard curve was prepared using a phosphate standard (range: 0-5 nmol) and the

assay was performed according to the manufacturer's instructions. Specifically, the phosphate content was measured from 1 µl of medium. The absorbance was read at 650 nm using a VictorX3 plate reader and interpolated on the standard curve. The obtained values were then normalized to 1 ml to calculate the total phosphate content. To quantify the cell-mediated phosphate release, the values measured in the culture medium of cell-free hydrogels were subtracted from the values of the corresponding cell-laden hydrogels at each time point. Based on this, negative values reported for cell-laden hydrogels indicate that phosphate was incorporated in the hydrogels, conversely positive values are indicative of cell-mediated phosphate release.

5.2.12 Histological and immunofluorescent staining

After 3 and 10 days of culture, hydrogels were fixed for 1 hour in 4% neutral buffered formalin, washed three times in PBS and then processed either for histology or immunofluorescent staining.

Histological samples were dehydrated through a graded series of ethanol and embedded in paraffin. 5 µm-thick sections were mounted on glass slides and stained for hematoxylin and eosin (H&E) to evaluate the cellular morphology and matrix structure. Histological sections were analyzed using an Olympus IX71 microscope. Immunofluorescence analysis was performed to assess the composition of the tetraculture system using antibodies against: human Secreted Protein Acidic and Rich in Cysteine (SPARC, rabbit anti-human, Santa Cruz, 1:60), human Receptor Activator of NFKB (RANK, mouse anti-human, Santa Cruz, 1:100) and human alpha-Smooth Muscle Actin (α-SMA, mouse anti-human, Abcam, 1:60). Fixed samples were permeabilized with 0.1% Triton X-100 for 10 min and treated with 4% bovine serum albumin (Sigma Aldrich) for 3 hours. Primary antibodies diluted in PBS were incubated at 4°C for 24 hours. Then, samples were washed twice in PBS. Secondary antibodies (FITC goat anti-mouse,

Ancell, 1:60; Far-red goat anti-rabbit, Alexa Fluor® 647, Invitrogen, 1:200) and 300 nM 4'6-Diamidino-2-Phenylindole (DAPI) diluted in PBS were added to the samples and incubated at 4°C overnight. Sections were analyzed using a confocal microscope (Leica TCS-SP5).

5.2.13 Statistical analyses

Two-Way Analysis of Variance (ANOVA), followed by Bonferroni post-hoc test, was performed with Prism Graph Pad software to analyze differences between multiple groups at different time points. Differences were considered significant for $p<0.05$ (*), $p<0.01$ (**), and $p<0.005$ (***). Results are presented as mean±standard deviation. All the quantifications were analyzed considering at least 3 samples for each experimental condition per time point. A total number of 170 samples were prepared and analyzed in the entire study.

5.3 Results

5.3.1 Cytotoxicity of CaPn-enriched hydrogels

Plated BMSCs were exposed to Col/Fib hydrogels containing different concentration of CaPn (from 0 to 10 mg/mL) for 7 days and cytotoxicity was determined with MTT assay (Fig2A). At day 1, significant loss of cell viability was notable only upon exposure to Col/Fib hydrogels with the highest concentration of CaPn (i.e. 10 mg/ml). At day 7, the absorbance values were approximately two-fold higher for all groups, indicating an increase in cell viability. Markedly, no difference in viability was detected between cells exposed to Col/Fib with 10 mg/mL CaPn and the other groups, indicating that cells recovered over time after an initial decrease in the presence of a high concentration of CaPn.

5.3.2 Vascularization in Col/Fib hydrogels enriched with different CaPn concentrations

HUVECs and BMSCs (10:1) were embedded in Col/Fib hydrogel composites to identify the maximum concentration of CaPn not affecting microvessel formation. After 10 days of culture, confocal imaging (Fig2B) showed a copious network of rather thin and elongated branches (red) dispersed throughout all constructs in all the tested conditions, with a slight decrease in network formation with increasing concentrations of CaPn. No significant differences in terms of DNA content were detected between plain Col/Fib and Col/Fib enriched with increasing amounts of CaPn (Fig2C), demonstrating that CaPn did not exert any cytotoxic effect on cells embedded within the hydrogel. Quantification of key network parameters (Fig2C) detected a similar average branch length among groups (~ 60 μm). Differently, the value of total network length within plain Col/Fib hydrogels (24384±2804 μm) was statistically higher compared to Col/Fib hydrogels enriched with CaPn at a concentration of 7.5 mg/mL (13003±5143 μm, $p<0.01$) and 10 mg/mL (15254±5190 μm, $p<0.05$), but not compared to Col/Fib hydrogels enriched with lower concentrations of CaPn (from 1.25 to 5 mg/mL). These data indicated that the number of branches, but not the average branch length, was influenced by CaPn concentration and suggested that 5 mg/mL was the highest concentration of CaPn that could be added to Col/Fib hydrogels without disturbing microvascular network formation. Thus, the CaPn concentration of 5 mg/mL was selected for the subsequent experiments.
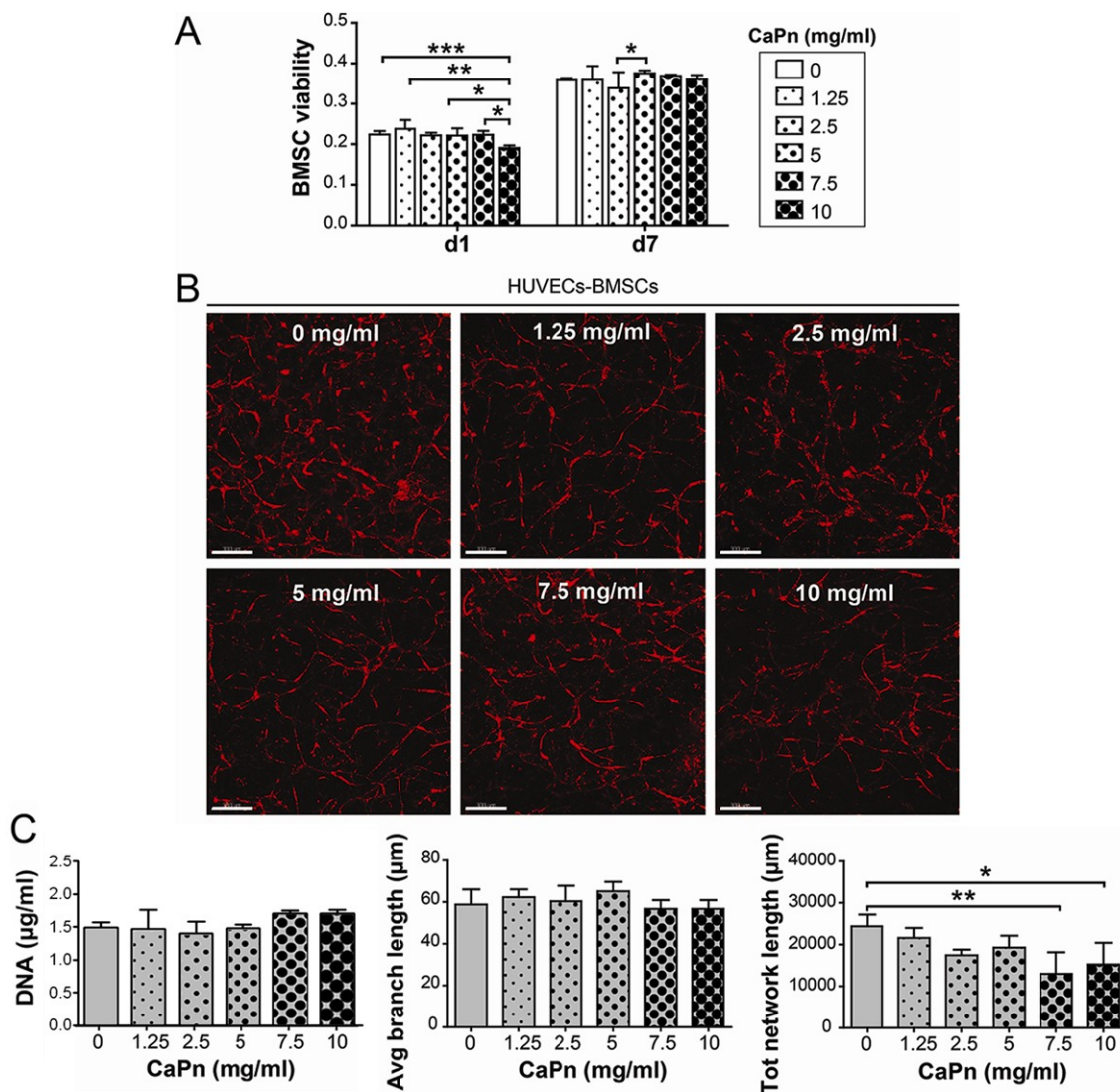
Fig.2: Cytotoxicity of Col/Fib hydrogels with different concentrations of CaPn assessed through the MTT assay (A). Micrographs showing the microvascular network formation in HUVECs-BMSCs cocultures embedded in plain and CaPn-enriched Col/Fib hydrogels after 10 days of culture (scale bar 300 µm) (B). Quantification of DNA content and microvessel parameters in HUVEC-BMSC cocultures in plain and CaPn-enriched hydrogels (C) (*$p<0.05$, **$p<0.01$, ***$p<0.001$).

5.3.3 OB monoculture

Prior to OB encapsulation within Col/Fib hydrogels, the induction of BMSCs into osteoblast precursors was verified by comparing ALP activity in BMSCs cultured either in osteoblastic or complete medium for 7 days. As expected, superior ALP activity was measured in differentiated BMSCs, indicating that 7 days of culture in osteoblastic medium induced the commitment of BMSCs into the osteoblastic lineage (data not shown).

Cell viability of OBs, obtained by osteogenic pre-differentiation of BMSCs, embedded within Col/Fib hydrogels was assessed after 3 and 10 days of culture (Fig3A). At day 3, OBs exhibited a spread morphology and showed green fluorescence, as indicator of viability, in both groups. Yet, in CaPn-enriched Col/Fib hydrogels, cells were less abundant and not homogeneously distributed as in plain Col/Fib hydrogels. At day 10, the majority of cells was still viable in both groups, although a few dead cells (red color) were also detected. Quantification of DNA content after 3 days of culture showed a similar cell number in both groups. At day 10, the DNA content was substantially increased, though it was significantly higher in plain Col/Fib hydrogels (0.95±0.1 µg/mL) than in CaPn-enriched Col/Fib hydrogels (0.67±0.1 µg/mL, *p*<0.01) (Fig3B).

Measurement of ALP activity as marker of osteogenic differentiation revealed a significant increase for CaPn-enriched hydrogels at day 3 compared to plain hydrogels (89±18 mU ALP/µg DNA versus 42±6 mU ALP/µg DNA, *p*<0.01). As expected, a substantial decline in ALP activity was observed at day 10 for both groups (Fig3C). Cell-mediated mineralization (Fig3D) was quantified by subtracting the values of calcium levels measured in cell-free hydrogels (Fig3E) from those of their cell-laden counterparts at each time point. Cell-mediated mineralization was barely detectable in plain Col/Fib hydrogels both at day 3 and day 10. On the contrary, cell-mediated mineralization was elevated for CaPn-

enriched hydrogels with a significant increase of calcium at day 10 (7622±563 ng) compared to plain hydrogels (5±72 ng, $p<0.01$). In cell-free CaPn-enriched hydrogels , the calcium levels remained constant from day 3 to day 10 (~67000 ng) and, as expected, were drastically higher compared to the plain analogs (~1000 ng) (Fig3E).
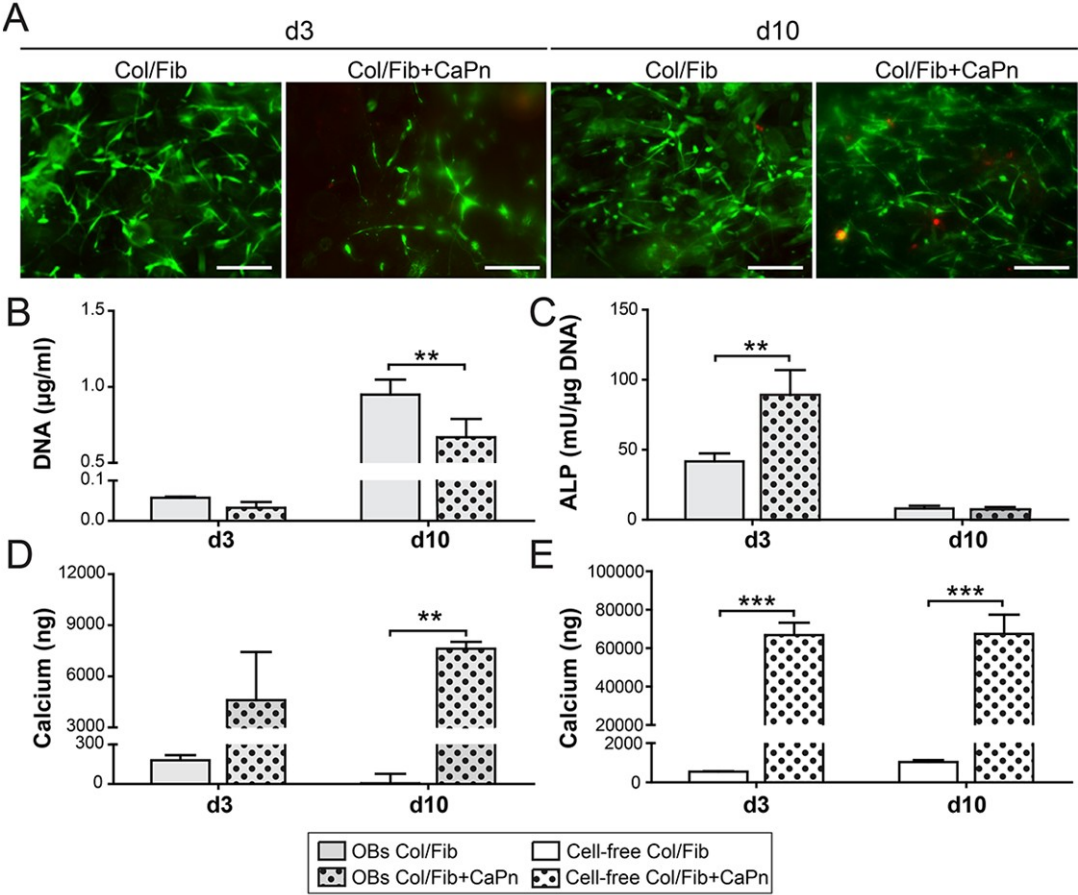
Fig3: Cell viability (A, scale bars 200 μm), DNA content (B) and characterization of the osteoblastic cell response (C,D) in OB monocultures embedded in plain and CaPn-enriched (5 mg/ml) Col/Fib hydrogels after 3 and 10 days of culture. The osteoblastic cell response was assessed through the quantification of ALP activity (C) and cell-mediated mineralization (D). Total calcium content measured in cell-free plain and CaPn-enriched hydrogels (E).The amount of cell-mediated mineralization was obtained by subtracting the values of cell-free

hydrogels from the total calcium content measured in the corresponding cell-laden hydrogels. (**_p_<0.01, ***_p_<0.001).

5.3.4 OC monoculture

Prior to OC encapsulation within Col/Fib hydrogels, the induction of PBMCs into osteoclast precursors was verified by comparing the TRAP activity measured in PBMCs cultured for 7 days with M-CSF and RANK-L or with M-CSF alone. Superior TRAP activity was measured in PBMCs upon the combined exposure to M-CSF and RANK-L, indicating that 7 days of culture in osteoclastic medium induced the commitment of PBMCs into the osteoclastic lineage. This result was confirmed by microscopical analysis showing that over time PBMCs assumed the typical osteoclast morphology upon exposure to M-CSF and RANK-L (data not shown).

Fluorescent microscopy imaging of the LIVE/DEAD dye at day 3 showed that the majority of OCs in both groups were viable, exhibited a round morphology and arranged in clusters (Fig4A). Nevertheless, plain hydrogels displayed an apparent higher number of cells than CaPn-enriched Col/Fib hydrogels. After 10 days, a relatively small number of dead cells (red color) was identified within both groups. Additionally, OCs incorporated in CaPn-enriched Col/Fib hydrogels appeared not organized into clusters but were rather isolated from each other compared to OCs embedded in plain Col/Fib hydrogels, which still appeared as clusters.

As can be seen from Fig4B, the amount of DNA at day 3 was significantly higher in plain Col/Fib hydrogels (0.2 µg/mL) compared to the CaPn-enriched Col/Fib hydrogels (0.07 µg/mL, $p<0.001$), thus confirming the data previously described for the cell viability. After 10 days, a decrease in cell number was observed in both groups with no differences in DNA content.

In order to characterize the osteoclastic cell response, TRAP activity in the hydrogels and phosphate levels in the culture medium were measured. At day 3, no

differences in TRAP activity were detected between the groups (Fig4C). Differently, after 10 days of culture, OCs in CaPn-enriched Col/Fib hydrogels showed a significantly higher stage of osteoclastic differentiation, as demonstrated by a two-fold increase in TRAP activity (1.9 mU/µg DNA, $p < 0.001$) compared to the plain analog (0.8 mU/µg DNA). Furthermore, a substantial increase of phosphate levels (up to 3.5 fold) released in culture medium was observed from day 3 to day 10 in CaPn-enriched Col/Fib hydrogels, indicating an active osteoclast-mediated resorption of the mineral matrix (Fig4D). Differently, phosphate release in culture medium from plain Col/Fib hydrogels was negative at day 3 and slightly increased at day 10, though remaining significantly lower compared to the phosphate released measured from CaPn-enriched Col/Fib hydrogels ($p < 0.001$).
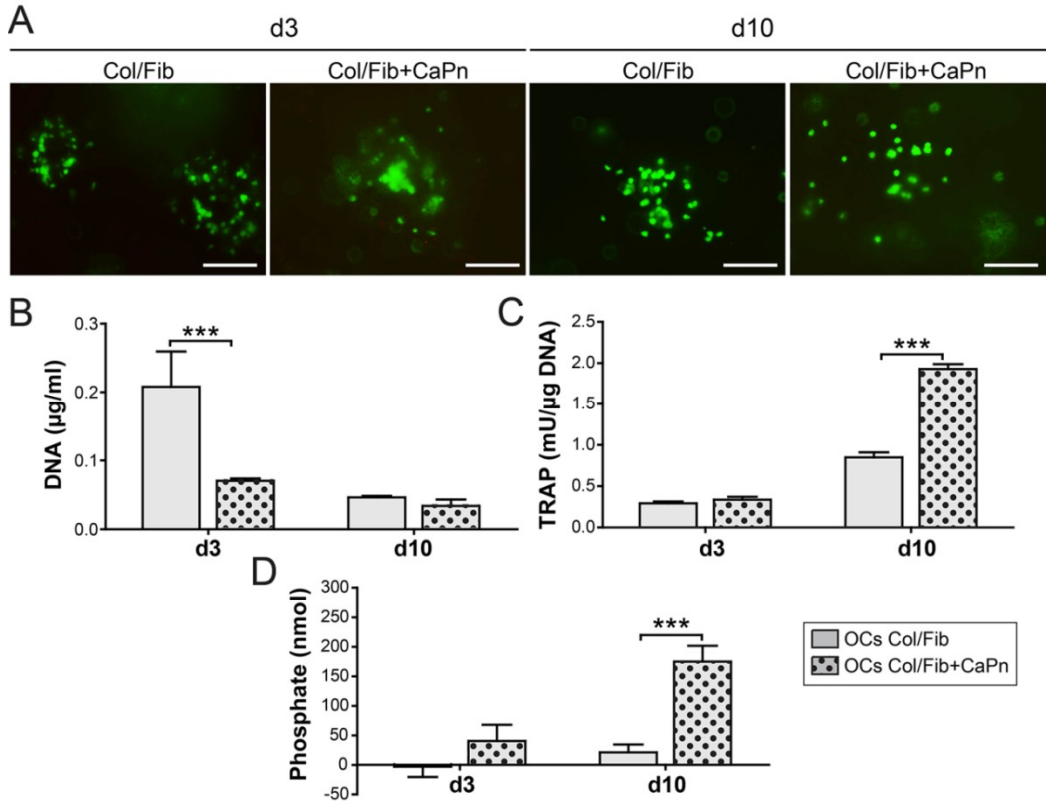
(**$p < 0.01$, ***$p < 0.001$).

Fig4: Cell viability (A, scale bars 200 μm), DNA content (B) and characterization of the osteoclastic cell response (C,D) in OC monocultures embedded in plain and CaPn-enriched (5 mg/ml) Col/Fib hydrogels after 3 and 10 days of culture. The osteoclastic cell response was assessed through the quantification of TRAP activity (C) and cell-mediated phosphate release, indicative of matrix resorption, in the culture medium (D). The amount of cell-mediated phosphate release was obtained by subtracting the values measured in the medium of cell-free hydrogels from the phosphate content in the medium of the corresponding cell-laden hydrogels (***p<0.001).

5.3.5 Vascularization in HUVEC-BMSC coculture versus HUVEC-BMSC-OB-OC tetraculture

An abundant vasculature composed of thin branched microvessels was formed in coculture and tetraculture systems embedded in both plain and CaPn-enriched Col/Fib hydrogels (Fig5A), in accordance with the results reported in Fig2B. Regarding the quantification of network parameters (Fig5B), the tetraculture embedded in CaPn-enriched Col/Fib hydrogels displayed the highest value of average branch length (65±7 μm), with a significant difference from the coculture embedded in plain Col/Fib hydrogels (p<0.01). Conversely, the highest total network length was measured for the coculture embedded in plain Col/Fib hydrogels (29721±3445 μm). Noticeably, tetraculture embedded in either plain or CaPn-enriched Col/Fib hydrogels yielded significantly lower values of total network length compared to their respective coculture counterparts (i.e. HUVECs-BMSCs). This result suggested that the presence of OBs and OCs diminished the overall vascularization of the hydrogels, inducing a reduction in the number of branches. Differently, the presence of CaPn had only a limited impact on branch formation as demonstrated by the fact that no significant differences were detected between CaPn-enriched cocultures and tetracultures and their plain analogs. Taken together, the results of the average branch length and total network length demonstrated that the simultaneous presence of OBs, OCs, and CaPn resulted in

less numerous but longer microvessels, as revealed by the significant differences found for these two parameters between the tetraculture in CaPn-enriched Col/Fib and the coculture in plain Col/Fib ($p<0.001$).
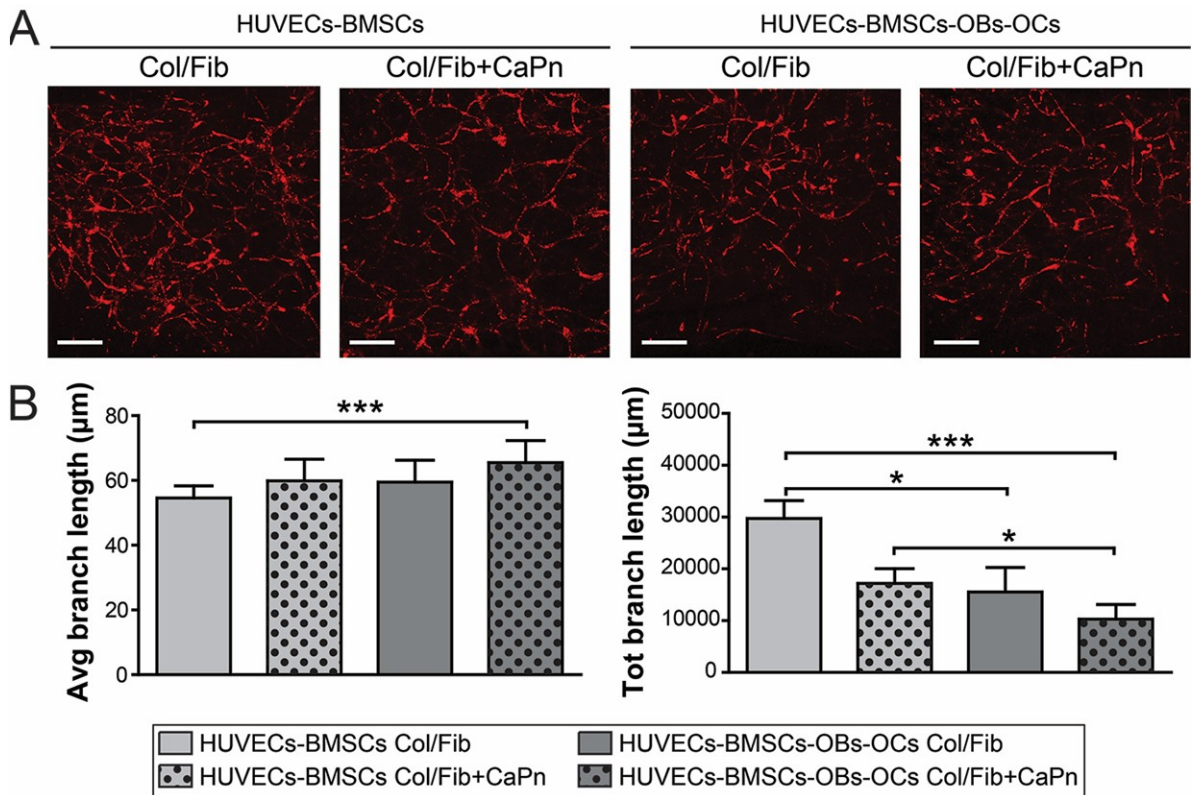
Fig5: Confocal images of microvessel formation (A, scale bars 300 μm) and quantification of microvessel parameters (B) in HUVEC-BMSC coculture versus HUVEC-BMSC-OB-OC tetraculture embedded in plain or CaPn-enriched (5 mg/ml) Col/Fib hydrogels, after 10 days of culture (*$p<0.05$, ***$p<0.001$).

5.3.6 Characterization of the osteoblastic and osteoclastic response in OB-OC coculture versus HUVEC-BMSC-OB-OC tetraculture

The characterization of the osteoblastic and osteoclastic response in coculture and tetraculture systems is presented in Fig6. At day 3, ALP activity was higher in

CaPn-enriched Col/Fib hydrogels compared to the plain counterparts, both for the coculture ($p<0.001$) and for the tetraculture ($p<0.001$) (Fig6A). Notably, the ALP activity in the tetraculture embedded in CaPn-enriched Col/Fib hydrogels (309 ± 55 mU/µg DNA) was also statistically greater than the coculture embedded in the same type of hydrogel (212 ± 45 mU/µg DNA, $p<0.001$). At day 10, there was a marked decrease in ALP activity in all groups, though it was still significantly higher in the tetraculture in CaPn-enriched Col/Fib hydrogels (72 ± 1 mU/µg DNA) than in the OB-OC coculture analog (14 ± 4 mU/µg DNA, $p<0.05$). The quantification of calcium levels confirmed that cell-mediated mineralization was statistically higher in CaPn-enriched Col/Fib hydrogels than in plain Col/Fib hydrogels ($p<0.001$) at both time points (Fig6B). These data indicate that the differentiation towards the osteoblastic lineage and the deposition of mineral matrix was enhanced when CaPn were present.

Differently from ALP activity, TRAP activity values increased from day 3 to day 10 for all the experimental groups. Specifically, no significant differences in TRAP activity were detected among the groups at day 3, whereas both tetraculture systems (i.e. with and without CaPn) displayed significantly higher TRAP activity values compared to the OB-OC coculture analog at day 10 ($p<0.001$) (Fig6C). Remarkably, the tetraculture embedded in CaPn-enriched Col/Fib hydrogels showed the highest values of TRAP activity (18 ± 3 mU/µg DNA), which was also significantly different from its plain analog (7 ± 2 mU/µg DNA, $p<0.001$). The levels of phosphate released in the culture medium at day 3 were relatively low without differences among the groups (Fig6D). At day 10, there was a considerable increase in phosphate release in the culture medium for all the groups for both tetraculture systems compared to the coculture counterparts. These results suggest that the resorption activity is increased when OCs are cultured together with OBs and HUVECs, rather than only with OBs.
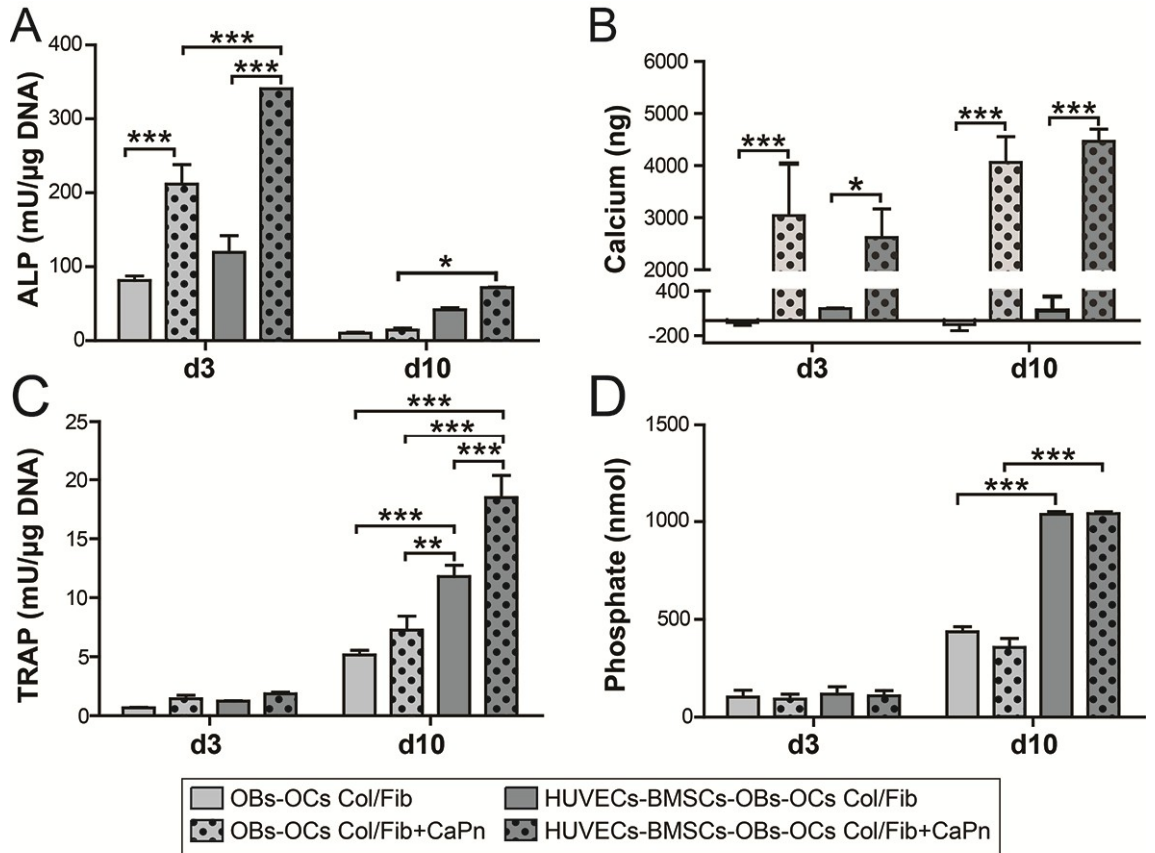
Fig6: Characterization of the osteoblastic response, based on ALP activity (A) and cell-mediated mineralization (B), and of the osteoclastic response, based on TRAP activity (C) and cell-mediated phosphate release in culture medium (D) in OB-OC coculture versus HUVEC-BMSC-OB-OC tetraculture, either in plain or CaPn-enriched (5 mg/ml) Col/Fib hydrogels after 3 and 10 days of culture. Cell-mediated mineralization (B) and phosphate release (D) were obtained by subtracting the calcium and phosphate values measured for cell-free hydrogels from the values measured for the corresponding cell-laden hydrogels (*$p<0.05$, **$p<0.01$, ***$p<0.001$).

5.3.7 Histological and immunofluorescent staining

Representative H&E stained sections of cell-laden Col/Fib hydrogels after 3 and 10 days of culture are shown in Fig7. Plain Col/Fib hydrogels (first and third column)

presented a smooth light-pink structure, while CaPn-enriched Col/Fib hydrogels (second and fourth column) displayed CaPn, represented as tiny purple dots, highly dispersed within the polymeric matrix. In all conditions, cells were homogeneously distributed throughout the constructs. As expected, a lower number of cells was found in the monocultures compared to coculture and tetraculture. At day 3 and day 10, OBs in monoculture showed a thin and elongated morphology, indicating their strong attachment to the Col/Fib hydrogels both in plain and CaPn-enriched samples. Differently, at both time points, OCs in monoculture were mainly round and, notably, displayed an increased size in CaPn-enriched hydrogels compared to plain hydrogels. Furthermore, at day 10, some OCs were detected within rounded light-colored areas (dashed circles in the second row), indicative of OC-mediated matrix resorption. In OB-OC coculture (third row), it was possible to detect the simultaneous presence of cells with either elongated or rounded morphology, corresponding to OBs and OCs respectively. As previously described for the OC monoculture, at day 10 small resorption areas were detected nearby the OCs (dashed circles). In tetraculture systems (fourth row), cells with different morphology were identified, although it was not possible to distinguish HUVECs, BMSCs, and OBs based on cell morphology. Differently, the presence of OCs was clearly detectable nearby or within cave structures lined by cells (indicated by arrowheads) which may correspond to resorbing areas or, more likely, to newly formed microvessels. Remarkably, in these areas was possible to distinguish a few larger and multi-nucleated OCs indicative of fully differentiated cells.
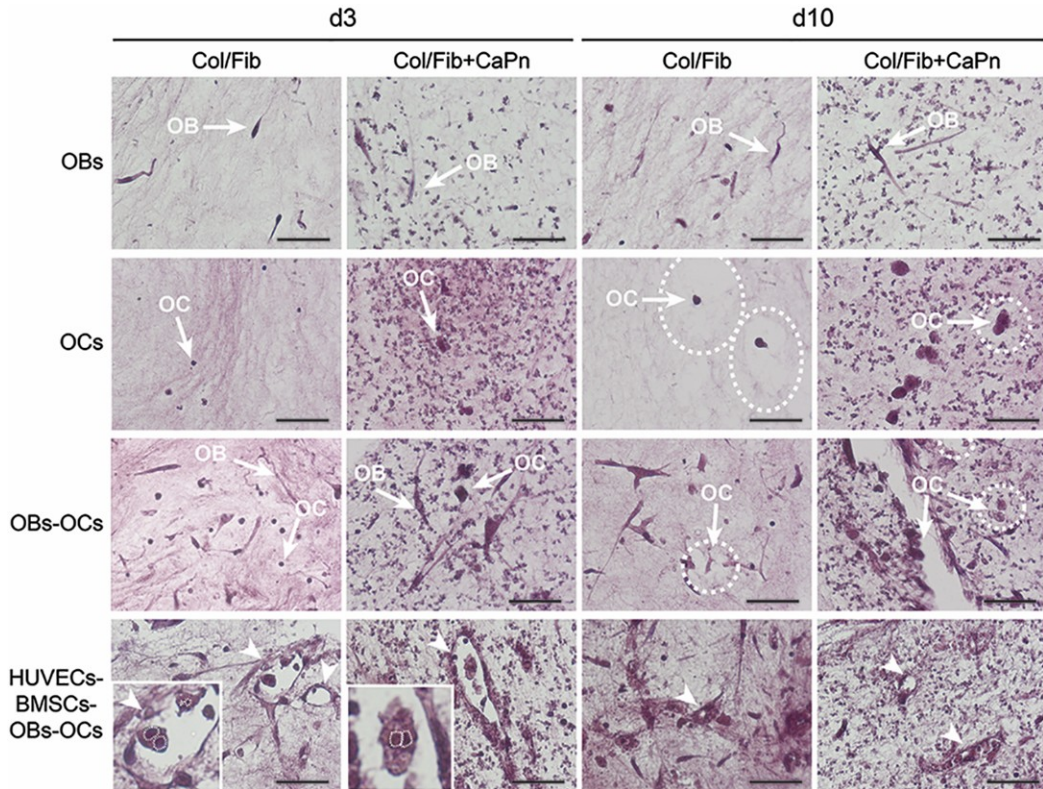
Fig7: Histological evaluation of cellular composition and morphology within Col/Fib hydrogels after 3 and 10 days of culture (scale bars 50 μm). OBs presented a thin and elongated morphology. OCs were mainly round. In tetraculture systems, many OCs were detected nearby or within cave structures lined by cells (arrowheads) which may correspond to resorbing areas or, more likely, to newly formed microvessels. Square boxes show high magnifications of multi-nucleated cells, indicating mature osteoclasts. Nuclei are outlined by dashed lines.

Immunofluorescent stainings (Fig8) were performed to observe the multiple cell types included in the tetraculture. It was possible to detect the presence of BMSCs differentiated into mural cells, which expressed α-SMA in both plain and CaPn-enriched hydrogels. In particular, the localization around the newly formed microvessels of α-SMA-expressing mural cells was particularly evident in plain Col/Fib hydrogels and indicated that mural cells supported microvascular network

formation. Moreover, we found that OBs expressed high levels of SPARC, which was detected both intracellularly and inside the hydrogel. Finally, both plain and CaPn-enriched samples were positively stained for RANK . This marker was found to be expressed by isolated cells, most likely OCs, but also co-localized with HUVECs. This finding was consistent with the results provided by HE staining and further indicated a tendency of OCs to localize nearby newly formed microvessels.
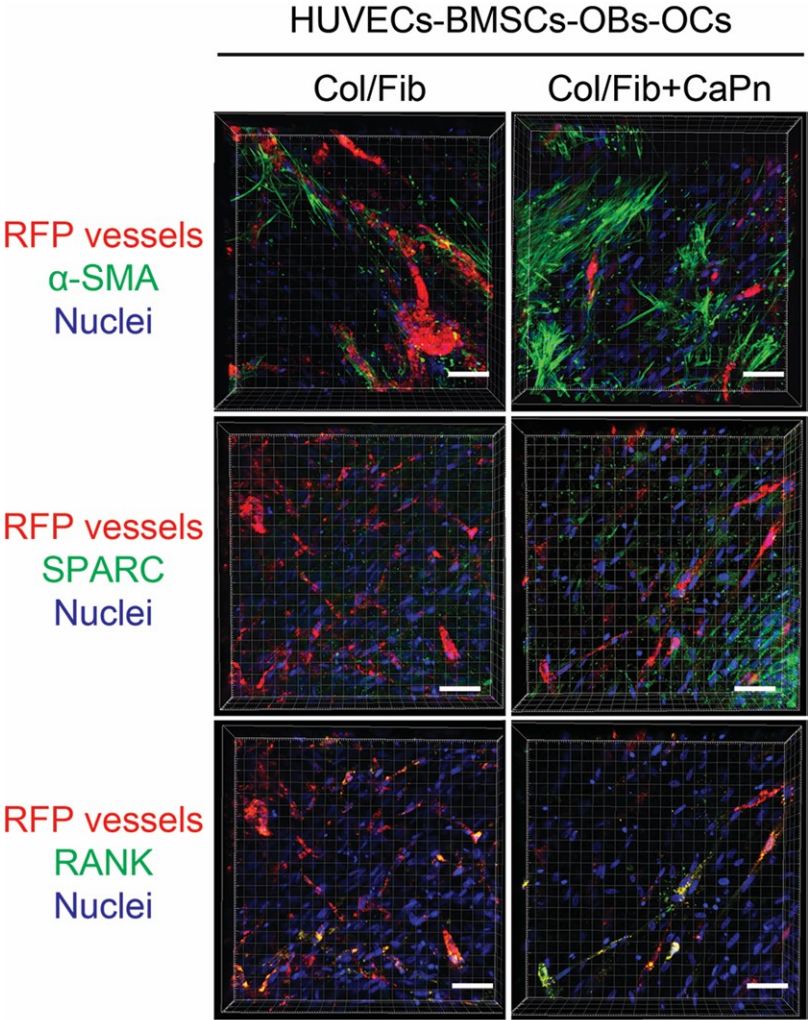
Fig8: Characterization of the vascularized tetraculture system. Immunofluorescence staining of vascular (α-SMA), osteoblast-specific (SPARC) and osteoclast-specific (RANK) markers

within Col/Fib hydrogels after 10 days of culture (scale bars 70 μm). Red: HUVECs. Blue: nuclei (DAPI).

5.4 Discussion

In the present study, we developed a vascularized tetraculture, based on the 3D MiniTissue system established in our laboratory, with the aim to generate an in vitro bone remodeling model. Specifically, endothelial cells from umbilical veins, bone marrow derived mesenchymal stem cells, and precursors of osteoblasts and osteoclasts, all of human origin, were embedded in Col/Fib hydrogels enriched with CaPn to examine the interplay between cells and CaPn in microvascular network formation and osteoblast and osteoclast differentiation. We first identified the highest concentration of CaPn which could be incorporated in the hydrogels without disturbing the formation of endothelial networks. Then, we independently analyzed the specific role of single cells (i.e. monoculture) and their combinations (i.e. coculture and tetraculture) ~~in~~ within both plain and CaPn-enriched hydrogels. Bone remodeling is defined as the process involving the removal of a quantum of bone from a surface, followed by the formation of new bone within the resorbed area [1, 2]. In vivo, osteoclast-mediated bone resorption takes approximately 2-4 weeks, whereas osteoblast-mediated bone deposition and mineralization lasts up to 6 months [36, 37]. Development of in vitro models for bone remodeling has proven to be a significant challenge, due to the high complexity of this tissue and to the long timeframe required for bone cells to mature and exert their functions. Nevertheless, effective in vitro models should satisfy the balance between biological complexity and experimental feasibility in a reasonable timescale. Here, the development of Col/Fib hydrogels pre-mineralized with CaP nanocrystals and the incorporation of pre-differentiated osteoblasts and osteoclasts permitted to capture some crucial aspects of the process of bone remodeling in a shorter time frame (i.e. 10 days) compared to the in vivo process.

The published literature describes different 3D in vitro models aiming to replicate the physiological process of bone remodeling. Yet, only a few recent studies have addressed the possibility to establish a 3D coculture system using more than two different cell types [13, 14]. A previous work by our research group, based on a statistical method (i.e. the Design of Experiment approach), analyzed the combinations of several experimental parameters obtaining the formation of a 3D microvascular network from the coculture of HUVECs, BMSCs, and OBs (ratio 10:1:1) within 2x2x5 mm^3 Col/Fib hydrogels [13]. The choice to use a mixture of collagen and fibrin to create 3D models of vasculogenesis was based on their attractive features for tissue engineering, including availability, ease of handling, cell affinity, and bioactive qualities [38]. Type I collagen is the most abundant structural protein in mammals and the major organic component of bone, where it provides high stiffness and tensile strength [39]. Fibrin biopolymer is the main constituent in blood clots and plays a key role in wound healing and angiogenesis [40]. Our aforementioned work [13], together with other findings [11], showed that Col/Fib hydrogels are able to provide a permissive environment for vessel formation. Specifically, we demonstrated that collagen/fibrin mixture at a 40:60 ratio generated a superior vascularization compared to pure fibrin hydrogels [13]. However, this study was focused on the optimization of the microvascular network formation in a 3D matrix rather than on the interaction of multiple bone cell types and did not take into account some major features of physiological bone, including the presence of a mineralized component. Here, we further exploited this 3D MiniTissue system to engineer a vascularized bone remodeling model, by adding osteoclast precursors and CaPn to more closely resemble both the cellular and mineral components of bone. As aforementioned, the triculture of HUVECs, BMSCs, and OBs at a 10:1:1 ratio produced large cell clusters which gradually remodeled into tiny microvessels [13]. Here, the same experimental set-up was implemented by adding osteoclast precursors to obtain a tetraculture system composed of HUVECs-BMSCs-OBs-OCs at a final 10:1:1:2 ratio. Since osteoblast

precursors are characterized by a superior proliferative potential than osteoclast precursors [4, 41, 42], a higher number of the latter was added to the system, coherently with other literature studies [15, 43]. Recently, Papadimitropoulos and co-workers [14] established a 3D osteoblastic-osteoclastic-endothelial cell coculture system using 3D porous ceramic scaffolds as templates to recapitulate the cellular mechanisms behind bone turnover. Although this model showed the ability to capture some aspects of the functional coupling of matrix deposition and resorption, that study was mainly addressed to establish an efficient strategy to improve the vascularization of bone implants, and the formation of a microvascular network was not investigated in vitro, but only in a subcutaneous model. Differently, in the present study, we focused on the in vitro performance of our system and we detected a copious vascularization thanks to the presence of both HUVECs and BMSCs that acted as perivascular cells, as indicated by the abundant expression of α-SMA.

To the best of our knowledge, the 3D bone remodeling MiniTissue model presented in this study is the first in vitro model that, combining four different primary human cell types in a hydrogel-based matrix enriched with CaPn, was able to mimic some key features of native bone such as the presence of a robust microvascular network, the interaction between bone cells and endothelial cells, and the osteoblast/osteoclast-mediated remodeling of the mineralized matrix. The originality of the present study lies in the methodology used to investigate the bone remodeling process in a vascularized 3D bone-mimicking microenvironment. Indeed, we applied a step-by-step process, from monocultures to more complex direct coculture systems, to examine the behavior and the reciprocal interaction of four different primary human cell types within a microscale 3D tissue. This approach allowed to highlight the positive effect of endothelial cells and CaPn on osteoblast and osteoclast differentiation and to evaluate the influence of bone cells on microvascular network formation. The high versatility represents a distinct feature of our 3D MiniTissue system, as it can be exploited to generate different

vascularized human microscale tissues or to model pathological conditions by embedding specific primary cell types or patient-derived cells. Furthermore, this system allows to study several experimental conditions using minimal amounts of cells and reagents compared to standard macroscale 3D cultures, is characterized by a superior ease of use compared to microfluidic 3D systems, and is compatible with standard analyses, including biochemical assays, histology, and immunofluorescence.

It is well documented that in vivo osteoclasts originate from mononuclear cells of the hematopoietic stem cell lineage under the influence of several factors produced by osteoprogenitor mesenchymal cells and osteoblasts, including M-CSF and RANK-L [1]. Specifically, the direct cell-to-cell interaction mediated by the binding of M-CSF and RANK-L to their receptors on osteoclast precursors stimulate their proliferation and differentiation, respectively. Reciprocally, osteoclasts produce signals that stimulate osteoblast activation, including secreted and cell surface proteins, such as Sphingosine 1-phosphate [44], Cathepsin K [45], and Ephrin-B2 [46]. Conversely, Bernhardt and collaborators reported that the indirect coculture of monocyte-derived osteoclast precursors and osteogenically induced BMSCs has a stimulatory effect only on osteogenesis but not on osteoclastogenesis, as determined by a decrease in TRAP activity and gene expression of osteoclast markers [47]. With the attempt to accurately mimic the in vivo environment, recent studies [15, 48] reported the development of 3D cocultures of osteoblasts and osteoclasts seeded onto porous ceramic scaffolds and demonstrated that the direct coculture positively influences the osteogenic differentiation and mineral deposition as well as osteoclast development. Taken together with our findings, showing that the coculture of OBs and OCs resulted in a reciprocal positive effect on their differentiation compared to the cells cultured alone, the coupling between bone formation and bone resorption is confirmed to be tightly and mutually regulated through the direct crosstalk between these two cell types in a 3D environment. Remarkably, in the current study, ALP activity and

TRAP activity were even more enhanced when OBs and OCs were cocultured together with HUVECs and BMSCs, implying that also HUVECs and BMSCs participate in the differentiation processes. It has been reported that vascular endothelial cells communicate with osteoclasts and their precursors [49], although their interaction in controlling osteoclast differentiation is not clearly understood. In accordance with the results presented here, a recent study demonstrated that endothelial precursor cells greatly enhanced the survival, migration, and differentiation potential of osteoclast precursors, thanks to a strong synergistic effect exerted by cytokines (VEGF-A, SDF-1, and TGF-β1) secreted by endothelial cells [50]. Moreover, other studies indicated that VEGF exert a positive action on osteoblasts differentiation, enhancing matrix mineralization [51] and ALP activity [52], further supporting our data. Yet, a limitation of the current study was that we did not test the perfusability of the microvascular network, which is instead crucial to model and investigate more complex biological events, such as cell extravasation [7, 12, 53]. Hence, further studies will need to be performed to establish whether the positive effect observed on osteoblastic and osteoclastic differentiation in the tetraculture was dependent also on the direct access of cells to nutrients rather than only on the presence of endothelial and mural cells.

CaPn were introduced in Col/Fib hydrogels to mimic the mineral matrix of bone and, hence, to better model the physiological environment. The ease of handling of Col/Fib hydrogels permitted to simply mix the CaPn into the solution prior to gelation enabling a highly uniform distribution of the nanoparticles The possibility to incorporate HA nanoparticles into the Col/Fib hydrogels was previously investigated by Rao and colleagues [16], who showed that HA-enriched hydrogels were significantly stiffer than the plain analog, thereby corroborating the rationale to develop a hydrogel-based matrix pre-mineralized with CaPn with physical and mechanical properties more similar to those of native bone. The same study also showed that concentrations of HA nanoparticles superior to 2.5 mg/mL were detrimental for microvascular network formation in Col/Fib hydrogels [16].

Differently, in our study we showed that the addition of up to 5 mg/mL CaPn resulted in a similar level of microvascular network formation as in plain Col/Fib hydrogels, and that undifferentiated BMSCs, which were included in the system to support microvessel formation, were able to effectively differentiate into α-SMA-expressing mural cells despite the presence of the strong osteogenic signal provided by CaPn. Conversely, amounts of CaPn above 7.5 mg/mL negatively affected the process of microvascular network formation in terms of total network length, most likely due to the higher concentration of CaPn embedded within the hydrogel that affected matrix architecture and porosity, thus preventing the formation of longer branches. One possible explanation for the dissimilarity with the findings of Rao and colleagues may lie in the greater size (up to 200 nm) of the HA nanoparticles used in their study [16] that could cause a bigger hindrance for endothelial cell migration and growth compared to the smaller CaPn (<100 nm) used here. The amount of CaP included in our system was far below the physiological amount of CaP that can be found in native bone matrix, representing one of the limiting factors of our 3D MiniTissue bone remodeling model. However, this choice was forced by the need to have a mineralized matrix allowing the development of a microvascular network. In accordance with the abovementioned results, it was not surprising to detect a decline in microvascular network formation with respect to the increasing complexity of our model. Specifically, the total network length was significantly reduced in the tetraculture compared to the HUVEC-BMSC coculture systems, irrespective of the presence of CaPn. This effect could depend on the presence of a high number of OBs, which greatly proliferated in both plain and CaPn-enriched Col/Fib, representing a steric obstacle for endothelial cells. Further, even though the OB-mediated production of matrix proteins was not specifically investigated in this study, according to the literature [54, 55] we can reasonably hypothesize that, during culture, OBs deposited type I collagen and modified the hydrogel properties, thus hindering HUVEC migration and microvessel formation.

Visual examination of the cells via the LIVE/DEAD assay showed that the vast majority of cells that remained embedded in the hydrogels were alive, thereby confirming the high biocompatibility of CaPn [25]. The cell density changed over a 10-day period time and differed between cell types. Specifically, OB density increased and cells remained homogeneously distributed throughout the constructs, while OC density visibly diminished over time. The quantification of DNA content, related to the number of cells present in the hydrogels, confirmed the cell viability results. OBs proliferated, whereas the number of OCs decreased over time, indicating both a lack of proliferation and progressive cell loss from the hydrogels. These results may reflect the intrinsic nature of each cell type: while osteoprogenitor cells are migratory and highly proliferative, at least at an early stage of differentiation [41], mononuclear osteoclast precursors, after a short initial proliferation phase, fuse into mature terminally differentiated cells with a limited life span [4, 42]. Yet, it has also been reported that HA nanoparticles elicit different cellular responses in bone-related cells depending on their physicochemical properties, including composition, size, and shape [56-58]. High crystalline CaPn of needle-like shape, with a Ca/P ratio of 1.67 and an average diameter and length of 18±7 and 76 ± 23 nm, respectively [25, 31, 32], as those used in the present study, have been already shown to remarkably stimulate the osteogenic differentiation of encapsulated BMSCs in hydrogel composites [25]. Likewise, another study on the in vitro cytotoxicity of nano- and micro-particles on human monocytes [59] showed that needle-like HA nanoparticles (long axis 70 nm, short axis 48 nm, and a Ca/P ratio equal to 1.64), resembling the CaPn used in this study, exhibited the lowest cytotoxicity compared to the other particle preparations, thus supporting our experimental setup.

For both OBs and OCs, the decrease in cell number observed in the presence of CaPn was associated with an increase in cell differentiation, as demonstrated by the quantitative evaluation of typical markers. ALP activity, as an early marker of osteogenesis produced during the post-proliferative period [60], and calcium

deposition, as a late marker of osteogenesis [61], reached significantly elevated levels in CaPn-enriched Col/Fib hydrogels by day 3 and 10, respectively. These results were observed in all cell culture conditions containing OBs, according to the following order: OB monoculture < OB-OC coculture < tetraculture, from the least to the most differentiated. These data are consistent with previous findings [25] showing that highly dispersed CaPn with high specific surface area provide abundant nucleation sites for cell-mediated mineralization, which were not available in plain hydrogels. The lack of nucleation sites in plain hydrogels together with the relatively short differentiation period explain the scarce cell-mediated mineralization observed in these samples. Interestingly, the amount of calcium measured in cell-free Col/Fib hydrogels loaded with CaPn remained constant through the entire culture period, thereby indicating that the increase of calcium deposition observed in the cell-laden hydrogels was undoubtedly attributed to the direct effect of CaPn on OBs, which actively participated to the hydrogel mineralization, rather than to ionic exchanges during the culture period.

Osteoclasts have been demonstrated to degrade calcium phosphate ceramics in a similar way to bone mineral. During the degradation process, osteoclasts create a sealing contact with the bone matrix, express high level of TRAP and produce hydrogen ions, lowering the local pH to 4–5 [62]. As a result, the solubility of HA crystals increases and bone resorption pits are formed [63]. In the present study, CaPn remarkably stimulated the osteoclast activity, and such increase was more pronounced when OCs were cultured together with OBs and even higher when OCs were in tetraculture with OBs, HUVECs, and BMSCs.

5.5 Conclusion

The data presented here collectively indicate that all the cell types incorporated in our system, including HUVECs, BMSCs, OBs and OCs, exerted their specific functions resulting in a vascularized 3D bone remodeling model. Noteworthy, cell

differentiation into the osteogenic and osteoclastic lineage was positively influenced by the presence of CaPn and to an even greater extent by the combination of the tetraculture system and CaPn, thereby demonstrating the synergistic effect of specific bone matrix components and cell-cell signaling.

5.6 Future perspectives

The 3D vascularized bone remodeling model presented here highlighted the interplay between endothelial cells and bone cells. Hence, this system holds great potential to be used as a platform to investigate the molecular basis underlying the reciprocal interaction between bone cells, such as the OPG/RANK-L/RANK axis, and the interaction of bone cells and endothelial cells. Furthermore, this miniaturized model allows to simultaneously prepare a high number of samples minimizing the use of cells reagents. These features, together with the use of human cells, perfectly fit with the requirements for a drug screening platform. Hence, we envision that our system may be applied to screen drugs for the treatment of diseases related to bone homeostasis dysregulation, such as osteoporosis and sclerosteosis. The possibility to use patient-derived cells will further enhance its relevance as a personalized drug screening platform, possibly resulting in a reduction in the use of lab animals and in a significant shift towards patient-specific treatments.

5.7 Ethical conduct of research

The authors state that they have obtained appropriate institutional review board approval coherently with the principles outlined in the Declaration of Helsinki. In addition, for investigations involving biological samples from human subjects, informed consent has been obtained from the participants involved and samples have been assigned random numerical codes to grant patients' privacy.

References

1.   Florencio-Silva R, Sasso GR, Sasso-Cerri E, Simoes MJ, Cerri PS. Biology of Bone Tissue: Structure, Function, and Factors That Influence Bone Cells. *BioMed research international* 2015 421746 (2015).

2.   Parfitt AM. The cellular basis of bone remodeling: the quantum concept reexamined in light of recent advances in the cell biology of bone. *Calcified tissue international* 36 Suppl 1 S37-45 (1984).

3.   Portal-Nunez S, Lozano D, Esbrit P. Role of angiogenesis on bone formation. *Histology and histopathology* 27(5), 559-566 (2012).

4.   Udagawa N, Takahashi N, Akatsu T *et al*. Origin of osteoclasts: mature monocytes and macrophages are capable of differentiating into osteoclasts under a suitable microenvironment prepared by bone marrow-derived stromal cells. *Proceedings of the National Academy of Sciences of the United States of America* 87(18), 7260-7264 (1990).

5.   Kusumbe AP, Adams RH. Osteoclast progenitors promote bone vascularization and osteogenesis. *Nature medicine* 20(11), 1238-1240 (2014).

6.   Kusumbe AP, Ramasamy SK, Adams RH. Coupling of angiogenesis and osteogenesis by a specific vessel subtype in bone. *Nature* 507(7492), 323-328 (2014).

7.   Jeon JS, Bersini S, Whisler JA *et al*. Generation of 3D functional microvascular networks with human mesenchymal stem cells in microfluidic systems. *Integrative biology : quantitative biosciences from nano to macro* 6(5), 555-563 (2014).

8.   Armulik A, Abramsson A, Betsholtz C. Endothelial/pericyte interactions. *Circulation research* 97(6), 512-523 (2005).

9.   Maes C. Role and regulation of vascularization processes in endochondral bones. *Calcified tissue international* 92(4), 307-323 (2013).

10. Bongio M, Van Den Beucken JJ, Leeuwenburgh SC, Jansen JA. Preclinical evaluation of injectable bone substitute materials. *Journal of tissue engineering and regenerative medicine* 9(3), 191-209 (2015).

11. Rao RR, Peterson AW, Ceccarelli J, Putnam AJ, Stegemann JP. Matrix composition regulates three-dimensional network formation by endothelial cells and mesenchymal stem cells in collagen/fibrin materials. *Angiogenesis* 15(2), 253-264 (2012).

12. Jeon JS, Bersini S, Gilardi M *et al*. Human 3D vascularized organotypic microfluidic assays to study breast cancer cell extravasation. *Proceedings of the National Academy of Sciences of the United States of America* 112(1), 214-219 (2015).

13. Bersini S, Gilardi M, Arrigoni C *et al*. Human in vitro 3D co-culture model to engineer vascularized bone-mimicking tissues combining computational tools and statistical experimental approach. *Biomaterials* 76 157-172 (2015).

14. Papadimitropoulos A, Scherberich A, Guven S *et al*. A 3D in vitro bone organ model using human progenitor cells. *European cells & materials* 21 445-458; discussion 458 (2011).

15. Sinclair SS, Burg KJ. Effect of osteoclast co-culture on the differentiation of human mesenchymal stem cells grown on bone graft granules. *Journal of biomaterials science. Polymer edition* 22(4-6), 789-808 (2011).

16. Rao RR, Ceccarelli J, Vigen ML *et al*. Effects of hydroxyapatite on endothelial network formation in collagen/fibrin composite hydrogels in vitro and in vivo. *Acta biomaterialia* 10(7), 3091-3097 (2014).

17. Heinemann S, Heinemann C, Wenisch S, Alt V, Worch H, Hanke T. Calcium phosphate phases integrated in silica/collagen nanocomposite xerogels enhance the bioactivity and ultimately manipulate the osteoblast/osteoclast ratio in a human co-culture model. *Acta biomaterialia* 9(1), 4878-4888 (2013).

18.   Arrigoni C, Bongio M, Talò G *et al*. Rational Design of Prevascularized Large 3D Tissue Constructs using Computational Simulations and Biofabrication of Geometrically Controlled Microvessels. *Adv Healthc Mater* (2016).

19.   Vallet-Regí M, González-Calbet, J. M., . Calcium phosphates as substitution of bone tissues. *Prog. Solid State Chem.* (32), 32 (2004).

20.   Pepla E, Besharat LK, Palaia G, Tenore G, Migliau G. Nano-hydroxyapatite and its applications in preventive, restorative and regenerative dentistry: a review of literature. *Annali di stomatologia* 5(3), 108-114 (2014).

21.   Moriarty P. Nanostructured materials. *Rep. Prog. Phys*. 64 5 (2001).

22.   Padilla S, Izquierdo-Barba, I., and Vallet-Regí, M., . High specific surface area in nanometric carbonated hydroxyapatite. *Chem. Mater.* 20(19), 3 (2008).

23.   Narayan RJ, Kumta PN, Sfeir C, Lee D, Choi D, Olton D. Nanostructured ceramics in medical devices: Applications and prospects. *Overview Nanomaterials And Surfaces JOM* 56(10), 38-43 (2004).

24.   Kandori K, Kuroda T, Togashi S, Katayama E. Preparation of calcium hydroxyapatite nanoparticles using microreactor and their characteristics of protein adsorption. *The journal of physical chemistry. B* 115(4), 653-659 (2011).

25.   Bongio M, Van Den Beucken JJ, Nejadnik MR *et al*. Biomimetic modification of synthetic hydrogels by incorporation of adhesive peptides and calcium phosphate nanoparticles: in vitro evaluation of cell behavior. *European cells & materials* 22 359-376 (2011).

26.   Engler AJ, Sen S, Sweeney HL, Discher DE. Matrix elasticity directs stem cell lineage specification. *Cell* 126(4), 677-689 (2006).

27.   Tan S, Fang JY, Yang Z, Nimni ME, Han B. The synergetic effect of hydrogel stiffness and growth factor on osteogenic differentiation. *Biomaterials* 35(20), 5294-5306 (2014).

28. Costa-Rodrigues J, Silva A, Santos C, Almeida MM, Costa ME, Fernandes MH. Complex effect of hydroxyapatite nanoparticles on the differentiation and functional activity of human pre-osteoclastic cells. *Journal of biomedical nanotechnology* 10(12), 3590-3600 (2014).

29. He J, Genetos DC, Leach JK. Osteogenesis and trophic factor secretion are influenced by the composition of hydroxyapatite/poly(lactide-co-glycolide) composite scaffolds. *Tissue engineering. Part A* 16(1), 127-137 (2010).

30. He J, Decaris ML, Leach JK. Bioceramic-mediated trophic factor secretion by mesenchymal stem cells enhances in vitro endothelial cell persistence and in vivo angiogenesis. *Tissue engineering. Part A* 18(13-14), 1520-1528 (2012).

31. Wang H, Bongio M, Farbod K *et al*. Development of injectable organic/inorganic colloidal composite gels made of self-assembling gelatin nanospheres and calcium phosphate nanocrystals. *Acta biomaterialia* 10(1), 508-519 (2014).

32. Leeuwenburgh SC, Jansen JA, Mikos AG. Functionalization of oligo(poly(ethylene glycol)fumarate) hydrogels with finely dispersed calcium phosphate nanocrystals for bone-substituting purposes. *Journal of biomaterials science. Polymer edition* 18(12), 1547-1564 (2007).

33. Lopa S, Mercuri D, Colombini A *et al*. Orthopedic bioactive implants: Hydrogel enrichment of macroporous titanium for the delivery of mesenchymal stem cells and strontium. *Journal of biomedical materials research. Part A* 101(12), 3396-3403 (2013).

34. Lopa S, Colombini A, Stanco D, De Girolamo L, Sansone V, Moretti M. Donor-matched mesenchymal stem cells from knee infrapatellar and subcutaneous adipose tissue of osteoarthritic donors display differential chondrogenic and osteogenic commitment. *European cells & materials* 27 298-311 (2014).

35. Yazid MD, Ariffin SH, Senafi S, Razak MA, Wahab RM. Determination of the differentiation capacities of murines' primary mononucleated cells and MC3T3-E1 cells. *Cancer cell international* 10 42 (2010).

36. Kini U, Nandeesh BN. Physiology of bone formation, remodeling, and metabolism In: *Radionuclide and Hybrid Bone Imaging*, Springer-Verlag (2012).

37. Compston JE, Vedi S, Kaptoge S, Seeman E. Bone remodeling rate and remodeling balance are not co-regulated in adulthood: implications for the use of activation frequency as an index of remodeling rate. *Journal of bone and mineral research : the official journal of the American Society for Bone and Mineral Research* 22(7), 1031-1036 (2007).

38. Hong H, Stegemann JP. 2D and 3D collagen and fibrin biopolymers promote specific ECM and integrin gene expression by vascular smooth muscle cells. *Journal of biomaterials science. Polymer edition* 19(10), 1279-1293 (2008).

39. Turner CH. Bone strength: current concepts. *Annals of the New York Academy of Sciences* 1068 429-446 (2006).

40. Laurens N, Koolwijk P, De Maat MP. Fibrin structure and wound healing. *Journal of thrombosis and haemostasis : JTH* 4(5), 932-939 (2006).

41. Stein GS, Lian JB, Owen TA. Relationship of cell growth to the regulation of tissue-specific gene expression during osteoblast differentiation. *FASEB journal : official publication of the Federation of American Societies for Experimental Biology* 4(13), 3111-3123 (1990).

42. Motiur Rahman M, Takeshita S, Matsuoka K *et al*. Proliferation-coupled osteoclast differentiation by RANKL: Cell density as a determinant of osteoclast formation. *Bone* 81 392-399 (2015).

43. Forte L, Torricelli P, Boanini E *et al*. Antioxidant and bone repair properties of quercetin-functionalized hydroxyapatite: An in vitro

osteoblast-osteoclast-endothelial cell co-culture study. *Acta biomaterialia* doi:10.1016/j.actbio.2015.12.013 (2015).

44. Ryu J, Kim HJ, Chang EJ, Huang H, Banno Y, Kim HH. Sphingosine 1-phosphate as a regulator of osteoclast differentiation and osteoclast-osteoblast coupling. *The EMBO journal* 25(24), 5840-5851 (2006).

45. Lotinun S, Kiviranta R, Matsubara T *et al*. Osteoclast-specific cathepsin K deletion stimulates S1P-dependent bone formation. *The Journal of clinical investigation* 123(2), 666-681 (2013).

46. Zhao C, Irie N, Takada Y *et al*. Bidirectional ephrinB2-EphB4 signaling controls bone homeostasis. *Cell metabolism* 4(2), 111-121 (2006).

47. Bernhardt A, Thieme S, Domaschke H, Springer A, Rosen-Wolff A, Gelinsky M. Crosstalk of osteoblast and osteoclast precursors on mineralized collagen--towards an in vitro model for bone remodeling. *Journal of biomedical materials research. Part A* 95(3), 848-856 (2010).

48. Tortelli F, Pujic N, Liu Y, Laroche N, Vico L, Cancedda R. Osteoblast and osteoclast differentiation in an in vitro three-dimensional model of bone. *Tissue engineering. Part A* 15(9), 2373-2383 (2009).

49. Chim SM, Tickner J, Chow ST *et al*. Angiogenic factors in bone local environment. *Cytokine & growth factor reviews* 24(3), 297-310 (2013).

50. Pang H, Wu XH, Fu SL *et al*. Co-culture with endothelial progenitor cells promotes survival, migration, and differentiation of osteoclast precursors. *Biochemical and biophysical research communications* 430(2), 729-734 (2013).

51. Mayer H, Bertram H, Lindenmaier W, Korff T, Weber H, Weich H. Vascular endothelial growth factor (VEGF-A) expression in human mesenchymal stem cells: autocrine and paracrine role on osteoblastic and endothelial differentiation. *Journal of cellular biochemistry* 95(4), 827-839 (2005).

52. Street J, Bao M, Deguzman L *et al*. Vascular endothelial growth factor stimulates bone repair by promoting angiogenesis and bone turnover. *Proceedings of the National Academy of Sciences of the United States of America* 99(15), 9656-9661 (2002).

53. Bersini S, Moretti M. 3D functional and perfusable microvascular networks for organotypic microfluidic models. *Journal of materials science. Materials in medicine* 26(5), 180 (2015).

54. Castillo Diaz LA, Saiani A, Gough JE, Miller AF. Human osteoblasts within soft peptide hydrogels promote mineralisation in vitro. *Journal of tissue engineering* 5 2041731414539344 (2014).

55. Wakatsuki T, Elson EL. Reciprocal interactions between cells and extracellular matrix during remodeling of tissue constructs. *Biophysical chemistry* 100(1-3), 593-605 (2003).

56. Tautzenberger A, Kovtun A, Ignatius A. Nanoparticles and their potential for application in bone. *International journal of nanomedicine* 7 4545-4557 (2012).

57. Gratton SE, Ropp PA, Pohlhaus PD *et al*. The effect of particle design on cellular internalization pathways. *Proceedings of the National Academy of Sciences of the United States of America* 105(33), 11613-11618 (2008).

58. Cai Y, Tang R. Calcium phosphate nanoparticles in biomineralization and biomaterials. *J. Mater. Chem.* 18 3775-3787 (2008).

59. Motskin M, Wright DM, Muller K *et al*. Hydroxyapatite nano and microparticles: correlation of particle properties with cytotoxicity and biostability. *Biomaterials* 30(19), 3307-3317 (2009).

60. Golub EE, Boesze-Battaglia K. The role of alkaline phosphatase in mineralization. *Current Opinion in Orthopaedics* 18 444–448 (2007).

61. Matsuoka F, Takeuchi I, Agata H *et al*. Morphology-based prediction of osteogenic differentiation potential of human mesenchymal stem cells. *PloS one* 8(2), e55082 (2013).

62. Mulari MT, Zhao H, Lakkakorpi PT, Vaananen HK. Osteoclast ruffled border has distinct subdomains for secretion and degraded matrix uptake. *Traffic* 4(2), 113-125 (2003).

63. Vaananen HK, Laitala-Leinonen T. Osteoclast lineage and function. *Archives of biochemistry and biophysics* 473(2), 132-138 (2008).

Chapter 6

Induction of endothelium muscle-specificity and fibroblast recruitment in an engineered 3D human environment of multiple vascularized skeletal muscle bundles

From: S. Bersini*, M. Gilardi*, GS Ugolini*, V. Sansoni, G. Talò, S. Perego, M. Soncini, M. Vanoni, G. Lombardi, M. Moretti
*Authors contributed equally to this work

6.1 Main text

The integration of vascular structures into *in vitro* cultured tissues is of paramount importance not only to ultimately engineer effective tissue constructs capable of integrating within a host body, but also to provide realistic models of complex interactions between the vascular compartment and the tissues of interest (e.g. cancer cell extravasation and metastasis formation, immune cell homing towards target tissues, angiogenesis or vasculogenesis in physiological or pathological tissues). It is widely accepted that vascularized tissue models have better similarity

with *in vivo* conditions and that tissue growth and maturation are deeply influenced by the presence of vasculature [1]. Similarly, it has been recently observed within *in vivo* animal models how vascular structures exhibit a peculiar phenotype and architecture, depending on the tissue where they are located [2]. The generation of stable vascularized 3D tissue models is, for these reasons, one of the most popular challenges of current *in vitro* research, including meso- and micro-scale muscle tissue engineering [3,4].

Skeletal muscles exhibit a bundled architecture, where multinucleated myofibers show diameters ranging from tens of microns to a few hundreds of microns. Muscle-supporting cells (fibroblasts and Pax7-positive satellite cells) are enclosed in a connective tissue sheath that covers muscle cells (endomysium) and plays an important role in myogenesis and regulation of tissue repair [5,6]. Indeed, these cells represent major targets in regenerative therapies for muscle-wasting disorders [7] or pathological tissue remodeling [8]. In skeletal muscles, vascular networks of endothelial cells (ECs) intertwine with the fibers ensuring blood supply throughout the tissue. In addition, smooth muscle actin-positive mural cells are recruited by nascent vessels to promote network maturation [9].

Attempts of biofabricating skeletal muscle tissues by co-culturing muscle cells and ECs have been previously reported. Tissue patches generated by co-culturing mouse myoblasts and ECs within an unarranged 3D matrix were shown to exhibit vessel-like structures [10] [11]. Unorganized lumen structures were identified in 3D co-cultures of muscle cells and ECs [12,13]. Among others, we previously described microvascular networks of human ECs co-cultured with mouse myoblasts in a 3D hydrogel [14]. These models mostly highlighted a single specific feature but, overall, were not able to replicate the complex skeletal muscle environment. Indeed, these approaches lack similarity with the human physiological tissue architecture, where the muscle compartment is organized into long fascicle-like structures covered by a continuous and fibroblasts-rich endomysium [15] and surrounded by a vascular

network. Moreover, no *in vitro* model succeeded in demonstrating organ-specificity of the endothelium, a feature up to now only described by *in vivo* observations [2]. These organ-specific endothelia contribute to the establishment of vascular niches which secrete angiocrine factors involved in organ regeneration, homeostasis and metabolism [16]. For these reasons, there is an urgent requirement of reliable models recreating a true skeletal muscle environment by combining both muscle tissue organization and endothelial specificity in a human 3D context. The development of such a complex environment is necessary to analyze the heterogeneous interactions occurring among multiple cell types contributing to the skeletal muscle tissue homeostasis.

Herein we describe a miniaturized method for generating physiologically structured human vascularized 3D skeletal muscle environments with embedded muscle bundles, muscle fibroblasts and mural-cell supported patent vascular networks (Fig1A). Meso-scale models have been previously reported for developing human vascularized bone-mimicking tissue constructs within 3D-printed arch-shaped structures [17–19]. Here we have employed a meso-scale system to enable casting of three non-planar bundles (600 µm diameter) of differentiated human muscle cells next to each other (600 µm distance between bundles) and subsequent addition of human cell-laden hydrogels surrounding the fibers to form a physiologically relevant vascularized muscle model. Computational simulations of oxygen consumption/diffusion demonstrated that the oxygen level within the arch-shaped structure was above the critical threshold for cell survival [20] (Fig1B).

Three muscle bundles were seeded by injecting human myoblasts embedded in human fibrin gel inside three cylindrical cavities formed in a sacrificial gel (Fig1C). After sacrificial gel removal, suspended muscle bundles were differentiated for 5 days allowing myoblast fusion into myotubes. Muscle bundles underwent compaction from 600 µm diameter (hole dimension) to 137±7µm (after 5 days) and 68±3µm (after 34 days) (Fig1D). As shown by histological sections

(Fig1E), this architecture more closely resembles the structure of the native muscle (Fig1F) compared to muscle cells homogeneously embedded in a fibrin matrix (Fig1G). Viability for long-term culture was demonstrated by LIVE/DEAD imaging of muscle bundles after 34 days of culture (Fig1H).
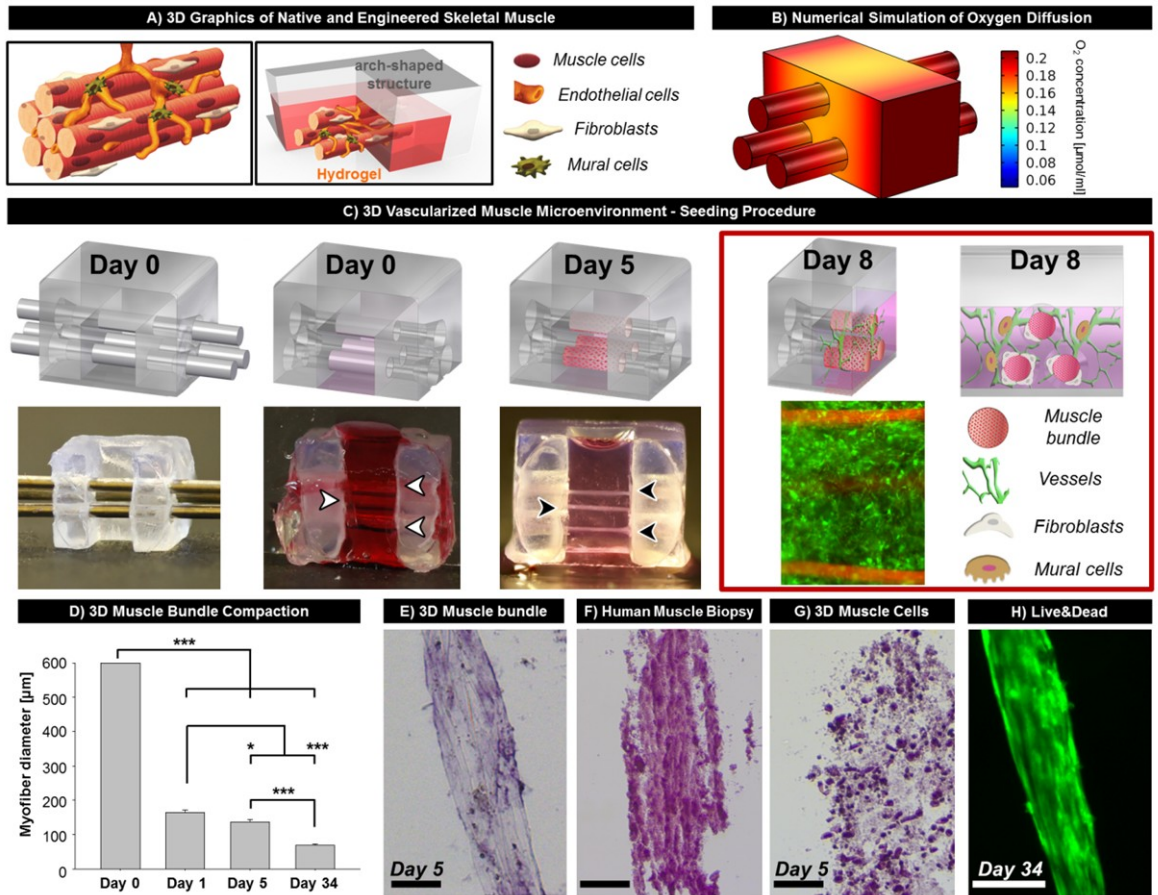

Fig1: Design and bio-fabrication of 3D vascularized muscle model. (A) 3D graphics of skeletal muscle cellular architecture (left) with muscle cells arranged in packed myofibers intertwined with endothelial cells (ECs) forming blood capillaries. Mural cells support vascular structures whereas fibroblasts are located in a connective sheath around myofibers. Right panel shows target configuration of our human 3D vascularized muscle model. Three human differentiated muscle bundles are formed in a 3D hydrogel matrix (red) encased in a 3D printed arch-shaped mask (white) and surrounded by human endothelial microvascular networks supported by human bone marrow-derived mesenchymal stem cell (MSC)-derived mural cells and human muscle-derived fibroblasts. (B) Numerical simulation of oxygen diffusion/consumption within the 3D vascularized muscle model. Values of oxygen concentration within both hydrogel and

muscle bundles are maintained above the critical threshold for cell survival. **(C)** 3D vascularized muscle model seeding procedure: three steel rods are inserted in the arch-shaped structure side holes and used to cast three cylindrical cavities in gelatin sacrificial gel (day 0; gelatin colored with red dye for imaging purposes; white arrowheads indicate cylindrical cavities). High-density human muscle cells are injected in the cavities, gelatin is dissolved and suspended muscle fibers (black arrowheads) are allowed to differentiate for 5 days (the cell culture medium appears pink in the image). Finally, human ECs-laden fibrin gel is pipetted into the central structure gap to surround the three fibers and after 3 days of maturation vascular networks are formed and surround the muscle bundles (day 8). **(D)** Compaction of muscle bundles with time. From a starting diameter of 600 µm, human muscle cells progressively compact the matrix and exhibit diameters of approximately 140 µm (day 5) and 70 µm (day 34). **E, F, G)** Histological sections of different 3D organizations of muscle cells. 3D in vitro muscle bundles **(E)** show aligned and elongated myotubes more closely resembling the in vivo architecture **(F)** compared to muscle cells homogeneously embedded and differentiated in a 3D fibrin hydrogel **(G)**. **H)** LIVE/DEAD staining of muscle bundles demonstrating cell viability for long-term culture (day 34). Viable cells appear in green. No dead cells (red signal) were detected. Scale bars: 100 µm.

For the vascular compartment, ECs were embedded in a second fibrin-based hydrogel and pipetted inside the arch-shaped 3D structure surrounding the three muscle bundles after 5 days of differentiation. Finally, ECs were allowed to mature and organize in a microvascular network for additional 3 or 6 days (Fig2A and 2B). The resulting 3D constructs were characterized by means of confocal imaging. ECs developed a network of patent microvessels (Fig2C), which wrapped and connected to muscle bundles (Fig2E) made of terminally differentiated myotubes uniformly positive for myosin heavy chain (MHC) immunostaining (Fig2D, Supplementary FigS1). Co-culturing ECs with non-bundled, randomly distributed muscle cells in a fibrin hydrogel only led to the formation of sparse and disconnected branches of microvessels (Supplementary FigS2).
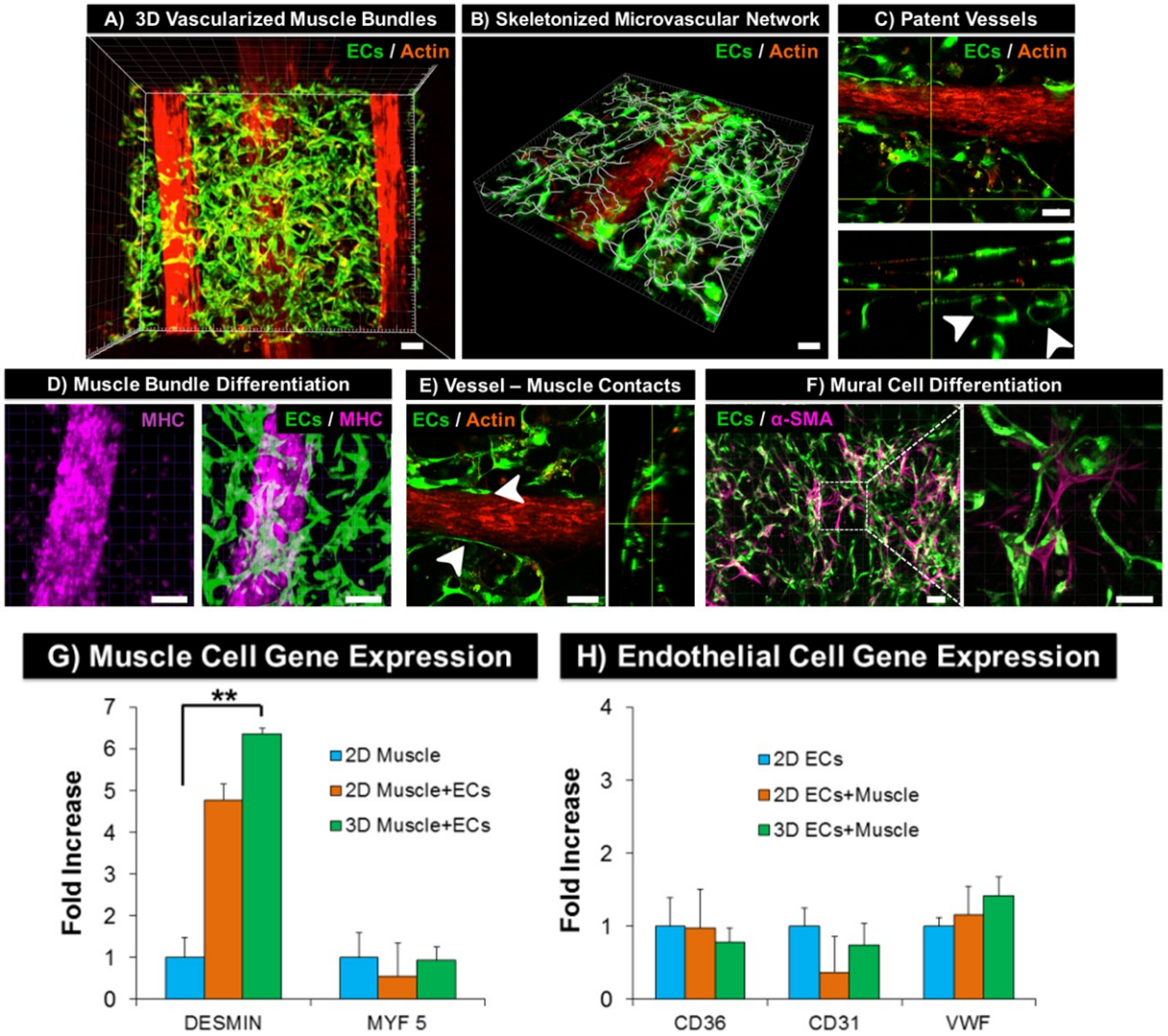
Fig2: Confocal imaging of 3D vascularized muscle model. (A) Confocal reconstruction of the whole system embedding muscle cells (red, actin staining) and ECs (green). ECs self-organize in a uniform vascular network enclosing the three muscle bundles. **(B)** 3D skeletonization of the microvascular network surrounding a muscle bundle. Muscle cells (red, actin staining) and ECs (green). **(C)** Patency of microvessels. The top view of representative microvessels and confocal reconstruction of its cross-section show how ECs formed hollow vessels with lumens (white arrowheads). Muscle cells (red, actin staining) and ECs (green). **(D)** Muscle bundles differentiation evaluated by immunostaining for myosin heavy chain (MHC, pink). The muscle bundles exhibit myotubes uniformly positive for MHC. Green: ECs. **(E)** Detailed

imaging of the contact between ECs and muscle cells in the vascularized muscle construct. Muscle bundle (actin: red) wrapped by microvessels (ECs: green) shows ECs-muscle contacts (white arrowheads) from top view (left) and reconstructed cross-section (right). (F) Differentiation of MSCs in alpha smooth muscle actin (α-SMA)-expressing mural cells. ECs are represented in green and α-SMA staining in pink. α-SMA positive MSCs are found to wrap ECs and sustain the vascular structures that surround muscle bundles. (G, H) Gene expression qRT-PCR analyses performed on muscle cells (G, Desmin and MYF5) and ECs (H, CD36, CD31 and vWF) isolated from the 3D vascularized muscle model and from 2D control conditions. Fold increase relative to house-keeping gene RPL32 vs. 2D ECs culture only. Scale bars: 100 μm.

To recreate key interactions between muscle bundles and fibroblasts, ECs were mixed with fibroblasts derived from human muscle biopsies (Supplementary Fig S3). Strikingly, homogeneously distributed fibroblasts progressively migrated towards the muscle bundles (day 8) and finally adhered to the outer part of the bundles generating a sheath enveloping the fiber (day 11) (Fig3A) resembling the *in vivo* localization of muscle fibroblasts [21]. Noteworthy, we found that a subpopulation of muscle fibroblasts exhibited Pax7-positive staining, which is a marker of satellite cells surrounding individual myofibers *in vivo* [22] (Supplementary FigS4). This migratory behavior of supporting fibroblasts mimics the physiological regeneration of the muscle fibers. It is known that this turnover is also relevant for various muscle pathologies where muscle fiber degeneration, oxidative stress and inflammation lead to fibrotic replacement of muscle cells [23].
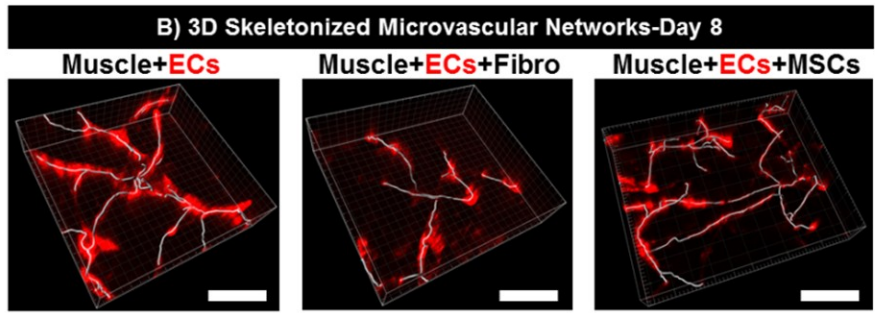
To evaluate the role of vascular supporting cells in microvascular network development, ECs were mixed with human bone marrow-derived mesenchymal stem cells (MSCs). Interestingly, this led to the formation of physiologically relevant vascular interactions within the constructs. MSCs differentiated towards alpha smooth muscle actin (α-SMA)-expressing mural cells (Fig2F) and sustained the network by wrapping vascular ECs. In addition, muscle-derived fibroblasts were also found to similarly interact and maintain the endothelial networks.

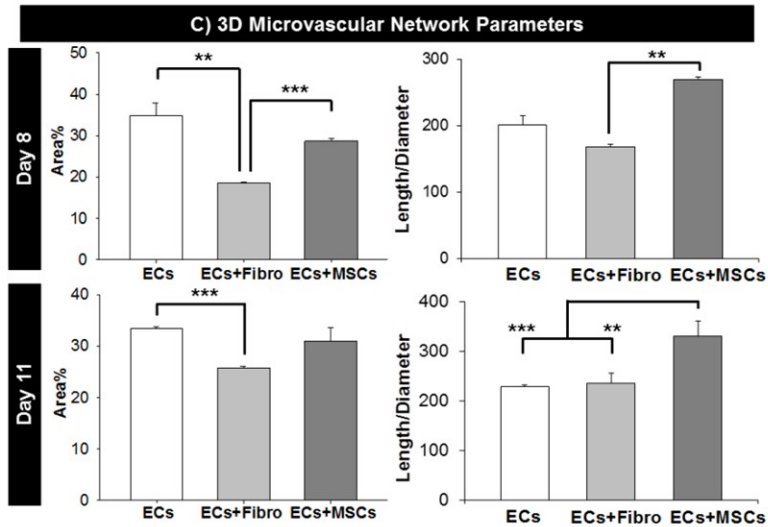Parameters of vascular networks (total network length, diameter and area covered) found near muscle bundles (600 μm × 600 μm square regions centered on muscle bundles) and quantified from confocal images demonstrated that supporting cells significantly influenced both morphology and architecture of the vascular structures wrapping the muscle bundles at day 8 and day 11 (Fig3B, Fig3C and Supplementary FigS5). In particular, the presence of MSCs led to significantly lower vessel diameters compared to ECs only cultures (18±1 μm vs. 33±3 μm; p<0.01 (day 11)) (Supplementary FigS6), in agreement with our previous findings [24]. This observation was supported by the length/diameter ratio which was significantly higher in presence of MSCs with respect to ECs networks without MSCs (330.2±30.2 vs. 228.3±3.9; p<0.001 (day 11)) (Fig3C). No statistical difference was found between ECs without and with MSCs co-culture in terms of total network length (7,015±315 μm vs. 6,363±637 μm (day 11)) and area covered (33.4±0.3% vs. 30.9±2.% (day 11)) (Fig3C and Supplementary FigS6). Similar trends were observed earlier at day 8 (Fig3C and Supplementary FigS6), despite the difference in the length/diameter ratio between ECs with MSCs and ECs without MSCs was lower (269.1±3.6 vs. 201.5±12.6). Overall, MSCs led to a dramatic decrease in vessel diameter while concurrently maintaining a similar network coverage (area and network length comparable to ECs only cultures). This aspect was confirmed by volumetric analyses of the vascular network (Supplementary FigS7). The presence of fibroblasts instead of MSCs was able to significantly narrow the vessel diameter compared to ECs only cultures (22±1 vs. 33±3 μm; p<0.05 (day 11)) (Supplementary FigS6), but failed in maintaining high network coverage parameters in terms of network length (5,213±34 μm vs. 7,015±315 μm; p<0.001 (day 11)) and area covered (25.7±0.3% vs. 33.4±0.3%; p<0.001 (day 11)), as happened when instead adding MSCs (Fig3C and Supplementary FigS6). Accordingly, the length/diameter ratio was greatly enhanced only in ECs + MSCs co-cultures (Fig3C).

It has been recently shown that *in vivo* endothelia acquire organ-specific genotypic and phenotypic signatures that drive important organotypic features of the vascular compartment, e.g. expression of specific genes and proteins, fenestrations, junctions, network sizes [2]. To date, none of the approaches aimed at forming vascularized models successfully reproduced this aspect *in vitro*. To evaluate phenotypic features of ECs networks and muscle bundles we performed enzymatic digestion of tissue constructs, cell sorting and cell type-specific gene expression analysis, demonstrating the versatility of our proposed *in vitro* model. More in detail, we performed qRT-PCR analyses of genes relevant for basic muscular (desmin and myogenin factor 5 (MYF5)) (Fig2G) and endothelial phenotypes (CD36, CD31 and von Willebrand Factor, vWF) (Fig2H). In addition, we quantified expression of genes peculiar of *in vivo* muscle-specific ECs [2] (tetraspanin 7 (TSPAN7) and peroxisome proliferator-activated receptor gamma (PPARG)) (Fig3D). The expression of these genes in ECs or muscle cells cultured in the 3D vascularized muscle models was compared to 2D monocultures (muscle cells alone or ECs alone) and 2D co-cultures (muscle cells and ECs). Interestingly, the expression of the myogenic marker desmin showed peak expression in muscle cells harvested from the 3D vascularized muscle model compared to 2D muscle cell monocultures ($p<0.01$, Fig2G). Desmin expression in muscle cells from 2D ECs-muscle cells co-cultures was higher compared to 2D muscle cell monocultures, despite it did not reach the same level of the 3D vascularized muscle model (Fig2G). In addition, muscle cells showed similar expression levels for myogenic factor 5 (MYF5) in 2D muscle cell monoculture, 2D ECs-muscle cells co-cultures and muscle cells sorted from the 3D vascularized muscle model (Fig2G). Overall, these results allow to suggest that co-culture of muscle cells with ECs positively influences muscle differentiation.

Strikingly, levels of expression of TSPAN7 and PPARG (genetic footprints of muscle-derived ECs [2]) were significantly upregulated in the 3D vascularized

muscle model compared to ECs monocultures (p<0.01, Fig3D). A greater increase in gene expression was observed in 2D co-cultures of ECs and muscle cells, confirming that the presence of muscle cells did induce vessels to exhibit a muscle-specific phenotype. We hypothesize that the muscle-induced expression of TSPAN7 is related to cell-cell paracrine interactions and to the distance between ECs and muscle cells, which is significantly different between 2D and 3D co-cultures (Fig3E and 3F). Indeed, in the 3D vascularized muscle model we found TSPAN7-positive ECs mostly in close proximity to the muscle bundle (Fig3F and Supplementary FigS8). Conversely, 2D co-cultures highlighted a uniform distribution of TSPAN7-positive ECs, always in contact with the muscle cells monolayer (Fig3E), while 3D constructs embedding non-bundled, randomly distributed muscle cells were characterized by an intermediate profile (Supplementary FigS9). Overall, genetic analyses and immunofluorescence images allow to suggest that the expression of TSPAN7 by ECs in close proximity with 3D muscle bundles is higher compared to the average expression of TSPAN7 by 2D ECs co-cultured with muscle cells. Finally, endothelial markers such as CD36, CD31 and vWF were consistently expressed by ECs cultured in the 3D vascularized muscle model, with levels of expression comparable to standard 2D ECs culture and 2D ECs-muscle cells co-cultures (Fig2H).

A) Fibroblast Recruitment - Day 8 | **Day 11**

Merge

Muscle Fibroblasts

Actin

ECs

B) 3D Skeletonized Microvascular Networks-Day 8

Muscle+ECs | Muscle+ECs+Fibro | Muscle+ECs+MSCs
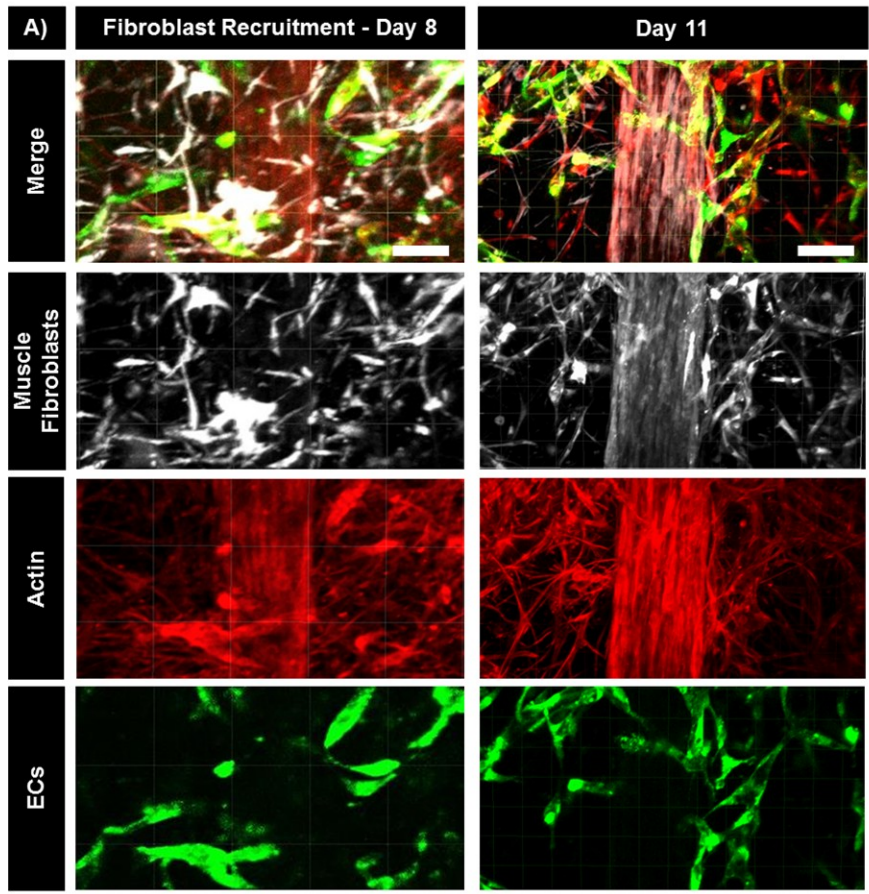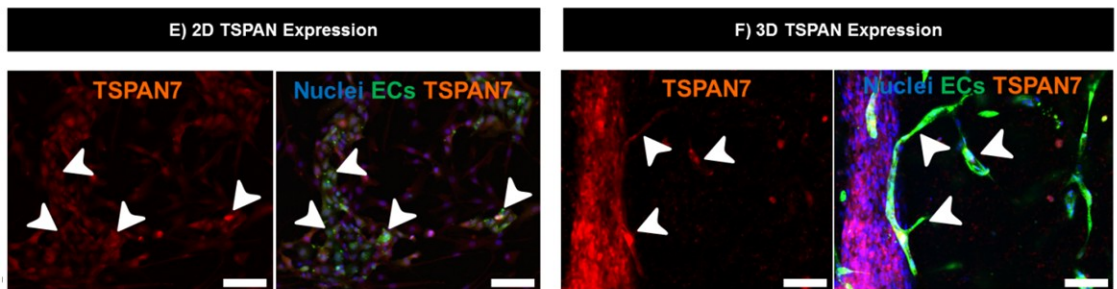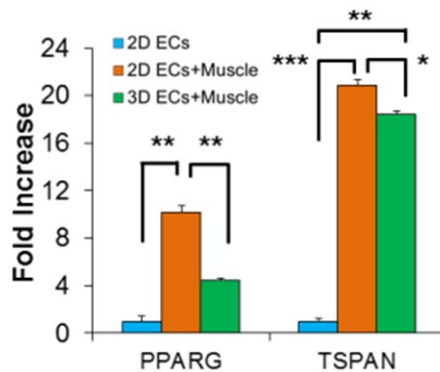
Fig3: Characterization of 3D vascularized muscle model by quantitative analyses of vascular network parameters and cell type-specific gene expression analyses (qRT-PCR). (A) Distribution of human muscle-derived fibroblasts in the 3D vascularized muscle model at day 8 and day 11. Vybrant cell labeling was employed to specifically track human muscle-derived fibroblasts (white). Actin staining (red) highlights all cell populations including differentiated

muscle bundles while ECs are shown in green. Muscle-derived fibroblasts interact with the vascular structures and, most significantly, progressively adhere to the muscle bundles forming a fibroblast sheath around the differentiated muscle bundles that resembles the in vivo endomysial localization of muscle fibroblasts. (B) Representative images of 3D skeletonized vascular networks at day 8 and day 11 under different monoculture and co-culture conditions (ECs are represented in red, muscle bundles are not shown). (C) Histogram graphs of network parameters (area coverage and length/diameter ratio) quantified from images of vascular networks at day 8 and day 11 under different co-culture conditions with muscle cells (ECs, ECs+muscle-derived fibroblasts, ECs+MSCs). (D) Gene expression qRT-PCR analyses performed on ECs isolated from the 3D vascularized muscle model and from 2D control conditions. Histogram graph shows fold increase of PPARG and TSPAN7 relative to house-keeping gene RPL32 vs. 2D ECs culture only. A dramatic increase in gene expression is observed for PPARG and TSPAN7 (genetic footprints of vessels in muscle tissue) in ECs co-cultured with muscle cells in standard 2D culture platforms and in the 3D vascularized muscle model. (E) 2D assay demonstrating that ECs covering a monolayer of muscle cells express TSPAN7 (red). ECs: green. Nuclei: blue. Arrowheads indicate representative TSPAN7 positive ECs. (F) 3D vascularized muscle model showing that highly fluorescent TSPAN7 positive (red) ECs were in close proximity (white arrowheads) with the muscle bundle. ECs: green. Nuclei: blue. Scale bars: 100 μm.

In summary, we have reported a novel method for recreating *in vitro* the human skeletal muscle environment by bio-fabricating 3D human vascularized skeletal muscle bundles. The model here described is not only compatible with high resolution imaging techniques but also with mRNA retrieval for in-depth gene expression analyses. With respect to previous muscle models, we incorporated and put together multiple physiological aspects that contribute to recreating a true muscle environment. First, compared to previous muscle models based on single muscle bundle/sheet [25,26] we added a self-organizing patent vascular compartment supported by mural cells that wraps multiple non-planar bundles of differentiated muscle cells. In addition, compared to approaches including muscle and unorganized vascular structures within unarranged matrices [10,12], we successfully

induced muscle-specificity of the endothelium, with patent vascular structures that acquired phenotypic characteristics of *in vivo* muscle-specific ECs. Importantly, we introduced self-organizing, supporting muscle-derived fibroblasts, overlooked by all previous reports, that lined muscle bundles in an *in vivo*-like fashion. All these aspects come together in a comprehensive 3D human vascularized skeletal muscle environment.

Concluding, we successfully demonstrated for the first time the *in vitro* acquisition of phenotypic characteristics of *in vivo* muscle specific ECs, as well as the self-organization of endomysial muscle fibroblasts into muscle bundle sheaths, in a 3D human vascularized model of differentiated muscle bundles. Thanks to the multiple relevant cell types involved and to the recapitulation of functional interactions, the present method achieves high similarity with *in vivo* conditions and paves the way for the generation of advanced *in vitro* models of muscle physiology and pathology, along with progresses in engineering 3D human vascularized muscle tissue constructs. In particular, we believe in the future exploitation of this new model for regenerative medicine applications and development of new therapies for muscle diseases.

6.2 Experimental procedures

6.2.1 Constructs frame fabrication

Arch-shaped 3D structures were fabricated by 3D printing of Clear Resin Formlabs (Formlabs Inc. USA). Geometric parameters were set as follows: gap size: 2x2x4 mm^3; side through-holes diameter: 600 µm. The structures were irreversibly glued to a glass coverslip and sterilized with iso-propanol before use.

6.2.2. Cell isolation and culture

Immortalized human myoblasts were kindly provided by Prof. Gabellini (San Raffaele Hospital, Milan, Italy) and were grown in muscle growth medium (4:1 DMEM:Medium199 (LifeTech) supplemented with 15% Fetal Bovine Serum (FBS, GE Healthcare Life Sciences), 2% HEPES (LifeTech), 0.03 µg/ml ZnSO4 (Sigma-Aldrich), 1.4 µg/ml vitamin B12 (Sigma-Aldrich), 0.055 µg/ml dexamethasone (Sigma-Aldrich), 1% penicillin/streptomycin/glutamine (PSG, LifeTech), 1% sodium pyruvate (LifeTech), 2.5 ng/ml hepatocyte growth factor (PeproTech) and 10 ng/ml basic fibroblast growth factor (PeproTech)). For myoblast fusion and differentiation, cells were switched to 4:1 DMEM:Medium199 supplemented with 2% FBS, 1% PSG and 1% sodium pyruvate.

Human umbilical vein endothelial cells (HUVECs) were purchased from Angioproteomie and cultured in endothelial growth medium-2 (Lonza) up to passage 7.

Human bone-marrow derived mesenchymal stem cells (MSCs) and muscle-derived fibroblasts were collected from patients undergoing hip surgery following informed consent (approval of the Ethics Committee of the San Raffaele Hospital (April 2015)). MSCs were isolated as previously described [18] and used up to passage 6. Cells were cultured using α-MEM (LifeTech) supplemented with 10% FBS, 1% penicillin/streptomycin, 1% HEPES, 5 ng/ml basic fibroblast growth factor. Muscle fibroblasts were isolated from connective tissue chunks. Briefly, the connective tissue was minced in small pieces and plated on standard plastic dishes. Outgrowth cells were collected and used up to passage 4. Muscle fibroblasts were cultured using DMEM supplemented with 10% FBS, 1% penicillin/streptomycin and 5 ng/ml basic fibroblast growth factor.

6.2.3 3D Construct preparation

Preparation of muscle bundles was performed adapting previously described protocols [25]. Three steel rods (600 µm diameter) were firstly inserted into the three side holes of the 3D arch-shaped structures. A warm solution of porcine skin gelatin (50 mg/ml) in muscle growth medium supplemented with 2.5 mg/ml 6-aminocaproic acid (Sigma-Aldrich) was pipetted in the central frame gap and cooled at 4°C for 15'. The steel rods were pulled out of the frame forming three cylindrical cavities in the cooled gelatin. Highly concentrated human myoblasts (20M cells/ml) were 1:1 mixed with a fibrin gel solution (5 mg/ml) and immediately injected in the cavities. The gel was allowed to polymerize for 15' at room temperature. The constructs were then immersed in 1 ml muscle differentiation medium for 5 days to dissolve gelatin and induce myoblast differentiation. A second fibrin gel (5 mg/ml) was then prepared to surround the differentiated muscle bundles and 1:1 mixed with different cell suspensions: 5M cells/ml ECs alone; 5M cells/ml ECs : 0.5M cells/ml MSCs; 5M cells/ml ECs : 0.5M cells/ml muscle-derived fibroblasts. The constructs were dried by pipetting medium out of the central gap and the fibrin gel solution was subsequently injected. The gel was allowed to polymerize for 15' at room temperature in humidity chambers. The constructs were then immersed in 1 ml EGM-2 and cultured for additional 3 or 6 days.

6.2.4 Immunofluorescence

Constructs were fixed with 2.5% paraformaldehyde for 30'. Permeabilization and blocking steps were performed with Triton-X-100 (0.1%) and Bovine Serum Albumin (5%). Cells were then probed with the following primary antibodies (overnight at 4°C): anti-α Smooth Muscle Actin (1:60, mouse anti-human, AbCam) to highlight differentiation of MSCs into mural cells; anti-Fast Myosin Heavy

Chain (1:100, mouse anti-human, AbCam) to highlight muscle cells differentiation. Samples were washed with Phosphate Buffered Saline (PBS) and overnight incubated with secondary antibodies at 4°C. Vybrant cell labeling (DiD, LifeTech) was employed to track muscle-derived fibroblasts. Nuclear staining was performed with DAPI whereas actin fibers staining was performed with Phalloidin.

6.2.5 Image acquisition and analysis

High-resolution images of the constructs were acquired with a two-photon confocal microscope (Nikon A1R MP+ with Coherent UltraII). Images for vascular network quantifications were acquired with confocal microscope (Leica TCS SP2). Fiji software (http://fiji.sc/Fiji) and Imaris software (Bitplane) were used for image analysis, as detailed in our previous work [17]. Imaris software was employed to capture qualitative images of the vascular network skeleton using the FilamentTracer plugin.

6.2.6 Cell sorting

Hydrogels were digested using 50 U/ml nattokinase (JBSL-USA) under stirring for 30 min at 37°C. Next, cell populations were sorted as previously described [18]. Briefly, cells were incubated with biotinylated anti-CD31 (AbCam) for 10' at 4°C under stirring. Streptavidin coupled dynabeads (LifeTech) were then added and incubated for 20 min at 4°C under stirring. Following interaction with the magnet, anti-CD31 labeled ECs were collected while muscle cells were obtained from the supernatant. Each cell population was then used for gene expression analyses.

6.2.7 qRT-PCR

Total RNA of each cell population (cells isolated from 3D vascularized muscle models and cells isolated from 2D standard monocultures or ECs-muscle cells co-cultures) was extracted by using the PureLink RNA Mini Kit (Ambion). cDNA was obtained using the iScript cDNA Synthesis Kit (Bio-Rad). Gene expression of selected markers was analyzed by quantitative reverse transcription polymerase chain reaction (qRT-PCR). The following primers were employed for ECs: CD36, CD31, vWF, TSPAN7 and PPARG. Muscle cells were analyzed using the following probes: MYF5 and Desmin. Details are reported in Supplementary Figure S10. Three experimental replicates were analyzed for each marker. The gene expression was normalized to the housekeeping gene ribosomal protein L32 (RPL32) and to the experimental control (ECs monocultures or muscle cells monocultures performed in standard 2D culture plates) using the $2^{-\Delta\Delta CT}$ method.

6.2.8 Statistical analysis

Unpaired Student's t-test and one-way analysis of variance (ANOVA) were performed using the Prism Graph Pad and SigmaPlot. Data were first analyzed for normality with normality test and then compared with parametric statistics. Differences were considered significant with $p < 0.05$ (*), $p < 0.01$ (**) and $p < 0.001$ (***). Results are presented as mean ± standard error of the mean (SEM). Network parameters were computed from at least 4 regions of interest (ROIs) while qRT-PCR results were obtained from three independent experimental replicates.

6.3 Supplementary Information

6.3.1 Computational simulations

The oxygen diffusion/consumption was modeled with Comsol Multiphysics. The model considered the presence of a 3D fibrin matrix embedding ECs and 3 bundles of muscle cells. Cell constructs were modeled with 1,000,000 tetrahedral elements. Atmospheric oxygen level was assumed at the 2 lateral openings of the 3D arch-shaped structure and at the side through-holes for muscle cell injection. All other boundaries were assigned as "no flux" boundary conditions in order to reproduce the presence of the oxygen impermeable arch-shaped structure. The oxygen diffusion coefficient was assumed equal to 2×10^{-9} m^2/s [27]. The oxygen consumption was assumed to be 5.51×10^{-5} mol/(m$^3 \times$s) for ECs [28] and 3.23×10^{-4} mol/(m$^3 \times$s) for muscle cells [29] A Michaelis-Menten kinetics was assumed for ECs considering a Michaelis constant of 5.5×10^{-4} mol/m^3 [28].

6.3.2 2D culture

In order to compare cellular behaviors in the 3D vascularized muscle model with cells cultured in standard 2D culture plates, control 2D ECs-muscle cells co-cultures were performed following the same procedures detailed for the 3D vascularized muscle model. Briefly, muscle cells were seeded in standard plates and differentiated for 5 days. Next, ECs were seeded on top of differentiated muscle cells and the co-culture incubated in EGM-2. After 3 days additional culture, cells were sorted and qRT-PCR analyses were performed on each cell population. Control gene expression studies were performed on monocultures of each cell population.

6.3.3 Histological analysis

Histological sections were obtained from three different muscle cells arrangements: 3D *in vitro* muscle bundles, 3D *in vitro* muscle cells homogeneously dispersed in a fibrin hydrogel (same cell density as the muscle bundle model) and a muscle biopsy obtained after informed consent from patients undergoing hip surgery. Briefly, samples were fixed with 2.5% paraformaldehyde for 30'. Samples were dehydrated in ethanol (graded series) and included in paraffin. 2.5 µm thick sections were mounted on glass coverslips and stained for Hematoxylin & Eosin. Images were analyzed with Olympus IX71 microscope.

References

[1]   E. C. Novosel, C. Kleinhans, P. J. Kluger, *Adv. Drug Deliv. Rev.* **2011**, *63*, 300.

[2]   D. Nolan, M. Ginsberg, E. Israely, B. Palikuqi, M. G. Poulos, D. James, B. Sen Ding, W. Schachterle, Y. Liu, Z. Rosenwaks, J. Butler, J. Xiang, A. Rafii, K. Shido, S. Rabbany, O. Elemento, S. Rafii, *Dev. Cell* **2013**, *26*, 204.

[3]   R. Visone, M. Gilardi, A. Marsano, M. Rasponi, S. Bersini, M. Moretti, *Molecules* **2016**, *21*, 1128.

[4]   J. P. Mertens, K. B. Sugg, J. D. Lee, L. M. Larkin, *Regen. Med.* **2014**, *9*, 89.

[5]   S. J. Mathew, J. M. Hansen, A. J. Merrell, M. M. Murphy, J. a Lawson, D. a Hutcheson, M. S. Hansen, M. Angus-Hill, G. Kardon, *Development* **2011**, *138*, 371.

[6]   M. M. Murphy, J. a Lawson, S. J. Mathew, D. a Hutcheson, G. Kardon, *Development* **2011**, *138*, 3625.

[7]   H. Yin, F. Price, M. a Rudnicki, *Physiol. Rev.* **2013**, *93*, 23.

[8]   C. J. Mann, E. Perdiguero, Y. Kharraz, S. Aguilar, P. Pessina, A. L. Serrano, P. Muñoz-Cánoves, *Skelet. Muscle* **2011**, *1*, 21.

[9]   S. Bersini, I. K. Yazdi, G. Talò, S. R. Shin, M. Moretti, A. Khademhosseini, *Biotechnol. Adv.* **2016**, *34*, 1113.

[10]   S. Levenberg, J. Rouwkema, M. Macdonald, E. S. Garfein, D. S. Kohane, D. C. Darland, R. Marini, C. a van Blitterswijk, R. C. Mulligan, P. a D'Amore, R. Langer, *Nat. Biotechnol.* **2005**, *23*, 879.

[11]   Y. Shandalov, D. Egozi, J. Koffler, D. Dado-Rosenfeld, D. Ben-Shimol, A. Freiman, E. Shor, A. Kabala, S. Levenberg, *Proc. Natl. Acad. Sci. U. S. A.*

2014, *111*, 6010.

[12]   D. Gholobova, L. Decroix, V. Van Muylder, L. Desender, M. Gerard, G. Carpentier, H. Vandenburgh, L. Thorrez, *Tissue Eng. Part A* **2015**, *21*, 2548.

[13]   S. Carosio, L. Barberi, E. Rizzuto, C. Nicoletti, Z. Del Prete, A. Musarò, *Sci. Rep.* **2013**, *3*, 1420.

[14]   J. S. Jeon, S. Bersini, M. Gilardi, G. Dubini, J. L. Charest, M. Moretti, R. D. Kamm, *Proc. Natl. Acad. Sci. U. S. A.* **2015**, *112*, 214.

[15]   T. K. Borg, J. B. Caulfield, *Tissue Cell* **1980**, *12*, 197.

[16]   S. Rafii, J. M. Butler, B. S. Ding, Nature **2016**, *529*, 316.

[17]   M. Bongio, S. Lopa, M. Gilardi, S. Bersini, M. Moretti, *Nanomedicine (Lond).* **2016**, *11*, 1073.

[18]   S. Bersini, M. Gilardi, C. Arrigoni, G. Talò, M. Zamai, L. Zagra, V. Caiolfa, M. Moretti, *Biomaterials* **2016**, *76*, 157.

[19]   C. Arrigoni, M. Bongio, G. Talò, S. Bersini, J. Enomoto, J. Fukuda, M. Moretti, *Adv. Healthc. Mater.* **2016**, *5*, 1617.

[20]   A. Carreau, B. El Hafny-Rahbi, A. Matejuk, C. Grillon, C. Kieda, *J. Cell. Mol. Med.* **2011**, *15*, 1239.

[21]   C. C. Agley, A. M. Rowlerson, C. P. Velloso, N. R. Lazarus, S. D. R. Harridge, *J. Cell Sci.* **2013**, *126*, 5610.

[22]   R. Sambasivan, R. Yao, A. Kissenpfennig, L. Van Wittenberghe, A. Paldi, B. Gayraud-Morel, H. Guenou, B. Malissen, S. Tajbakhsh, A. Galy, *Development and Stem Cells.* **2011**, 138, 3647.

[23]   W. Klingler, K. Jurkat-Rott, F. Lehmann-Horn, R. Schleip, *Acta Myol.* **2012**,

31, 184.

[24]   J. S. Jeon, S. Bersini, J. a Whisler, M. B. Chen, G. Dubini, J. L. Charest, M. Moretti, R. D. Kamm, *Integr. Biol. (Camb)*. **2014**, *6*, 555.

[25]   D. Neal, M. S. Sakar, L. L. Ong, H. Harry Asada, *Lab Chip* **2014**, *14*, 1907.

[26]   L. Madden, M. Juhas, W. E. Kraus, G. A. Truskey, N. Bursac, *Elife* **2015**, *2015*, DOI 10.7554/eLife.04885.

[27]   A. Colom, R. Galgoczy, I. Almendros, A. Xaubet, R. Farr??, J. Alcaraz, *J. Biomed. Mater. Res. - Part A* **2014**, *102*, 2776.

[28]   H. E. Abaci, R. Truitt, S. Tan, S. Gerecht, *Am. J. Physiol. Cell Physiol.* **2011**, *301*, C431.

[29]   R. Motterlini, H. Kerger, C. J. Green, R. M. Winslow, M. Intaglietta, *Am. J. Physiol.* **1998**, *275*, H776.
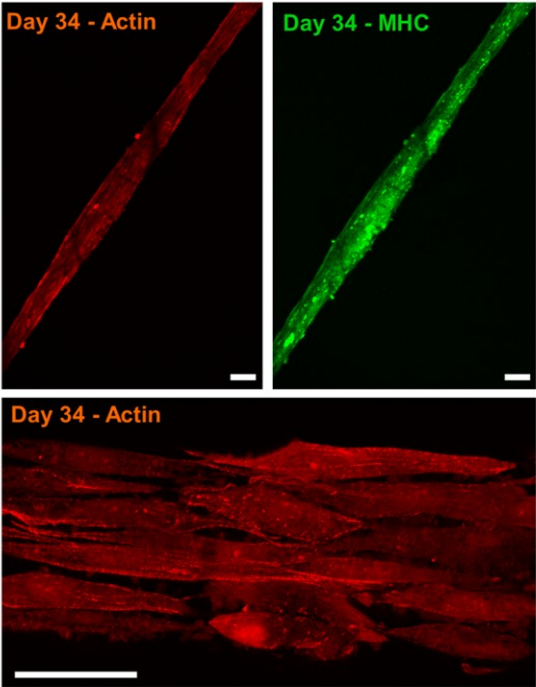
Supplementary FigS1: Long term cultured muscle bundles (actin, red) showed positive MHC immunostaining (green), indication of muscle maturation. Scale bars: 50 µm.
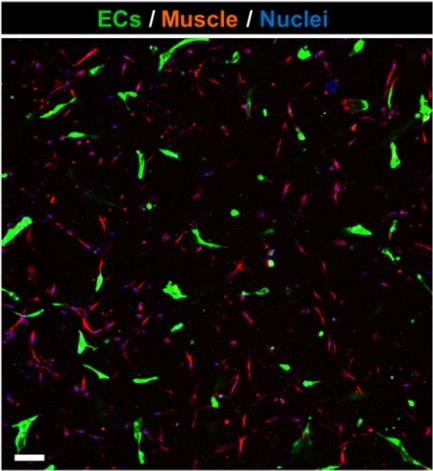

Supplementary FigS2: Co-culture of ECs (green) with non-bundled, randomly embedded muscle cells (red) only led to the formation of sparse and disconnected branches of

microvessels. Muscle cells were seeded at the same density used for the development of the 3D vascularized muscle model. Nuclei: blue. Scale bar: 50 µm.
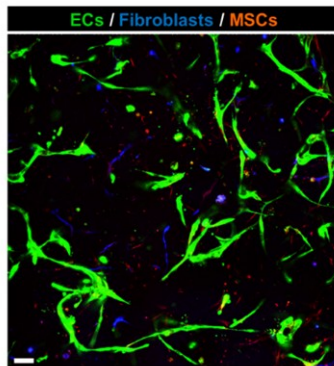
Supplementary FigS3: 3D vascularized muscle model with embedded ECs (green), muscle-derived fibroblasts (blue) and MSCs (red). Scale bar: 50 µm.
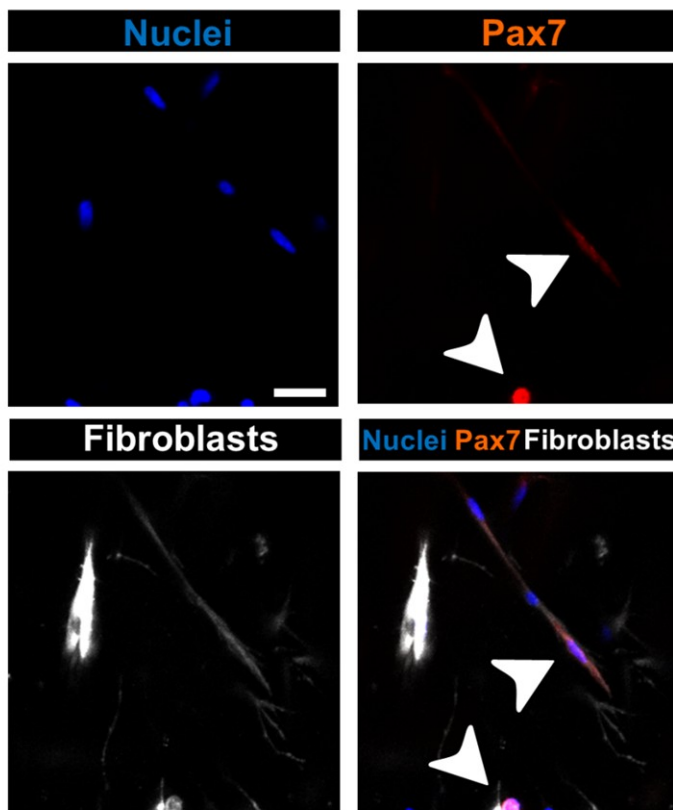
Supplementary FigS4: Detail of the 3D vascularized muscle model showing Pax-7 positive fibroblasts (red), demonstrating the presence of satellite cells in the muscle-derived fibroblast population (white). Nuclei: blue. Scale bar: 25 µm.
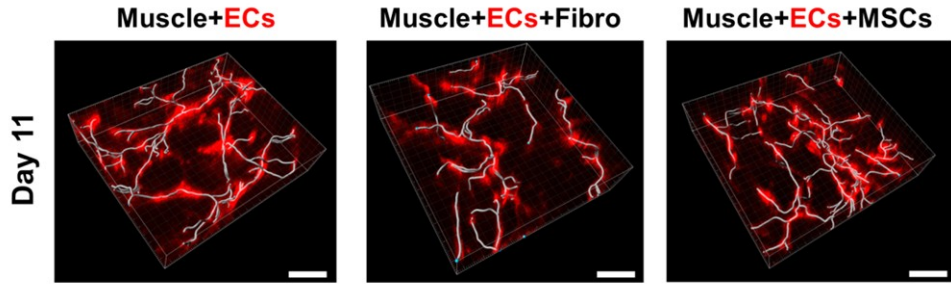
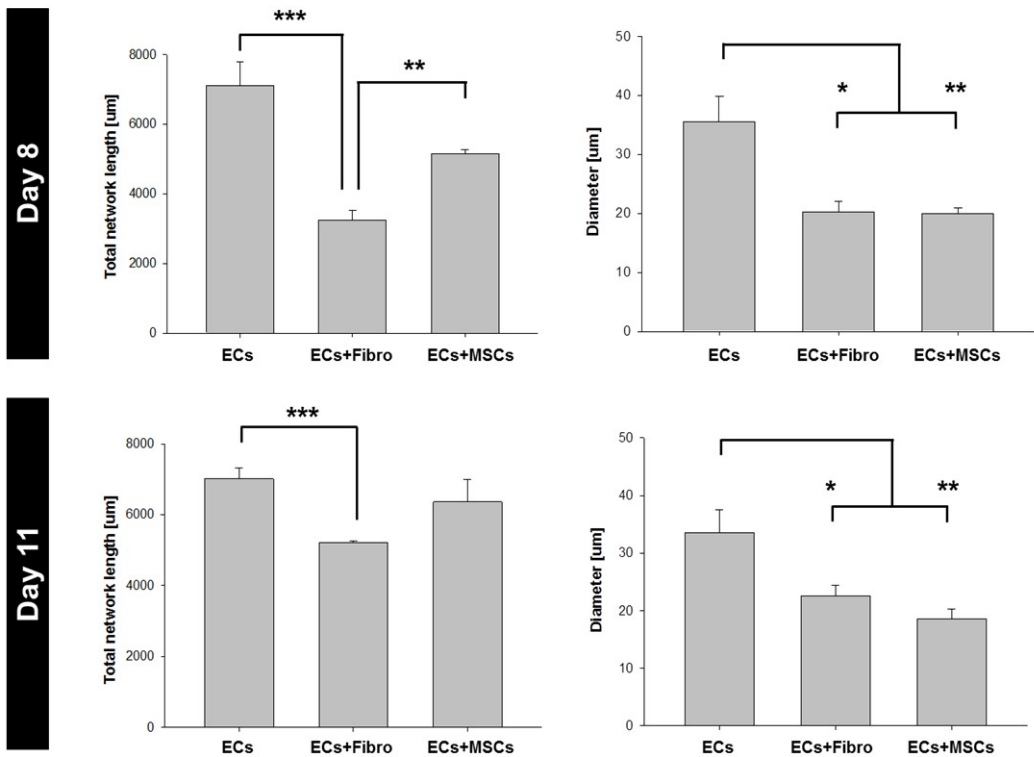**Supplementary FigS5: Representative images of 3D skeletonized vascular networks at day 11 under different monoculture and co-culture conditions (ECs are represented in red, muscle bundles are not shown). Scale bars: 50 µm.**

Supplementary FigS6: Network parameters (length and vessel diameter) at day 8 and day 11 under different monoculture and co-culture conditions (Muscle+ECs, Muscle+ECs+muscle-derived fibroblasts, Muscle+ECs+MSCs).
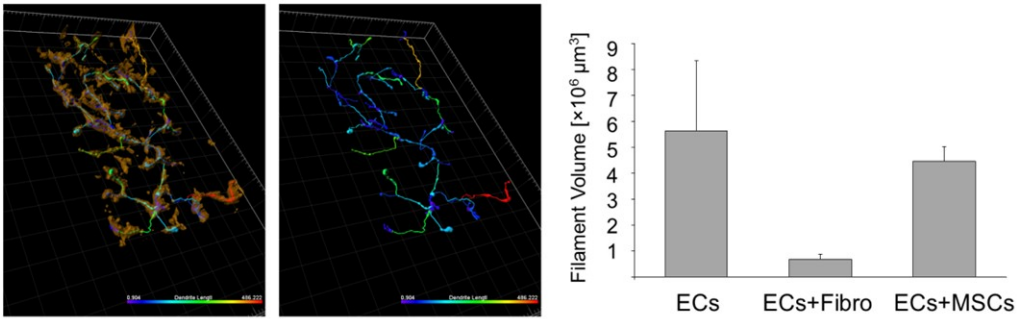
Supplementary FigS7: 3D reconstruction of vascular networks showing the presence of interconnected branches characterized by different length. Quantification of the volume occupied by vascular networks under different monoculture and co-culture conditions (Muscle+ECs, Muscle+ECs+muscle-derived fibroblasts Muscle+ECs+MSCs).
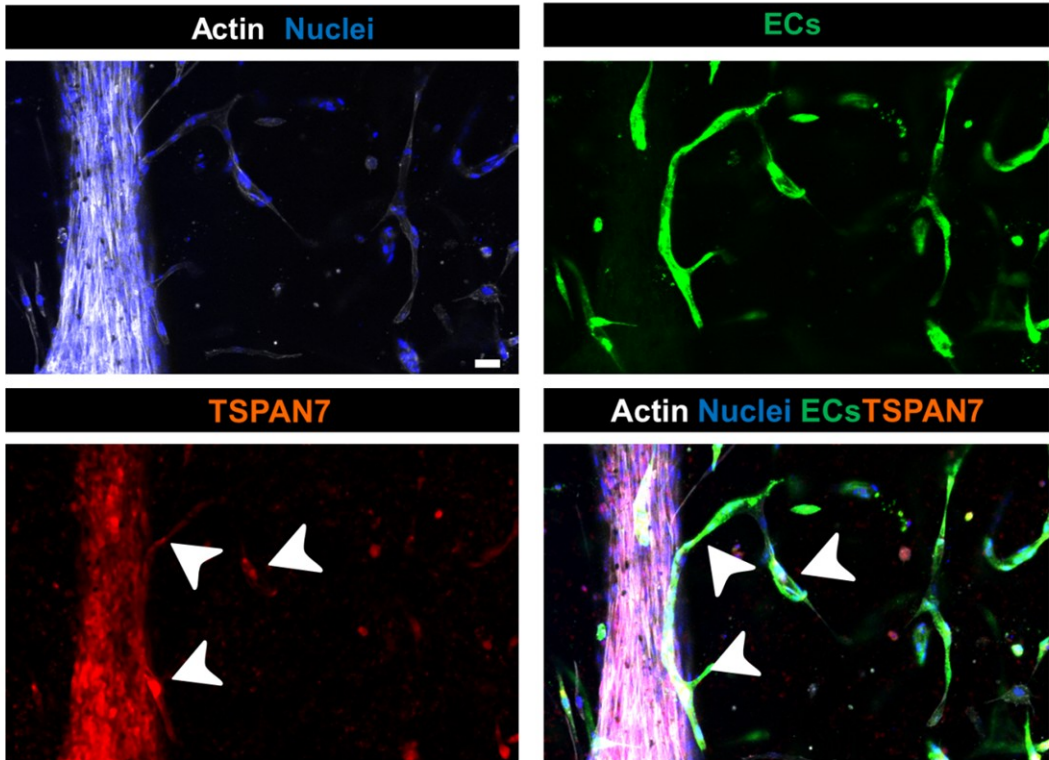
Supplementary FigS8: 3D vascularized muscle model showing the presence of TSPAN7 positive ECs (red) in contact with the muscle bundle. ECs: green. Actin: white. Nuclei: blue. Scale bar: 50 μm.
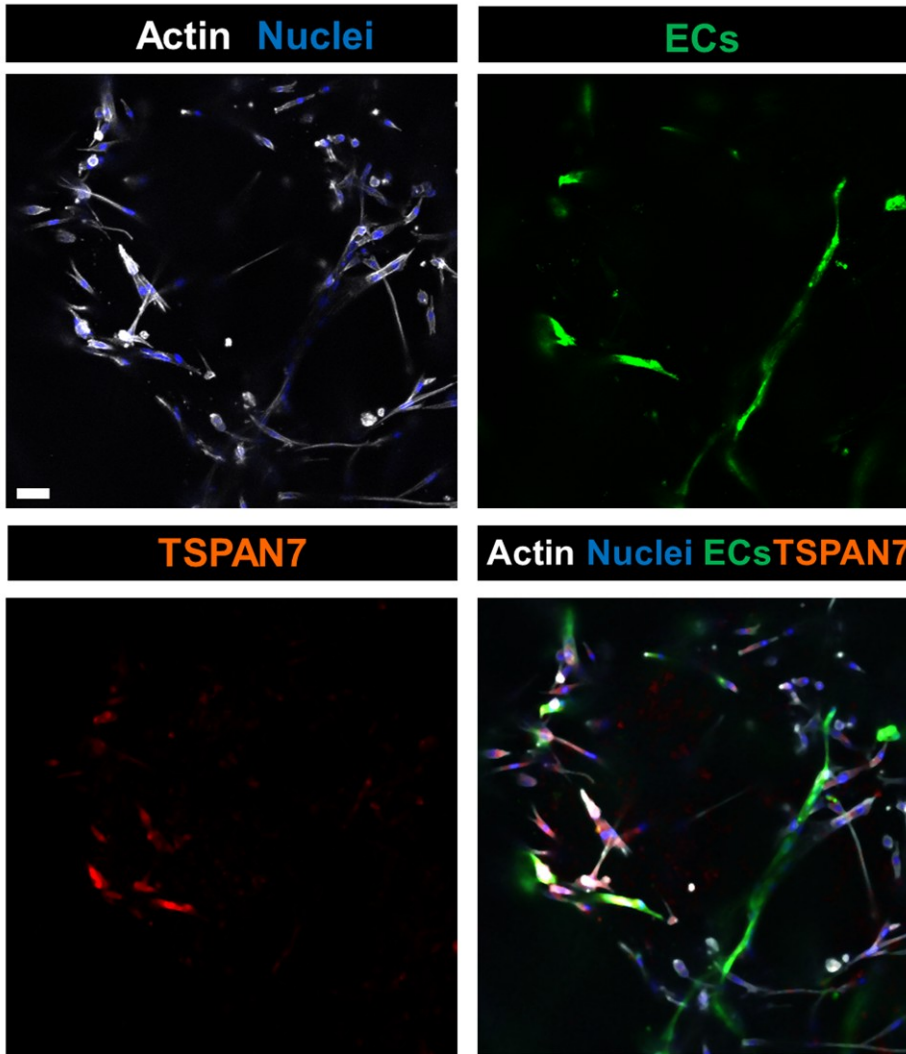
Supplementary FigS9: Co-culture of ECs (green) with non-bundled, randomly embedded muscle cells showing more uniformly distributed TSPAN7 positive ECs compared to the 3D vascularized muscle model. ECs: green. Actin: white. Nuclei: blue. Scale bar: 50 μm.

GENE	DESCRIPTION	TRANSCRIPT ID	REF SEQ		PRIMER SEQUENCE 5'→3'
DES	desmin	ENST00000373960.3	NM_001927	Fw	AGGACCGATTTGCCAGTGAG
				rev	CTTGAGGTGCCGGATTTCCT
MYF5	myogenic factor 5	ENST00000228663 44.3	NM_005593	Fw	ATGCCATCCGCTACATCGAG
				rev	TGTCCCGGCAGGGTATAGTA
PECA M-1 (CD31)	platelet and endothelial cell adhesion molecule 1	ENST00000563924.5	NM_000442	Fw	GGGACCCTCGTGGATGTTG
				rev	ATAGATGCATGTGGCCCCTC
VWF	von Willebrand factor	ENST00000226145.9	NM_000552	Fw	CCTTGACCTCGGACCCTTATG
				rev	GATGCCCGTTCACACCACT
CD36	CD36 molecule	ENST00000435819.5	-	Fw	TGGTAGGCATTCAACTGGCA
				rev	CACTTCCATATGTCCCCTCCAG
TSPAN 7	tetraspanin 7	ENST00000378482.6	NM_004615	Fw	GTCTGCATAGCGTCCGTGTA
				rev	TCGTAGCTGGCATTTCAGGG
PPARG	peroxisome proliferator activated receptor gamma	ENST00000397012.6	NM_138711	Fw	CTCCTCCTTGGGAGCCTAACT
				rev	CTACACACCCACCTTCCACC
RPL32	ribosomal protein L32	ENST00000429711.6	NM_000994	Fw	GAAGTTCCTGGTCCACAACG
				rev	GAGCGGATCTCGGCACAGTA

Supplementary FigS10: List of genes and relative primers employed for qRT-PCR experiments.

Chapter 7

RANKL/OPG regulation in early Bone metastatic niche is mediated by Cancer cell induced M1 macrophage polarization

From: M. Gilardi*, S. Bersini*, MV Colombo, V. Sansoni, G. Lombardi, M. Vanoni , M. Moretti

*Authors contributed equally to this work

Article in preparation

7.1 Main text

The seed and soil theory of cancer metastases hypothesizes that specific primary tumors only colonize specific target tissues/organs [1]. For instance, breast cancer cells preferentially metastasize to the bone with more than 70% of advanced breast cancer patients affected by disabling and incurable skeletal metastases [2, 3]. Conversely, the skeletal muscle environment seems to elicit cytostatic and cytotoxic effects on metastatic cancer cells, possibly due to the presence of adenosine and other muscle secreted molecules with impair tumor growth [4].

One of the main reasons underlying the absence of clinically effective, organ-specific anti-metastatic drugs is that both *in vitro* and *in vivo* models do not fully recapitulate the human physiology and particularly the immune system. In this

context, species-specificity may explain why potentially effective therapeutics fail after promising pre-clinical trials [5]. On the other side, traditional *in vitro* models simplistically claim to better reproduce human physiological tissue units by monoculturing or co-culturing their basic components while overlooking other equally significant cell populations. This issue is particularly true for the bone microenvironment where a light balance among bone osteoblasts, osteoclasts, resident macrophages and organ-specific endothelium regulates the tissue homeostasis.

Previous studies demonstrated that 3D co-culture of endothelial cells (ECs) and osteoblasts synergistically increases both bone matrix deposition and vessel formation [6]. Similarly, endothelium-bone interactions were investigated by the Vunjak-Novakovic group through 3D models embedding mesenchymal stem cells from different sources [7, 8] and exposed to steady or pulsatile flow [9]. Other studies focused on the development of suitable scaffolds mimicking the architecture of the native bone [10], or introduced calcium phosphate nanoparticles within the extracellular matrix surrounding bone-like cells [11]. However, it should be considered that mutual interactions between bone-forming osteoblasts and bone-resorbing osteoclasts characterize the physiological process of bone remodeling involved in bone metastases. In this context, only a few studies reported the combined use of these cell types [12, 13]. Furthermore, a striking example of bone tissue engineering is represented by the work by Mastro and co-authors who reported one of the first examples of *in vitro* model recapitulating long-term osteolytic breast cancer metastases to bone [14, 15]. A different approach was adopted by Salamanna and colleagues, who employed an *ex vivo* human bone model to analyze differences characterizing breast and prostate cancer metastases [16]. These strategies allow to characterize the global effect of different metastatic cancer cells on the bone homeostasis, even though it is not possible to track single cells and analyze specific cell-cell interactions through high resolution real time

imaging. In addition, these models do not allow to tune the behavior of single cell populations and to analyze their specific effect on the whole microenvironment.

Overall, previous 3D bone models generally overlooked the specific role of multiple components of basic bone tissue units during healthy and diseased conditions. For instance, specific EC subpopulations [17] as well as biomechanical stimuli and flow patterns [18] are tightly related to bone tissue remodeling. The vascular niche plays a fundamental role during the establishment of cancer metastases, being involved in both cancer cell adhesion/trapping at specific locations of the vascular tree [19, 20] and in the activation of dormancy programs [21]. At the same time, osteoblasts, osteoclasts and bone resident cells together with invading cancer cells concur to the deregulation of multiple signaling pathways involved in the metastatic dissemination, including the RANKL-RANK-OPG signaling (receptor activator of nuclear factor kappa-B ligand, receptor activator of nuclear factor kappa-B, osteoprotegerin, respectively) [22-24]. Furthermore, bone resident macrophages are commonly recruited to sites undergoing extensive anabolism [25]. These so-called osteomacs create canopy-like structures over bone-forming osteoblasts, thus promoting bone deposition [26]. In addition, macrophages can polarize towards inflammatory M1 and anti-inflammatory M2 phenotypes influencing the initial and late steps of the metastatic colonization [27].

The aim of the present work was to characterize the behavior of the early bone metastatic niche through engineered functional, vascularized bone models embedding the key components of a physiological bone remodeling unit. We developed human *in vitro* 3D models mimicking physiological and metastatic environments demonstrating that the presence of early invading breast cancer cells influence the behavior of each component of the bone niche. In particular, cancer cells inside the early metastatic niche polarize macrophages from M2 to M1 and alter the bone metabolism by inducing changes in the RANKL-OPG ratio.

7.2 Results and Discussion

The mechanisms driving organ-specific metastases are far from being fully elucidated. In particular, analyzing the initial steps of bone colonization of metastatic breast and prostate cancers is challenging both *in vivo* and *in vitro*, due to imaging problems and limited control over the cell-cell/cell-matrix interactions and the biochemical/biophysical properties of the surrounding environment [28]. Here we present the design and application of mesoscale vascularized human 3D bone environments (Fig1) which overcome simplified systems based on simple co-cultures of ECs and osteoblasts [6] in order to study the effect of early bone invasion of breast cancer cells and the effects on the bone metabolism.

We previously developed a computational/statistical approach which allowed to customize the physical properties of mural cell-wrapped microvascular networks embedded within 3D mesoscale bone tissues based on osteo-differentiated mesenchymal stem cells (MSCs) [29, 30]. Here we employed a mesoscale system (Fig1) to develop functional bone niches embedding the key components of a bone tissue unit under physiological and pathological conditions. In particular, we engineered vascularized healthy bone tissue constructs including fully differentiated osteoblasts, osteoclasts (Fig2) and ECs in a fibrin matrix. In a second model, bone resident macrophages [26] were mixed with the cellular components of the healthy bone tissue. Finally, breast cancer cells were included in each of the two physiological models of bone, hence simulating the early invasion of metastatic cancer cells (Fig1).
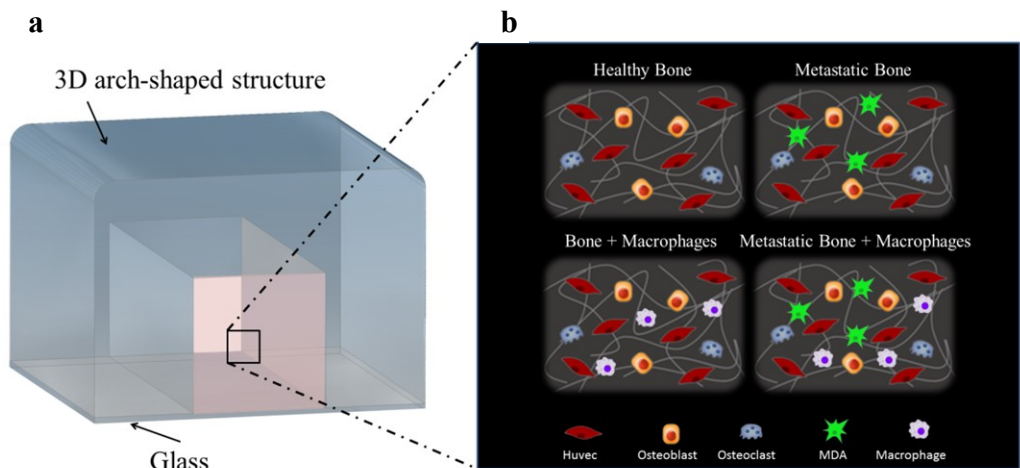
Fig1: (a) 3D PMMA masks were designed according to computational simulations through a CAD software. The external cage appears in grey while the gel is represented in pink. (b) schematics of 3D co-culture.

Osteoblasts were characterized for their ability to secrete bone proteins including collagen I, osteocalcin (OCN) and osteopontin (OPN) (Fig2). In particular, confocal imaging revealed that osteoblasts acquired an elongated morphology and that collagen type I was mainly localized on the cell periphery or secreted in the surrounding extracellular matrix. Osteoclasts were derived from monocytes extracted from whole blood and subsequently differentiated following treatment with macrophage colony-stimulating factor (M-CSF) and RANKL for 14 days. Fully differentiated osteoclasts were characterized in terms of RANK expression, tartrate-resistant acid phosphatase (TRAP) staining and quantification with respect to undifferentiated osteoclasts (Fig2b). Osteoclasts showed a typical rounded morphology with TRAP mainly localized around the cell nucleus. In addition, we observed typical matrix resorbing pseudopodia (yellowarrow) and the formation of multinucleated cells during the process of differentiation (white arrow) (Fig2a).
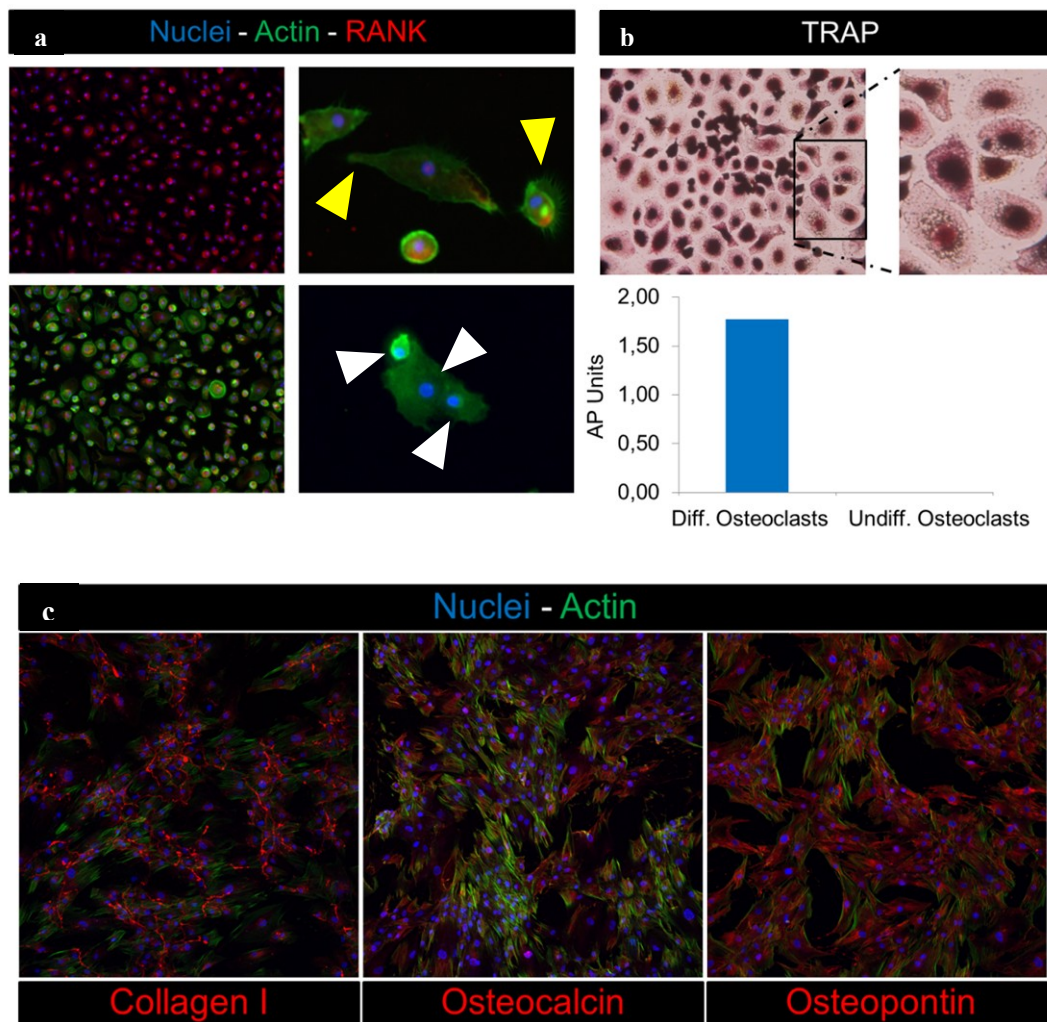
Fig2: (a) Fully differentiated osteoclasts were characterized in terms of RANK expression. (b) tartrate-resistant acid phosphatase (TRAP) staining and quantification with respect to undifferentiated osteoclasts. (c) Osteoblast markers, collagen I, osteocalcin (OCN) and osteopontin (OPN)

Healthy bone tissue constructs were characterized by the presence of interconnected microvascular networks surrounded by elongated osteoblasts which mainly co-localized with the vessels (Fig3). The synergistic relationship between these two cell types was previously reported both *in vivo* and *in vitro* demonstrating

that secreted factors produced by each cell type positively influence the processes of angiogenesis and osteogenesis [31, 32]. Osteoclasts showed a typical rounded phenotype and were imaged either inside the matrix or closely associated with osteoblasts and microvascular networks. This issue is in agreement with *in vivo* observations since osteoblasts and osteoclasts cross-talk through both paracrine secretions and direct contact [33].
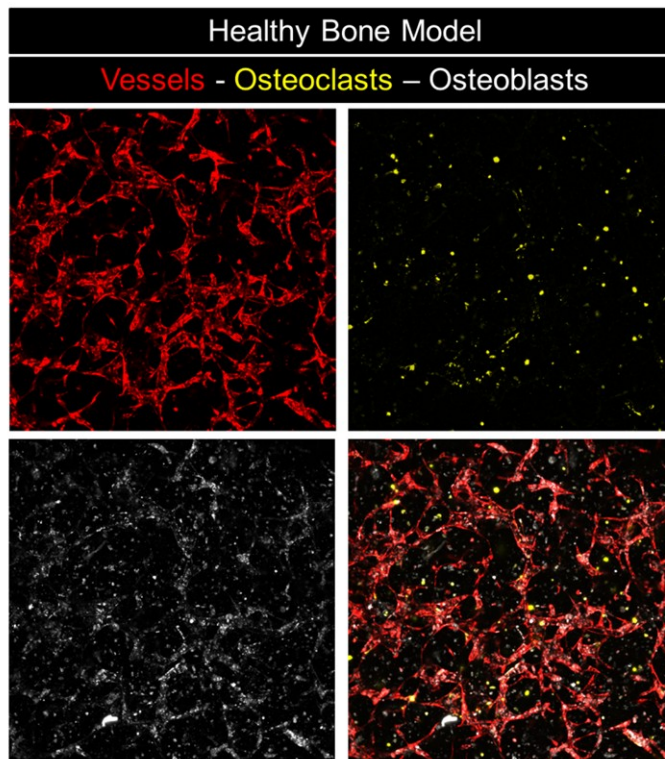

Fig3: Confocal image of 3D healthy bone tissue construct

Surprisingly, breast cancer cells mainly co-localized with microvascular networks in the metastatic bone model forming the typical perivascular niche (magenta arrow) (Fig4).
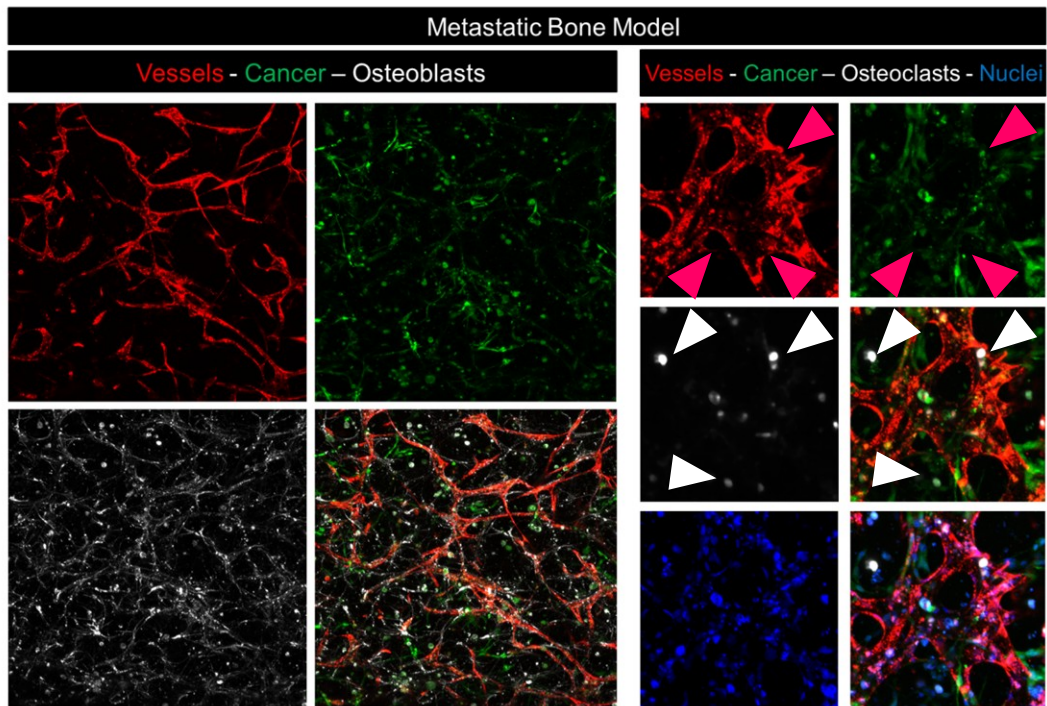
Fig4: Confocal image of 3D bone tissue construct evidencing cancer cell (green) localization at vessel boundaries (magenta arrow)

Previous *in vivo* and simplified *in vitro* models discussed the key role of the perivascular niche in mediating the process of early invasion and regulating the dormancy state experienced by metastatic cancer cells in the colonized environment [21]. Noteworthy, cancer cells introduced within 3D skeletal muscle environments (Fig5a) were not able to elongate, wrap around microvascular networks and finally proliferate as detected within the metastatic bone model (Fig5b).

Fig5: (a) Confocal image of 3D muscle environment. (b) Confocal images of muscle and bone tissue constructs evidencing cancer cell (green) major growth in bone microenvironment respect to the muscle environment

These data extends our previous observations that metastatic breast cancer cells cannot extravasate within muscle-mimicking compared to bone-mimicking
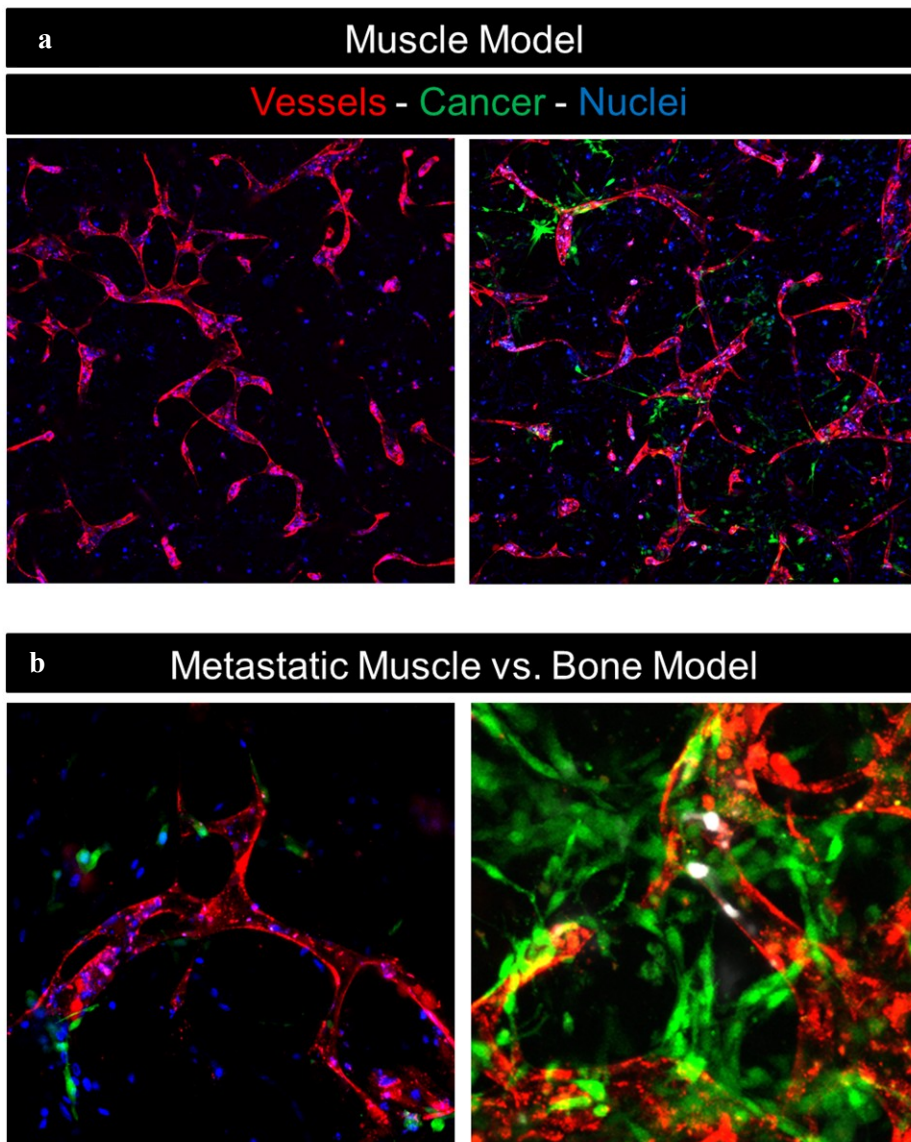
microenvironments [20]. Another key aspect observed in our model was the association between breast cancer cells and osteoclasts (white arrow) (Fig4), which interact through multiple signaling pathways to induce osteolytic metastases [34]. Overall, despite these observations highlight that our healthy and metastatic bone tissue constructs reproduce key features of their *in vivo* counterparts, these models still lack a key component of the basic bone physiological unit, i.e. resident macrophages or osteomacs. These cells are involved in multiple processes including bone remodeling and fracture healing [25], but the role of resident macrophages has been also associated with tissue development and vascularization [35, 36]. Addition of osteomacs to the healthy bone tissue model increased the quality of the microvascular networks in terms of interconnections and ramifications (Fig6a). A key feature observed in the model was that MΘ polarized macrophages added to the system spontaneously differentiated towards an anti-inflammatory M2 phenotype as demonstrated by positive CD163 staining (Fig6b). At the same time, no M1 macrophages were detected within the healthy bone model, as highlighted by the negative staining for Human Leukocyte Antigen - antigen D Related (HLA-DR) (Fig6b).

Fig6: (a) Confocal image of 3D bone environment with macrophages. **(b)** Confocal images macrophages in bone model characterizing the typical M2 polarization of "osteomacs" the bone resident macrophage population.

These findings are in agreement with previous reports demonstrating that inflammatory macrophages are not present in the bone environment under physiological conditions [25]. Regarding tissue vascularization, the role of macrophages is still controversial. Different studies reported that high M2 to M1 ratios increase vascularization, with M2a and M2c polarized macrophages involved in vessel stabilization [35, 36]. Our results are in agreement with these findings, since co-culture with MΘ macrophages generally increased the quality of the network architecture due to their differentiation towards an M2 phenotype. The

metastatic bone model with embedded resident macrophages maintained the major features characterizing the other bone models (Fig7a). Indeed, we found cancer cell-vessel co-localization as well as cancer cell-osteoclast association. In addition superior microvascular network ramification was detected due to the presence of macrophages when compared to metastatic bone tissue constructs without this particular cell type. However, we identified a key difference in macrophage polarization. Indeed, the presence of breast cancer cells induced the macrophage polarization towards an M1 inflammatory phenotype (HLA-DR), which is typical of the early establishment of metastatic foci (Fig7b).
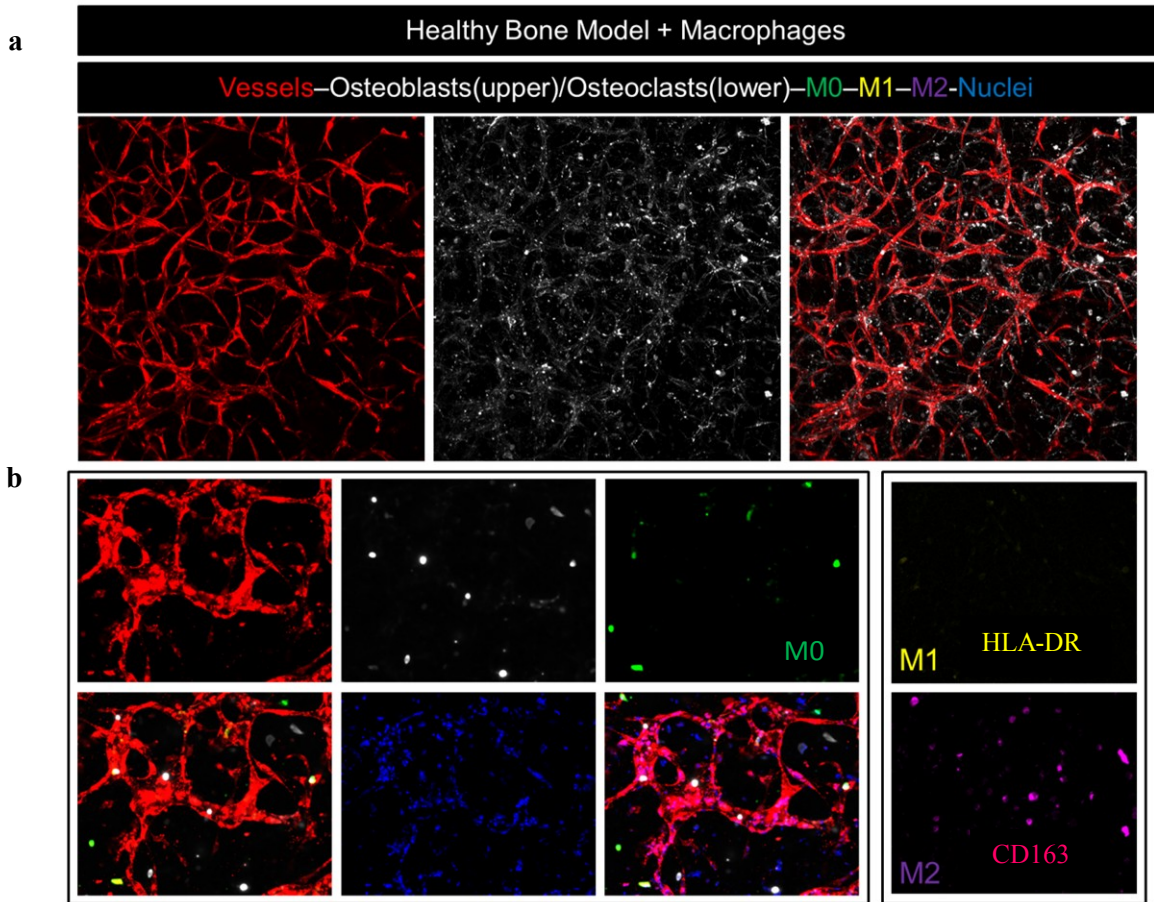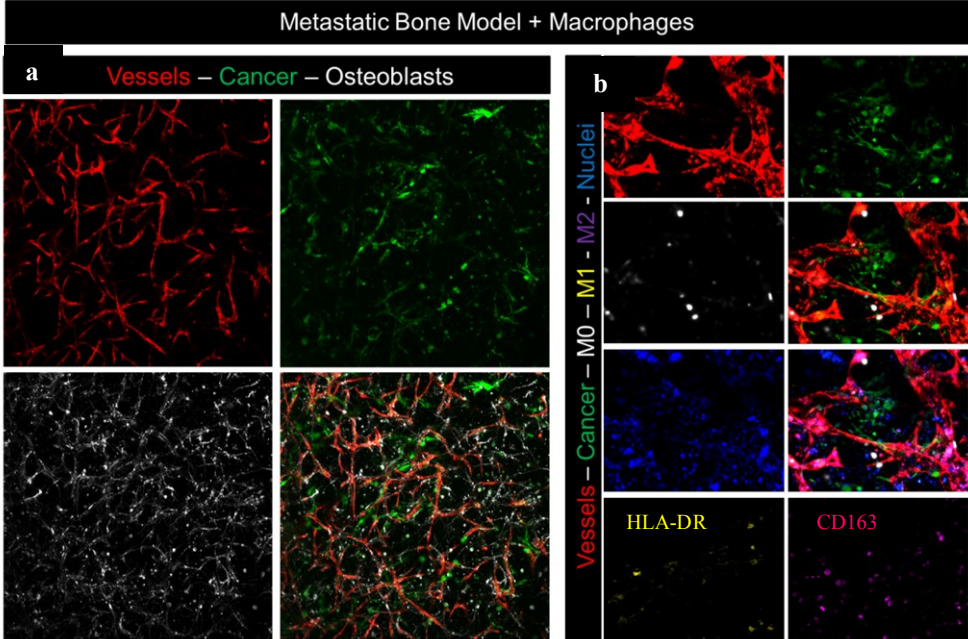

Fig7: (a) Confocal image of 3D bone environment with macrophages. (b) Confocal images macrophages in bone model characterizing the M1 polarization of macrophages in the bone during metastatic colonization.

In this framework, we analyzed the secretion of RANKL and OPG within each 3D vascularized bone model finding significant differences in terms of RANKL/OPG

ratio comparing healthy bone and metastatic bone models (p<0.01), particularly when resident macrophages were introduced (p<0.001) (Fig8).
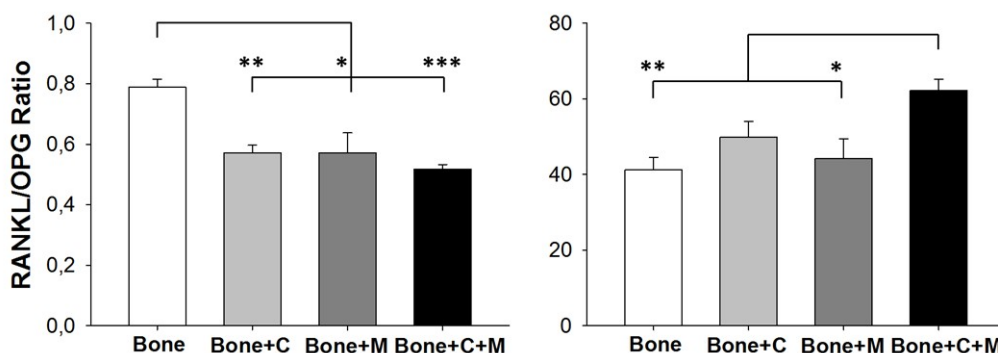
Fig8: ELISA analyses of RANKL/OPG ration and OPG secretion from the bone 3D models

It is interesting to highlight that the difference in the RANKL/OPG ratio was mainly due to changes in OPG rather than in RANKL secretion. Indeed, we found a statistical upregulation of OPG in the metastatic bone model with embedded macrophages compared to healthy bone samples (p<0.01) (Fig8). These data allow to suggest that complex interactions are occurring between cancer cells, resident macrophages and bone cells, since the presence of cancer cells induced macrophage polarization towards an M1 phenotype. We hypothesize that cancer cells induce an inflammatory condition which represents an early stage of breast cancer bone metastases. At the same time OPG secreting osteoblasts [37] try to counterbalance the pro-inflammatory role of interacting cancer cells and macrophages determining the increase in the RANKL/OPG ratio. No previous model was able to analyze the complex environment and events characterizing the formation of the early bone metastatic niche. Indeed, literature studies are generally focused on the study of already established breast cancer macrometastases to the bone with detailed analyses of bone resorption and biochemical imbalances characterizing the RANKL/OPG ratio [38]. In addition, several studies focused on

potential therapeutics to limit bone loss after metastatic colonization [39, 40]. Our models paves the way for a novel scenario focused on the study of the mechanisms driving the early colonization of the bone and the identification of effective treatment to inhibit the development of macrometastases, which are currently incurable.

Concluding, we have engineered novel vascularized human 3D bone models which allowed us to analyze the basic interactions occurring in complex bone environments where osteoblasts, osteoclasts, endothelial cells and resident macrophages cross-talk under physiological and metastatic conditions. We have demonstrated that resident macrophages play a key role in bone homeostasis and that breast cancer cell-induced M1 polarization is associated with changes in bone metabolism representing the establishment of an early bone metastatic niche. We believe in the future exploitation of these new models for the discovery and screening of novel organ-specific therapeutics which could limit or even impair the development of bone metastases rather than treating already established macrometastatic lesions.

7.3. Material and methods

7.3.1 3D mask fabrication

3D arch-shaped masks with 2 mm × 2 mm × 5 mm openings were previously designed through computational simulations [29]. Briefly, following CAD design, poly-methyl-methacrylate cages with two open faces were fabricated by laser cutting and bonded to 100 μm thick glass coverslips. Masks were sterilized with 70% ethanol. Pre-polymerized gels with embedded cell suspensions were encased in the masks and daily monitored during the maturation of the tissue.

7.3.2 Cell culture and hydrogel preparation

Primary red fluorescent protein (RFP)-transfected human umbilical vein endothelial cells (HUVECs) were purchased from Angio-Proteomie, cultured in endothelial growth medium (EGM) 2 (Lonza) and used up to passage 7. Adult human osteoblasts (Sigma) were cultured in dulbecco's modified eagle medium (DMEM, Life Technologies) with addition of 15% fetal bovine serum (FBS, Hyclone), 1% penicillin-streptomycin-glutamine (PSG, Life Technologies) and 1% fungizone. Osteoclasts and MΘ macrophages were differentiated from circulating monocytes isolated from whole blood following previously optimized protocols [12]. Monocytes were cultured in RPMI containing 10% FBS, 1% PSG, 1% fungizone and 25 ng/ml M-CSF to promote MΘ macrophage differentiation. After 24 h, attached macrophages were cultured in the same medium while osteoclasts were differentiated from MΘ macrophages by adding 50 ng/ml RANKL to the cell culture medium. Green fluorescent protein (GFP)-transfected MDA-231 breast cancer cells were cultured in DMEM supplemented with 10% FBS and 1% PSG. Cells were embedded in 2.5 mg/ml fibrin hydrogels with the following final concentrations: 3 Mcells/ml ECs, 1.5 Mcells/ml osteoblasts, 150,000 cells/ml osteoclasts, 150,000 cells/ml MΘ macrophages and 150,000 cells/ml breast cancer cells. Four different models were designed: healthy bone tissue containing ECs, osteoblasts and osteoclasts; metastatic bone tissue containing ECs, osteoblasts, osteoclasts and breast cancer cells; healthy and metastatic bone tissues with embedded resident MΘ macrophages. Hydrogels were polymerized within humidity boxes at 37° for 20 min and cultured in EGM-2 until day 7.

7.3.3 Immunofluorescence, tartrate resistant acid phosphatase (TRAP) assay and ELISA

Immunofluorescent staining for RANK (mouse anti-human, santacruz, 1:50), collagen type I (rabbit anti-human, abcam, 1:500), osteocalcin (rabbit anti-human, abcam, 1:100), osteopontin (rabbit anti-human, abcam, 1:100), HLA-DR (mouse anti-human, biolegend, 5 μg/ml), CD163 (rabbit anti-human, santacruz, 1:50) were performed following cell fixation with 2% paraformaldehyde, membrane permeabilization with 0.1% Triton-X 100 and overnight incubation with 5% bovine serum albumin at 4°. Following 24 h incubation (extruded 3D samples) or overnight incubation (2D samples) at 4°, samples were washed in phosphate buffered saline (PBS, Life Technologies) and secondary antibodies were incubated following the same protocol applied to primary antibodies. More in detail, we used goat anti-rabbit or goat anti-mouse Alexa Fluor 647 (Life Technologies, 1:200). If required, samples were stained with phalloidin (1:100, Life Technologies) and DAPI (300 nM final concentration).

TRAP staining and quantification were performed following manufacturer instructions. Finally, samples were twice rinsed in PBS and observed under a confocal microscope (Nikon Eclipse Ti).

ELISA kits for RANKL and OPG were purchased from Boster Biological and Ray Biotech, respectively.

7.3.4 Statistical Analysis

Prism Graph Pad software was used to perform Analysis of variance (ANOVA) and unpaired Student's t-test. ANOVA was followed by Bonferroni post-hoc test to determine significant differences between groups. Differences were considered significant for $p < 0.05$ (*), $p < 0.01$ (**) and $p < 0.005$ (***). Results are presented as mean ± standard error of the mean.

References

[1] Paget S. The distribution of secondary growths in cancer of the breast. 1889. Cancer Metastasis Rev. 1989;8:98-101.

[2] Bersini S, Jeon JS, Moretti M, Kamm RD. In vitro models of the metastatic cascade: from local invasion to extravasation. Drug Discov Today. 2014;19:735-42.

[3] Coleman RE. Bone cancer in 2011: Prevention and treatment of bone metastases. Nat Rev Clin Oncol. 2012;9:76-8.

[4] Parlakian A, Gomaa I, Solly S, Arandel L, Mahale A, Born G, et al. Skeletal muscle phenotypically converts and selectively inhibits metastatic cells in mice. PLoS One. 2010;5:e9299.

[5] Shay T, Jojic V, Zuk O, Rothamel K, Puyraimond-Zemmour D, Feng T, et al. Conservation and divergence in the transcriptional programs of the human and mouse immune systems. Proc Natl Acad Sci U S A. 2013;110:2946-51.

[6] Ma J, van den Beucken JJ, Yang F, Both SK, Cui FZ, Pan J, et al. Coculture of osteoblasts and endothelial cells: optimization of culture medium and cell ratio. Tissue Eng Part C Methods. 2011;17:349-57.

[7] Correia C, Grayson W, Eton R, Gimble JM, Sousa RA, Reis RL, et al. Human adipose-derived cells can serve as a single-cell source for the in vitro cultivation of vascularized bone grafts. J Tissue Eng Regen Med. 2012.

[8] Correia C, Grayson WL, Park M, Hutton D, Zhou B, Guo XE, et al. In vitro model of vascularized bone: synergizing vascular development and osteogenesis. PLoS One. 2011;6:e28352.

[9] Correia C, Bhumiratana S, Sousa RA, Reis RL, Vunjak-Novakovic G. Sequential application of steady and pulsatile medium perfusion enhanced the formation of engineered bone. Tissue Eng Part A. 2013;19:1244-54.

[10] Thein-Han W, Xu HH. Prevascularization of a gas-foaming macroporous calcium phosphate cement scaffold via coculture of human umbilical vein endothelial cells and osteoblasts. Tissue Eng Part A. 2013;19:1675-85.

[11] Rao RR, Ceccarelli J, Vigen ML, Gudur M, Singh R, Deng CX, et al. Effects of hydroxyapatite on endothelial network formation in collagen/fibrin composite hydrogels in vitro and in vivo. Acta Biomater. 2014.

[12] Bongio M, Lopa S, Gilardi M, Bersini S, Moretti M. A 3D vascularized bone remodeling model combining osteoblasts and osteoclasts in a CaP nanoparticle-enriched matrix. Nanomedicine (Lond). 2016;11:1073-91.

[13] Papadimitropoulos A, Scherberich A, Guven S, Theilgaard N, Crooijmans HJ, Santini F, et al. A 3D in vitro bone organ model using human progenitor cells. Eur Cell Mater. 2011;21:445-58; discussion 58.

[14] Krishnan V, Vogler EA, Sosnoski DM, Mastro AM. In vitro mimics of bone remodeling and the vicious cycle of cancer in bone. J Cell Physiol. 2014;229:453-62.

[15] Mastro AM, Vogler EA. A three-dimensional osteogenic tissue model for the study of metastatic tumor cell interactions with bone. Cancer Res. 2009;69:4097-100.

[16] Salamanna F, Borsari V, Brogini S, Giavaresi G, Parrilli A, Cepollaro S, et al. An in vitro 3D bone metastasis model by using a human bone tissue culture and human sex-related cancer cells. Oncotarget. 2016.

[17] Kusumbe AP, Ramasamy SK, Adams RH. Coupling of angiogenesis and osteogenesis by a specific vessel subtype in bone. Nature. 2014;507:323-8.

[18] Ramasamy SK, Kusumbe AP, Schiller M, Zeuschner D, Bixel MG, Milia C, et al. Blood flow controls bone vascular function and osteogenesis. Nat Commun. 2016;7:13601.

[19] Bersini S, Jeon JS, Dubini G, Arrigoni C, Chung S, Charest JL, et al. A microfluidic 3D in vitro model for specificity of breast cancer metastasis to bone. Biomaterials. 2014;35:2454-61.

[20] Jeon JS, Bersini S, Gilardi M, Dubini G, Charest JL, Moretti M, et al. Human 3D vascularized organotypic microfluidic assays to study breast cancer cell extravasation. Proc Natl Acad Sci U S A. 2015;112:214-9.

[21] Ghajar CM, Peinado H, Mori H, Matei IR, Evason KJ, Brazier H, et al. The perivascular niche regulates breast tumour dormancy. Nat Cell Biol. 2013;15:807-17.

[22] Arrigoni C, De Luca P, Gilardi M, Previdi S, Broggini M, Moretti M. Direct but not indirect co-culture with osteogenically differentiated human bone marrow stromal cells increases RANKL/OPG ratio in human breast cancer cells generating bone metastases. Mol Cancer. 2014;13:238.

[23] Bussard KM, Gay CV, Mastro AM. The bone microenvironment in metastasis; what is special about bone? Cancer Metastasis Rev. 2008;27:41-55.

[24] Ell B, Kang Y. SnapShot: Bone Metastasis. Cell. 2012;151:690- e1.

[25] Wu AC, Raggatt LJ, Alexander KA, Pettit AR. Unraveling macrophage contributions to bone repair. Bonekey Rep. 2013;2:373.

[26] Chang MK, Raggatt LJ, Alexander KA, Kuliwaba JS, Fazzalari NL, Schroder K, et al. Osteal tissue macrophages are intercalated throughout human and mouse bone lining tissues and regulate osteoblast function in vitro and in vivo. J Immunol. 2008;181:1232-44.

[27] Lewis CE, Harney AS, Pollard JW. The Multifaceted Role of Perivascular Macrophages in Tumors. Cancer Cell. 2016;30:365.

[28] Arrigoni C, Bersini S, Gilardi M, Moretti M. In Vitro Co-Culture Models of Breast Cancer Metastatic Progression towards Bone. Int J Mol Sci. 2016;17.

[29] Bersini S, Gilardi M, Arrigoni C, Talo G, Zamai M, Zagra L, et al. Human in vitro 3D co-culture model to engineer vascularized bone-mimicking tissues combining computational tools and statistical experimental approach. Biomaterials. 2016;76:157-72.

[30] Arrigoni C, Bongio M, Talo G, Bersini S, Enomoto J, Fukuda J, et al. Rational Design of Prevascularized Large 3D Tissue Constructs Using Computational

Simulations and Biofabrication of Geometrically Controlled Microvessels. Adv Healthc Mater. 2016;5:1617-26.

[31] Ramasamy SK, Kusumbe AP, Wang L, Adams RH. Endothelial Notch activity promotes angiogenesis and osteogenesis in bone. Nature. 2014;507:376-80.

[32] Kim J, Kim HN, Lim KT, Kim Y, Pandey S, Garg P, et al. Synergistic effects of nanotopography and co-culture with endothelial cells on osteogenesis of mesenchymal stem cells. Biomaterials. 2013;34:7257-68.

[33] Florencio-Silva R, Sasso GR, Sasso-Cerri E, Simoes MJ, Cerri PS. Biology of Bone Tissue: Structure, Function, and Factors That Influence Bone Cells. Biomed Res Int. 2015;2015:421746.

[34] Andrade K, Fornetti J, Zhao L, Miller SC, Randall RL, Anderson N, et al. RON kinase: A target for treatment of cancer-induced bone destruction and osteoporosis. Sci Transl Med. 2017;9.

[35] Spiller KL, Anfang RR, Spiller KJ, Ng J, Nakazawa KR, Daulton JW, et al. The role of macrophage phenotype in vascularization of tissue engineering scaffolds. Biomaterials. 2014;35:4477-88.

[36] Spiller KL, Nassiri S, Witherel CE, Anfang RR, Ng J, Nakazawa KR, et al. Sequential delivery of immunomodulatory cytokines to facilitate the M1-to-M2 transition of macrophages and enhance vascularization of bone scaffolds. Biomaterials. 2015;37:194-207.

[37] Boyce BF, Xing L. Functions of RANKL/RANK/OPG in bone modeling and remodeling. Arch Biochem Biophys. 2008;473:139-46.

[38] Canon JR, Roudier M, Bryant R, Morony S, Stolina M, Kostenuik PJ, et al. Inhibition of RANKL blocks skeletal tumor progression and improves survival in a mouse model of breast cancer bone metastasis. Clin Exp Metastasis. 2008;25:119-29.

[39] Canon J, Bryant R, Roudier M, Branstetter DG, Dougall WC. RANKL inhibition combined with tamoxifen treatment increases anti-tumor efficacy and prevents tumor-induced bone destruction in an estrogen receptor-positive breast cancer bone metastasis model. Breast Cancer Res Treat. 2012;135:771-80.

[40] van Beek ER, Lowik CW, van Wijngaarden J, Ebetino FH, Papapoulos SE. Synergistic effect of bisphosphonate and docetaxel on the growth of bone metastasis in an animal model of established metastatic bone disease. Breast Cancer Res Treat. 2009;118:307-13.

Chapter 8

Molecular signatures of human organ-specific endothelial cell heterogeneity in metastatic progression to bone

From: C. Arrigoni*, M. Gilardi*, S. Bersini, P. Ostano, MR Bani, M. Broggini, RD Kamm, G. Chiorino, M. Moretti,
 *equally contributing authors

8.1. Main text

Metastasis is the most devastating consequence of cancer. It is composed by a complex multistep processes resulting in spread of tumor cells to secondary sites in various organs. The metastatic dissemination is not a random process (1). Once reached the circulatory system tumor cells encounter different environmental challenges and stimuli that profoundly regulate their metastatic potential and extravasation site. In fact, different tumor types show preferential homing to specific organs and in particular the most common sites of bone metastases are the spine, the ribs, the femur and the skull. Breast cancer preferentially metastasizes to the bones and lungs. (2-5), but not to skeletal muscle (5, 6). Furthermore, bone metastases occur in up to 70 percent of patients with advanced breast or prostate cancer (7). Even though many factors have been identified to contribute to the preferential homing of different subtypes of primary tumor to specific secondary

loci (8) however no one is able to exhaustively elucidate the preferential metastatization of breast cancer to bone.

Recently the most accepted hypothesis is that the initial delivery and arrest of cancer cells to specific vascular districts it is probably primarily 'mechanical' according with Ewing theory. After that, once seeded the secondary organ, cancer cells growth is dependent on the affinity of the 'seed' with the 'soil' according with Paget theory (9).

Preferential homing of breast cancer to bone could be explain by the fenestrated structure of the bone marrow sinusoid capillaries, high blood flow rate in the red marrow areas and on tumor cells adhesive capacity to attach the bone matrix and stroma cells (6, 7). Furthermore, the cell types composing the vascular-bone niche play an important role in bone metastasis establishment (10). In this context, the endothelium starts to get an important consideration in the landscape of the factors driving organotypic metastases. In fact, the last key event of cancer progression before the secondary organ site is the interaction of cancer cells with the vessels through extravasation process (11). In particular, the Vascular adhesion of cancer cells is the first step of the extravasation process which mostly requires size trapping and the expression of specific and coupled ligands and receptors on cancer cells and endothelium. A wide range of ligands and receptors contribute to the process, including selectins, integrins, cadherins which are selectively expressed in different vascular beds (12).

Recently, in this framework, Nolan et al. highlighted the existence of tissue specific molecular signatures in microvascular endothelial cells after isolation from different organs. Even though these results evidenced interesting unique gene expression in diverse vascular beds, however this study was performed in mouse tissues which could lead in aberrant results in further clinical trial due to species specific differences (13).

In human context, our group recently demonstrated that the 3D co-culture of primary human endothelial and muscle cells induced the expression of muscle endothelial specific signatures on endothelium due to the intricated signaling in the engineered vascularized micro-environment. Furthermore, through 3D microvasculature in microfluidic model, we demonstrated that the organ specificity is the driver of the preferential breast cancer cell extravasation to bone instead to muscle (5). However, in human, endothelial specific signatures peculiar of different organs have not been previously coupled with organ specific tropism of metastases. The reason why this challenge and ambitious hypothesis has not been verified yet could be the limited availability of human tissue belonging to a unique donor and the difficulties in the isolation of pure human microvascular endothelial cell populations (14).

Here, we reported the isolation of human pure bone (Bec+) and muscle (Mec+) microvascular endothelial cell population from the same donor. In addition, we have focused on the isolation of specific tissue counterpart represented by the bone (Bec-) and muscle (Mec-) stromal cells .Furthermore, employing microarray profiling, we demonstrated the existence of vascular heterogeneity in human bone and muscle endothelia. These results led to the identification of new potential targets gathered together in a "target list" including only endothelial specific signature of bone and muscle which will be exploited to identify cancer homing drivers to the bone.

After hip surgery and informed consensus we collected bone and muscle tissue biopsies from healthy donors. More in detail, we optimized the tissue digestion procedure, by adapting the most promising approaches to our fine aim. In particular, bone biopsies were finely chopped in small pieces and enzymatically digested to harvest tissue embedded cells. In particular, trabecular bone tissue has been fragmented in small pieces (around 2 mm) with tweezers and a scalpel, before being digested in a collagenase type I solution at 2 mg/ml, for 1 hour at 37°C in an

orbital shaker. After digestion, the cell solution was filtered through a 100 um cell strainer and an heterogeneous cell suspension, containing mostly red blood cells was obtained, and adherent cells were visible by day 3 from plating on a fibronectin coated flask (Fig a and b).
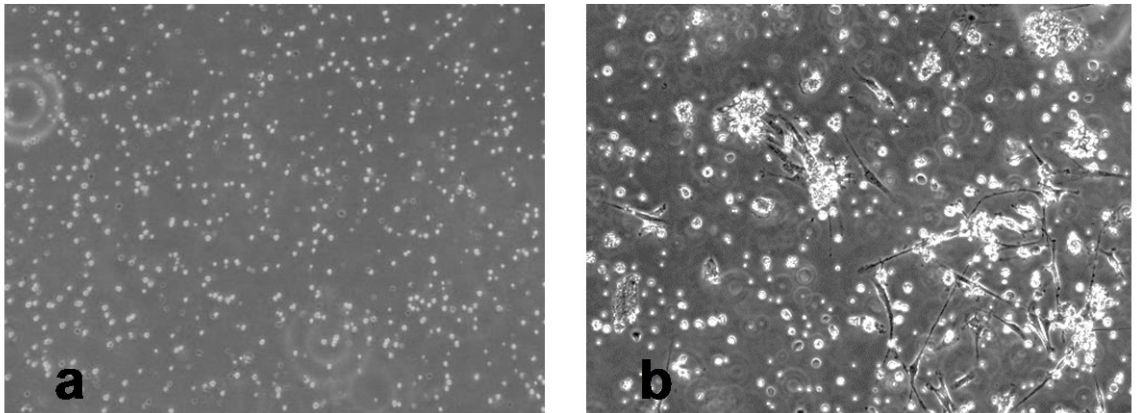

Fig1: (a) cell suspension after bone digestion and plating, (b) adherent cells after 3 days

Adherent cells were of heterogeneous phenotype, being composed of both endothelial-like cells and more elongated, mesenchymal-like cells. To sort the endothelial cell population present in the flask we used immunomagnetic sorting (Dynabeads) based on CD31, a widely recognized endothelial marker (15). Generally, two rounds of selection with CD31 immunomagnetic beads were necessary to obtain a sufficiently pure population.

After sorting, we re-plated positive and negative cells on two different flasks, obtaining phenotypically distinct populations. CD31 negative cells were homogeneously distributed, elongated and grew faster than the endothelial population, which presented small clones with rounded morphology and cobblestone appearance (Fig2a and b).

After two passages in culture cells were partly frozen for RNA extraction and a last aliquot was conserved for subsequent experiments.
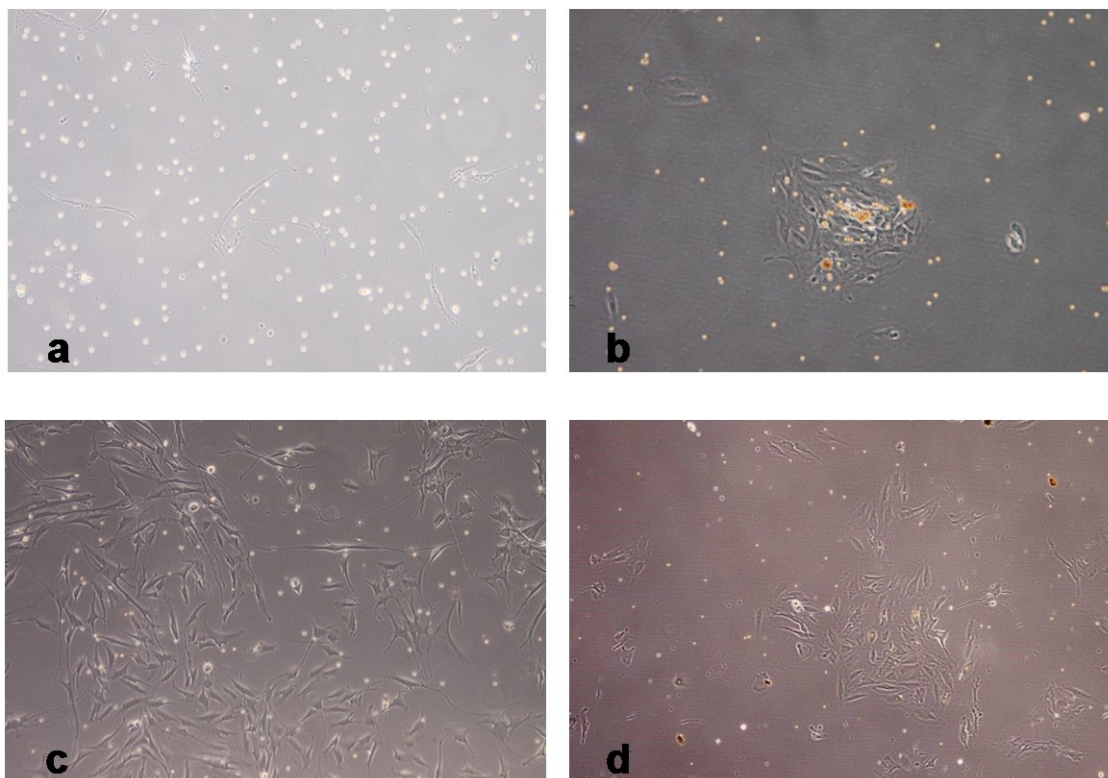
Fig2: upper row, after 3 days from selection: (a) CD31 negative fraction, (b) CD31 positive fraction: immunomagnetic beads are visible in the cells. Lower row: after 6 days from selection: (c) CD31 negative fraction, (d) CD31 positive fraction

Isolated bone specific endothelial cells were characterized through immunofluorescence for specific endothelial markers after the plating on the glass slide. Fluorescent images showed the visible formation of cell-cell junction in multiple areas, as demonstrated by the positive, organized staining for VE-cadherin (Fig3a). CD31 and UEA-1 were found expressed in all the cells, demonstrating the obtainment of a pure endothelial population (Fig3b and c).
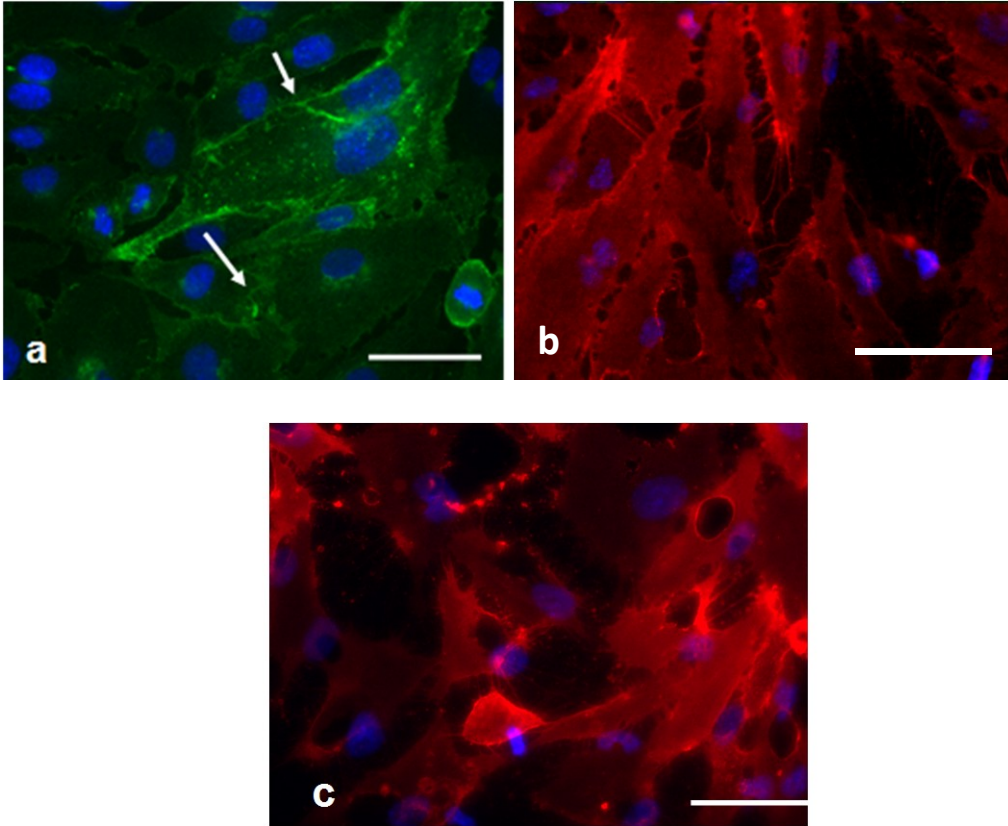
Fig3: immunofluorescence for endothelial markers in bone endothelial cells (a) VE-cadherin (green), (b) CD31 (red),(c) UEA-1 (red) In all images nuclei ar countertained with Nuc-blu® (blue).Scale bars: 50um

Regarding muscle specific endothelial cell isolation we elaborated a novel protocol, based on existing procedures used for animal tissues, to harvest ECs from human skeletal muscle. Particularly, muscle tissue from patient biopsy was fragmented in small pieces (around 1 mm) with tweezers and scissors, then it was digested in an enzymatic mix (Miltenyi Biotech), for 1 hour at 37°C in an orbital shaker. An heterogeneous cell suspension, containing cells and extracellular matrix residues was obtained and filtered through a 70 um cell strainer. After that, cell suspension was then immediately subjected to CD31 positive immunomagnetic selection (Miltenyi). A further selection was carried out due to the presence of cells of non-

endothelial phenotype, with UEA-1 coated immunomagnetic beads. two rounds of immunomgnetic selection, it was possible to obtain a purer population of ECs and the plating of CD31 negative population resulting from the first selection brought to a population of cells similar to myoblasts (Fig4a and b).
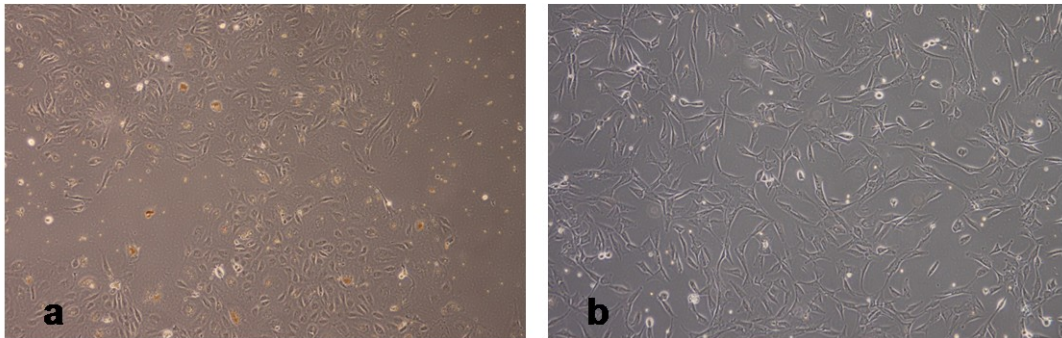
Fig4: (a) confluent muscle endothelial cells obtained with the optimized protocol (b) CD31 negative fraction, 6 days after selection.

To characterize the obtained skeletal muscle endothelial cells, we performed an immunostaining for typical endothelial markers, showing the expression of VE-cadherin in some areas of the cell monolayer associated to the expression of CD31 and UEA-1 in all the cells (Fig5). As for bone cells, also muscle ECs can be frozen and thawed for further experiment, retaining viability
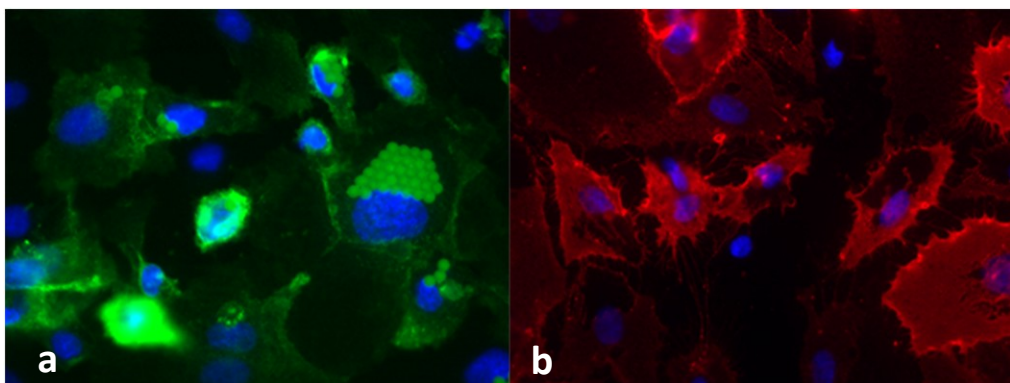
Fig5: immunofluorescence for endothelial markers in muscle endothelial cells (a) VE-cadherin (green), (b) CD31 (red), (c) UEA-1 (red) In all images nuclei ar countertained with Nuc-blu® (blue). White arrows indicate cell- cell junctions stained with VE-cadherin. Scale bars: 50um

Once demonstrated that isolated cells are actually endothelial cells from bone and muscle tissues, we performed gene expression profiling (GEP) to identifies organ specific signatures peculiar of each cell population. We focused on the analyses of two patients gene expressio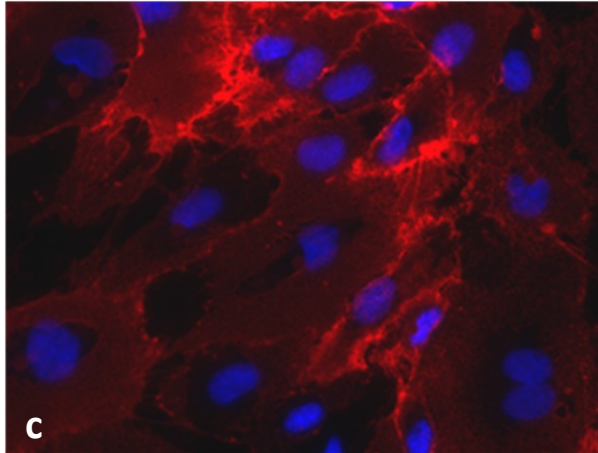n profiling. Given that different people are characterized by heterogeneous gene expression profiles, we specifically analyzed coupled population of endothelial cells from bone and muscle tissues harvested from the same donor. In fact this approach allow us to avoid aberrant results due to differences in patients instead to tissue specific endothelia.

More in detail, RNA extraction (PureLink RNA Mini Kit Ambion) followed by DNAse treatment were performed on isolated endothelial cells from the both populations. After that mRNA quality control and quantitation were performed (Fig6). The RNA Integrity Number (RIN) indicated the high quality of all RNA samples. Then, RNA amplification and labeling, quality control and microarray hybridization were carried out as previously described (16).
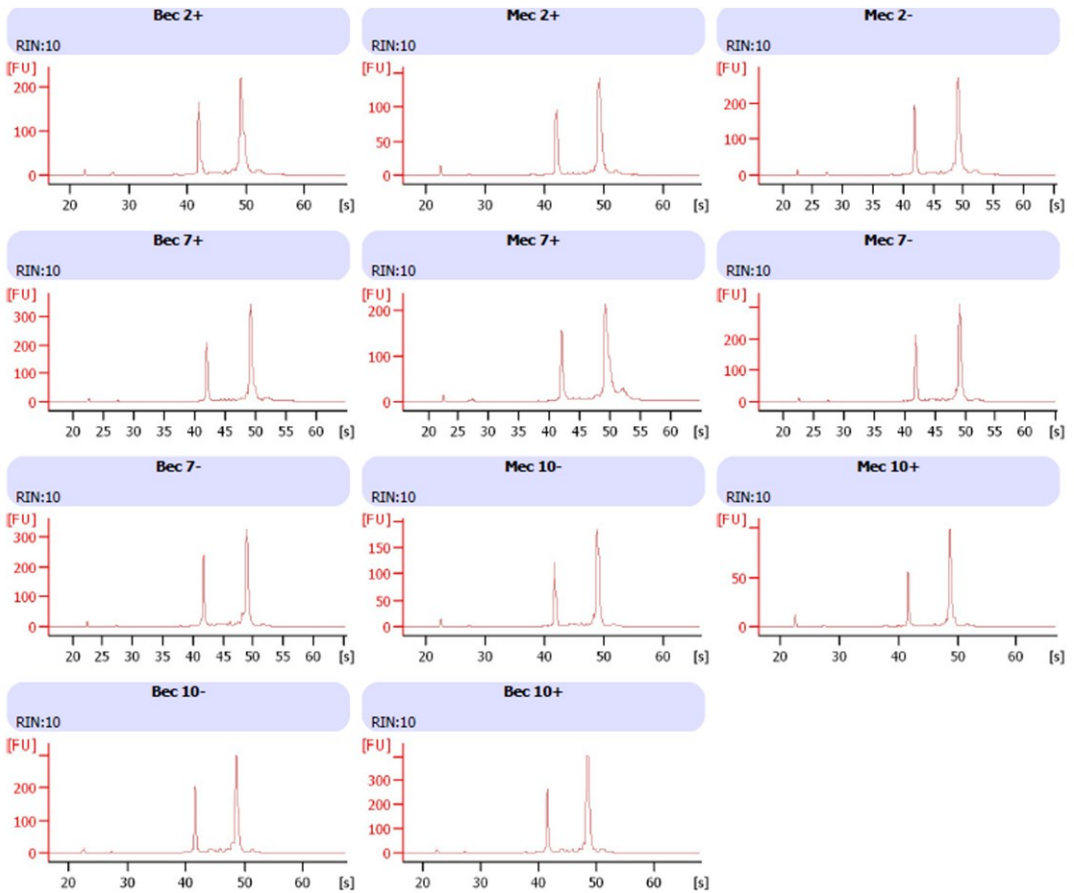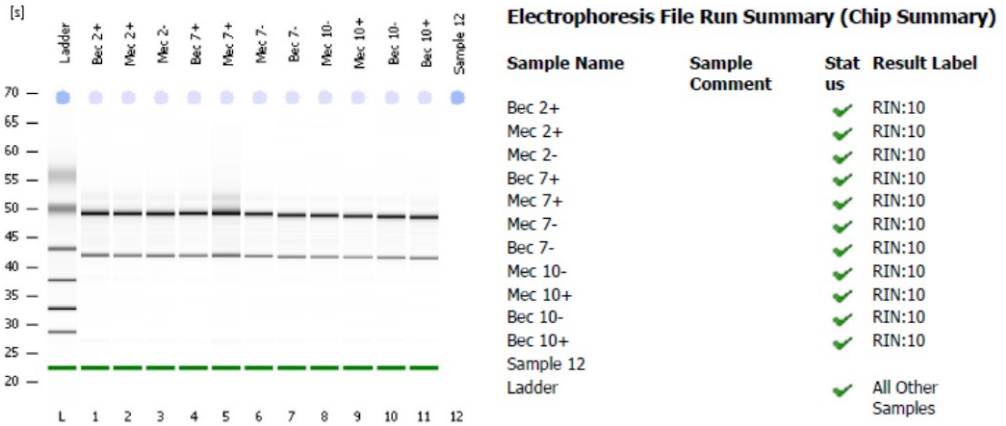
Fig6: Quality control of RNA samples through bioanalyzer

The one color microarray (SurePrint G3 Human Gene Expression v3 8x60K Microarray Kit) were utilized for the sample analysis. Slides were scanned with the Agilent G2505B scanner and the TIFF images loaded into the Feature Extraction software (Agilent Technologies). Raw data were first background corrected and then processed using the statistical computing software ''R''. In order to set log-ratios average to zero within each array and to have similar log-ratio distributions across all arrays, "quantile'' normalization were performed (17). Subsequentially, ''limma'' was used for preprocessing and differential expression analysis. Gene ontology analysis was accomplished with pathway analysis with ''MetaCore 5.0'' (GeneGO, St. Joseph, MI). The first hierarchical clustering (Fig7) of data demonstrated that endothelial cells from the same tissue had more common signatures respect to the cells belonging to the same person. This highlighted the effective existence of bone and muscle specific characteristics in tissue specific human endothelia.
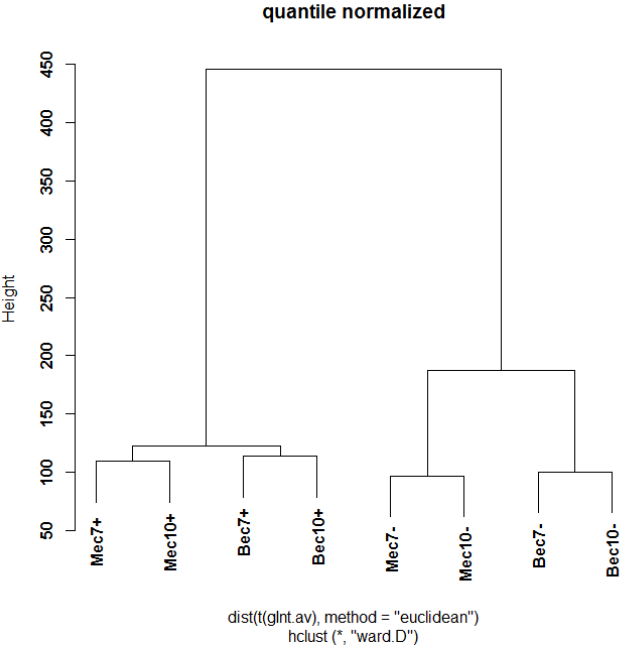
Fig7: Hierarchical clustering of microarray profiling data

Differential expression in genes expression profiles comparing Mec+ vs Bec+ (Fig8) identified 461 up regulated genes in muscle endothelial cells respect to 176 genes down regulated.

Some of these genes could be responsible of the preferential homing of breast cancer to bone instead the muscle as we previously showed in chapters 3 and 7 (5).

	Sonde UP-regolate	Sonde DOWN-regolate
Mec+ vs Bec+	461	176
Mec- vs Bec-	786	727

Absolute logFC > 1 and pvalue < 0.01

Fig8: Differentially expressed genes by comparing Mec+ vs Bec+ expression profiles

A further refinement of analyses reported in Venn diagrams (Fig9) let us exclude some of the genes which are expressed both by stromal and endothelial cells of specific tissue. This refinement was necessary to include in the target list only the real endothelial specific genes.
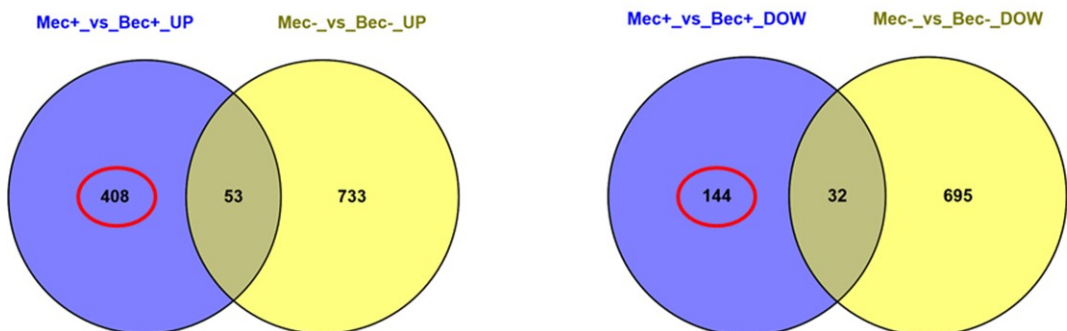
Fig9: Venn diagram of differentially expressed genes by comparing Mec+ vs Bec+ expression profiles. In red circles only the genes expressed by Mec+ and Bec+ excluding those in common with Mec- and Bec-.

To date many studies focused on cancer organotropism to secondary organ site in metastatic progression (3, 8, 9, 18-20). In addition, it has been recently shown that *in vivo* endothelia in mice acquire organ-specific genotypic and phenotypic signatures contributing to organotypic features of the vasculature (21). However, in our knowledge, probably due to the challenging isolation of the delicate primary endothelial cells no data was previously published reporting the presence of human endothelial specificity in bone and muscle tissue.

It is now evident that the human vasculature is more than an inert conduit for blood flow. In particular, in this project we demonstrated that the microvascular bed of bone and muscle, beyond structural differences (21, 22), is composed of specialized ECs, expressing unique plethora of genes including angiocrine molecules, transcription factors, adhesion molecules and chemokines.

The metastatic mechanisms seems not only dependent to the primary tumor characteristics but rather they appear more complex involving the interaction of all members of the early metastatic niche (23, 24) in particular the endothelium (11). In fact our hypothesis was that among the molecules characterizing endothelium, specific differences is hidden the key of organotropism of breast cancer to bone.

In the future, we will verify the actual importance of the genes contained in the list with the aim to identify potential targets for new anti-metastatic therapies. These therapies will be combined, they will be able to challenge not only cancer cells but they will prevent the supportive function of the micro environment in metastatic progression.

References

1. Cristofanilli M*, et al.* (2004) Circulating tumor cells, disease progression, and survival in metastatic breast cancer. *The New England journal of medicine* 351(8):781-791.
2. Kang Y*, et al.* (2005) Breast cancer bone metastasis mediated by the Smad tumor suppressor pathway. *Proc Natl Acad Sci U S A* 102(39):13909-13914.
3. Minn AJ*, et al.* (2005) Distinct organ-specific metastatic potential of individual breast cancer cells and primary tumors. *J Clin Invest* 115(1):44-55.
4. Arrigoni C*, et al.* (2014) Direct but not indirect co-culture with osteogenically differentiated human bone marrow stromal cells increases RANKL/OPG ratio in human breast cancer cells generating bone metastases. *Mol Cancer* 13:238.
5. Jeon JS*, et al.* (2015) Human 3D vascularized organotypic microfluidic assays to study breast cancer cell extravasation. *Proc Natl Acad Sci U S A* 112(1):214-219.
6. Parlakian A*, et al.* (2010) Skeletal muscle phenotypically converts and selectively inhibits metastatic cells in mice. *PLoS One* 5(2):e9299.
7. Roodman GD (2004) Mechanisms of bone metastasis. *Discovery medicine* 4(22):144-148.
8. Nguyen DX, Bos PD, & Massague J (2009) Metastasis: from dissemination to organ-specific colonization. *Nat Rev Cancer* 9(4):274-284.
9. Massague J & Obenauf AC (2016) Metastatic colonization by circulating tumour cells. *Nature* 529(7586):298-306.
10. Ghajar CM*, et al.* (2013) The perivascular niche regulates breast tumour dormancy. *Nat Cell Biol* 15(7):807-817.
11. Reymond N, d'Agua BB, & Ridley AJ (2013) Crossing the endothelial barrier during metastasis. *Nat Rev Cancer* 13(12):858-870.
12. Barthel SR*, et al.* (2013) Definition of molecular determinants of prostate cancer cell bone extravasation. *Cancer Res* 73(2):942-952.
13. Shay T, Lederer JA, & Benoist C (2015) Genomic responses to inflammation in mouse models mimic humans: we concur, apples to oranges comparisons won't do. *Proc Natl Acad Sci U S A* 112(4):E346.
14. Gorman MW, Bassingthwaighte JB, Olsson RA, & Sparks HV (1986) Endothelial cell uptake of adenosine in canine skeletal muscle. *Am J Physiol* 250(3 Pt 2):H482-489.
15. Hewett PW & Murray JC (1993) Human microvessel endothelial cells: isolation, culture and characterization. *In vitro cellular & developmental biology. Animal* 29A(11):823-830.

16. Deaglio S, *et al.* (2007) CD38 and ZAP-70 are functionally linked and mark CLL cells with high migratory potential. *Blood* 110(12):4012-4021.

17. Smyth GK (2004) Linear models and empirical bayes methods for assessing differential expression in microarray experiments. *Statistical applications in genetics and molecular biology* 3:Article3.

18. Valastyan S & Weinberg RA (2011) Tumor metastasis: molecular insights and evolving paradigms. *Cell* 147(2):275-292.

19. Nguyen DX, *et al.* (2009) WNT/TCF signaling through LEF1 and HOXB9 mediates lung adenocarcinoma metastasis. *Cell* 138(1):51-62.

20. Zhang XH, *et al.* (2013) Selection of bone metastasis seeds by mesenchymal signals in the primary tumor stroma. *Cell* 154(5):1060-1073.

21. Nolan DJ, *et al.* (2013) Molecular signatures of tissue-specific microvascular endothelial cell heterogeneity in organ maintenance and regeneration. *Developmental cell* 26(2):204-219.

22. Butler JM, *et al.* (2010) Endothelial cells are essential for the self-renewal and repopulation of Notch-dependent hematopoietic stem cells. *Cell Stem Cell* 6(3):251-264.

23. Labelle M, Begum S, & Hynes RO (2014) Platelets guide the formation of early metastatic niches. *Proc Natl Acad Sci U S A* 111(30):E3053-3061.

24. Labelle M & Hynes RO (2012) The initial hours of metastasis: the importance of cooperative host-tumor cell interactions during hematogenous dissemination. *Cancer discovery* 2(12):1091-1099.

Chapter9

The driving role of FAK^{s732} phosphorylation in cancer cell extravasation dissected by human vascularized 3d microfluidic models

From: M. Gilardi, S. Bersini, S. Valtorta, A. Boussommier-Calleja, M. Labelle, RM Moresco, M. Vanoni, M. Moretti, RD Kamm

Article in preparation

9.1 Introduction

Metastasis is a complex process which is responsible of more than 90% of cancer related mortality (1). The extravasation, a key step in metastatic cascade, is a sequence of tightly concerted interactions between cancer cells and vessels which has been defined as a rate-regulating step for the establishment of metastases (2). Extravasation can be dissected in three main steps: adhesion to endothelium, trans endothelial migration (TEM) and early invasion of the secondary site (Fig1a). All these steps involve remodeling of endothelial junctions and dramatic changes in cell shape and cytoskeleton (3).

In vivo assays do not fully recapitulate the behavior of human cancer metastases. This is due to species-specific differences and challenges in analyzing *in vivo* the

initial steps of cancer dissemination in a biochemically and biophysically controlled environment (4).

Recently, advances in 3D modeling and imaging techniques have permitted cell biology studies within *in vivo*-like complex systems (5). For this reason, several human *in vitro* models from simple 2D assays (6) to 3D meso-scale (7) and microscale organ-specific vascular models (8) have been developed to reproduce human tissues and overcome *in vivo* models related problems. In particular, microfluidic approaches allow to analyze the extravasation process of cancer cells by coupling high resolution real time imaging with biochemically and biophysically tightly controlled niches representing the metastatic micro-environment.

Focal adhesions (FA) are subcellular structures in which ECM-binding integrin receptors are connected through adaptor proteins with the intracellular actin cytoskeleton (9). Moreover, focal adhesion proteins acting by integrin signaling, are widely known to be up-regulated (10) (11) in cancer and to be involved in mechano-transduction events associated with the development of metastases. Several studies have shown that two of the most important early recruited focal-adhesion proteins, i.e. Talin-1 (Tln-1) and Focal Adhesion Kinase (FAK), have both structural and functional features involved in integrin signaling (12-15). In particular, these proteins are overexpressed in triple negative breast cancer and sarcoma (10). Tln-1 is required for pseudopodia regulation (16), it is a critical mediator of integrin activation and its silencing limits the formation of lung metastases (17). FAK recruits several proteins including Tln-1 and allows tensile force generation through interaction with the cytoskeleton (18). Furthermore Tln-1 and FAK phosphorylation mediated by cyclin-dependent-like kinase 5 (CDK-5) is an important switch for integrin regulation (17).

Although the critical role of individual integrin subunits and different FA molecules such as FAK and TLN-1 has been investigated in metastasis, the central mechanism coupling these proteins with specific extravasation steps remains

unknown. Thus, it is evident that Tln-1 and FAK and their activation could play a key role in the converging signaling pathways regulating integrin functions and the invasive properties of metastatic cancer cells. In fact, animal studies have recently supported the hypothesis that metastatic deficiency lies in focal adhesion alterations (19). However, it still needs to be elucidated which are the specific regulators of each step of the metastatic cascade.

Here, we have exploited three independent and "ad hoc" engineered models providing the powerful possibility to effectively dissect extravasation in its main steps: adhesion to endothelium, trans-endothelial migration (TEM) and early invasion in a 3D matrix. Our 3D microfluidic approach provides higher physiological significance concerning 3D architecture, vascular barrier and cell-ECM interactions than standard 2D models (ref). In addition, the presence of cells of human origin only allows to overcome species-specific differences, thus complementing the lacks of *in vivo* assays (20). In particular, we have dissected for the first time the role of TLN-1, FAK and CDK-5, key focal adhesion proteins, in different steps of cancer cell extravasation. Collected results, confirmed by in vivo assays, prove that vascular adhesion occurs mainly via CDK-5 engagement, and that Tln-1 and FAK are required for TEM and 3D matrix invasion through actin polymerization. In this framework, we have demonstrated that FAK[S732] phosphorylation is a key event promoting cancer cell trans-endothelial migration.

9.2 Results

9.2.1 Development and characterization of the engineered models to dissect the role of TLN-1 and FAK in extravasation steps

We generated advanced *in vitro* models mimicking different aspects of the vascular niche to dissect the extravasation process in its main steps from vascular adhesion to TEM and early invasion of the metastatic site. Our strategy provides forefront

tools to follow single cell behavior in a more reliable, reproducible and quantitative way with respect to traditional models. Each assay allows to isolate a specific step of the extravasation cascade and avoid the effects of upstream events.

Vascular adhesion, i.e. the attachment of circulating tumor cells to the vessel lumen in the microvasculature, is a critical step in the metastatic cascade determining the organ site of metastasis (21). We used the vascular adhesion assay to selectively study the attachment of cancer cells to the endothelium. The endothelium was characterized by the presence of adherens (Fig1b) and tight junctions (Fig1c), and vascular adhesion was quantified through fluorescence imaging analyses of adhered cancer cells. Following adhesion, cancer cells emitted pseudopodia through endothelial-junction and then they pull themselves out of vessels in the process called TEM. A 3D human microvascular network assay was generated to precisely analyze TEM events in a physiological like environment. The engineered microvasculature does not merely perform the barrier function of the endothelium, but in addition it mimics the hierarchical architecture of *in vivo* vessels. We demonstrated the presence of vascular maturation markers such as vascular endothelial (VE)-cadherin (Fig1d) and zonula occludens (ZO)-1 (Fig1e). We verified the presence of hollow lumens (fig1f), (supplementary movie-1) and permeability measurements ($1.5 \pm 0.76*10^{-6}$ cm/s) (Fig1g) were close to *in vivo* values (22). Finally, we injected cancer cells through the vessels and quantified TEM and pseudopodia formation by high resolution real time single cell imaging (Fig1h) (supplementary movie 2_Cancer injection). Once breached the endothelial barrier, cancer cells proceed to the last step of extravasation, i.e. the early invasion of the surrounding microenvironment. In order to analyze this phenomenon, we set up a microfluidic 3D invasion assay embedding fluorescent cancer cells in a 3D matrix mimicking the invasion of a secondary organ during early colonization. Then, we set up a quantification method to track the three-dimensional migration patterns of individual cancer cells based on previous studies (23) (24) (Fig1i),

allowing us to highlight the specific role of focal adhesion proteins in cell migration.
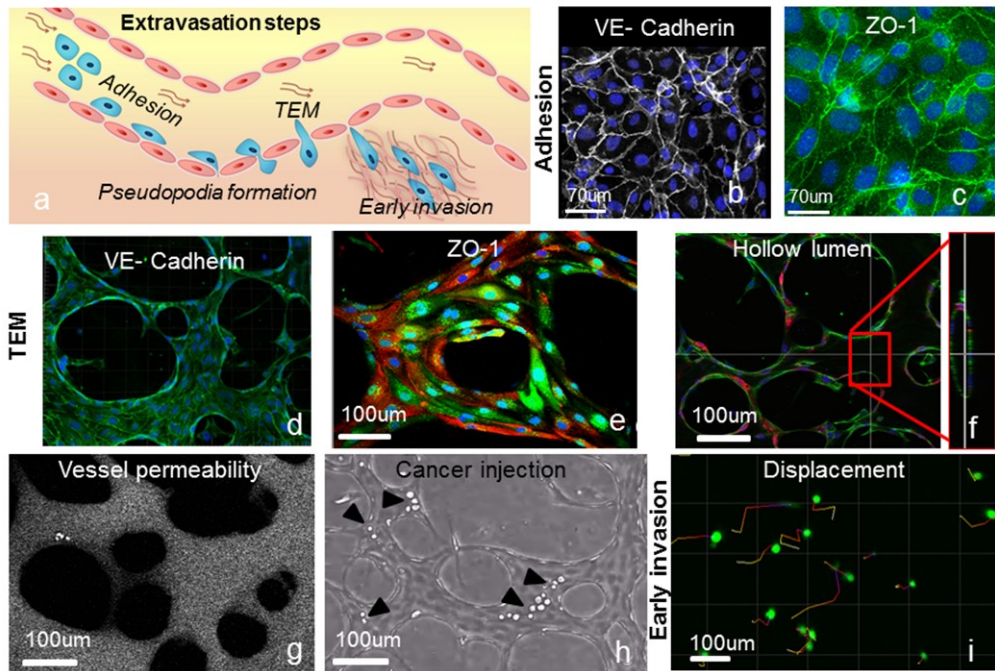
Fig1: Characterization of the extravasation models. (a) schematics of extravasation main steps. (b-c) Immunofluorescence staining of adherence and tight junctions respectively in vascular adhesion assay. (d-e) Immunofluorescence staining of adherence and tight junctions respectively in microvascular network in mivrofluidic device. (f) Cross section of confocal stack evidencing hollow lumens in microvasculature. (g) Fluorescent dextran injection in microvessels allowing the measurement of their permeability. (h) Cancer cell injection in hollow lumens of microvascular network. (i) Cell tracking performed in 3D matrix in microfluidic cancer invasion assay.

9.2.2 Within the extravasation cascade, TLN-1 regulates vascular adhesion while FAK governs TEM

To analyze the role of the most important focal adhesion proteins in the main steps of extravasation, we performed the knock down (KD) of TLN-1 and FAK

individually by means of SiRNA in two tumor cell lines: MDA-MB 231 and HT1080. Furthermore, since TLN-1 and FAK interact with each other and with integrins, our aim was to define the nature of their interaction, if concerted or additive. To verify this hypothesis, we silenced both targets alone and together, then single (FigS1a) and additive knock down (++ KD) (FigS2a) was verified by Western blot in both analyzed cell lines.

In terms of morphology (FigS1b), the comparison revealed that the MDA-MB231 TLN-1 KD exhibited a rounded phenotype while FAK KD cells displayed a blebbing phenotype with respect to the epithelial morphology of the control. TLN-1 KD HT10810 displayed spindle-like morphology while FAK KD showed flat and squished boundaries compared with the elongated epithelial shape of the control. Moreover, the morphology of the ++ KD in both cell lines reflected the rounded (MDA-MB231) or elongated (HT1080) shape of TLN-1 KD (FigS2b) suggesting a strong TLN-1 involvement in cell shape regulation.
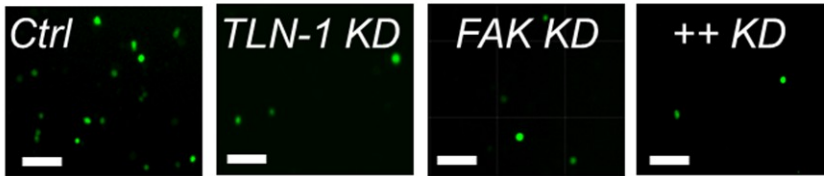
Doubling time in both cancer cell lines was significantly affected by TLN-1 KD (MDA-MB231 and HT1080: $P<0.001$), conversely FAK KD only decreased the doubling time in MDA-MB231 ($P<0.05$) while it did not affect doubling time in HT1080 (n.s.) (FigS3a). The doubling time of ++KD was affected in a significant way in both cancer cell lines ($P<0.001$) (FigS3b).

In order to have a global view of cancer cell adhesion, we analyzed both cancer cell vascular adhesion by means of adhesion assay and the cell adhesion to the culture substrate through the measurement of trypsinization time. Both type of adhesion followed the same trend indicating a relationship between the two phenomena. Moreover, we demonstrated the involvement of TLN-1 and FAK in cancer cell adhesion to the endothelium in both cancer cell lines. In detail, TLN-1 KD and FAK KD trypsinization time (FigS4) and vascular adhesion (Fig2a) was statistically lower in both analyzed cell lines compared to the control ($P<0.001$). The key driving role of TLN-1 in adhesion was demonstrated in both cell lines. In fact, TLN-1 KD trypsinization time was lower than FAK KD in a significant way

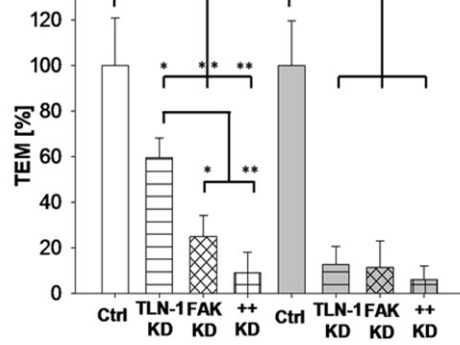(P<0.001) and the values related to TLN-1 KD adhesion to endothelium were lower with respect to FAK KD in a statistically relevant manner (MDA-MB231 p<0.05). Although ++ KD significantly decreased adhesion in both cell lines with respect to the control (P<0.001), no additive effect was detected with respect to the single KD (Fig2). Noteworthy, since TLN-1 impacted adhesion more than 60% and FAK more than 50% with respect to the control, these data highlighted that both targets are involved in vascular adhesion but TLN-1 seems to be the major player.

After the characterization of the microvascular network in the microfluidic environment, we employed the microvascular model for the analysis of cancer cell TEM in order to assess the role of focal adhesion players in breaching the endothelial barrier. We quantified TEM as the complete outpacing of the endothelial barrier (25). TEM percentage in MDA-MB231 TLN-1 KD (P<0.05) and in the FAK KD (P<0.01) significantly decreased with respect to the control in a significant way (Fig2b). This assay allowed to demonstrate the crucial role of FAK as the main TEM regulator, since FAK KD and ++ KD TEM values were significantly lower compared to TLN-1 KD in MDA-MB231 (P<0.01). Similarly, for HT1080 TLN-1 KD and FAK KD TEM values were lower than in the control (P<0.01). As expected, ++KD cancer cells significantly affected TEM events in both cell lines (P<0.01) with respect to the control. In addition, we showed that there were not any additive effect in the ++ KD TEM behaviors analyzed by means of the microvascular network assay.

a *Vascular adhesion*

b *TEM*

Ctrl

TLN-1 KD

FAK KD

++ KD

c 3D Matrix Invasion

d

e

f Adhesion/TEM   Invasion/TEM

g In vivo Extravasation

n=3
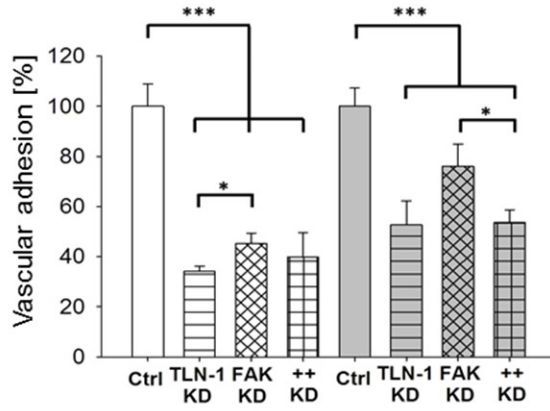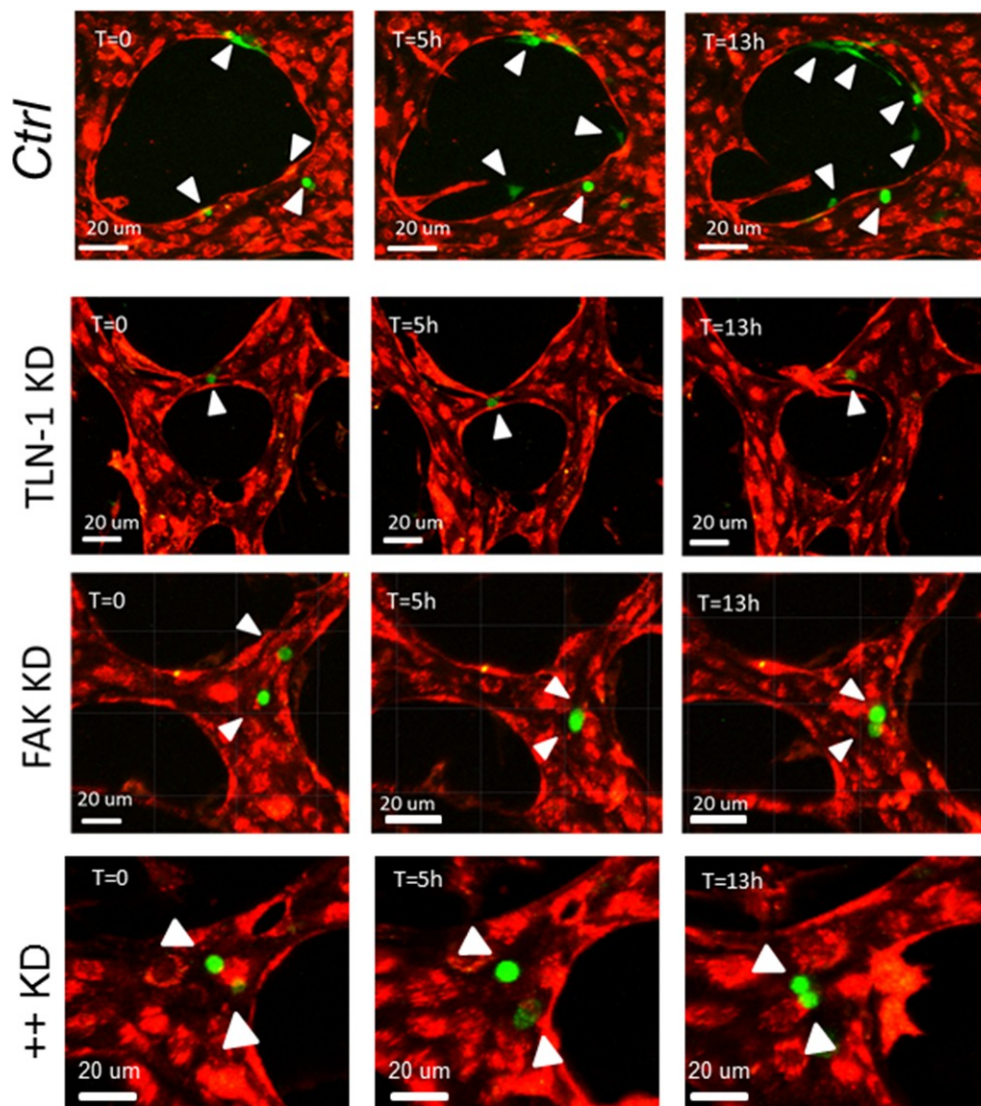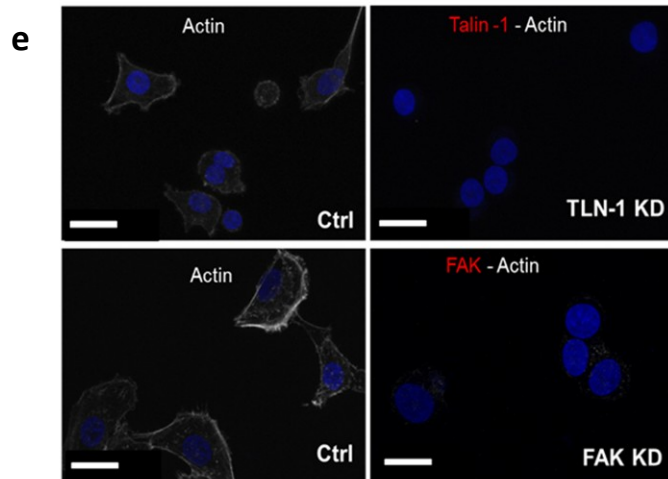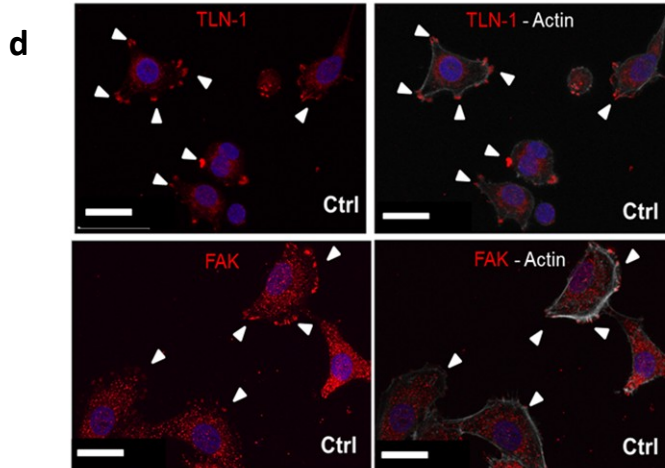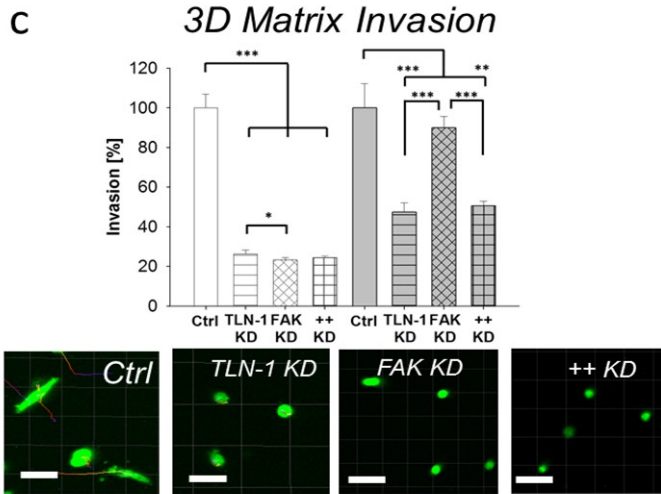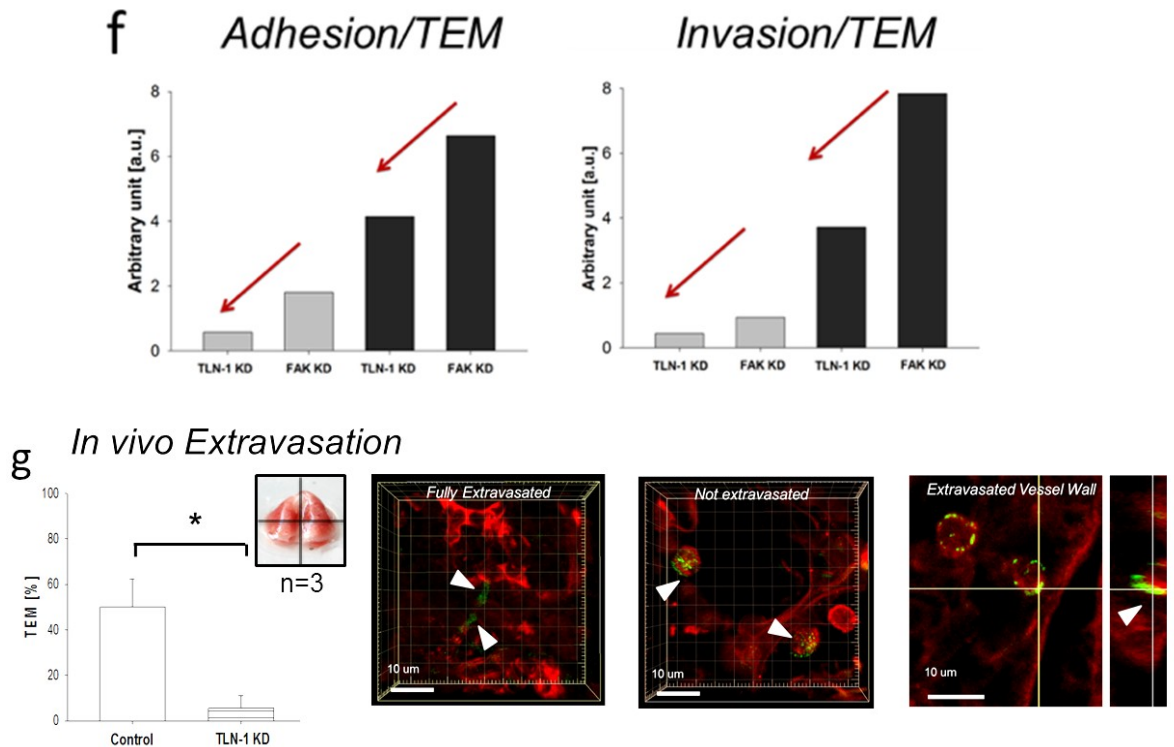
Fig2: Dissection of extravasation steps through engineered in vitro models, TLN-1 and FAK. (a) Graph and images showing vascular adhesion analysis in different conditions. (b) Graph and images showing TEM quantification in different conditions and time lapse progression of TEM. (c) Graph and images showing invasion measurement in 3D matrix. (d) TLN-1 and FAK localization at pseudopodia of cancer cells. (e) Deficit in the F-actin polymerization in TLN-1 and FAK KD cells. (f) Graphs representing the ratio between adhesion/TEM invasion and /TEM evidencing key role of FAK in TEM. (g) in vivo extravasation in mice lung.

The microvascular network assay provides a performing tool for the analyses of pseudopodia formation. In fact, the exploitation of this property highlighted that both targets, TLN-1 and FAK are required for pseudopodia formation in both cell lines. More in detail, real time single cell imaging showed that both TLN-1, FAK and ++KD cells were trapped into the vessels and were not able to extend pseudopodia (Fig2b). Conversely, control cells were able to breach the

endothelium through the generation of pseudopodia which allowed the migration from inside the vessel toward the secondary metastatic site (Fig2b).

Finally, the microfluidic invasion assay was employed to verify TLN-1 and FAK involvement in the process of early invasion. Indeed, real time imaging demonstrated a statistically relevant decrease in 3D cell invasion in all KD vs. control and between different cell lines (Fig2c). Particularly, the migration of TLN-1 KD in both cell lines was significantly lower compared to control cells (MDA-MB231 and HT1080: $P<0.001$). Surprisingly, our findings showed FAK dependent migration in MDA-MB231 and FAK-independent in HT1080. Indeed, FAK KD led to significantly impaired cell migration in MDA-MB 231 ($P<0.001$) while not affecting the behavior of HT1080 (n.s.). Analyzing the ++ KD features in terms of invasion in the 3D microfluidic assay, we showed that ++KD invasion was significantly lower with respect to the control (MDA-MB: $P<0.001$; HT1080 $P<0.01$) (Fig2c). Furthermore, invasion assay revealed that ++KD reflected the phenotype of both TLN-1 and FAK KD cells (n.s.) in MDA-MB231, while ++KD mirrored TLN-1 KD behaviors in HT1080 highlighting FAK independent invasion in this cell line ($P<0.001$).

In the end, our results highlighted that there were not additive effects in analyzed extravasation steps, in fact ++KD mimicked the effect of the knock down that more significantly affected each specific step of extravasation. The calculated ratios of adhesion/TEM and invasion/TEM were lower in TLN-1 compared to FAK KD, demonstrating the crucial role of FAK as the main driver in TEM (Fig2f).

We analyzed different cancer cell invasion patterns, highlighting the requirements of pseudopodia to probe the environment and perform the invasion of the 3D matrix (Fig2c). The requirement of TLN-1 and FAK in the generation of functional protrusion was supported by TLN-1 and FAK co-localization with the tips of cancer cell pseudopodia (Fig2d), which are required for extravasation. Furthermore, immunostaining demonstrated that TLN-1 and FAK promoted F-actin polymerization at the protrusion level, regulating cell interaction with the

endothelium (Fig2e). In fact, both TLN-1 and FAK KD showed a noticeable cell deficit in actin polymerization coincident with defects in protrusion formation during TEM (Fig2b).

In order to verify the reliability of our models in reproducing spatio-temporally the specific steps involved in the metastatic cascade, we performed *in vivo* experiments analyzing extravasation in mice lungs after tail injection of cancer cells. *In vivo* extravasation tests demonstrated the reliability of the results obtained through the use of our vascularized microfluidic models. Indeed, we showed that TLN-1 KD reduced extravasation *in vivo* ($P<0.05$) (Fig2g), supporting the hypothesis that extravasation defects were due to TLN-1 silencing.

9.2.3 *CDK-5 silencing dramatically impact vascular adhesion while actin polymerization is dependent by TLN-1 and FAK structural role rather than their phosphorylation*

CDK-5 is a kinase interacting with TLN-1 and FAK (Fig3a) that catalyzes the phosphorylation of TLN-1^{S425} (26). In addition, CDK-5 induces FAK phosphorylation in many aminoacid positions, including FAK^{Y397}, which is the main site recognized for FAK activation (27) and FAK^{S732}, which is involved in nuclear movements (28) required for extravasation (29). We verified if the phosphorylation of TLN-1 and FAK affects each step of extravasation, focusing on the effect of CDK-5 silencing.

CDK-5 silencing was determined by Western blot (FigS5a). Cell morphology revealed blebbing-like corrugated cell boundaries in CDK-5 KD similar to FAK KD, suggesting a correlation between FAK phosphorylation and blebbing phenotype generation (FigS5b) (30). Western blot on CDK-5 KD highlighted a reduction in TLN-1^{S425}, FAK$^{Y397 \text{ and } S732}$ phosphorylation with respect to control (Fig3b), confirming its kinase effects in both, MDA MB 231 and HT1080.

Doubling time in both cell lines was significantly decreased by CDK-5 KD (P<0.001) (FigS3).
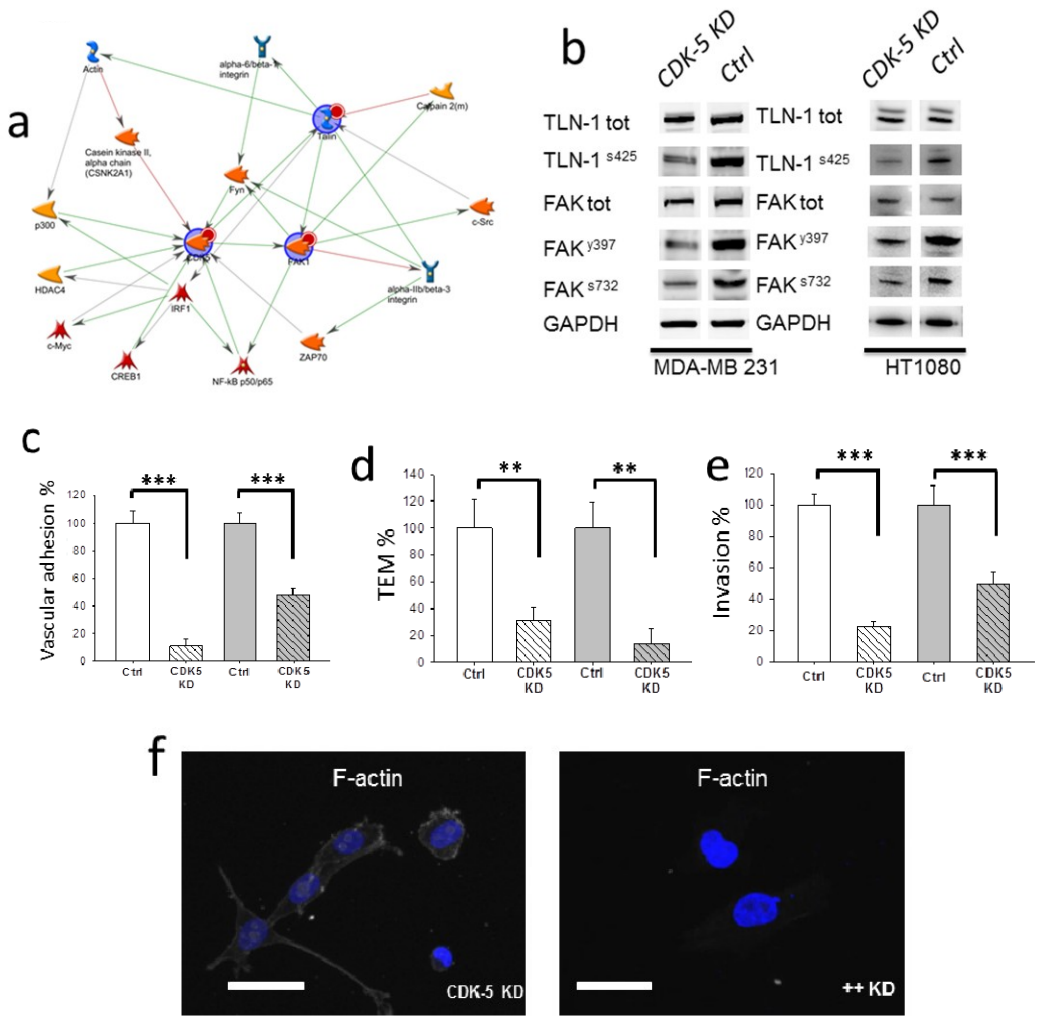
Fig3: Dissection of extravasation steps, CDK-5 (a) CDK-5 interactome. (b) CDK-5 phosphorylation sites on TLN-1 and FAK in both cancer cell lines. (c) Graph and images showing vascular adhesion analysis in different conditions. (d) Graph and images showing TEM quantification in different conditions and time lapse progression of TEM. (e) Graph and images showing invasion measurement in 3D matrix. (f) Deficit in the F-actin polymerization in CDK-5 KD and ++ KD cells.

CDK-5 dramatically affects each step of the extravasation cascade. More in detail, CDK-5 KD trypsinization time was significantly lower in both analyzed cell lines with respect to the control (FigS4). Further, CDK-5 KD affected vascular adhesion in both analyzed cell lines with respect to the control (P<0.001), (Fig3c). Surprisingly, CDK-5 KD impaired MDA-MB 231 vascular adhesion in a statistical way with respect to the double KD (P<0.05), indicating that CDK-5 did not only abrogate the adhesion to restore the double KD levels but had a major inhibitory effect. No significant differences were detected in HT1080 between CDK-5 KD and ++KD (n.s.) indicating a specific effect of CDK-5 in adhesion regulation in MDA-MB231. CDK-5 KD significantly abrogated TEM through microvasculature in MDA-MB-231 and HT1080 with respect to the control (P<0.01) (Fig3d), while it did not affect TEM with respect to the ++KD in both cell lines (n.s.), indicating a specific role of target site phosphorylation in driving TEM events.

Also, CDK-5 KD affected invasion in both breast and fibrosarcoma cell lines with respect to the control (P<0.001) (Fig3e). Furthermore, CDK-5 KD invasion behaviors recapitulated those of ++ KD, indicating that TLN-1 and FAK phosphorylation could be good targets to tackle cancer cell invasion.

Moreover, F-actin staining showed the presence of polymerized actin in CDK-5 KD cells which was not found in ++KD. This finding, evidenced that F-actin polymerization is independent from both CDK-5 expression and kinase function (Fig3f). These data demonstrated that actin polymerization is dependent by the structural role of TLN-1 and FAK while it is independent by their phosphorylation.

Although, these results highlight that CDK-5 silencing could be a suitable strategy to mimic TLN-1 and FAK de-phosphorylation, however since the wide CDK-5 interactome (FigS6) the phosphorylation analyses of TLN-1 and FAK need to be further meticulously analyzed (analyzed through pathway commons tool, http://www.pathwaycommons.org/pcviz/#neighborhood/CDK5,TLN1,FAK).

Since potential side effects resulting from therapeutics based on the inhibition of proteins belonging to the cyclin family, i.e CDK-5, it appears clear that the most

promising step forward could be the employment of a specific phosphorylation inhibitor instead of CDK-5 silencing to analyze focal adhesion protein activation.

9.2.4 *Inhibition of FAK^{S732} phosphorylation abrogates trans-endothelial migration in extravasation*

We demonstrated that FAK is a key driver in TEM process. However, it is still not clear if the phosphorylation of specific sites may play a major role in extravasation steps. To isolate the effect of FAK phosphorylation in extravasation, we employed a FAK phosphorylation inhibitor, i.e. 1,2,4,5-benzenetetramine tetrahydrochloride (Y15). First, we analyzed the effects of different concentrations of the inhibitor to define the one which better mimicked the FAK KD, i.e. 3 μM. After Y15 incubation, cells displayed a morphological phenotype similar to FAK KD in both cell lines (Fig S7a).

Y15 (3μM) impaired vascular adhesion in both cell lines (P<0.001) (Fig4a) showing unspecific effects in terms of phosphorylation (FigS7b) and adhesive behavior at increased concentrations with respect to 3 μM (FigS7c).

TEM was statistically decreased by Y15 in both cell lines (P<0.01) (Fig4b), displaying similar results compared to FAK KD. FAK inhibitor impaired extravasation for at least 13 hours from injection in engineered vascular networks (Fig4d).

As expected, invasion was significantly affected by Y15 in MDA-MB 231 (P<0.001), despite it was not influenced in HT1080 (n.s.). This result is in agreement with FAK KD HT1080, whose invasive behavior was not altered by FAK silencing (Fig4c). These results, in line with FAK silencing data, suggest that invasion of MDA-MB 231 is dependent on FAK phosphorylation while for HT1080 invasion resulted independent on FAK phosphorylation.

In summary, Y15 treatment led to a decreased phosphorylation in FAK^{S732}, which could be correlated with TEM deficiency. All together these data provided by

human vascularized 3D microfluidic models highlighted the requirement of FAK[S732] activation to accomplish cancer TEM process in both analyzed cell lines.
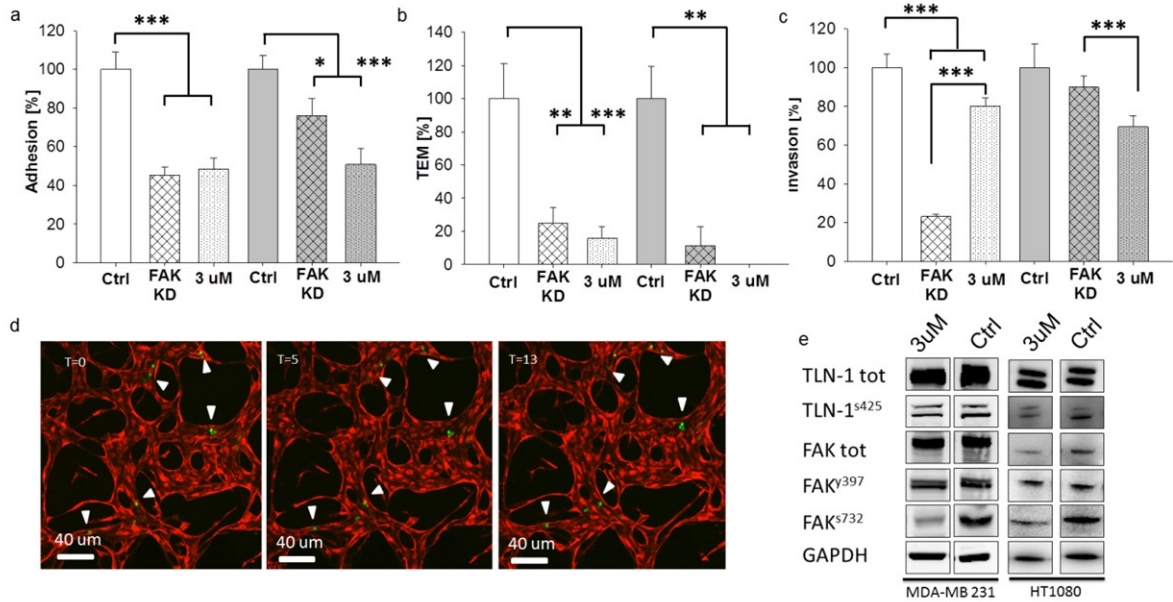
Fig4: Dissection of extravasation steps evidencing FAK s732 phosphorylation key role in extravasation (a) Graph and images showing vascular adhesion analysis with FAK inhibitor. (b) Graph and images showing TEM quantification with FAK inhibitor. (c) Graph and images showing invasion measurement in 3D matrix. (d) Time lapse progression of TEM with inhibitor. (e) Western blot showing inhibitor effects on FAK and TLN-1 in cancer cells

9.3 Discussion

The ability of cancer cells to extravasate is crucial for metastasis formation. In fact, extravasation steps culminate in the outpacing of vessel membrane which is the last effort of cancer cells before reaching the secondary site (29). Yet, it has been challenging to elucidate the molecular mechanisms driving extravasation because suitable methods to dissect this process across its main steps have been missing. The strength of the present study lies in the application of engineered models embedding human cells in 3D physiological vascular environments to identify the

role of key focal adhesion proteins in each step composing extravasation. In particular, we were able to quantitatively discern the contribute of each target and elucidate the extravasation mechanism through our assays allowing dynamic high resolution single cell imaging.

Recent emerging findings suggest that integrins and focal adhesion proteins play a key role in cell migration and pseudopodia formation (16, 31). Although recent observations suggest that integrins are required in cancer cell extravasation (32), the downstream pathway driving these events is not clear yet.

TLN-1 and FAK are well known proteins interacting with the integrin tail in the cytoplasm (17, 33). We focused on these proteins among more than 150 targets (34) composing the focal adhesion complex, due to their unique and dual role as structural stabilizers and activators of integrins (35). In particular, we exploited genetic and chemical inhibition of selected targets to examine their effect on extravasation.

An overall of our data demonstrated that all analyzed targets significantly affected each step of extravasation, indicating a crucial role of the focal adhesion pathway in this event.

Here, based on obtained data (Table1,2,3,4 supplementary), we propose a new extravasation driving mechanism induced by the axis CDK-5/TLN-1/FAK^{S732p} acting in different time points of the cascade.

More in detail, in initial steps of the interactions between cancer cells and vessels CDK-5 and TLN-1 regulate cancer cell vascular adhesion. Then, a cooperative mechanism through TLN-1/FAK structural engagement results in F-actin polymerization which supports the generation of stable pseudopodia which penetrate the vessels culminating in vascular breaching. Next, cancer cell TEM is mediated by FAK^{S732} phosphorylation which also likely arrange nuclear movement through tiny holes (~8 μm) established in the vessels during TEM. Once overtaken the vascular barrier, cancer cells grip to the basal membrane pulling themselves in the ECM of new secondary organ site.

Although *in vivo* extravasation assays did not allow the independent dissection of each step belonging to the extravasation cascade as well as microfluidic assays, data collected from *in vivo* experiments corroborates the validity of the developed engineered tools and the biological significance of the results.

Different works have previously reported TLN-1, FAK and CDK-5 dependent adhesion to cell culture substrate (17, 36, 37), despite vascular adhesion related to these target is still missing. Moreover, integrin-dependent adhesive interactions between cancer cells and vessels is considered one of the major regulators of adhesion step (38, 39), but the specific role of cancer cell focal adhesion proteins in vascular arrest and adhesion is still not clear. Thus, the analysis of vascular adhesion representing the initial arrest of cancer cells within the vessel niche (the starting point of extravasation (33)) demonstrated the key role played by CDK-5 in driving vascular adhesion, in particular in MDA-MB 231. In fact, CDK-5 silencing broke down about the 90% of cancer cell adhesion. Furthermore, data highlighted that beyond the huge effect of CDK-5 silencing on vascular adhesion, both TLN-1/FAK silencing and FAK phosphorylation were also required in the regulation of vascular adhesion preceding the TEM.

Here, beyond the evidence of CDK-5 dependent proliferation and vascular adhesion in cancer cells, we showed its importance in TEM and invasion. In addition, we demonstrated CDK-5 importance in phosphorylation of TLN-1 ^{S425}, FAK^{Y397} and FAK^{S732} in breast and fibrosarcoma cancer cells. Despite CDK-5 overexpression has been significantly correlated with several poor prognostic parameters in cancer (40), silencing this target could result in relevant side effects on healthy tissue, being CDK-5 involved in a wide spectrum of pathways (Supplementary FigS6) and in cell cycle regulation.

Since we demonstrated that CDK-5 played a critical role in extravasation and it was involved in FAK activation, we hypothesized that FAK phosphorylation could be the switch for an effective TEM process. FAK phosphorylation is a wide field of study (41-45), being FAK implicated and up-regulated in several human cancers

(27, 46, 47). In fact, phosphorylation-dependent protein interactions are critical for transducing signals intracellularly. Moreover, phosphorylation can also regulate the subcellular location or lead to ubiquitin-dependent protein degradation (48). The FAK gene is mapped on human chromosome 8q24.3 (49) and it encodes for a protein kinase activated and overexpressed in many cancer types such as breast and fibrosarcoma (10, 11) In addition, in many cases FAK mRNA levels are correlated with poor patient survival (27). Recently FAK^{S732} phosphorylation has been associated with centrosome regulation in mitosis (50, 51). However, the specific FAK^{S732} phosphorylation site itself has not been previously coupled to human malignancy. Here, we are the first to attribute to FAK^{S732} phosphorylation site, located in the COOH-terminal region of FAK, the trans-endothelial migration switching role. In fact, FAK^{S732} phosphorylation inhibition avoided TEM in cancer cells thus providing evidence of the existence of a novel biochemical route by which phosphorylation of FAK^{S732} regulates TEM of cancer cells.

Fibronectin is one of the proteins which compose the vascular basal membrane supporting vessel growth (52) and is recognized by at least ten cell integrin receptors, including α5β1 which is probably the major fibronectin receptor (53). In addition, our group previously evidenced the presence of fibronectin and laminin in a microvascular model and the importance of α3 and α6 integrin sub-units in laminin basal membrane adhesion (39). Furthermore, since FAK^{S732} is up-regulated in cancer cells adhered to fibronectin (54), the inhibition of FAK^{S732} which abolish TEM may act through the interdiction of integrin α5β1 binding to fibronectin (34).

Furthermore, previous studies demonstrated that FAK plays an important role in the nucleus (55) and in particular FAK^{S732} phosphorylation was shown to be involved in the regulation of nucleus movement in neuronal cells (28). Since nuclear translocation through the tiny holes of endothelial junctions represents the most strenuous effort for cancer cells to accomplish extravasation (29), it is likely that the block in extravasation induced by FAK^{S732} phosphorylation inhibition is due, beyond evidenced pseudopodia defects, to compromised nuclear movements.

Looking with more detail at protrusion formation, we demonstrated that both TLN-1 and FAK co-localize with pseudopodia tips in cancer cells, and we evidenced that cancer cells silenced for both targets were characterized by a deficit in F-actin polymerization, demonstrating the necessity of their structural function instead to their activation in protrusion generation. Because TLN-1 and FAK KD are uneffective in TEM and they both displayed pseudopodia deficit, we hypothesized that pseudopodia formation was required to complete the extravasation process. This could be due to the inability to attach to and/or degrade the underlying matrix proteins. This is supported by other studies regarding the importance of integrins and focal adhesions in pseudopodia generation and attachment to the basal membrane (56, 57). Hence, we demonstrated the involvement of TLN-1 and FAK in extravasation and pseudopodia formation by means of single and additive KD.

Concluding, there is a clear need to increase the efforts to better investigate the emerging role of FAK^{S732} phosphorylation, going beyond already developed molecules targeting FAK^{Y397} activation. Noteworthy, Tavora et al. reported that physiological vascular barrier functions were not affected by FAK inhibition rather loss of endothelial-cell FAK is sufficient to sensitize tumour cells to chemotherapy by affecting endothelial cytokine production (58) supporting a possible beneficial effect of a future therapy based on FAK inhibitors affecting not only cancer cells for a boost in therapy success. Concluding, FAK may represent a target challenging the entire metastatic niche being at the intersection of various signaling pathways promoting cancer growth and metastasis.

9.4 Materials and methods

9.4.1 Development of the experimental models and cell culture

9.4.1.1 Cell culture

Cell culture HUVECs (Lonza) were cultured in EGM-2 MV (Lonza) growth medium and used in experiments between passages 6–8. Normal human lung fibroblasts (NHLF; Lonza) were cultured in FBM-2 (Lonza) growth medium and used in experiments between passages 6–10.

MDA-MB 231 and HT1080 cell lines expressing fluorescent proteins were used and cultured in DMEM high glucose 10% FBS and glutamine.

9.4.1.2 Gene silencing and Western blot

Small interfering RNA (si-RNA) targeting focal adhesion protein TLN-1, FAK, CDK-5 and non-silencing si-RNA were purchased from Invitrogen, gene-specific Si-RNA was transfected into cancer cells using lipofectamine 2000 according to the manufacturer's instructions.

To verify the silencing, cancer cells were lysed in lysis buffer and the protein concentration of 30 ng of each sample was electrophoresed on a 10% SDS-PAGE. The gel was transferred to nitrocellulose membrane and specific proteins are detected after primary antibody and secondary antibody treatments using ECL kit (Invitrogen).

9.4.1.3 Adhesion assay

Endothelial monolayers were plated in multiwall and cancer cells were seeded on the top and let adhered for 1h. After that we washer carefully 3 times and quantify the adhered cells.

9.4.1.4 Microvascular network assay

A standard procedure for generating microfluidic devices was followed (8, 59). Briefly, PDMS (Ellsworth) and a curing agent were mixed at a 10:1 ratio and polymerized onto the wafer model. Single devices were then cut and a biopsy punch was used to create reservoirs for gel and medium filling.

The surface of the devices were cleaned and they were sterilized with autoclave. The Harrick Plasma was used to bonded devices on the glass slide to produce the final model. The width of each gel and medium channel was 1.3 mm. The device was composed from 3 channel, in the middle the vascularized region (ECs) and in the lateral channel the supportive stromal cells (Human lung fibroblasts. The process of network formation studied occurs over a period of 4 days. The medium was refreshed every day. 3D culture in gel were performed as previously reported by our group (8).After network maturation at day 4 the cancer cell suspension was injected in the microvasculature and time lapse confocal imaging were performed with an Olympus IX81 microscope (Olympus America, Inc.) and analyzed to quantify extravasation. The cross section of confocal images revealed the extravasated cells defined as the one which passed through the endothelial barrier.

9.4.1.5 Invasion assay

3D culture in gel were performed as previously reported by our group in the mono-channel device (8). Cancer cells were injected in the gel region of the devices and

time lapse confocal imaging were performed with an Olympus IX81 microscope (Olympus America, Inc.). Tracking of cell migration was performed by IMARIS (bit plane) through the development of an optimized protocol.

9.4.2 Characterization of the models

9.4.2.1 Immunofluorescent Staining.

All devices were washed with and fixed with 4% paraformaldehyde (PFA) then they were permeabilized with 0.1% Triton-X 100 Samples were treated with 5% BSA + 3% (wt/vol) goat serum solution for at least 3 h at 4 °C before incubation with primary antibody. rabbit polyclonal VE-cadherin antibody (cell signaling dilution 1:100), mouse polyclonal ZO-1 antibody (Abcam; dilution 1:100), were used for staining. Red fluorescently labeled secondary antibodies (Invitrogen) were used at 1:200 dilution. Cell nuclei were stained with DAPI (5 mg/mL; Invitrogen) at 1:500 dilution, and F-actin filaments were stained with AlexaFluor 633 phalloidin (Invitrogen) at 1:100 dilution. All images were captured using a Olympus IX81 microscope (Olympus America, Inc.) and processed with IMARIS software (Bitplane Scientific Software).

9.4.2.2 Permeability

Permeability of the microvascular network was measured as described previously (22). Briefly, the medium was aspirated from the system. Then, fluorescent dextran (70 kDa,; Invitrogen) was dissolved in medium and then added to two reservoirs of the opposite media channels. After confocal time lapse imaging of dextran diffusion the permeability was measured by quantifying the average intensity at the initial and final time points. Permeability values were calculated with the following formula:

$$P_D = \frac{1}{I_i - I_b} \left(\frac{I_f - I_i}{\Delta t} \right) \times \frac{d}{4},$$

(I_b, I_i, and I_f are the background, initial, and final average intensities, respectively, Δt is the time interval between images, and d is the diameter of the imaged microvessel).

9.4.2.3 In vivo extravasation assays

Extravasation were performed as previously reported by our group (60). Cells were resuspended at a constant number of cells for all mice in a given experiment (250,000 cells/injection). One hundred microliters of cell suspension were then injected via the tail vein of mice. The numbers of single extravasated cells were quantified in mice lung section stained with CD31 to evidence vessels boundaries after confocal imaging.

References

1. Valastyan S & Weinberg RA (2011) Tumor metastasis: molecular insights and evolving paradigms. *Cell* 147(2):275-292.
2. Orr FW, Wang HH, Lafrenie RM, Scherbarth S, & Nance DM (2000) Interactions between cancer cells and the endothelium in metastasis. *The Journal of pathology* 190(3):310-329.
3. Bersini S, Jeon JS, Moretti M, & Kamm RD (2014) In vitro models of the metastatic cascade: from local invasion to extravasation. *Drug Discov Today* 19(6):735-742.
4. Visone R, *et al.* (2016) Cardiac Meets Skeletal: What's New in Microfluidic Models for Muscle Tissue Engineering. *Molecules* 21(9).
5. Rosenfeld D, *et al.* (2016) Morphogenesis of 3D vascular networks is regulated by tensile forces. *Proc Natl Acad Sci U S A* 113(12):3215-3220.
6. Arrigoni C, *et al.* (2014) Direct but not indirect co-culture with osteogenically differentiated human bone marrow stromal cells increases RANKL/OPG ratio in human breast cancer cells generating bone metastases. *Mol Cancer* 13:238.
7. Bersini S, *et al.* (2016) Human in vitro 3D co-culture model to engineer vascularized bone-mimicking tissues combining computational tools and statistical experimental approach. *Biomaterials* 76:157-172.
8. Jeon JS, *et al.* (2015) Human 3D vascularized organotypic microfluidic assays to study breast cancer cell extravasation. *Proc Natl Acad Sci U S A* 112(1):214-219.
9. Geiger B, Spatz JP, & Bershadsky AD (2009) Environmental sensing through focal adhesions. *Nature reviews. Molecular cell biology* 10(1):21-33.
10. Singel SM, *et al.* (2013) A targeted RNAi screen of the breast cancer genome identifies KIF14 and TLN1 as genes that modulate docetaxel chemosensitivity in triple-negative breast cancer. *Clin Cancer Res* 19(8):2061-2070.
11. Sarhadi VK, *et al.* (2014) Copy number alterations and neoplasia-specific mutations in MELK, PDCD1LG2, TLN1, and PAX5 at 9p in different neoplasias. *Genes Chromosomes Cancer* 53(7):579-588.
12. Liu J, *et al.* (2015) Talin determines the nanoscale architecture of focal adhesions. *Proc Natl Acad Sci U S A* 112(35):E4864-4873.
13. Desiniotis A & Kyprianou N (2011) Significance of talin in cancer progression and metastasis. *International review of cell and molecular biology* 289:117-147.
14. Calderwood DA, Tai V, Di Paolo G, De Camilli P, & Ginsberg MH (2004) Competition for talin results in trans-dominant inhibition of integrin activation. *J Biol Chem* 279(28):28889-28895.

15. Critchley DR & Gingras AR (2008) Talin at a glance. *J Cell Sci* 121(Pt 9):1345-1347.

16. Beaty BT*, et al.* (2014) Talin regulates moesin-NHE-1 recruitment to invadopodia and promotes mammary tumor metastasis. *J Cell Biol* 205(5):737-751.

17. Jin JK*, et al.* (2014) Talin1 phosphorylation activates beta1 integrins: a novel mechanism to promote prostate cancer bone metastasis. *Oncogene*.

18. Austen K*, et al.* (2015) Extracellular rigidity sensing by talin isoform-specific mechanical linkages. *Nat Cell Biol* 17(12):1597-1606.

19. Mierke CT (2013) The role of focal adhesion kinase in the regulation of cellular mechanical properties. *Phys Biol* 10(6):065005.

20. Bersini S & Moretti M (2015) 3D functional and perfusable microvascular networks for organotypic microfluidic models. *Journal of materials science. Materials in medicine* 26(5):180.

21. Chambers AF, Groom AC, & MacDonald IC (2002) Dissemination and growth of cancer cells in metastatic sites. *Nat Rev Cancer* 2(8):563-572.

22. Jeon JS*, et al.* (2014) Generation of 3D functional microvascular networks with human mesenchymal stem cells in microfluidic systems. *Integr Biol (Camb)* 6(5):555-563.

23. Polacheck WJ, Charest JL, & Kamm RD (2011) Interstitial flow influences direction of tumor cell migration through competing mechanisms. *Proc Natl Acad Sci U S A* 108(27):11115-11120.

24. Polacheck WJ, German AE, Mammoto A, Ingber DE, & Kamm RD (2014) Mechanotransduction of fluid stresses governs 3D cell migration. *Proc Natl Acad Sci U S A* 111(7):2447-2452.

25. Kim Y*, et al.* (2016) Quantification of cancer cell extravasation in vivo. *Nature protocols* 11(5):937-948.

26. Huang C*, et al.* (2009) Talin phosphorylation by Cdk5 regulates Smurf1-mediated talin head ubiquitylation and cell migration. *Nat Cell Biol* 11(5):624-630.

27. Sulzmaier FJ, Jean C, & Schlaepfer DD (2014) FAK in cancer: mechanistic findings and clinical applications. *Nat Rev Cancer* 14(9):598-610.

28. Xie Z, Sanada K, Samuels BA, Shih H, & Tsai LH (2003) Serine 732 phosphorylation of FAK by Cdk5 is important for microtubule organization, nuclear movement, and neuronal migration. *Cell* 114(4):469-482.

29. Chen MB, Whisler JA, Jeon JS, & Kamm RD (2013) Mechanisms of tumor cell extravasation in an in vitro microvascular network platform. *Integr Biol (Camb)* 5(10):1262-1271.

30. Cobb JP, Hotchkiss RS, Karl IE, & Buchman TG (1996) Mechanisms of cell injury and death. *British journal of anaesthesia* 77(1):3-10.

31. Serrels B & Frame MC (2012) FAK and talin: who is taking whom to the integrin engagement party? *J Cell Biol* 196(2):185-187.

32. Stoletov K*, et al.* (2010) Visualizing extravasation dynamics of metastatic tumor cells. *J Cell Sci* 123(Pt 13):2332-2341.

33. McFarlane S, McFarlane C, Montgomery N, Hill A, & Waugh DJ (2015) CD44-mediated activation of alpha5beta1-integrin, cortactin and paxillin signaling underpins adhesion of basal-like breast cancer cells to endothelium and fibronectin-enriched matrices. *Oncotarget* 6(34):36762-36773.

34. Zaidel-Bar R, Itzkovitz S, Ma'ayan A, Iyengar R, & Geiger B (2007) Functional atlas of the integrin adhesome. *Nat Cell Biol* 9(8):858-867.

35. Zhang H, Chang YC, Huang Q, Brennan ML, & Wu J (2016) Structural and Functional Analysis of a Talin Triple-Domain Module Suggests an Alternative Talin Autoinhibitory Configuration. *Structure* 24(5):721-729.

36. Moser M, Legate KR, Zent R, & Fassler R (2009) The tail of integrins, talin, and kindlins. *Science* 324(5929):895-899.

37. Shattil SJ, Kim C, & Ginsberg MH (2010) The final steps of integrin activation: the end game. *Nature reviews. Molecular cell biology* 11(4):288-300.

38. Brooks SA, Lomax-Browne HJ, Carter TM, Kinch CE, & Hall DM (2010) Molecular interactions in cancer cell metastasis. *Acta histochemica* 112(1):3-25.

39. Chen MB, Lamar JM, Li R, Hynes RO, & Kamm RD (2016) Elucidation of the Roles of Tumor Integrin beta1 in the Extravasation Stage of the Metastasis Cascade. *Cancer Res* 76(9):2513-2524.

40. Liang Q*, et al.* (2013) CDK5 is essential for TGF-beta1-induced epithelial-mesenchymal transition and breast cancer progression. *Sci Rep* 3:2932.

41. Grigera PR*, et al.* (2005) FAK phosphorylation sites mapped by mass spectrometry. *J Cell Sci* 118(Pt 21):4931-4935.

42. Lie PP*, et al.* (2012) Focal adhesion kinase-Tyr407 and -Tyr397 exhibit antagonistic effects on blood-testis barrier dynamics in the rat. *Proc Natl Acad Sci U S A* 109(31):12562-12567.

43. Li S*, et al.* (2002) The role of the dynamics of focal adhesion kinase in the mechanotaxis of endothelial cells. *Proc Natl Acad Sci U S A* 99(6):3546-3551.

44. Meves A*, et al.* (2011) Beta1 integrin cytoplasmic tyrosines promote skin tumorigenesis independent of their phosphorylation. *Proc Natl Acad Sci U S A* 108(37):15213-15218.

45. Serrels B*, et al.* (2007) Focal adhesion kinase controls actin assembly via a FERM-mediated interaction with the Arp2/3 complex. *Nat Cell Biol* 9(9):1046-1056.

46. Miyazaki T*, et al.* (2003) FAK overexpression is correlated with tumour invasiveness and lymph node metastasis in oesophageal squamous cell carcinoma. *British journal of cancer* 89(1):140-145.

47. Tancioni I*, et al.* (2014) FAK Inhibition disrupts a beta5 integrin signaling axis controlling anchorage-independent ovarian carcinoma growth. *Molecular cancer therapeutics* 13(8):2050-2061.

48. Hunter T (2012) Why nature chose phosphate to modify proteins. *Philosophical transactions of the Royal Society of London. Series B, Biological sciences* 367(1602):2513-2516.

49. Szwergold BS, Kappler F, Moldes M, Shaller C, & Brown TR (1994) Characterization of a phosphonium analog of choline as a probe in 31P NMR studies of phospholipid metabolism. *NMR in biomedicine* 7(3):121-127.

50. Rea K, Sensi M, Anichini A, Canevari S, & Tomassetti A (2013) EGFR/MEK/ERK/CDK5-dependent integrin-independent FAK phosphorylated on serine 732 contributes to microtubule depolymerization and mitosis in tumor cells. *Cell death & disease* 4:e815.

51. Park AY, Shen TL, Chien S, & Guan JL (2009) Role of focal adhesion kinase Ser-732 phosphorylation in centrosome function during mitosis. *J Biol Chem* 284(14):9418-9425.

52. Mandarino LJ, Sundarraj N, Finlayson J, & Hassell HR (1993) Regulation of fibronectin and laminin synthesis by retinal capillary endothelial cells and pericytes in vitro. *Experimental eye research* 57(5):609-621.

53. Johansson S, Svineng G, Wennerberg K, Armulik A, & Lohikangas L (1997) Fibronectin-integrin interactions. *Front Biosci* 2:d126-146.

54. Jacamo R, Jiang X, Lunn JA, & Rozengurt E (2007) FAK phosphorylation at Ser-843 inhibits Tyr-397 phosphorylation, cell spreading and migration. *J Cell Physiol* 210(2):436-444.

55. Lim ST (2013) Nuclear FAK: a new mode of gene regulation from cellular adhesions. *Mol Cells* 36(1):1-6.

56. Destaing O*, et al.* (2010) beta1A integrin is a master regulator of invadosome organization and function. *Mol Biol Cell* 21(23):4108-4119.

57. Albiges-Rizo C, Destaing O, Fourcade B, Planus E, & Block MR (2009) Actin machinery and mechanosensitivity in invadopodia, podosomes and focal adhesions. *J Cell Sci* 122(Pt 17):3037-3049.

58. Tavora B*, et al.* (2014) Endothelial-cell FAK targeting sensitizes tumours to DNA-damaging therapy. *Nature* 514(7520):112-116.

59. Whisler JA, Chen MB, & Kamm RD (2014) Control of perfusable microvascular network morphology using a multiculture microfluidic system. *Tissue Eng Part C Methods* 20(7):543-552.

60. Labelle M, Begum S, & Hynes RO (2011) Direct signaling between platelets and cancer cells induces an epithelial-mesenchymal-like transition and promotes metastasis. *Cancer Cell* 20(5):576-590.
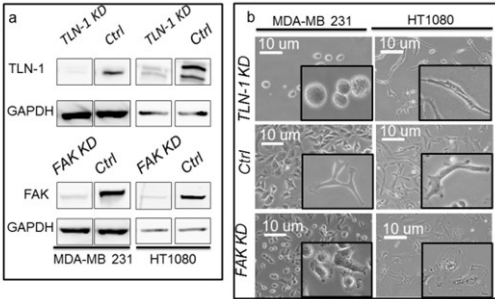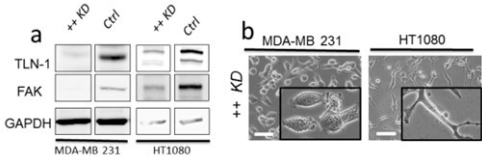
Supplementary information

Fig S1

Fig S2

Fig S3

Fig S4

Fig S5

Fig S6

(http://www.pathwaycommons.org/pcviz/#neighborhood/CDK5,TLN1,FAK)
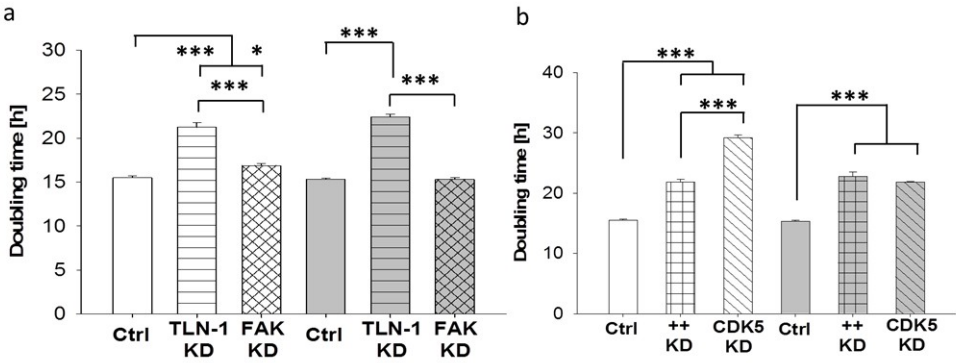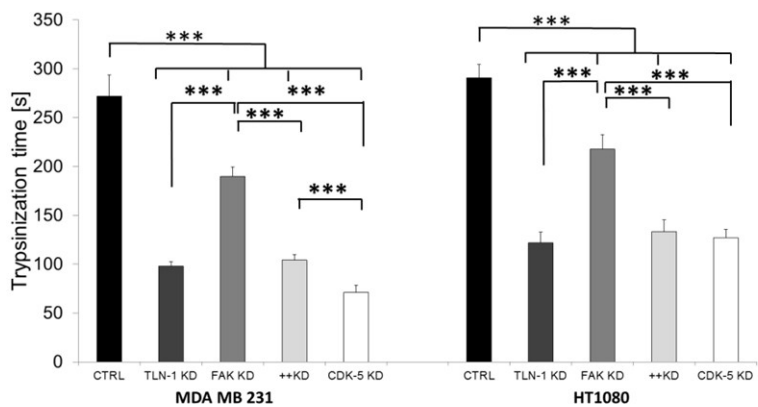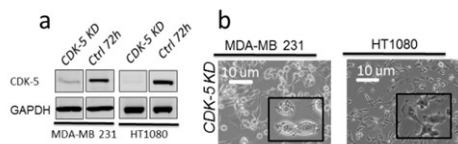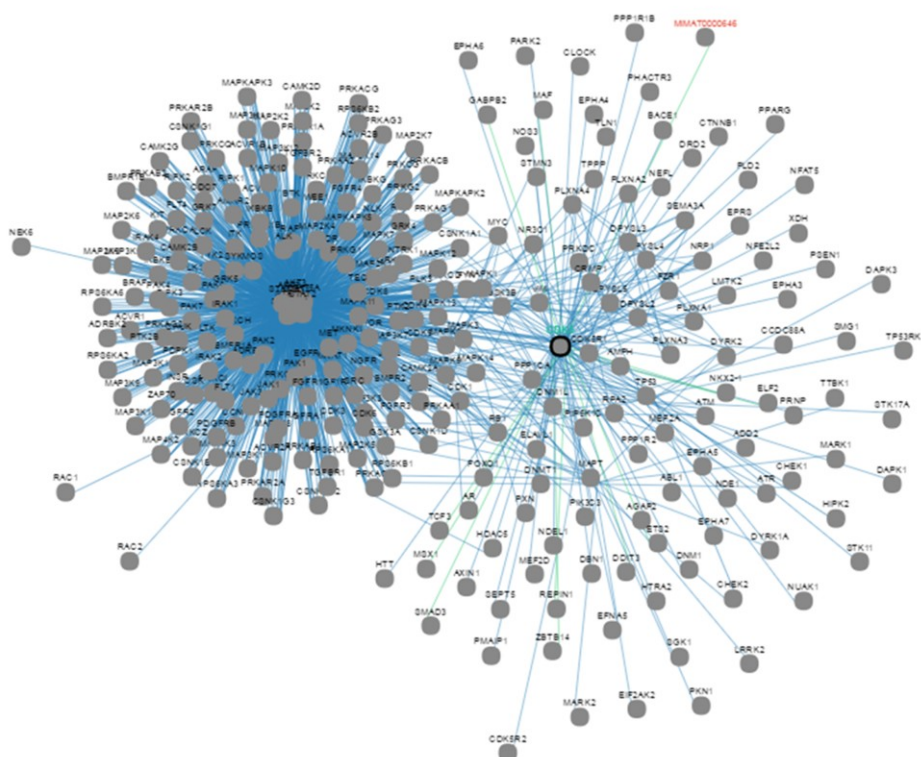
Supplementary Fig 7
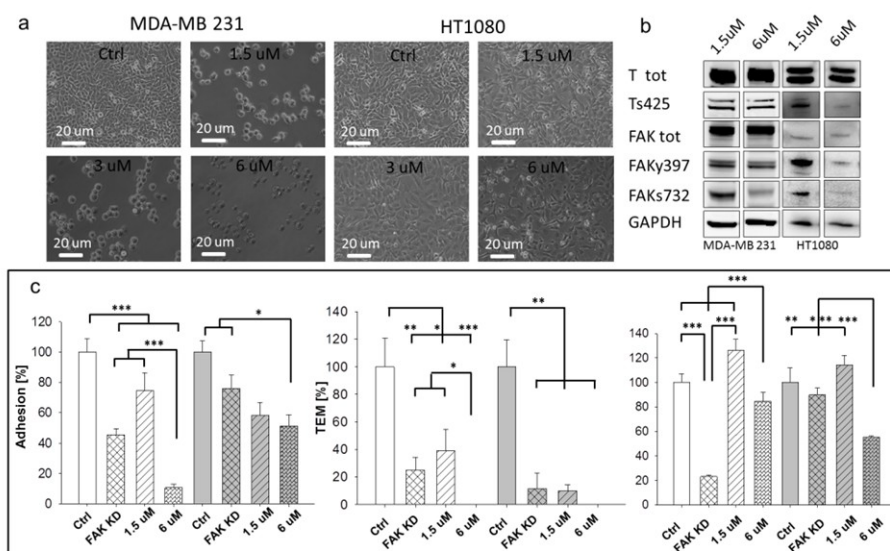
Supplementary Table 1

Significance Tests - Adhesion - MDA-231

	Ctrl	TLN1 KD	FAK KD	++ KD	CDK5 KD
Ctrl		P<0.001	P<0.001	P<0.001	P<0.001
TLN1 KD	P<0.001		P<0.05	n.s.	P<0.05
FAK KD	P<0.001	P<0.05		n.s.	P<0.01
++ KD	P<0.001	n.s.	n.s.		P<0.05
CDK5 KD	P<0.001	P<0.05	P<0.01	P<0.05	

Significance Tests - Adhesion - HT-1080

	Ctrl	TLN1 KD	FAK KD	++ KD	CDK5 KD
Ctrl		P<0.001	n.s.	P<0.001	P<0.001
TLN1 KD	P<0.001		n.s.	n.s.	n.s.
FAK KD	n.s.	n.s.		P<0.05	P<0.05
++ KD	P<0.001	n.s.	P<0.05		n.s.
CDK5 KD	P<0.001	n.s.	P<0.05	n.s.	

Supplementary Table 2

Significance Tests - TEM - MDA-231

	Ctrl	TLN1 KD	FAK KD	++ KD	CDK5 KD
Ctrl		P<0.05	P<0.01	P<0.01	P<0.01
TLN1 KD	P<0.05		P<0.05	P<0.01	P<0.05
FAK KD	P<0.01	P<0.05		n.s.	n.s.
++ KD	P<0.01	P<0.01	n.s.		n.s.
CDK5 KD	P<0.01	P<0.05	n.s.	n.s.	

Significance Tests - TEM - HT-1080

	Ctrl	TLN1 KD	FAK KD	++ KD	CDK5 KD
Ctrl		P<0.01	P<0.01	P<0.01	P<0.01
TLN1 KD	P<0.01		n.s.	n.s.	n.s.
FAK KD	P<0.01	n.s.		n.s.	n.s.
++ KD	P<0.01	n.s.	n.s.		n.s.
CDK5 KD	P<0.01	n.s.	n.s.	n.s.	

Supplementary Table 3

Significance Tests - Invasion - MDA-231

	Ctrl	TLN1 KD	FAK KD	++ KD	CDK5 KD
Ctrl		P<0.001	P<0.001	P<0.001	P<0.001
TLN1 KD	P<0.001		P<0.05	n.s.	P<0.01
FAK KD	P<0.001	P<0.05		n.s.	P<0.05
++ KD	P<0.001	n.s.	n.s.		P<0.001
CDK5 KD	P<0.001	P<0.01	n.s.	P<0.001	

Significance Tests - Invasion - HT-1080

	Ctrl	TLN1 KD	FAK KD	++ KD	CDK5 KD
Ctrl		P<0.001	n.s.	P<0.01	P<0.001
TLN1 KD	P<0.001		P<0.001	n.s.	n.s.
FAK KD	n.s.	P<0.001		P<0.001	P<0.001
++ KD	P<0.01	n.s.	P<0.001		P<0.001
CDK5 KD	P<0.001	n.s.	P<0.001	P<0.001	

Supplementary Table 4

	CTRL		Talin-1 KD		FAK KD		Double KD		CDK-5 KD	
	MDA-MB231	HT1080	MDA-MB231	HT1080	MDA-MB231	HT1080	MDA-MB231	HT1080	MDA-MB231	HT1080
Adhesion	100±8.91%	100±7.25%	34.04±2.18%	52.66±9.54%	45.33±4.04%	76.15±8.81%	39.73±9.81%	53.55±5.12%	10.96±5.22%	48.31±4.46%;
Extravasation	22.66±4.75%	21.8±4.27%	13.49±1.94%	2.77±1.7%	5.67±2.09%	2.5±2.5%	2.38±2.38%	1.32±1.32%	6.99±2.15%	3.11±2.37%
Early invasion	100±6.86%	100±12.15 %	26.22±1.87 %	47.39±4.57 %	23.18±1.17 %	89.93±5.7%	24.45±0.75%	50.55±2.3%	22.83±2.34%	49.49±7.58%

FAK s732 inhibition

	MDA-MB231 1,5µM	MDA-MB231 3µM	MDA-MB231 6µM	HT1080 1,5µM	HT1080 3µM	HT1080 6µM
Adhesion	74.59±11.9%	48.52±5.55%	10.67±2.27%	58.45±8.5%	50.82±8.37%	51.3±7.36%
Extravasation	8.9±3.43%	3.55±1.64%	0.00±0.00%	2.19±0.97%	0.00±0.00%	0.00±0.00%
Early invasion	125.94±9.35%	80.06±4.31%	84.58±7.37%	114.29±7.65%	69.49±5.8%	55.22±0.97%

	CTRL		Talin-1 KD		FAK KD		Double KD		CDK-5 KD	
	MDA-MB231	HT1080	MDA-MB231	HT1080	MDA-MB231	HT1080	MDA-MB231	HT1080	MDA-MB231	HT1080
Doubling time	15.3±0.3	15.5±0.38	21.23±0.87	22.39±0.53	16.87±0.43	15.28±0.4	21.82±0.86	22.8±1.29	29.24±0.78	21.81±0.15

Chapter 10

Integrin α_{IIb}β₃ inhibition modulates the properties of the early metastatic niche and reduces breast cancer cell extravasation

From: M. Gilardi*, S. Bersini*, M. Crippa, C. Arrigoni, S. Gamba, A. Vignoli, M. Marchetti, M. Broggini, M. Vanoni, M. Moretti
*equally contributing authors

Article in preparation

10.1 Introduction

Metastases represent the leading cause of cancer related deaths. One of the major reasons is that clinical research has been traditionally focused on the treatment of primary tumors and no effective anti-metastatic therapies are currently available [1].

Metastasis is a multistep process consisting of many interrelated events, i.e. detachment from the primary tumor, intravasation into the vascular system, initial arrest on the endothelium, extravasation and colonization of distant target tissues [2]. A key aspect during metastatic dissemination is that multiple players establish

competitive mechanisms whereby cancer cells (CCs) experience both pro- and anti-metastatic effects [3, 4]. For instance, it is now accepted that platelets contribute to metastatic dissemination by creating a physical shield which protects CCs from the harsh fluid dynamic conditions experienced into the bloodstream and prevents the attacks of circulating natural killer cells [5, 6]. Platelets secrete multiple factors [7] which affect the epithelial to mesenchymal transition (EMT) of CCs and their invasive behavior [8], as well as the activation of the endothelium and the attraction of bone marrow derived cells and other cell types playing a positive role in the formation of metastases [9]. Particularly, Labelle and co-authors showed that platelet-derived transforming growth factor (TGF)-β and direct platelet-tumor cell interactions activate the TGFβ/Smad and NF-κB pathways in CCs, leading to an invasive mesenchymal-like phenotype and enhanced metastasis *in vivo* [8]. Looking at CC extravasation, Schumacher and colleagues demonstrated that tumor cell-activated platelets promote CC migration through the endothelial barrier [10].

On the other side, other immune cells including neutrophils play a much more controversial role. Indeed, Granot and colleagues demonstrated that tumor entrained neutrophils (TENs) inhibit metastatic seeding in the lungs by generating H_2O_2 and that tumor secreted CCL2 is a critical mediator for the optimal anti-metastatic entrainment of granulocyte-colony stimulating factor (G-CSF)-stimulated neutrophils [3]. TGFβ signaling within the tumor microenvironment polarizes tumor associated neutrophils (TAN) towards a pro-tumoral phenotype while TGF-β blockade increases the level of cytotoxic, anti-tumor neutrophils [11]. However, other studies showed that neutrophils positively regulate the development of metastases [12, 13]. In particular, neutrophils physically interact with circulating tumor cells and anchor them to the endothelium through the interaction between adhesion molecule-1 on CCs and β2 integrin on neutrophils [14]. Following CC extravasation in the secondary site, neutrophil-derived leukotrienes aid tissue colonization by selectively expanding the sub-pool of CCs

that retain high tumorigenic potential [15]. Similarly, Coffelt and colleagues demonstrated that neutrophils interact with γδT cells to induce breast cancer metastases [16]. Overall, these studies highlight an heterogeneous body of literature and allow to suggest that context-dependent stimuli from the local microenvironment could drive the phenotype of neutrophils and other immune cells [17]. In addition, even though previous studies often focused on the specific effect of neutrophils [3] or platelets [8], it should be considered that circulating tumor cells simultaneously interact with these and other blood components. Indeed, as recently discussed by the Hynes group, platelets and neutrophils interact with CCs and the endothelium in the so-called early metastatic niche [18]. In this framework, platelet and neutrophil secreted factors not only affect the invasive ability of CCs, but also alter the properties of the endothelium. Indeed, activated platelets secrete adenine nucleotides, which induce endothelial barrier opening through interaction with the endothelial P2Y2 receptor and increase CC extravasation [10]. Platelet and CC secreted vascular endothelial growth factor (VEGF) modifies the integrity of the endothelium through activation of the c-Src, focal adhesion kinase (FAK), vascular endothelial (VE)-cadherin signaling axis, which leads to VE-cadherin^{Y658} phosphorylation and adherens junction opening [19].

Since targeting CC extravasation could represent a promising strategy to limit the metastatic dissemination, it is fundamental to analyze the complex heterotypic interactions occurring among each component of the early metastatic niche. However, it should be noted that despite *in vivo* animal models allow to study the patho-physiology of a living organism, they do not fully recapitulate the complex events associated with cancer metastases in the human body. Indeed, it is known that significant differences exist between mouse and human immune systems and that species-specificity may explain why potentially effective therapeutics fail after promising pre-clinical trials [20]. On the other side, *in vitro* models allow to precisely analyze the biological interactions between multiple cells types, even

though the lack of the physiological 3D architecture and functionality characterizing *in vivo* tissues poses a significant limitation to understand complex biological systems. Microfluidic and microscale models [21] couple the analytical advantages of traditional 2D *in vitro* models with the possibility to more reliably mimic the biochemically and biophysically complex phenomena of the *in vivo* microenvironment. For these reasons, these models represent the natural and most effective bridge between 2D *in vitro* assays and *in vivo* models.

Previous *in vitro* and *in vivo* studies have reported the use of drugs targeting specific components of the early metastatic niche, with a particular emphasis on platelets [22, 23]. In this context, platelet glycoprotein IIb/IIIa ($\alpha_{II}b\beta3$ integrin) inhibitor eptifibatide is a clinically approved drug reducing the risk of acute cardiac ischemic events. However, this drug has been recently employed to inhibit platelet activation and reduce the invasive potential of CCs [24]. Here, we hypothesized that inhibition of $\alpha_{II}b\beta3$integrin may affect multiple components of the early metastatic niche, since it is known that integrin signaling plays a critical role in carcinogenesis and $\alpha_{II}b\beta3$ is expressed by different CC lines [25]. Hence, the aim of the present work was to analyze the effect of $\alpha_{II}b\beta3$ inhibitor on CC extravasation and elucidate the mechanisms of action of the drug on each component of the early metastatic niche. To reach our goal, we coupled traditional multi-culture experiments with advanced 3D vascularized microfluidic models, which allowed us to show that competitive mechanisms occurring in the early metastatic niche regulate the process of extravasation. We found that inhibition of $\alpha_{II}b\beta3$ integrin is a key modulator of the cellular interactions among early metastatic niche components. In addition, we demonstrated the existence of a new signaling pathway acting through $\alpha_{II}b\beta3$ integrin which is involved in endothelial junction regulation. In particular, we demonstrated that the inhibition of $\alpha_{II}b\beta3$ integrin impairs VE-cadherin[Y658] phosphorylation and its nuclear internalization, thus maintaining endothelial junction functionality and limiting CC extravasation.

10.2. Materials and Methods

Microfabrication

The microfluidic device contains three hydrogel regions each of them flanked by two lateral media channels. The device is made of poly-dimethyl-siloxane (PMDS) using soft lithography techniques, as previously shown in our other studies [ref jeon]. The reservoirs of each channel are created with biopsy punches and plasma treatment allows the bonding with a glass slide to generate 200 μm-deep microchannels.

Cell culture and hydrogel preparation

A 2.5 mg/ml fibrin gel with resuspended cells was injected in the channels. After 20 min gelation, the media channels were filled with EGM-2 media. The central channel was seeded with GFP HUVECs (3.5 Mcells/ml) and allowed to generate perfusable microvascular networks after 4 days. The two side channels were seeded with lung fibroblasts or bone marrow mesenchymal stem cells (4 Mcells/ml) to promote vessel formation and maturation. After 4 days a mixture of RFP MDA-231 breast cancer cells (400,000 cells/ml), platelets (200 Mcells/ml) and neutrophils (3,500 cells/ml) was seeded in the two media channels on both sides of the microvascular network. 5 h post-injection devices were fixed with 2.5% paraformaldehyde (PFA). Devices as well as cancer cells+platelets+neutrophils were pre-conditioned with $\alpha_{IIb}\beta_3$ inhibitor (eptifibatide, 7.5μl/ml) at day 3. Platelets and neutrophils were obtained by isolation from human buffy coat. A preliminary centrifugation with Ficoll gradient allowed to divide the blood components according to their molecular weight, then platelets were purified with Krebs washing and precipitated with successive centrifugations. Instead, neutrophils were obtained following treatment with 3% dextran and purified from red blood cells with washings at different pH.

2D co-cultures

Combinations of HUVECs (800,000 cells/well), MDA-231 (800,000 cells/well), platelets (200 Mcells/ml) and neutrophils (3,500 cells/ml) were analyzed with and without $\alpha_{IIb}\beta_3$ inhibitor. Images were captured 24 h post-seeding with a fluorescent microscope (Olympus). Images were processed with ImageJ software.

Western Blot

Lysates and conditioned media were collected from the same wells that were used for obtaining morphology images. The corpuscular elements were lysated and diluted 1:10 with lysis buffer. The following antibodies were used: GAPDH, PAI, MMP9, FAK (total and phosphorylated), ERK (total and phosphorylated), AKT (total and phosphorylated), KINDLIN, CDK-5, TALIN-1 (total and phosphorylated), Src (total and phosphorylated), VE-Cadherin (total and phosphorylated), INTαIIbβ3.

Immunofluorescence

Cells were washed with PBS, fixed with 2.5% PFA and treated with 0.1% Tryton X-100% for 10 minutes. Cells were incubated with 5% bovine serum albumin for 1h at room temperature. Then primary antibodies were incubated for 2h at room temperature. After washing in PBS, cells were incubated with secondary antibody for 1h at room temperature. The following antibodies were used: PAI, MMP9, INTαIIbβ3, PAC, CD11b. Images were acquired with a Nikon confocal microscope.

Scratch assay

50,000 MDA-231 were seeded in 24 wells. A scratch as long as the well diameter was created after formation of a cell monolayer. Images were captured with a

fluorescent microscope at day 0 and day 1. Images were processed and quantified with ImageJ software.

10.3 Results and Discussion

10.3.1 Contact with endothelial cells (ECs) and CCs increases platelet activation

Platelet activation represents a complex process whereby multiple signaling pathways synergistically act to further induce platelet aggregation [7]. Preliminary experiments were performed to quantify the effect of cell culture medium on platelet activation and demonstrate the role that both CCs and ECs play in this process. Platelets were isolated from whole blood (Supplementary FigS1A) and incubated with or without CCs and ECs in endothelial growth medium (EGM)-2 containing heat inactivated serum. The presence of EGM-2 slightly modified the expression of the activation marker P-selectin [26] after 24 h incubation compared to the basal level of P-selectin detected in fresh platelets (8.8% vs. 0.5%) (Fig. 1A and B) [27]. Noteworthy, platelet activation was significantly enhanced in presence of CCs-ECs co-culture compared to controls (average P-selectin expression 31% vs. 8.8%) after 24 h incubation (Fig1A and B). However, we found that the major determinant of platelet activation was the presence of ECs rather than CCs (average P-selectin expression 29.2% vs. 16.3%).
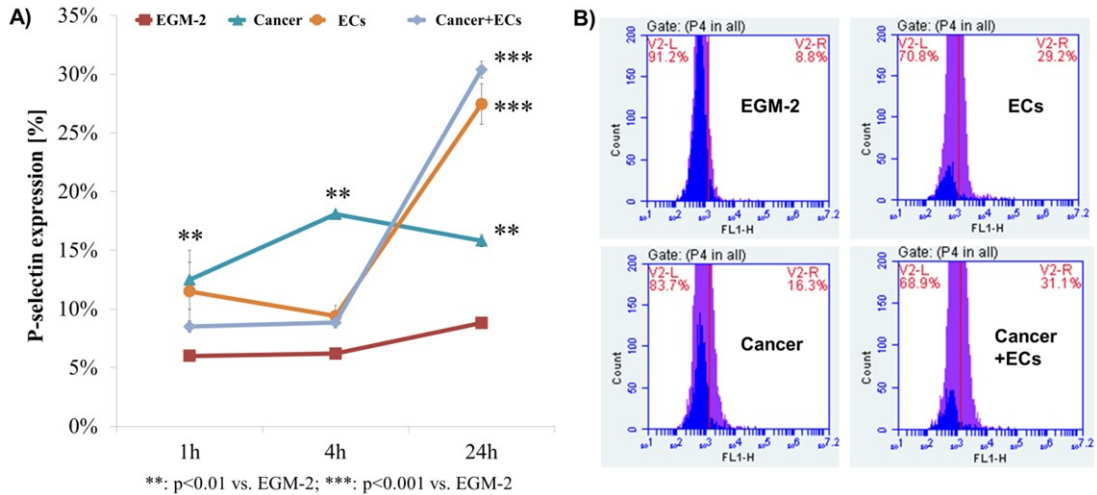
Fig1: Analyses of platelet activation in different condition through FACS analyses.

Overall, these data demonstrate that EGM-2 represents a suitable cell culture medium to perform platelet activation experiments, since it does not significantly alter the P-selectin expression profile of platelets. Indeed, preliminary experiments performed with standard CC medium containing heat inactivated serum showed higher P-selectin expression after 1 h incubation compared to EGM-2 treated platelets (average P-selectin expression 15.35% vs. 6.00%). Finally, our simple co-culture model including CCs, ECs and platelets significantly increased platelet activation suggesting that the heterotypic cross-talk among these cell types modulates platelet activation and aggregation.

10.3.2 A matter of 4 players: cell morphology, viability and proliferation in the early metastatic niche

Co-culture experiments were performed to analyze morphological features of each cell type involved in the early metastatic niche. Surprisingly, we found that the interaction among CCs, ECs and immune cells after 24 h not only affected CC morphology, as previously demonstrated by simpler co-culture studies of CCs and platelets [8], but also induced significant changes to EC shape and organization,

and platelets/neutrophils aggregation. In addition, we analyzed the effect of integrin $\alpha_{IIb}\beta_3$ inhibition, being this integrin expressed by each component of the early metastatic niche including neutrophils (Supplementary FigS2).

The addition of platelets induced CC elongation and formation of stable protrusion (Fig2A), which are markers of epithelial to mesenchymal transition (EMT) and invasive behavior [28, 29]. Similar effects were detected when CCs were co-cultured with ECs or both ECs and platelets (Fig2A), in agreement with previous studies [8, 30]. Interestingly, we found that co-culture of CCs and neutrophils induced opposite effects, since CCs exhibited a rounded shape (Fig2A), despite this particular phenotype was less evident when ECs, platelets or both were added to the initial co-culture (Fig2A). This issue is consistent with previous observations that neutrophil-derived tumor necrosis factor (TNF) superfamily members affect cancer cell proliferation and survival [31]. Adding the $\alpha_{IIb}\beta_3$ inhibitor did reduce CC elongation in presence of ECs and platelets. However, no effects were detected with CCs alone (Fig2A). Strikingly, we found that the effect of neutrophils on CC shape was even increased with $\alpha_{IIb}\beta_3$ inhibition (Fig2A), even though the presence of both ECs and platelets significantly counteracted this phenomenon (Fig2A).
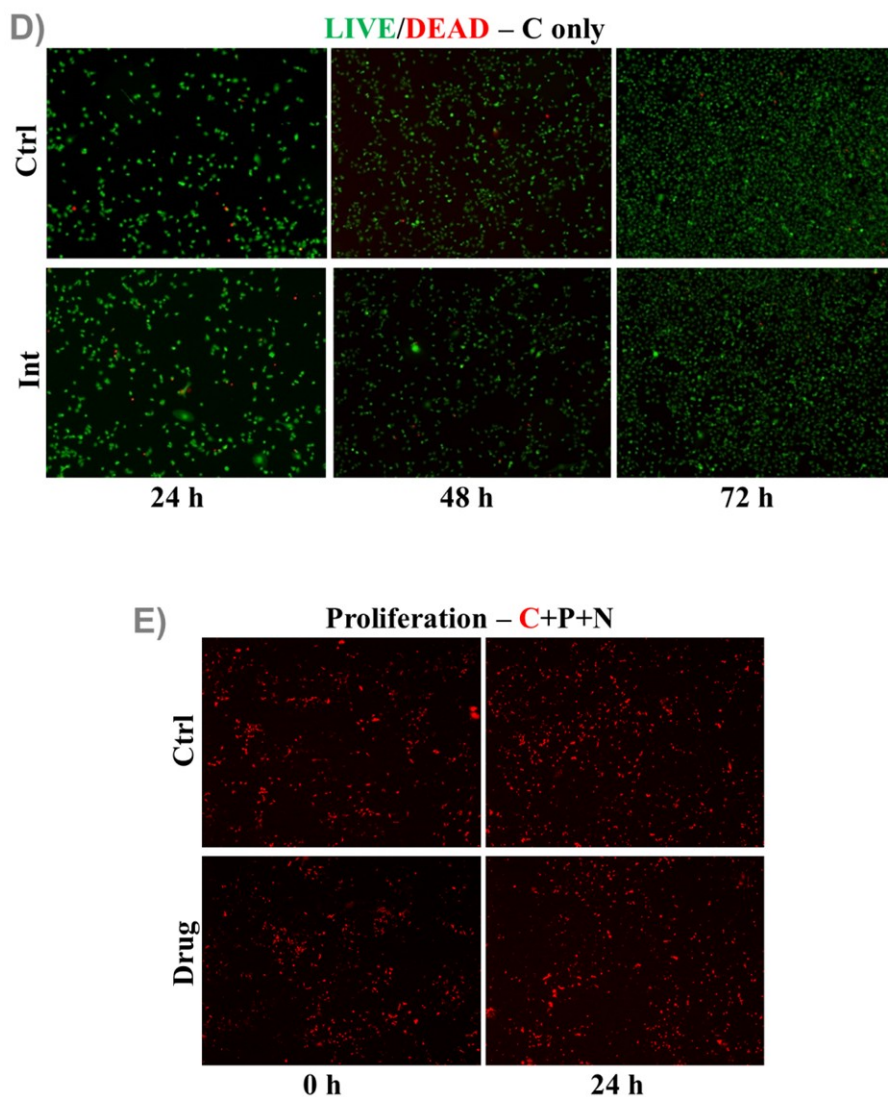
B)

C)

344
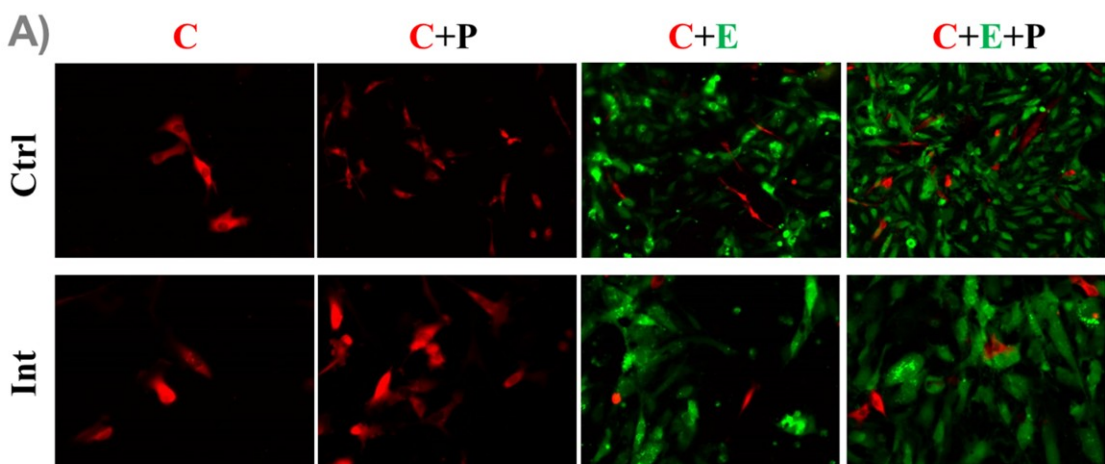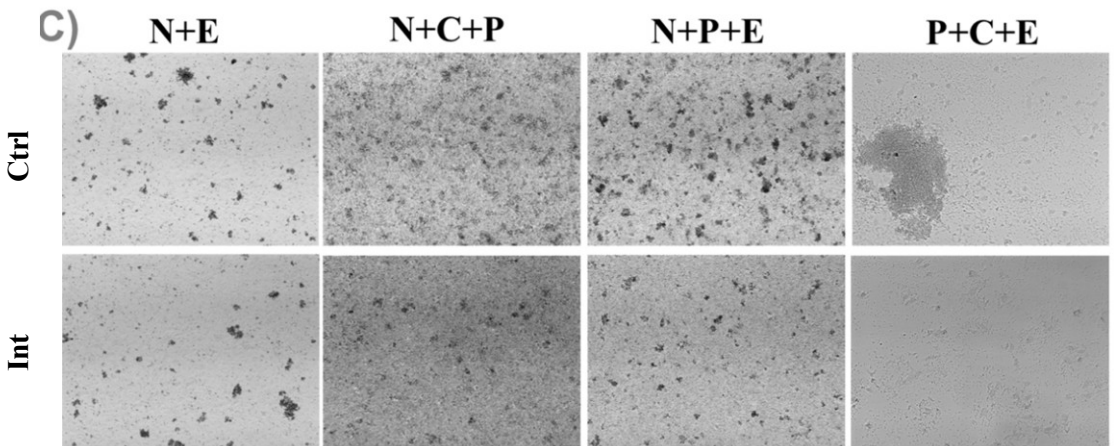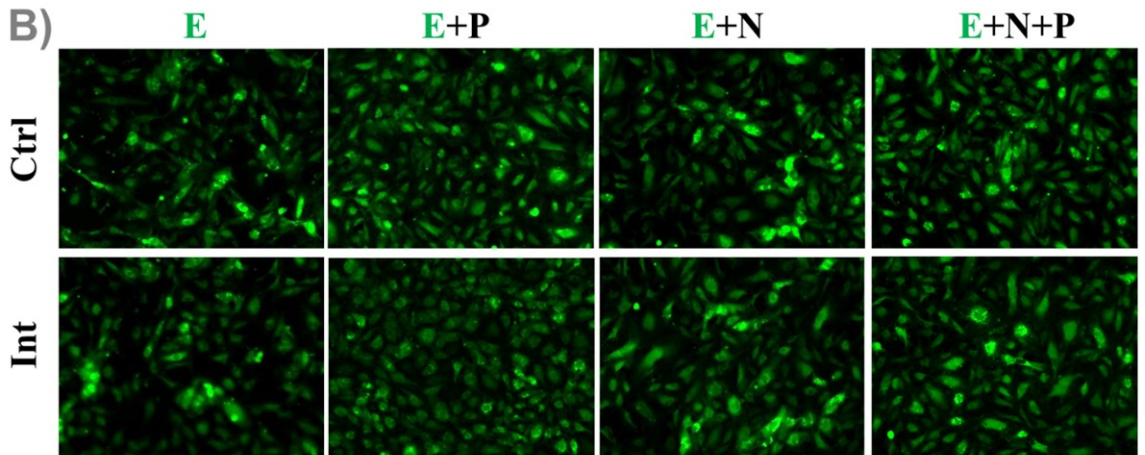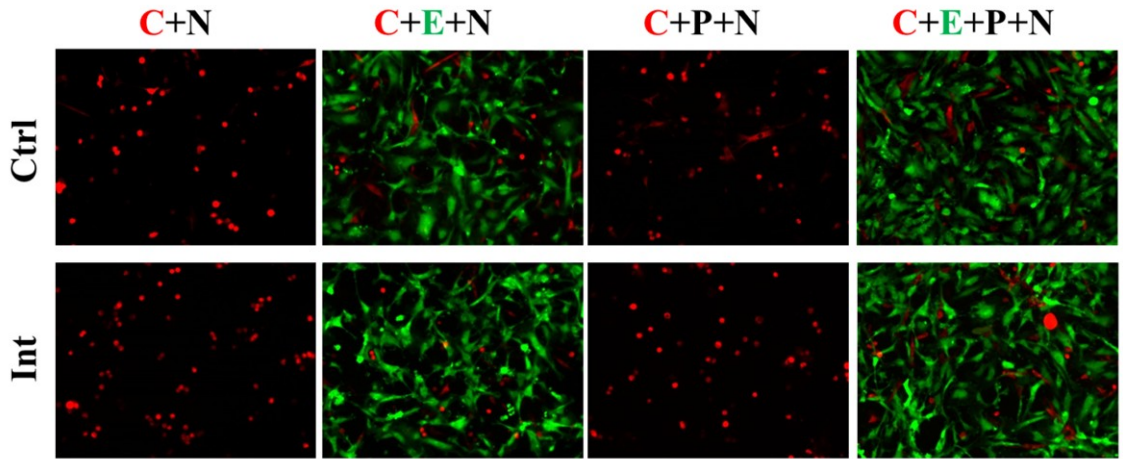
Fig2: Co-culture of cancer, endothelial cells and circulating elements in different condition. (a-b-c) Morphological features of EC, cancer, platelet and neutrophils. (d) Live and dead assays on cancer cells. (e) Proliferation assay.

Overall, the presence of ECs, platelets and neutrophils, which more closely resembles the specific microenvironment of the early metastatic niche, limited CC elongation induced by ECs or platelets alone. This effect was due to the presence of neutrophils and was even amplified following treatment with $\alpha_{IIb}\beta_3$ inhibitor, allowing us to suggest that neutrophils further increased their anti-tumor effect in

response to the drug or made CCs more receptive to the drug. Indeed, treatment with $\alpha_{IIb}\beta_3$ inhibitor limited CCs alone proliferation (Fig2D and Supplementary Fig S3), even though viability, morphology and adhesion were not impaired (Fig2D). Significantly, the same effect was found when CCs were co-cultured with platelets and neutrophils (Fig2E).

Since the endothelium represents another key component of the early metastatic niche mediating both CC extravasation [1, 32] and survival/dormancy of disseminated CCs [33], we sought to determine if the presence of CCs, platelets and neutrophils could modify its structural properties. We demonstrated that the addition of platelets or neutrophils or both increased the quality of endothelial monolayers, since it promoted EC proliferation and reduced the number of inter-endothelial gaps compared to control EC monolayers (Fig2B). No effects were detected when ECs were treated with $\alpha_{IIb}\beta_3$ inhibitor, demonstrating that $\alpha_{IIb}\beta_3$ was not required to maintain the structure of the endothelial monolayer (Fig2B). The addition of CCs compromised the integrity of the endothelium (Fig2B). This aspect is in agreement with previous studies demonstrating that CCs secrete molecules, e.g. VEGF [34], which impair both structure and function of the endothelium [35]. Furthermore, addition of platelets, neutrophils or both to CCs-ECs co-cultures partially restored the structure of the endothelium. This issue is consistent with previous findings showing that platelet-derived fibroblast growth factor (FGF)-2 and VEGF are key regulators of EC survival and proliferation [36]. At the same time, neutrophil secreted Bv8 represents a key pro-angiogenic factor mediating EC proliferation and angiogenesis [37] and could play a role in the formation and maintenance of the endothelium.

Overall, the presence of CCs, platelets and neutrophils only partially modified the structure of the endothelium. However, we found that ECs displayed an elongated morphology when co-cultured with CCs, platelets and neutrophils treated with

$\alpha_{IIb}\beta_3$ inhibitor (Fig2A). We hypothesize that this morphology could be dependent on talin modulation [38] due to integrin inactivation [39].

Finally, clusters of platelets, neutrophils or both cells were identified through co-culture experiments. Significantly, the addition of $\alpha_{IIb}\beta_3$ inhibitor generally reduced the number of platelet and neutrophil aggregates (Fig2C). Noteworthy, this aspect was also highlighted when all the components of the early metastatic niche were present. Overall, these data allow to suggest that the effect of $\alpha_{IIb}\beta_3$ inhibitor on CC morphology is not necessarily due to its anti-aggregation role on platelets and neutrophils.

Previous studies were not able to clarify the contribution of neutrophils on the metastatic dissemination. Indeed, it was shown that CCs can attract and activate neutrophils [14], which in turn promote the early survival of metastatic cells [15, 40]. However, other reports demonstrated that granulocytes can have potent anti-tumor activity and kill metastatic CCs [3, 11]. Our data on the morphological features, aggregation and survival/proliferation of different cell types involved in the early metastatic niche seem to highlight opposite anti-tumor (neutrophils) and pro-tumor (platelets) effects acting on CCs. Then, inhibition of $\alpha_{IIb}\beta_3$ reduces morphological signatures of CC invasiveness, e.g. cell protrusions and elongated cell shape, through different mechanisms involving both platelets and neutrophils.

10.3.3 $\alpha_{IIb}\beta_3$ inhibition alters the expression of CC invasion markers and $\alpha_{IIb}\beta_3$ expression/activation

Once demonstrated that addition of platelets/neutrophils and treatment with $\alpha_{IIb}\beta_3$ inhibitor influences specific signatures of the early metastatic niche, we investigated the expression of key proteins involved in cancer EMT and the activation level of $\alpha_{IIb}\beta_3$ integrin upon treatment with $\alpha_{IIb}\beta_3$ inhibitor. Immunofluorescence staining of co-cultures containing CCs, ECs, platelets and neutrophils demonstrated that $\alpha_{IIb}\beta_3$ inhibition reduced the expression of two key

markers of cancer EMT, i.e. plasminogen activator inhibitor (PAI)-1 (Fig3A and Fig3B) and matrix metalloprotease (MMP)-9 (Fig3C). Previous studies showed that PAI-1, MMP-9 and other markers including Snail and vimentin are significantly upregulated upon co-culture of CCs with platelets [8].
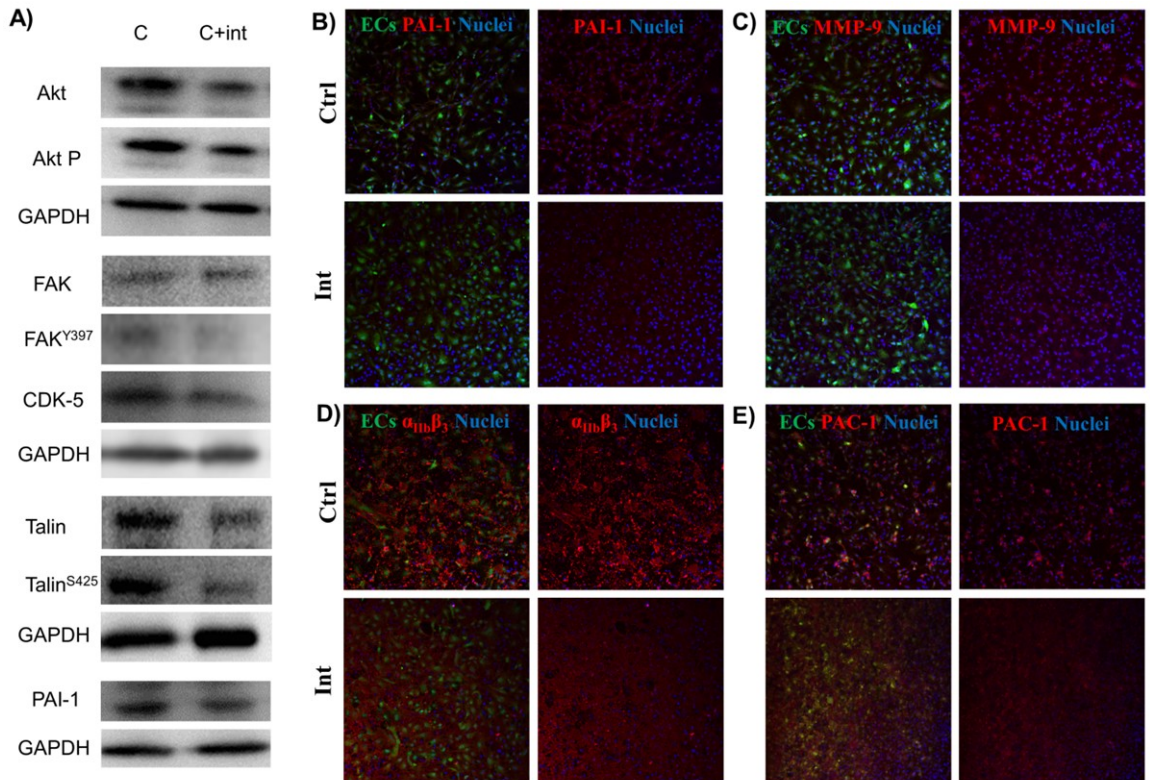

Fig3: Effects of $\alpha_{IIb}\beta_3$ inhibition (a) Protein expression determined by Western blot of cancer EMT markers and focal adhesion key player involved in aggressivness in cancer cells. (b-c) Immunofluorescence staining of co-cultures containing CCs, ECs, platelets and neutrophils of EMT markers on cancer cells (d-e) Immunofluorescence staining of co-cultures containing CCs, ECs, platelets and neutrophils and $\alpha_{IIb}\beta_3$ and its activation.

However, it was not previously demonstrated that inhibition of $\alpha_{IIb}\beta_3$ could impair cancer EMT. Reduced MMP-9 expression was also highlighted when co-cultures of CCs, ECs and platelets were treated with $\alpha_{IIb}\beta_3$ inhibitor (Supplementary FigS4A), while no differences in terms of PAI-1 were detected in the same

condition (Supplementary FigS4B). These data allow to suggest that the presence of neutrophils is necessary to mediate the reduced PAI-1 expression observed upon treatment with $\alpha_{IIb}\beta_3$ inhibitor. Surprisingly, we found that addition of $\alpha_{IIb}\beta_3$ inhibitor to co-cultures of CCs, ECs, platelets and neutrophils not only decreased the presence of activated $\alpha_{IIb}\beta_3$ on platelets and other components of the early metastatic niche (PAC-1 marker, Fig. 3E), but also reduced the expression of integrin $\alpha_{IIb}\beta_3$ (Fig3D) and the formation of platelet/neutrophil clusters (Fig2C). The positive effect of $\alpha_{IIb}\beta_3$ inhibitor in preventing cluster formation was particularly evident in specific conditions, as demonstrated by the absence of platelet aggregates when co-cultured with ECs and incubated with the drug (Supplementary FigS5).

Viable CCs and ECs from co-culture experiments were sorted from platelets and neutrophils, and analyzed through western blot looking for specific proteins involved in invasion/migration and focal adhesion. Indeed, we sought to determine if morphological differences and immunofluorescence data on classical EMT markers and integrin expression/activation were associated with more specific signatures of CC motility and endothelium remodeling. Focal adhesion proteins are upregulated in several cancers [41, 42]. Indeed, several studies have shown the central role of these proteins in the metastatic dissemination due to their involvement in cytoskeleton remodeling and cell mechanotransduction [43, 44]. In particular, the focal adhesion complex mediates multiple integrin-related signaling processes due to the specific structural organization and functionality of its constitutive proteins [45-47]. For these reasons, we investigated the effect of $\alpha_{IIb}\beta_3$ inhibitor on the focal adhesion signaling axis. We showed that treatment with $\alpha_{IIb}\beta_3$ inhibitor reduced CC expression of talin-1 and its phosphorylated form talin-1^{S425}, focal adhesion protein (FAK)^{Y397} and cyclin-dependent kinase (CDK)-5 (Fig3A). To our knowledge no previous work demonstrated that inhibition of integrin $\alpha_{IIb}\beta_3$ downregulates the expression of these focal adhesion proteins in CCs. In addition,

we found that the reduced expression of focal adhesion protein after $\alpha_{IIb}\beta_3$ inhibitor treatment was coupled with decreased expression of Akt and ERK (Fig3A) [48]. These data suggest that $\alpha_{IIb}\beta_3$ inhibition acts by means of the $\alpha_{IIb}\beta_3$/Talin-1/Akt axis.

Regarding the endothelium, we found that ECs from co-cultures with CCs, platelets and neutrophils treated with $\alpha_{IIb}\beta_3$ inhibitor showed reduced Src^{Y416} phosphorylation, FAK^{Y397} phosphorylation and vascular endothelial (VE)-cadherin^{Y658} phosphorylation (Fig4). These data, coupled with VE-cadherin cellular localization through immunofluorescence, clearly show that $\alpha_{IIb}\beta_3$ inhibition impairs the phosphorylation of key target sites of the Src-FAK-VE-cadherin signaling axis and lead to improved vascular function. We would like to highlight that treatment with $\alpha_{IIb}\beta_3$ inhibition not only restored the physiological architecture of inter-endothelial junctions but also reduced the nuclear localization of (VE)-cadherin^{658}, leading to a reduction in extravasation. Indeed, our data demonstrated that co-cultures of CCs, ECs, platelets and neutrophils significantly increased VE-cadherin^{Y658} phosphorylation and internalization toward the nucleus leading to junctions disruption, which is required for extravasation. This aspect is supported by previous findings by Jean and colleagues [19], who demonstrated the key role of Src and FAK activation in VE-cadherin^{Y658} phosphorylation and the architecture of inter-endothelial junctions.
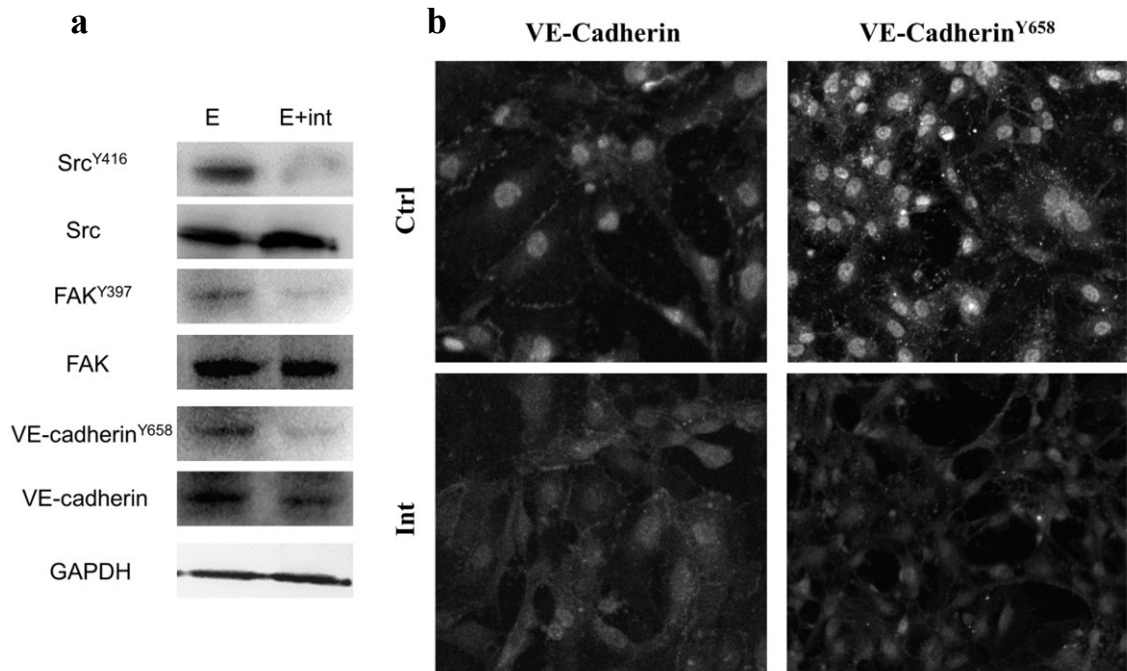
Fig4: Effects of $\alpha_{IIb}\beta_3$ inhibition on endothelial cells (a) Protein expression determined by Western blot of key player involved in junction regulation cells with or without $\alpha_{IIb}\beta_3$ inhibitor. (b) Immunofluorescence staining of co-cultures containing CCs, ECs, platelets and neutrophils of Ve-cadherine and its phosphorylation form on endothelial cells with or without $\alpha_{IIb}\beta_3$ inhibitor.

Here we show for the first time that endothelial integrin $\alpha_{IIb}\beta_3$ controls VE-cadherin phosphorylation and vascular function through the integrin $\alpha_{IIb}\beta_3$-Src-FAK-VE-cadherin signaling axis. Overall, our data demonstrate that $\alpha_{IIb}\beta_3$ represents a valuable target in the early metastatic niche since its inhibition affects both endothelial properties and CC extravasation.

10.3.4 *α_{2b}β₃ inhibition suppresses CC migration and extravasation without affecting adhesion to the endothelium*

10.3.4 $α_{2b}β_3$ inhibition suppresses CC migration and extravasation without affecting adhesion to the endothelium

Perfusable 3D microvascular networks were generated within microfluidic devices based on our previous models [32, 49]. CCs were incubated with platelets and neutrophils within standard EGM-2 or EGM-2 with $α_{IIb}β_3$ inhibitor.
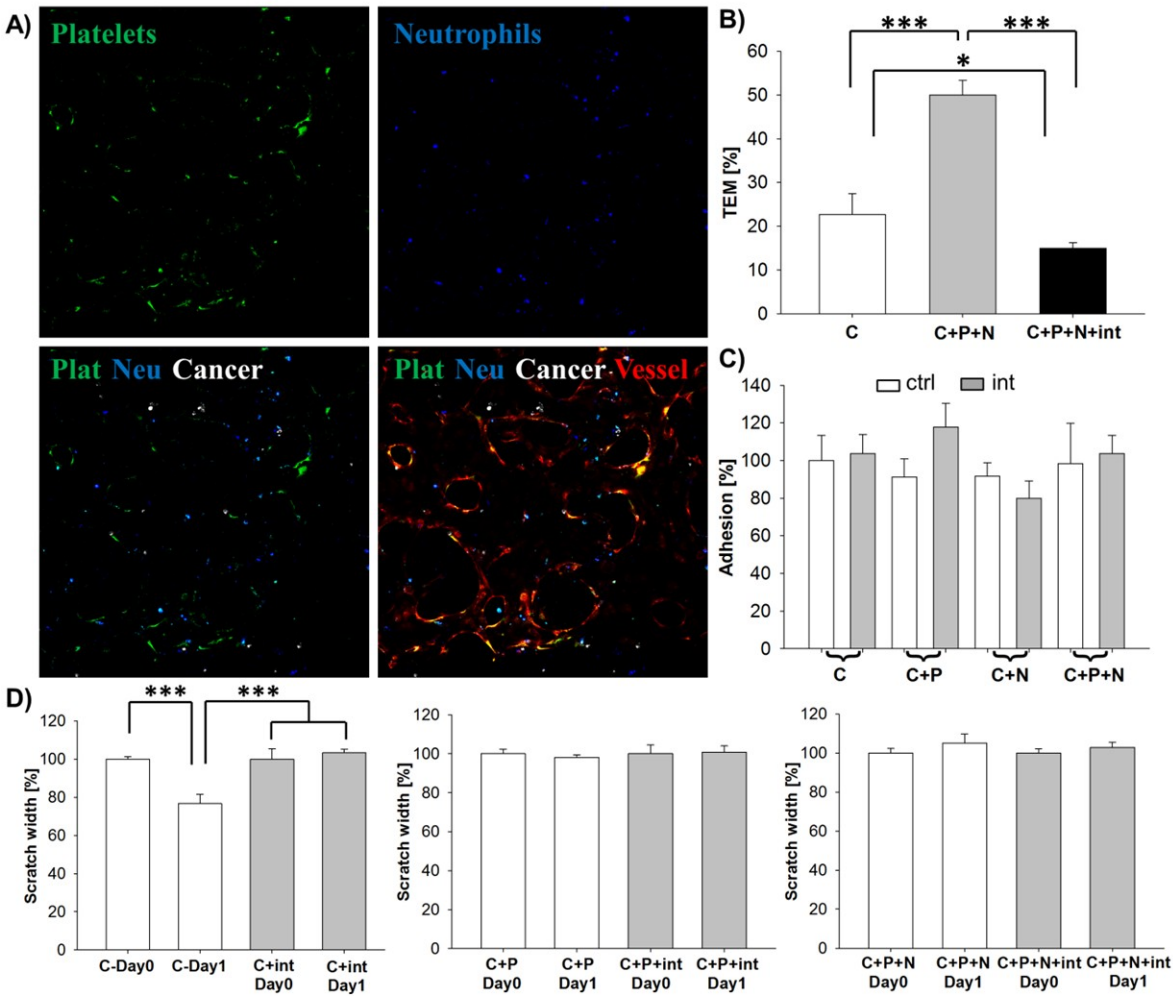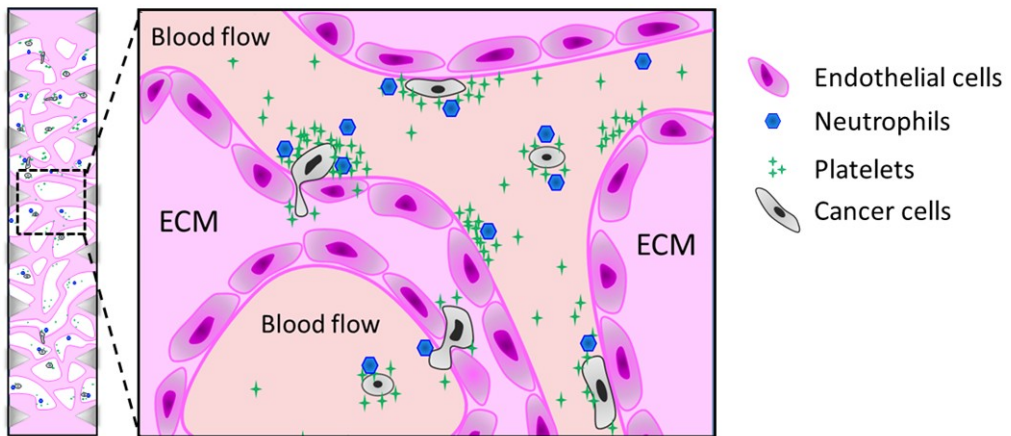
Fig5: Dissection of extravasation steps (a) Images showing the tetra-culture of platelet, neutrophils, cancer cells after the injection in microvascular network embedded in microfluidic device. (b) TEM quantification. (c) Vascular adhesion quantification (d) Scratch assay in different culture conditions. (e) Schematics of co-culture in microvascular network within microfluidic device

After 24 h, homogeneous cell suspensions containing CCs, platelets and neutrophils were injected in microvascular networks recreating the early metastatic niche (Fig5A) and CC transendothelial migration (TEM) was quantified after 5 h (Fig5B). The presence of platelets and neutrophils significantly increased the number of extravasation events compared to the injection of CCs alone. Strikingly, we found that incubation with $\alpha_{IIb}\beta_3$ inhibitor significantly impaired TEM. In addition, the number of extravasation events was even lower with respect to the introduction of CCs alone. We hypothesize that impaired extravasation is due to the combined effect of $\alpha_{IIb}\beta_3$ inhibitor on each component of the early metastatic niche, as previously shown through the analysis of cell morphology, viability, proliferation and marker expression (Fig2 and 3). In particular, $\alpha_{IIb}\beta_3$ inhibitor affects both localization and phosphorylation of VE-cadherins, thus increasing the tightness of inter-endothelial junctions and reducing CC extravasation.

Our data are in agreement with *in vivo* and *in vitro* studies demonstrating that platelets not only increase CC invasive potential [8], but also activate the endothelium [9] and increase vascular permeability [10]. The pro-tumor effect of platelets is counteracted by the presence of neutrophils, which impair CC invasiveness as demonstrated by co-culture experiments. Previous works did not clarify the role of neutrophils in the metastatic dissemination. Indeed, it is known that neutrophils can kill CCs [3] through different mechanisms, including secretion of cytotoxic inducible nitric oxide synthase (iNOS) [50]. However, several studies highlighted the pro-tumor effect of neutrophils and other immune cells [18, 40]. In the end, we hypothesize that the pro-tumor effect of platelets during extravasation overwhelms the anti-tumor role of neutrophils.

Since the presence of both platelets and neutrophils positively influenced cancer cell extravasation, we sought to determine which specific step of this process was mainly affected. Surprisingly, we did not identify significant differences in terms of CC vascular adhesion when CCs were co-incubated with platelets, neutrophils or both (Fig5C). Furthermore, treatment with $\alpha_{IIb}\beta_3$ inhibitor did not affect CC adhesion in any condition. These data highlight that platelets and neutrophils specifically influence the process of TEM and their presence does not affect CC vascular adhesion. This aspect confirms and extends previous studies which demonstrated how CC-platelet interactions are not required for CC vascular adhesion [5].

Finally, the invasive potential of CCs was analyzed through wound healing assay. Strikingly, we found that addition of platelets or combination of platelets and neutrophils did not promote CC migration and wound closure (Fig5D and Supplementary FigS6). Conversely, CCs alone were able to partially restore the initial CC monolayer, even though the incubation with $\alpha_{IIb}\beta_3$ inhibitor completely abrogated this process. We would like to highlight that the wound healing assay does not include ECs. Overall, these results demonstrate that the endothelium plays

an essential role during CC metastatic dissemination, since its presence is fundamental to mediate the functional effect of platelets and neutrophils on CC behavior.

10.3.5 Conclusions

We have characterized the behavior of the different components of the early metastatic niche through analyses of cell morphology, proliferation, protein level and adhesion/TEM/invasion assays, and we have quantified the effect of treatment with $\alpha_{IIb}\beta_3$ inhibitor. Our findings allow to suggest that competitive mechanisms occurring in the early metastatic niche regulate the process of extravasation. We have demonstrated that platelets exert pro-tumor effects which are counteracted by the anti-tumor role of neutrophils. In this framework, our data show for the first time that inhibiting integrin $\alpha_{IIb}\beta_3$ not only impairs platelet aggregation, but also affects each component of the early metastatic niche. Indeed, treatment with $\alpha_{IIb}\beta_3$ inhibitor makes CCs less aggressive due to direct (cell-cell contacts) and indirect (paracrine secretions) effects of platelets. In addition, $\alpha_{IIb}\beta_3$ inhibitor acts through neutrophils to make CCs less aggressive, even though the mechanisms regulating this process have not yet been identified. Finally, $\alpha_{IIb}\beta_3$ inhibition restores the architecture of inter-endothelial junctions acting through the integrin $\alpha_{IIb}\beta_3$-Src-FAK-VE-cadherin signaling axis, thus impairing the metastatic dissemination.

Overall, we have elucidated the mechanisms of action of a clinically approved anti-platelet drug demonstrating that a standard therapeutics for blood disorders could be a promising tool to target the early metastatic niche and the process of CC extravasation.

References

[1] Valastyan S, Weinberg RA. Tumor metastasis: molecular insights and evolving paradigms. Cell. 2011;147:275-92.

[2] Massague J, Obenauf AC. Metastatic colonization by circulating tumour cells. Nature. 2016;529:298-306.

[3] Granot Z, Henke E, Comen EA, King TA, Norton L, Benezra R. Tumor entrained neutrophils inhibit seeding in the premetastatic lung. Cancer Cell. 2011;20:300-14.

[4] Labelle M, Hynes RO. The initial hours of metastasis: the importance of cooperative host-tumor cell interactions during hematogenous dissemination. Cancer Discov. 2012;2:1091-9.

[5] Im JH, Fu W, Wang H, Bhatia SK, Hammer DA, Kowalska MA, et al. Coagulation facilitates tumor cell spreading in the pulmonary vasculature during early metastatic colony formation. Cancer Res. 2004;64:8613-9.

[6] Nieswandt B, Hafner M, Echtenacher B, Mannel DN. Lysis of tumor cells by natural killer cells in mice is impeded by platelets. Cancer Res. 1999;59:1295-300.

[7] Gay LJ, Felding-Habermann B. Contribution of platelets to tumour metastasis. Nat Rev Cancer. 2011;11:123-34.

[8] Labelle M, Begum S, Hynes RO. Direct signaling between platelets and cancer cells induces an epithelial-mesenchymal-like transition and promotes metastasis. Cancer Cell. 2011;20:576-90.

[9] Massberg S, Konrad I, Schurzinger K, Lorenz M, Schneider S, Zohlnhoefer D, et al. Platelets secrete stromal cell-derived factor 1alpha and recruit bone marrow-derived progenitor cells to arterial thrombi in vivo. J Exp Med. 2006;203:1221-33.

[10] Schumacher D, Strilic B, Sivaraj KK, Wettschureck N, Offermanns S. Platelet-derived nucleotides promote tumor-cell transendothelial migration and metastasis via P2Y2 receptor. Cancer Cell. 2013;24:130-7.

[11] Fridlender ZG, Sun J, Kim S, Kapoor V, Cheng G, Ling L, et al. Polarization of tumor-associated neutrophil phenotype by TGF-beta: "N1" versus "N2" TAN. Cancer Cell. 2009;16:183-94.

[12] Slattery MJ, Dong C. Neutrophils influence melanoma adhesion and migration under flow conditions. Int J Cancer. 2003;106:713-22.

[13] Spicer JD, McDonald B, Cools-Lartigue JJ, Chow SC, Giannias B, Kubes P, et al. Neutrophils promote liver metastasis via Mac-1-mediated interactions with circulating tumor cells. Cancer Res. 2012;72:3919-27.

[14] Huh SJ, Liang S, Sharma A, Dong C, Robertson GP. Transiently entrapped circulating tumor cells interact with neutrophils to facilitate lung metastasis development. Cancer Res. 2010;70:6071-82.

[15] Wculek SK, Malanchi I. Neutrophils support lung colonization of metastasis-initiating breast cancer cells. Nature. 2015;528:413-7.

[16] Coffelt SB, Kersten K, Doornebal CW, Weiden J, Vrijland K, Hau CS, et al. IL-17-producing gammadelta T cells and neutrophils conspire to promote breast cancer metastasis. Nature. 2015;522:345-8.

[17] Liang W, Ferrara N. The Complex Role of Neutrophils in Tumor Angiogenesis and Metastasis. Cancer Immunol Res. 2016;4:83-91.

[18] Labelle M, Begum S, Hynes RO. Platelets guide the formation of early metastatic niches. Proc Natl Acad Sci U S A. 2014;111:E3053-61.

[19] Jean C, Chen XL, Nam JO, Tancioni I, Uryu S, Lawson C, et al. Inhibition of endothelial FAK activity prevents tumor metastasis by enhancing barrier function. J Cell Biol. 2014;204:247-63.

[20] Shay T, Jojic V, Zuk O, Rothamel K, Puyraimond-Zemmour D, Feng T, et al. Conservation and divergence in the transcriptional programs of the human and mouse immune systems. Proc Natl Acad Sci U S A. 2013;110:2946-51.

[21] Bhatia SN, Ingber DE. Microfluidic organs-on-chips. Nat Biotechnol. 2014;32:760-72.

[22] Guillem-Llobat P, Dovizio M, Bruno A, Ricciotti E, Cufino V, Sacco A, et al. Aspirin prevents colorectal cancer metastasis in mice by splitting the crosstalk between platelets and tumor cells. Oncotarget. 2016;7:32462-77.

[23] Liverani E, Kilpatrick LE, Tsygankov AY, Kunapuli SP. The role of P2Y(1)(2) receptor and activated platelets during inflammation. Curr Drug Targets. 2014;15:720-8.

[24] Zhao F, Li L, Guan L, Yang H, Wu C, Liu Y. Roles for GP IIb/IIIa and alphavbeta3 integrins in MDA-MB-231 cell invasion and shear flow-induced cancer cell mechanotransduction. Cancer Lett. 2014;344:62-73.

[25] Kononczuk J, Surazynski A, Czyzewska U, Prokop I, Tomczyk M, Palka J, et al. alphaIIbbeta3-integrin Ligands: Abciximab and Eptifibatide as Proapoptotic Factors in MCF-7 Human Breast Cancer Cells. Curr Drug Targets. 2015;16:1429-37.

[26] Kim YJ, Borsig L, Han HL, Varki NM, Varki A. Distinct selectin ligands on colon carcinoma mucins can mediate pathological interactions among platelets, leukocytes, and endothelium. Am J Pathol. 1999;155:461-72.

[27] Villagra J, Shiva S, Hunter LA, Machado RF, Gladwin MT, Kato GJ. Platelet activation in patients with sickle disease, hemolysis-associated pulmonary hypertension, and nitric oxide scavenging by cell-free hemoglobin. Blood. 2007;110:2166-72.

[28] Bousquet E, Calvayrac O, Mazieres J, Lajoie-Mazenc I, Boubekeur N, Favre G, et al. RhoB loss induces Rac1-dependent mesenchymal cell invasion in lung cells through PP2A inhibition. Oncogene. 2016;35:1760-9.

[29] Shibue T, Brooks MW, Weinberg RA. An integrin-linked machinery of cytoskeletal regulation that enables experimental tumor initiation and metastatic colonization. Cancer Cell. 2013;24:481-98.

[30] Ghiabi P, Jiang J, Pasquier J, Maleki M, Abu-Kaoud N, Rafii S, et al. Endothelial cells provide a notch-dependent pro-tumoral niche for enhancing breast

cancer survival, stemness and pro-metastatic properties. PLoS One. 2014;9:e112424.

[31] Koga Y, Matsuzaki A, Suminoe A, Hattori H, Hara T. Neutrophil-derived TNF-related apoptosis-inducing ligand (TRAIL): a novel mechanism of antitumor effect by neutrophils. Cancer Res. 2004;64:1037-43.

[32] Jeon JS, Bersini S, Gilardi M, Dubini G, Charest JL, Moretti M, et al. Human 3D vascularized organotypic microfluidic assays to study breast cancer cell extravasation. Proc Natl Acad Sci U S A. 2015;112:214-9.

[33] Ghajar CM, Peinado H, Mori H, Matei IR, Evason KJ, Brazier H, et al. The perivascular niche regulates breast tumour dormancy. Nat Cell Biol. 2013;15:807-17.

[34] Poon RT, Lau CP, Cheung ST, Yu WC, Fan ST. Quantitative correlation of serum levels and tumor expression of vascular endothelial growth factor in patients with hepatocellular carcinoma. Cancer Res. 2003;63:3121-6.

[35] Potter MD, Barbero S, Cheresh DA. Tyrosine phosphorylation of VE-cadherin prevents binding of p120- and beta-catenin and maintains the cellular mesenchymal state. J Biol Chem. 2005;280:31906-12.

[36] Pintucci G, Froum S, Pinnell J, Mignatti P, Rafii S, Green D. Trophic effects of platelets on cultured endothelial cells are mediated by platelet-associated fibroblast growth factor-2 (FGF-2) and vascular endothelial growth factor (VEGF). Thromb Haemost. 2002;88:834-42.

[37] Shojaei F, Wu X, Zhong C, Yu L, Liang XH, Yao J, et al. Bv8 regulates myeloid-cell-dependent tumour angiogenesis. Nature. 2007;450:825-31.

[38] Lim IR, Joo HJ, Jeong M, Kim JH, Choi SC, Kim C, et al. Talin Modulation by a Synthetic N-Acylurea Derivative Reduces Angiogenesis in Human Endothelial Cells. Int J Mol Sci. 2017;18.

[39] Ye F, Petrich BG, Anekal P, Lefort CT, Kasirer-Friede A, Shattil SJ, et al. The mechanism of kindlin-mediated activation of integrin alphaIIbbeta3. Curr Biol. 2013;23:2288-95.

[40] Acuff HB, Carter KJ, Fingleton B, Gorden DL, Matrisian LM. Matrix metalloproteinase-9 from bone marrow-derived cells contributes to survival but not growth of tumor cells in the lung microenvironment. Cancer Res. 2006;66:259-66.

[41] Sarhadi VK, Lahti L, Scheinin I, Ellonen P, Kettunen E, Serra M, et al. Copy number alterations and neoplasia-specific mutations in MELK, PDCD1LG2, TLN1, and PAX5 at 9p in different neoplasias. Genes Chromosomes Cancer. 2014;53:579-88.

[42] Singel SM, Cornelius C, Batten K, Fasciani G, Wright WE, Lum L, et al. A targeted RNAi screen of the breast cancer genome identifies KIF14 and TLN1 as genes that modulate docetaxel chemosensitivity in triple-negative breast cancer. Clin Cancer Res. 2013;19:2061-70.

[43] Jin JK, Tien PC, Cheng CJ, Song JH, Huang C, Lin SH, et al. Talin1 phosphorylation activates beta1 integrins: a novel mechanism to promote prostate cancer bone metastasis. Oncogene. 2015;34:1811-21.

[44] Tavora B, Reynolds LE, Batista S, Demircioglu F, Fernandez I, Lechertier T, et al. Endothelial-cell FAK targeting sensitizes tumours to DNA-damaging therapy. Nature. 2014;514:112-6.

[45] Calderwood DA, Tai V, Di Paolo G, De Camilli P, Ginsberg MH. Competition for talin results in trans-dominant inhibition of integrin activation. J Biol Chem. 2004;279:28889-95.

[46] Critchley DR, Gingras AR. Talin at a glance. J Cell Sci. 2008;121:1345-7.

[47] Desiniotis A, Kyprianou N. Significance of talin in cancer progression and metastasis. Int Rev Cell Mol Biol. 2011;289:117-47.

[48] Steelman LS, Chappell WH, Abrams SL, Kempf RC, Long J, Laidler P, et al. Roles of the Raf/MEK/ERK and PI3K/PTEN/Akt/mTOR pathways in controlling growth and sensitivity to therapy-implications for cancer and aging. Aging (Albany NY). 2011;3:192-222.
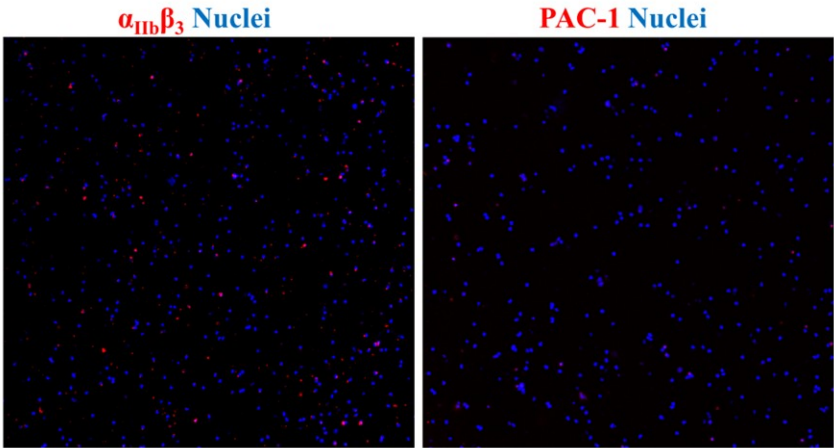
[49] Jeon JS, Bersini S, Whisler JA, Chen MB, Dubini G, Charest JL, et al. Generation of 3D functional microvascular networks with human mesenchymal stem cells in microfluidic systems. Integr Biol (Camb). 2014;6:555-63.

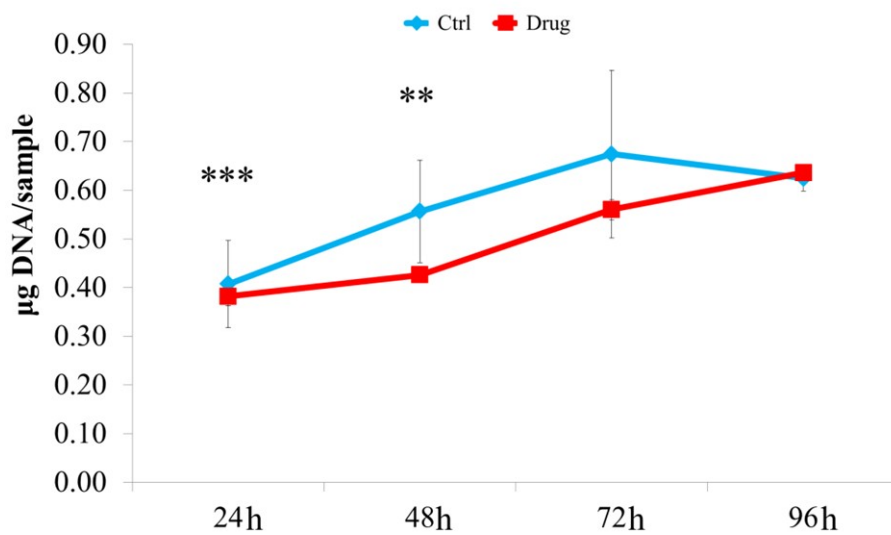[50] Coffelt SB, Wellenstein MD, de Visser KE. Neutrophils in cancer: neutral no more. Nat Rev Cancer. 2016;16:431-46.
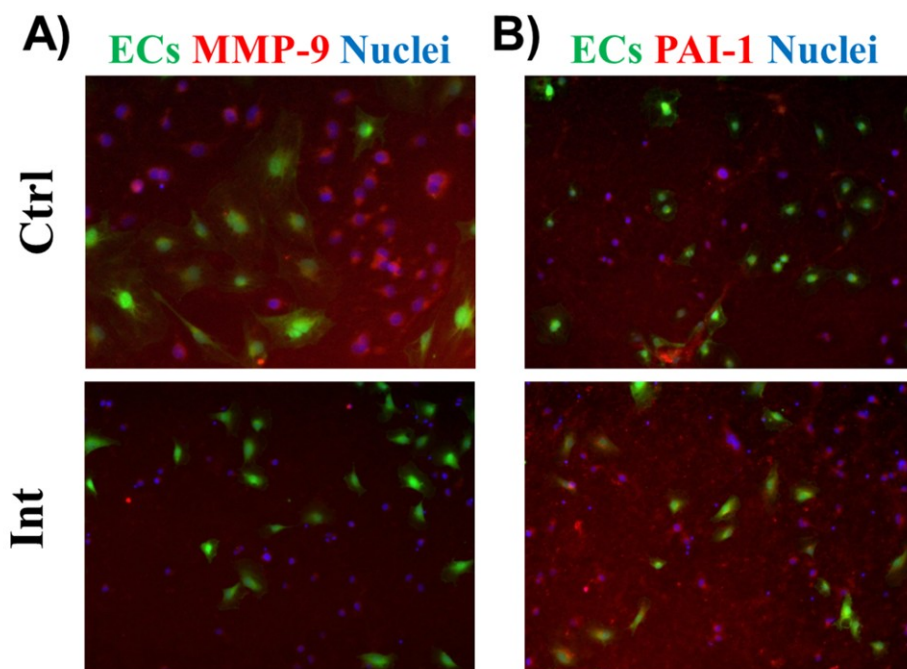
Supplementary Information
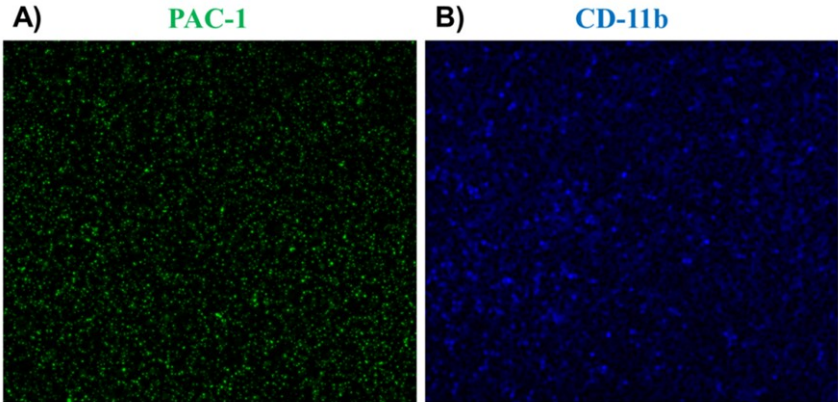
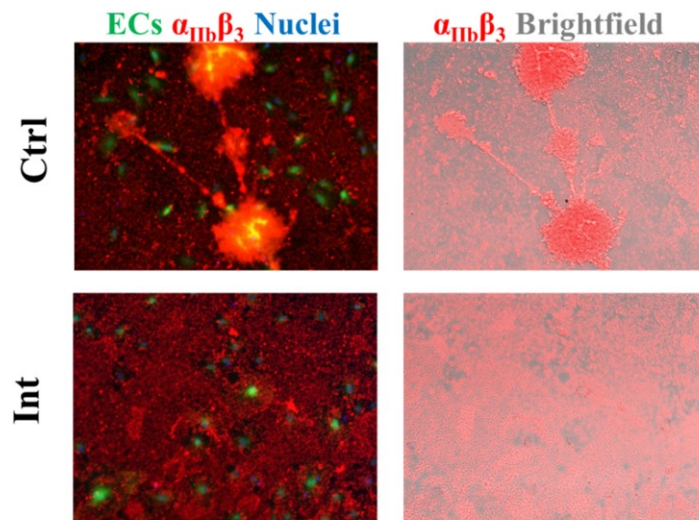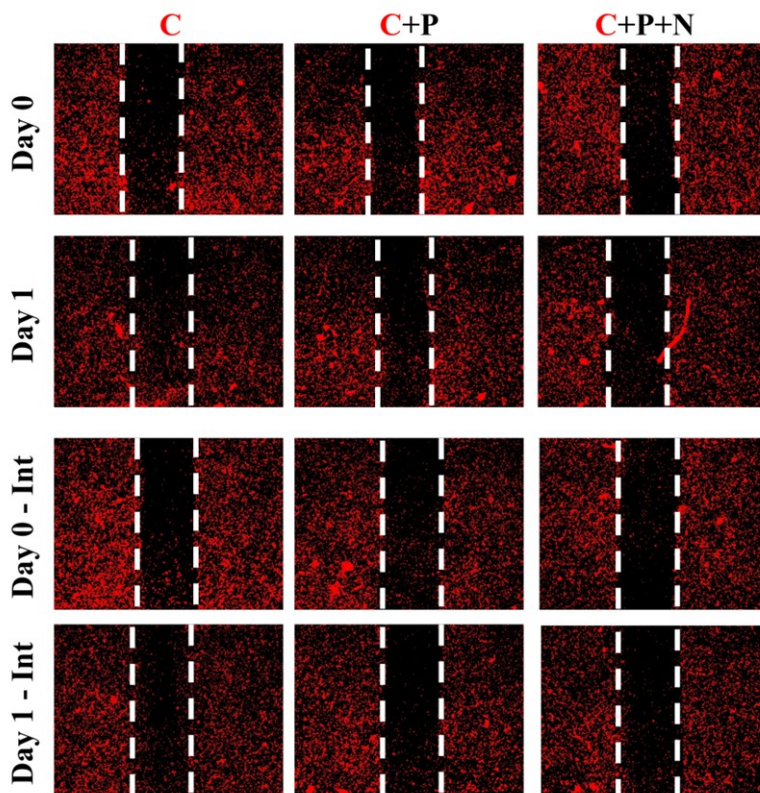**FigS1**

FigS2

FigS3

FigS4

FigS5

FigS6

Conclusions and future perspectives

In the last 30 years in landscape of cancer many progresses have been performed. Most of them has been done in the context of primary tumor treatments. In fact, it is now possible to promptly block tumor growth with surgery due to more sensible predictive analyses which allow to find hided small tumors leading to early diagnosis. Furthermore, in the framework of primary tumor a huge improvement in therapies after the diagnosis has been reported.

Unfortunately for patients with late diagnosis of primary tumor a new challenge arises, the metastasis. Cancer metastasis is the most life-threatening aspect of human cancer and it is responsible for around 90% of cancer patient mortality. Metastases could be found in many tissue in patients causing the death for organ failure. The reason of this dissemination is that cancer cells from a primary tumor can invade and colonize the surrounding tissues. During metastatic progression cancer cells encounter many obstacles. Indeed, metastatic dissemination is an inefficient process as only a small subset of cancer cells in a primary tumor has the potential to form metastases. This process is composed by many steps starting from primary tumor establishment it arises the growth of new blood vessels which also provide an escape route through which cancer cells can enter into the body's circulatory blood system through intravasation. To an effective metastatization, cells must survive to the circulation shear stress and to the with immune system defense until they extravasate towards the secondary organ site. Reached the new organ, cancer cells can enter in a quiescent state (dormancy) or start the growth sustained by the early-metastatic niche leading to the formation of metastasis.

Given that tumor cells can spread early during tumor progression, and it is likely that a subset of escaped cancer cells has already accomplished the early steps of the metastatic process by the time of tumor diagnosis. In fact, in the past, the early

steps of the metastatic cascade are not usually treated as attractive clinical targets. Thus, the later steps including awakening from dormancy, proliferation, growth and survival colonization of the metastatic niche have been considered better targets for therapeutic attack. Indeed, the colonization and dormancy escape can be significantly delayed and metastatic growth occurs over an extended period of time while circulating cancer cell can complete the metastatic process leading to extravasation within a few days. Furthermore, it is widely accepted that metastatic cells can re-seed the primary tumor site and that all the steps occur in parallel and dynamically. In addition, late steps in metastatic dissemination could be affected by cytotoxic or anti-proliferative effect of many traditional anticancer therapies. For these reasons, the early steps of metastatic dissemination may offer new opportunities for therapy development targeting molecular mechanisms belonging to the early metastatic niche such as epithelial–mesenchymal transition, vascular adhesion, trans endothelial migration and early invasion.

In the past, research has been focused mostly on late steps of metastatic progression and for these reasons there are not suitable and reproducible models providing reliable data to analyze the early steps of this cascade. Furthermore, since the endothelium and the circulation play a key role in the interaction among cancer cells and all the actors encountered during the early dissemination, it rises the need to develop vascularized functional models. This approach is required to physiologically analyze and characterize the weaknesses of early steps of metastasis transforming them in new therapeutic targets.

This PhD thesis is devoted to the generation and application of 3D advanced vascularized organ-specific models, which represents a breakthrough in current in vitro cancer related research bridging the gap between in vivo animal models and human body. More in detail, micro and macroscale organ-specific models have been engineered and exploited to investigate cancer cell interaction with the organ specific vascular niche. Indeed, the generation of both micro and macro models in

parallel provided additional tools in the new born landscape of the early metastatic niche.

In the beginning of my PhD trail, I focused on organotropism of breast cancer cells to bone (chapter 1) demonstrating the importance of direct contact of cancer cells with bone-like cells to induce a specific up-regulation of RANKL and clustering in 2D co-culture of human osteo-differentiated mesenchymal stem cells and a bone seeking clone breast cancer cells. Furthermore, given the requirement of functional vessels and 3D structure to reproduce the fine vascularization, cell-cell and cell-matrix interactions typical of the physiological tissues, subsequent efforts in the first year have been focused on this aim.

The novel model presented in Chapter 3 combined a 3D muscle and bone-mimicking microenvironment in microfluidic model embedding human 3D functional and perfusable microvasculature allowing to accurately quantify extravasation rate and migratory behavior of breast cancer cells through high resolution real time confocal imaging. Through this model we demonstrated the preferential tropism of breast cancer cells to bone instead to muscle environment. In addition, we evidenced that organspecific features drives extravasation according with Paget theory instead mechanical properties such as permeability. Noteworthy, the successful reproduction of the organ-specific extravasation in microfluidic device open a new chapter in research allowing the single cell high resolution analyses and the employment of a low number of cells. If this last characteristic of microfluidic provides new possibilities in the context of personalized medicine allowing the use of patient's derived cells and fluids, also evidences the key role of meso-scale models. In fact, once considered the extremely limited number of cells embedded within microfluidic assays it appears clear that genetic and proteomic analyzes are technically challenging. Given the diverse extravasation behavior demonstrated by cancer cell in bone and muscle microenvironments it has been interesting to deepen the role of organ-specificity in

this field. For this reason, in the second year of my PhD period I focused on the development of physiologically-like 3D human vascularized bone and muscle to obtain a reliable platform in which to embed cancer cells and study metastatic progression.

To overcome microfluidic related limitations, the present work reported the development of an innovative technique for the generation an original 3D system based on geometrically controlled poly(methyl-methacrylate) PMMA masks (chapter 4). This novel model has been successfully applied to screen (guided to a statistical software) for the best combination of experimental parameters which lead to the development of an optimized human 3D bone-mimicking tissues embedding osteoblast-like cells, mural cells and microvascular network.

Osteolytic metastases by breast primary tumor into the bone involve a tight cross-talk among cancer cells and osteoblast and osteoclast. Given the requirement of all the elements composing a complete healthy bone to mimic its remodeling, it has been reported the isolation, differentiation and addition of primary osteoclast (chapter 5) and the inclusion of primary osteoblast and resident osteomacs embedded in microvasculature (chapter 7) to the 3D mesoscale bone model, allowing the generation of a 3D human metabolic active vascularized bone.

Beyond the last described complete bone model, we developed an innovative 3D human 3D skeletal muscle environment. This novel mesoscale model, in which to further study cancer homing, was composed by only human primary cells mimicking both, the muscle fibroblasts and mural-cell recruitment to the generated muscle bundles and to the self assembled vessels respectively (chapter 6). In fact, we already demonstrated the inhibitory effect of this tissue in extravasation (chapter 3).

The generated models have been characterized demonstrating both the expression of peculiar markers of bone and muscle resident cells and the functionality of engineered vasculature. A plus of these engineered constructs is that no previously *in vitro* model succeeded in demonstrating that the belonging organ influences not

only the 3D structure of microvasculature but also endothelial gene expression leading to the definition of organ-specific endothelia, a feature up to now only described by *in vivo* observations. These results supported the critical role of endothelium which through the differential expression of adhesive molecules in organotypic vascular beds could drive organ-specific colonization.

Demonstrated the relevance of these 3D new models in the third year of my PhD it has been demonstrated that the presence of early invading breast cancer cells influenced the behavior of each component of the early bone metastatic niche (chapter 7). In particular, cancer cells inside the engineered early metastatic niche polarize macrophages from M2 to M1 and alter the bone metabolism by inducing changes in the RANKL-OPG ratio. Noteworthy, cancer cells once embedded in the engineered muscle niche were not able nor to proliferate neither to elongate becoming dormant. These observations extended my previous observations (chapter 3) that metastatic breast cancer cells cannot extravasate within muscle-mimicking compared to bone-mimicking microenvironments. However, the exact force driving cancer cell preferential extravasation and homing in specific organs is far to be defined.

Generally, the most accepted hypothesis is that the initial delivery and arrest of cancer cells to defined vascular districts it is probably primarily 'mechanical' according with Ewing theory. After that, once seeded the secondary organ cancer cells growth is dependent on the affinity of the 'seed' with the 'soil' according with Paget theory.

In this context, the endothelium starts to get an important consideration in the landscape of the factors driving organotypic metastases. In fact, the last key event of cancer progression before the secondary organ site is the interaction of cancer cells with the vessels through vascular adhesion and sub-sequent trans-endothelial migration (TEM). In particular, in these events, the selective expression of determined receptors in different vascular beds coupled with such subtypes of cancer cells is required.

For the first time in this work (chapter 8) has been described the isolation and characterization of endothelial primary human population from bone and muscle tissue derived from the same human donor.

Differential microarray profiling performed on isolated endothelial mRNA in this project led to the novel theory of the presence of specific endothelia also in human bone and muscle tissues. The rising idea is that this identified feature could be the driver of differential homing of cancer cells in bone and muscle tissue which will be further investigate.

The metastatic spreading is also defined by the expression of specific proteins regulating pseudopodia formation and in migration efficiency. In this framework, integrins and focal adhesion complex proteins are well known to have a central role in cytoskeletal remodeling required for effective ability to generate metastasis. All extravasation steps involve remodeling of endothelial junctions and dramatic changes in cell shape and cytoskeleton. In this context, even though many previous promising results focused on integrin inhibition provide support to potential therapies based on integrin inhibition, dramatic side effects could occur since their involvement in many vital signaling pathways. Despite the challenges it will be important to dissect the integrin downstream signaling pathways focusing on cancer cell specific protein activation limiting therapy side effects in patients to tackle only cancer.

To date, it has been challenging to elucidate the molecular mechanisms driving extravasation because suitable methods to dissect this process across its main steps have been missing. The strength of my interdisciplinary approach lies in the fusion of engineering and biology in the dynamic design of new tools able to adapt to the growing needed of cancer biology questions. This will allow to identify the critical role of key focal adhesion proteins in each step composing extravasation. In particular, we were able to quantitatively discern the contribute of each target and elucidate the extravasation mechanism.

Here, in chapter 9 has been proposed a new hypothesis regarding extravasation driving mechanism induced by the axis CDK-5/TLN-1/FAK^{S732P} acting in different time points of the cascade. In particular, it has been dissected for the first time the role of these key focal adhesion proteins, in different steps of cancer cell extravasation. *In vivo* assays confirmed the reliability of the results obtained through the application of advanced engineered tools. Data proved that vascular adhesion occurs mainly via CDK-5 engagement, and that Tln-1 and FAK are required for TEM and 3D matrix invasion through actin polymerization. In this framework, collected results demonstrated that FAK^{S732} phosphorylation is a key event promoting cancer cell trans-endothelial migration.

Another key aspect during metastatic dissemination is that multiple players establish competitive mechanisms whereby cancer cells upgrade giving rise to different metastatic effects. For instance, platelets contribute to extravasation by wrapping cancer cells in a physical shield protecting them from the bloodstream and prevents the attacks by immune cells. In addition, platelets secrete multiple factors regulating epithelial to mesenchymal transition and cancer cells invasive behavior, as well as the activation of the endothelium and the recruitment of neutrophils and other cell types playing a promotive role in the formation of metastatic niche.

Since the pro-metastatic effect of platelets in early metastatic niche formation and their regulator role in metastatic progression, in chapter 10 has been analyzed the effect of an approved drug acting on platelet activation (αIIbβ3 integrin).

More in detail, the hypothesis was that αIIbβ3 inhibition will lead to anti-metastatic action tackling platelet effects such as the recruitment of immune cells and endothelial activation in the early metastatic niche. Furthermore, given the wide expression of these integrins in different cells composing the early metastatic niche we hypothesized that inhibition of this protein may affect multiple components of the early metastatic niche. Thus, the anti-metastatic effect could be synergistically supported by drug action throughout the entire niche. Hence, the aim of the present

work was to analyze the effect of αIIbβ3 inhibitor on CC extravasation and elucidate the mechanisms of action of the drug on each component of the early metastatic niche. To reach the goal, traditional multi-culture experiments have been coupled with advanced 3D vascularized microfluidic models. We found that inhibition of αIIbβ3 integrin is a key modulator of the cellular interactions among early metastatic niche components. In addition, we demonstrated the existence of a new signaling pathway acting through αIIbβ3 integrin which is involved in endothelial junction regulation. In particular, we demonstrated that the inhibition of αIIbβ3 integrin impairs VE-cadherinY658 phosphorylation and its nuclear internalization, thus maintaining endothelial junction functionality and limiting CC extravasation.

It is well known that cancer metastasis is a complex phenomena dependent of many factors such as primary tumor genetic expression, immune cells, vascularization secondary organ site characteristics and circulatory system. Although, this plethora of interactors has been identified, however how cancer cells precisely interact with all of them is still to be elucidated. Furthermore, it will be essential to understand the timing of these interactions aimed to the generation of tuned therapies also in terms of the timing of drug administration in patient metastatic progression.

As evidenced in this section, the novelty of this doctoral thesis is constituted by the interdisciplinary approach combining engineering and biology generating a more detailed map of the cellular mechanisms on which the metastatic progression lies. All these objectives were reached through the combination of micro and macroscale models representing a new breakthrough in modern research to analyze cell-cell, cell-matrix crosstalk and new drugs and dosage effects in biophysically and biochemically controlled condition closely mimicking the human body.

In addition, in this work it appears clear the fact that muscle environment hinders metastatic progression. From here, it emerges that it will be important to focus not

only on the organ whereby a primary tumor spread and thrives. Contrariwise, the identification of molecules present in "the not preferential homing site" such as adenosine, could become a new source of inspiration for new therapies.

Furthermore, the focus on the steps composing the metastatic cascade revealed the central role of endothelium in primary cancer growth, spread and metastatic survival in secondary organ site. In particular, this PhD thesis evidences the presence of endothelial specific signatures hided in the genetic profile of different human endothelial cells, specifically bone and muscle. If these new identified features can be the responsible organ tropism of metastases is still an important question to be clarified.

The dissection of focal adhesion pathway in extravasation has led to the identification of new targets specifically related to extravasation efficiency including TLN-1 and FAK phosphorylation. These finding highlight the clear need to increase the efforts to better investigate in detail the underlying mechanisms involving the emerging role of protein post translational modification in specific steps of metastasis. This new direction should be coupled with efforts in chemical and synthesis research which will lead to more specific inhibitors. Finally, tackle only specific cancer mechanism, going beyond already developed molecules targeting also important function in heathy tissues that cause strong side effects.

The results obtained in this thesis suggest to improve the efforts to the employment of already existing drugs from new point of view. This approach lead to the advantage that already approved drugs have well characterized side effects and they could move from the bench to bed side quickly avoiding already performed prolonged and retarding clinical trials.

Moreover, to really impact the clinical side, engineered models could be employed such as drug screening platform. An other facet of this approach is the possibility to

realize different engineered human 3D organs and to link them each other to test the effect of many drugs or developed side-metabolites in a body-like platform.

Furthermore, given the power of developed microfluidic model to answer biological question in a reliable human environment employing only few cells, rises the possibility of an effective personalized medicine. In this context, highly tailored treatments according with the specific response of patient derived cells embedded in microfluidic tools could be developed improving the efficacy of the existing treatments.

All the experience generated in this 3 years trail lead me to conclude that an interdisciplinary approach in research appear to be the ideal strategy to bridge the gap between simplified *in vitro* and *in vivo* animal models. This will contribute to the reduction in the costs associated with clinical trials failure. Furthermore, I would add that there no yet perfect models to employ, nor *in vivo* neither *in vitro*, there is just more suitable models compared to other depending on the application. In fact, it resides in the abilities of each individual researcher to understand which model interrogate to get the sought answers.